

Advanced Structured Materials

Andreas Öchsner
Holm Altenbach *Editors*

Improved Performance of Materials

Design and Experimental Approaches

 Springer

Advanced Structured Materials

Volume 72

Series editors

Andreas Öchsner, Southport Queensland, Australia

Lucas F.M. da Silva, Porto, Portugal

Holm Altenbach, Magdeburg, Germany

More information about this series at <http://www.springer.com/series/8611>

Andreas Öchsner · Holm Altenbach
Editors

Improved Performance of Materials

Design and Experimental Approaches

 Springer

Editors

Andreas Öchsner
Griffith School of Engineering
Griffith University (Gold Coast Campus)
Southport, QLD
Australia

Holm Altenbach
Faculty of Mechanical Engineering,
Institut für Mechanik
Otto-von-Guericke-University Magdeburg
Magdeburg
Germany

ISSN 1869-8433

Advanced Structured Materials

ISBN 978-3-319-59589-4

DOI 10.1007/978-3-319-59590-0

ISSN 1869-8441 (electronic)

ISBN 978-3-319-59590-0 (eBook)

Library of Congress Control Number: 2017940822

© Springer International Publishing AG 2018

This work is subject to copyright. All rights are reserved by the Publisher, whether the whole or part of the material is concerned, specifically the rights of translation, reprinting, reuse of illustrations, recitation, broadcasting, reproduction on microfilms or in any other physical way, and transmission or information storage and retrieval, electronic adaptation, computer software, or by similar or dissimilar methodology now known or hereafter developed.

The use of general descriptive names, registered names, trademarks, service marks, etc. in this publication does not imply, even in the absence of a specific statement, that such names are exempt from the relevant protective laws and regulations and therefore free for general use.

The publisher, the authors and the editors are safe to assume that the advice and information in this book are believed to be true and accurate at the date of publication. Neither the publisher nor the authors or the editors give a warranty, express or implied, with respect to the material contained herein or for any errors or omissions that may have been made. The publisher remains neutral with regard to jurisdictional claims in published maps and institutional affiliations.

Printed on acid-free paper

This Springer imprint is published by Springer Nature

The registered company is Springer International Publishing AG

The registered company address is: Gewerbestrasse 11, 6330 Cham, Switzerland

Preface

There is a permanent demand to improve the properties and performance of engineering materials and structures. Competitiveness due to cost efficiency (e.g. lighter structures and the corresponding fuel savings for transportation systems) or sustainability (e.g. recyclability or reusability) are nowadays the driving factors for engineering developments. The outcomes of these efforts are difficult to be accurately monitored due to the ongoing evaluation cycles. Thus, this monograph aims at presenting a snapshot of recent developments. The properties covered are related to classical fields of mechanical, thermal, electrical and optical properties as well as related to surface-specific quantities (e.g. roughness, wear and modifications due to surface coatings). The material types which are collected in this monograph range from classical metals, over synthetic materials to composites.

We would like to express our sincere appreciation to the representatives of Springer, in particular to Dr. Christoph Baumann, Senior Editor Engineering, who made this volume possible.

Southport, Australia
Magdeburg, Germany

Prof. Dr.-Ing. Andreas Öchsner D.Sc.
Prof. Dr.-Ing. habil. Dr. h. c. mult. Holm Altenbach

Contents

Optimization on Wear Performance of Anti Wear Additive Added Biolubricant	1
M.H. Sakinah, M.A. Hassan, K. Kadirgama, Ganesan Kadirgama, D. Ramasamy, A.K. Amirruddin, M.M. Rahman and M.M. Noor	
Effect of Friction Stir Welding Parameters on the Peak Temperature and the Mechanical Properties of Aluminum Alloy 5083-O	11
Mostafa M. El-Sayed, Ahmed Y. Shash, Tamer S. Mahmoud and Mahmoud Abd Rabbou	
Artificial Neural Networks Prediction of Rubber Mechanical Properties in Aged and Nonaged State	27
Ivan Ružiak, Pavel Košťal, Zora Jančíková, Milada Gajtanska, Luboš Krišťák, Ivan Kopal and Peter Polakovič	
Semi-automated Gating System Design with Optimum Gate and Overflow Positions for Aluminum HPDC	37
Mohamed Refaat Abo El-Fotouh, Ahmed Yehia Shash and Mohamed Hasan Gadallah	
Dielectric Material Selection Optimization Based on Relative Dielectric Constant Dependencies in Operating Environment	53
Ivica Kuzmanić, Igor Vujović and Joško Šoda	
New Morphology of a Silver Chloride Surface Grown on Silver Wires	63
Salah Seghir Mechaour, Akila Derardja, M. Jamal Deen and Ponnambalam Ravi Selvaganapathy	
Development of Highly Effective Multiplex Integration Electric Charging Module for Range Extension of Hybrid Type Refrigeration Truck	73
Kee Joo Kim	

Experimental Numerical Model of Roughness in Finishing Face Milling of AISI 4140 Hardened Steel	83
Marco Stipkovic Filho, Marco Antônio Stipkovic, Éd Cláudio Bordinassi, Sérgio Delijaicov and Sérgio Luis Rabelo de Almeida	
A Flexible Numerical Framework for Engineering—A Response Surface Modelling Application	93
P. Viviani, M. Aldinucci, R. d’Ippolito, J. Lemeire and D. Vucinic	
Monitoring of the Thermal Properties of Cement Composites with an Addition of Steel Slag	107
Vojtěch Václavík, Milena Kušnerová, Tomáš Dvorský, Vojtěch Šimíček, Jan Valíček, Lukáš Gola and Marta Harničárová	
Plywood Experimental Investigation and Modeling Approach for Static and Dynamic Structural Applications	119
Samara Jadi Cruz de Oliveira, Ophelia Bolmin, Michel Arrigoni and Christian Jochum	
Monochrome Multitone Image Approximation on Lowered Dimension Palette with Sub-optimization Method Based on Genetic Algorithm	143
Rudolf Neydorf, Albert Aghajanyan, Anna Neydorf and Dean Vučinić	
“Cut-Glue” Approximation Method for Strongly Nonlinear and Multidimensional Object Dependencies Modeling	155
Rudolf Neydorf, Anna Neydorf and Dean Vučinić	
Robot Path Planning Based on Ant Colony Optimization Algorithm for Environments with Obstacles	175
Rudolf Neydorf, Orhan Yarakhmedov, Victor Polyakh, Ivan Chernogorov and Dean Vucinic	
“Cut-Glue” Approximation Based on Particle Swarm Sub-optimization for Strongly Nonlinear Parametric Dependencies of Mathematical Models	185
Rudolf Neydorf, Ivan Chernogorov, Orkhan Yarakhmedov, Victor Polyakh and Dean Vucinic	
Computational Evaluation of Transverse Thermal Conductivity of Natural Fiber Composites	197
Zia Javanbakht, Wayne Hall and Andreas Öchsner	
Morphology and Elemental Composition of Metal Based Granules in Wings of Bumblebees	207
Kateřina Dědková, Petr Jandačka, Rostislav Váňa, Jana Kukutschová and Nikola Vítkovská	

Modifications of Viscoelastic Properties of Natural Rubber/Styrene-Butadiene Rubber Blend by Electron Beam Irradiation.	219
Ivan Kopal, Pavel Košťal, Zora Jančíková, Jan Valíček, Marta Harničárová, Peter Hybler and Milena Kušnerová	
Chosen Electrical Properties of Montmorillonite/Polyaniline Composites.	231
Pavel Košťal, Ondrej Bošák, Ivan Kopal, Zora Košťalová Jančíková, Jan Valíček and Marta Harničárová	
Improvement of Optical Properties of White LED Lamps Using Green-Emitting Ce0.67Tb0.33MgAl11O19:Ce,Tb Phosphor	239
Nguyen Doan Quoc Anh and Nguyen Ngoc Long	
“Cut-Glue” Approximation Based on Pseudo-genetic Algorithm for Strongly Nonlinear Parametric Dependencies of Mathematical Models	245
Rudolf Neydorf, Victor Polyakh, Ivan Chernogorov, Orhan Yarahmedov and Dean Vucinic	
Design and Manufacturing of a Dry Electrode for EMG Signals Recording with Microneedles	259
Araceli Guadalupe Santana Rayo, Luis Héctor Hernández Gómez, Alejandro Tonatiu Velázquez Sánchez, Juan Alfonso Beltrán Fernández, Juan Alejandro Flores Campos, Guillermo Urriolagoitia Calderón, Víctor Manuel Santana Rayo and Arturo Enrique Flores Peñaloza	
Biped Robot Prototype Based on the Human Anthropometric Measurements	269
David Alvarado, Leonel Corona, Saúl Muñoz, Alfonso Campos and Alejandro Escamilla	

Optimization on Wear Performance of Anti Wear Additive Added Biolubricant

M.H. Sakinah, M.A. Hassan, K. Kadirgama, Ganesan Kadirgama, D. Ramasamy, A.K. Amirruddin, M.M. Rahman and M.M. Noor

Abstract Waste cooking oil is hard to dispose of and harmful to the environment. Recently, a considerable amount of research has been done to improve the properties of engine oil. In this study, engine oil was blended with waste cooking oil and an oil treatment solution. The blended oil was tested in a tribological wear tester. There are three parameters (rotational speed, loads and ratio of waste cooking oil) was consider in the experiments. Tribology wear and properties of the blended oil were investigated in FESEM. It was found that abrasive wear, adhesive wear, fatigue wear and corrosive wear were introduced during the course of the experiments. Normally, corrosive wear was found to be the main dominant in the tribology wear. It was discovered that 5% addition of waste oil to the engine oil treatment and base lubricant performed better than other oil blends.

Keywords Lubricant · Speeds · Engine · Waste

M.H. Sakinah · M.A. Hassan · K. Kadirgama (✉) · G. Kadirgama · D. Ramasamy
A.K. Amirruddin · M.M. Rahman · M.M. Noor
Faculty of Mechanical Engineering, Universiti Malaysia Pahang, 26600 Pekan,
Pahang, Malaysia
e-mail: kumaran@ump.edu.my

M.H. Sakinah
e-mail: sakinah.hisham0704@gmail.com

G. Kadirgama
e-mail: knight_35@hotmail.com

D. Ramasamy
e-mail: Deva@ump.edu.my

A.K. Amirruddin
e-mail: Amirruddin@ump.edu.my

M.M. Rahman
e-mail: Mustafizur@ump.edu.my

M.M. Noor
e-mail: Muhamad@ump.edu.my

1 Introduction

Lubricants are widely used in all fields of manufacturing and industrial applications and commonly used to reduce overheating and friction in a variety of engines, machinery, turbines, and gearboxes. They can also aid in maintaining reliable machine functions, expedite operations and the smooth operations and reduce the risks of failure. Furthermore, lubricants can reduce wear and heat loss from the contact of surfaces in motion, prevent rust, reduce oxidation on the contact surfaces and to act as a seal against dirt, dust and water [1]. Due to that, Therefore, petroleum was initially used as the main base stock lubricant, due to its low cost and superior performance. Unfortunately, the rising price of crude oil all over the world, the environmental awareness from various sectors and the depletion of the crude oil spurred scientists to start developing an alternative fuel and lubricant product from natural resources and agricultural feedstock aiming to replace the fossil products [2]. From the reported works, alternative forms of oil should increase to a volume about 36 billion gallons in 2022 [3]. From 2010 until now, several biolubricants are under investigation in different countries [4], e.g., soybean oils (The USA and South America), rapeseed oil (Europe), *Jatropha* oil [5, 6] and palm oil, (Asia), [7–10]. Most of the works show results regarding their properties. It was noted that vegetable oil-based bio-lubricants exhibit a high results on their properties and it was perceived that using vegetable oil-based bio-lubricants exhibits high lubricity, a high viscosity index (VI), high flash point and low evaporative losses. Moreover, researchers have reported that biolubricants provide better lubricity than petroleum-based oils [11]. Waste cooking oil can be considered the most promising bio-oil feedstock. As reported by many researchers, bio-fuels produced from waste cooking oils have numerous advantages such as low pollution (CO_2 , CO and NO_x), low cost and acceptable brake specific fuel consumption. Interest has drawn towards the potential of using waste cooking oil as a lubricant. Kalam [12] experimentally investigated the friction and wear characteristics of a normal lubricant, that is, an additive added lubricant and waste vegetable oil (WVO)-contaminated lubricants. The WVO-contaminated lubricants with amine phosphate as antiwear additive reduced the wear and friction coefficient and increased viscosity. Thus, waste palm oil with a normal lubricant and amine phosphate additive could be used as a lubricant substitute (maximum 4%). Based on four ball tribo testing results, the WVO contaminated lubricant with the presence of antiwear additives shows promising result to do better thermal and oxidative properties of waste vegetable oil consisting long chain saturated fatty acids [13]. Tribological behaviour measurements/factors such as the coefficient of friction (COF), specific wear rate and wear mechanism, play an important role in identifying the tribological performance of the bio-lubricant. In an internal combustion engine, mechanical friction occurs between engine components in contact with each other leading to wear and significant loss of efficiency. Loss of energy due to friction between the piston ring and cylinder liner constitutes 20–40% of total mechanical loss and is regarded as the greatest mechanical friction loss [14]. Different engine lubrication

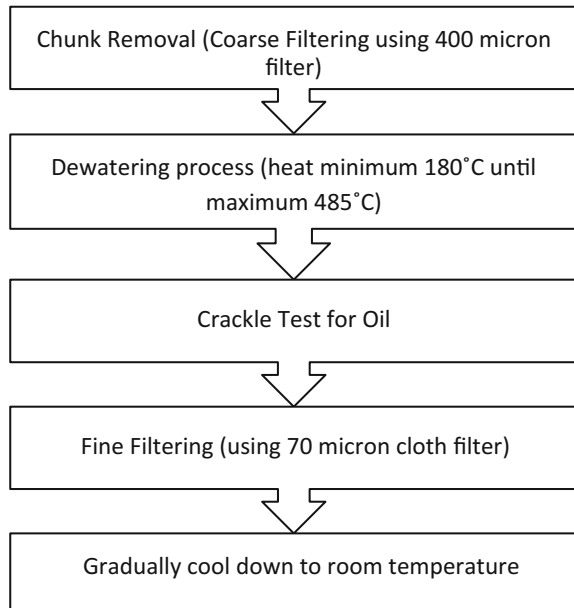
regimes significantly affect the tribological performance of the engine [15]. Wear occurs on all sliding surfaces. Since wear is a chaotic process, wear studies are mostly hence wear studies are mostly done experimentally due to the limited ability to accurately to simulate wear [16]. There are several mechanisms of wear which include seizure, melting, oxidation, adhesion, abrasion, delamination, fatigue, fretting, corrosion, and erosion [17]. A better lubricant which has great properties can reduce the amount of wear loss. The main objective of this study is to modify the current engine oil properties with waste cooking oil to reduce wear.

2 Experimental Setup

The base oil that was used in this experiment is SAE 40. The oil was obtained from the hostel cafeteria. For the preparation of waste cooking oil as bio-lubricant, waste cooking oil undergoes three different processes: coarse filtering, dewatering, and fine filtering. Figure 1 shows the schematic diagram for the filtration of waste cooking oil. Three samples were explicitly prepared, namely, Sample A which is SAE 40 as a reference lubricant (0% volume composition of waste oil), Sample B which are composed of 95% SAE 40+ 5% waste oil added with 0.3% oil treatment (EOT), Sample C, which is composed of 90% SAE 40+ 10% waste oil added with 0.3% (EOT) oil treatment.

The wear test was conducted under the lubricated sliding condition in compliance with ASTM G133-05 standard. The wear testing involves making linear

Fig. 1 Schematic diagram for filtration of waste cooking oil



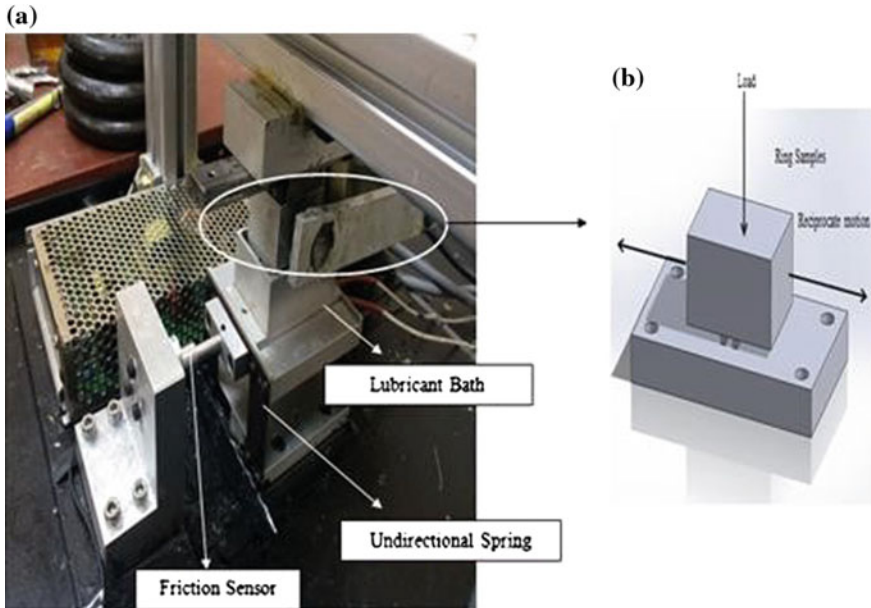


Fig. 2 Experimental setup

movements similar to a cylinder-piston pair operating under real conditions. Figure 2 depicts the wear tester. Normal loads applied to the device by hanging weights on the bearing lever where the piston ring sample is attached in order to produce the desired load. The test will be conducted at engine speed at 200–300 RPM with normal loads 2–9 kg. The temperature that will be used is room temperature and the operating time is 10 min per specimen. The coefficient of Friction (COF) was measured using ARDUINO and the wear rate was determined via weight differences using a weighing scale with a sensitivity of 0.1 mg. The test conditions are presented in Table 1.

The type of material for specimen used in this experiment is Aluminium 6061-T6 which is the material that commonly used for the piston. Flatbar Aluminium 6061-T6 was cut using a band saw and each specimen was prepared 45.12 mm long, 25.14 mm wide and 6 mm thickness. The block was drilled to each side of the rectangle using 4 and 6 mm drill bit. The chemical and physical properties for Aluminium 6061-T6 are shown in the Tables 2 and 3 [18, 19].

Table 1 Tribology test condition

Test specifications	Values
Load, kg	2.0–9.0
Engine Speed, rpm	200–300
Temperature	Room temperature
Operating time	10 min per specimen

Table 2 Chemical composition for Aluminium 6061-T6

Sample	Al	Cr	Cu	Fe	Mg	Mn	Si	Ti	Zn
Percentage (wt%)	95.8	0.04	0.15	0.7	0.8	0.15	0.4	0.14	0.25

Table 3 Physical properties of Aluminium 6061-T6

Properties	Value
Density (g/cc)	2.7
Thermal conductivity (W/m-K)	167
Modulus of elasticity (GPa)	68.9
Specific heat capacity (J/g.°C)	0.896
Melting point (°C)	652

3 Result and Discussion

3.1 Physico-Chemical Properties of Waste Cooking Oil in Base Lubricant

The data were used to evaluate the differences between base lubricant stock (SAE 40) and to serve as a basis for comparing the blended lubricant of palm oil and waste oil. Table 4 shows the properties of base oil (SAE 40), palm oil and waste oil. A good lubricant should have a high boiling point, adequate viscosity, low freezing point, high oxidation resistance, non-corrosive properties and good thermal stability. The most important property of oil is viscosity. It indicates resistance to flow and is directly related to temperature, pressure, and film formation. High viscosity initiates low resistance to flow [1]. Lubricants generally are less dense than water. If the density of an object is less than that of water, then that object will float. This is why if there is a moisture problem in the lubrication system that the water settles to the bottom of the sump and is drained out first whenever the plug is pulled or the valve is opened. The density of a lubricant fluid can provide indications of its composition and nature [20]. Less moisture content in lubricating oil also indicates rust and corrosion prevention.

Table 4 Properties of oil and blended oil

Properties	SAE 40	Waste oil	5% waste oil + SAE 40+ 0.3% EOT	10% waste oil + SAE 40+ 0.3% EOT
Viscosity (mpa.s)	179.2	180.6	176.0	163.2
Density (g/cm ³)	0.8609	0.9049	0.8624	0.8644
Moisture content (%)	0.19	0.28	0.14	0.19

3.2 Microstructure and Wear Mechanism

There are various types of wear in a mechanical systems such as abrasive wear, adhesive wear, fatigue wear and corrosive wear. Since the lubricant regime occurred in this experiment was boundary lubrication, therefore, abrasive wear, adhesive wear, fatigue wear and corrosive wear were observed in the wear regions [7]. There were many deep furrows and some corroded areas can be easily seen on surface lubricated with lubricant sample C as shown in Fig. 3a whereas the surface lubricated with lubricant sample A and lubricant sample B are relatively smooth although mark with wear debris due to the rough surface layer on the hard surface from the liner samples touched the soft surface for the piston samples and had close relationships with the thickness of lubricant film as shown in. According to earlier studies, corrosive wear is the main wear mechanism [21] for biolubricant and since the moisture content in the waste oil high which is 0.28% it does give the corrosion effect on the specimen. In sample C it was also observed that the surface of the pins was damaged due to adhesion [22], eventually leading to scuffing and tribochemical reactions of sliding contact surfaces as shown in Fig. 3b.

FESEM images of the aluminium plate were obtained using various types of volume concentrations of waste cooking oil blended with engine oil. Referring to Fig. 4, it was found that the honing lines decrease at 5% concentration compare with SAE 40 and wear start to increase when using 10% waste oil concentration [21]. This is due to 5% concentration of waste oil shows the highest viscosity results when compared to 10% concentration because high viscosity (thick) engine oils help to maintain a barrier between moving part and also drag in the movements between two contact surfaces. 10% also show the corroded area on the specimen [19]. According to EDX analysis as in Fig. 4, all specimens have a low percentage of oxygen in the surface of the specimen.

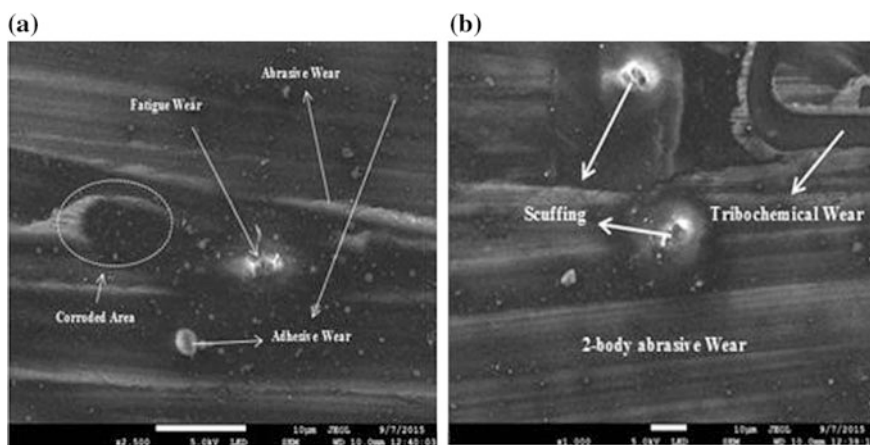


Fig. 3 a Sample C with 2500X magnification; b Sample C with 1000X magnification

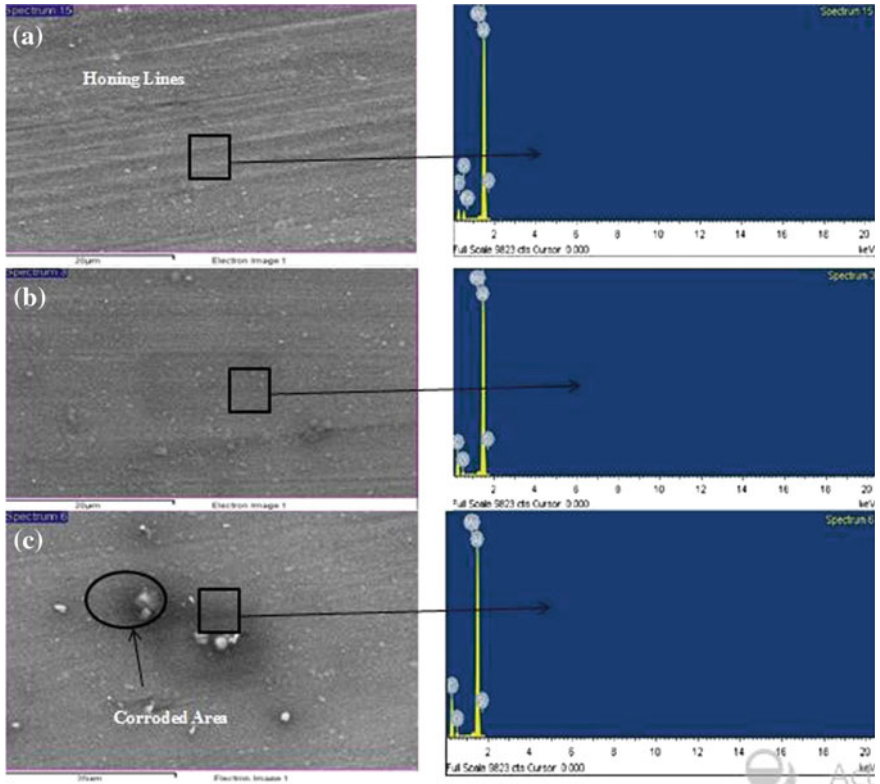


Fig. 4 a Sample A; b Sample B; Sample C

That means the oxidation occurs during the sliding process due to the water content in the waste palm oil.

4 Conclusion

Based on the experimental study,

- (a) According to SEM analysis on the worn surfaces, the maximum wear occurs on at 10% waste oil concentration, while minimum wear occurs at 5% waste oil concentration. concentration of waste oil while minimum wear occurs in 5% concentration waste oil. This shows that waste cooking oil has anti-wear characteristics when small amounts of waste cooking oil are present, and means that using waste cooking oil as an additive for engine oils will not have any severe wear causing consequences, which could potentially lead to premature failure.

- (b) In terms of their physico-chemical properties, 5% waste oil added with engine oil treatment were almost identical with the base lubricant.
- (c) Engine lubricants formulated from waste oils are renewable, eco-friendly and biodegradable. However, the challenge is an improvement of their performance specifically, with reference to their oxidative stability.

References

1. Mobarak HM et al (2014) The prospects of biolubricants as alternatives in automotive applications. *Renew Sustain Energy Rev* 33:34–43
2. Arumugam S, Sriram G (2012) Effect of bio-lubricant and biodiesel-contaminated lubricant on tribological behavior of cylinder liner-piston ring combination. *Tribol Trans* 55(4):438–445
3. Sadaka S, Boateng AA (2009) Pyrolysis and bio-oil. Cooperative Extension Service, University of Arkansas, US Department of Agriculture and county governments cooperating
4. Ting C-C, Chen C-C (2011) Viscosity and working efficiency analysis of soybean oil based bio-lubricants. *Measurement* 44(8):1337–1341
5. Mofijur M et al (2012) Prospects of biodiesel from *Jatropha* in Malaysia. *Renew Sustain Energy Rev* 16(7):5007–5020
6. Shahabuddin M et al (2013) Comparative tribological investigation of bio-lubricant formulated from a non-edible oil source (*Jatropha* oil). *Ind Crops Prod* 47:323–330
7. Cheenkachorn K, Fungtammanan B (2010) Development of engine oil using palm oil as a base stock for four-stroke engines. *Energy* 35(6):2552–2556
8. Syahrullail S et al (2011) Experimental evaluation of palm oil as lubricant in cold forward extrusion process. *Int J Mech Sci* 53(7):549555
9. Jayed MH et al (2009) Environmental aspects and challenges of oilseed produced biodiesel in Southeast Asia. *Renew Sustain Energy Rev* 13(9):24522462
10. Maleque MA, Masjuki HH, Haseeb ASMA (2000) Effect of mechanical factors on tribological properties of palm oil methyl ester blended lubricant. *Wear* 239(1):117–125
11. Jayadas NH, Prabhakaran Nair K, Ajithkumar G (2007) Tribological evaluation of coconut oil as an environment-friendly lubricant. *Tribol Int* 40(2):350–354
12. Kalam MA, Masjuki HH (2002) Biodiesel from palmoil—an analysis of its properties and potential. *Biomass Bioenerg* 23(6):471–479
13. Zeman A et al (1995) Biodegradable lubricants—studies on thermo-oxidation of metalworking and hydraulic fluids by differential scanning calorimetry (DSC). *Thermochim Acta* 268:9–15
14. Çakir M, Akçay IH (2014) Frictional behavior between piston ring and cylinder liner in engine condition with application of reciprocating test. *Int J Mater Eng Technol* 11(1):57
15. Cesur İ et al (2014) The effects of different fuels on wear between piston ring and cylinder. *Adv Mech Eng* 2014:1–8
16. Stachowiak GW, Batchelor AW, Stachowiak GB (2004) 2—Simulation of wear and friction. In: Gwidon AWB, Stachowiak W, Grazyna BS (ed) *Tribology series*, Elsevier, pp 13–23
17. Mehta DS, Masood SH, Song WQ (2004) Investigation of wear properties of magnesium and aluminum alloys for automotive applications. *J Mater Process Technol* 155–156:1526–1531
18. Holt JM (Tim), T.E.C.Y.H. (1996) *Structural alloys handbook*. CINDAS/Purdue University, West Lafayette, IN
19. Boyer HE, Gall TL (1985) *Metals handbook*. American Society for Metals, Materials Park, OH

20. Zulkifli NWM et al (2013) Wear prevention characteristics of a palm oil-based TMP (trimethylolpropane) ester as an engine lubricant. *Energy* 54:167–173
21. Lee EJ et al (2010) Morphology and toughness of abrasive particles and their effects on the friction and wear of friction materials: a case study with zircon and quartz. *Tribol Lett* 37 (3):637–644
22. Masjuki HH, Maleque MA (1996) The effect of palm oil diesel fuel contaminated lubricant on sliding wear of cast irons against mild steel. *Wear* 198(1–2):293299

Effect of Friction Stir Welding Parameters on the Peak Temperature and the Mechanical Properties of Aluminum Alloy 5083-O

Mostafa M. El-Sayed, Ahmed Y. Shash, Tamer S. Mahmoud and Mahmoud Abd Rabbou

Abstract In the present investigation, a 3D transient heat transfer model is developed to simulate the thermal distribution of aluminum alloy 5083-O friction stir welded by using Abaqus software. A 6 mm AA5083-O plates were friction stir welded at different conditions; two tools with tapered smooth and cylindrical threaded pin profiles, and 50, 100, 160 mm/min welding speeds at a constant rotational speed of 400 rpm. The temperature was measured using an infrared thermal image camera during the welding process at each operation condition. The measured temperature by IR camera was compared with temperatures obtained using the Abaqus. The welded joints were checked by visual inspection, macrostructure and microstructure evolution, in addition to tensile strength and hardness profiling. The welding speed and tool pin profile variations have a small effect on the peak temperature of the welded joints. The defect free welded joints were obtained at 50, 100, 160 mm/min welding speeds using a threaded tool pin profile. The tensile strength values obtained by using a threaded tool pin profile at all welding speeds are better than those obtained by using a tapered tool pin profile where the best one is at 50 mm/min welding speed. In terms of hardness results, the threaded tool pin profile gives better results at all welding speeds than the tapered tool pin profile.

Keywords Friction stir welding · Tool pin profile · Mechanical properties · Finite element modeling

M.M. El-Sayed · A.Y. Shash (✉) · T.S. Mahmoud · M.A. Rabbou
Mechanical Design and Production Engineering Dept, Cairo University,
Giza 12311, Egypt
e-mail: ahmed.shash@cu.edu.eg

M.M. El-Sayed
e-mail: mostafamohammed30@yahoo.com

M.A. Rabbou
e-mail: mahmoud.abdrabou@gmail.com

1 Introduction

Friction Stir Welding (FSW) was invented by Wayne Thomas at TWI (The Welding Institute), in the UK in 1991. FSW is a solid state joining process, in which the objects are welded together without reaching the melting point of the base metal [1].

In FSW, a non-consumable shouldered tool with a profiled pin is rotated and immersed into the abutting faces of work-pieces, thereby generating frictional heating at tool-work piece interface, leading to softening of the work-piece material. After that, the tool is moved along the joint line producing a continuous welded joint [2].

FSW is considered to be environmentally friendly because there is no cover gas. Since no melting occurs during FSW, it can be used for joining the 2xxx and 7xxx aluminum alloys which are difficult to weld using traditional methods due to the poor solidification of the microstructure and porosity in the fusion zone. Also, it can be used for welding any kinds of materials, material composites, and dissimilar materials, with ease [3].

These days, FSW is applied in many industries such as: aerospace, shipbuilding and automotive industries [4].

There are many parameters affecting the mechanical properties and microstructure of friction stir welded joints. These parameters are: tool design, rotational speed, welding speed, axial force, plunge depth and tool tilt angle. Rotation speed affects the frictional heat, welding speed control which affects the heat generated, tool tilt angles which affects the efficiency of the weld, plunge depth which produces sound welds, axial force which generates further heating and tool design which affects the flow and the power required for the process [5].

The microstructure of aluminum friction stir welded joints is classified into four zones. This classification is based on the effect of the heat and plastic deformation on the material. These zones are: the first one is an unaffected zone in which neither heating nor plastic deformation affect the microstructure of the material. The second one is the heat affected zone (HAZ) which is adjacent to the unaffected zone, where the heat generated has no effect on the microstructure of the material. The third one is the thermo-mechanically affected zone (TMAZ) which is adjacent to the HAZ, where both heat and plastic deformation affect the microstructure but, there is no recrystallization occurred because the deformation strain is not enough. The fourth one is the dynamically recrystallized zone (DXZ) which is lying in the weld center line beside the TMAZ and subject to both higher deformation strain and higher temperature which cause recrystallization of the material resulting in finer grains sizes [6].

Many investigators [7–11] have studied and reported on the effect of FSW parameters on the mechanical properties and microstructure of friction stir welded aluminum joints.

FSW has three main phases: the plunge phase, dwell phase and welding phase [7]. The generated heat from the FSW process is frictional heat and plastic dissipation heat generation. The first one is due to the contact between the tool and work-piece, while the second one is due to plastic energy dissipation [12].

Since FSW has both thermal and mechanical loads, simulation of that process is quite complicated to obtain the thermal history and stresses produced from it. Some investigators have built a heat transfer model to predict the temperature distribution during the FSW process, while others have built a thermo-mechanical model to simulate the plunge phase during the process. However, a few investigators have built a heat and material flow models to simulate the flow of material during the process [13].

2 Experimental Investigations

2.1 Numerical Simulation

A 3D transient heat transfer finite element model was developed to simulate the thermal distribution during friction stir welding of AA5083-O using the Abaqus software. The part dimensions are $100 \times 50 \times 6$ mm for one piece where half of welding was simulated to reduce running time. The heat losses due to convection and radiation are neglected. Temperature dependent properties of the model are shown in Table 1.

Boundary conditions (BCs): the model is completely fixed in all directions except along the welding line, where it is partially fixed.

Load: a heat flux load is subjected to the surface of the part with a certain value. This value is obtained from the following formula:

$$\text{Heat flux}(Q) = \frac{\text{heat input}(q)}{\text{Area}(A)} \text{ (W/m}^2\text{)}$$

Table 1 The temperature dependent properties of AA5083

Temperature	Conductivity (W/m °C)	Specific heat (J/kg °C)	Density (kg/m ³)
-20	112.5	924.1	2673.9
80	122.7	984.2	2642.7
180	131.6	1039.6	2629.4
280	142.3	1081.2	2611.5
380	152.5	1136.6	2589.3
480	159.5	1178.2	2567
580	177.2	1261.4	2549.2

Heat input (q) is calculated from the *Frigard* equation

$$q = \int_0^R 2\omega\pi\mu Pr^2 dr \text{ (W)},$$

$$\omega = \frac{2\pi n}{60}$$

$$q = \int_0^R \frac{2}{30}\pi^2\mu Pnr^2 dr = \frac{1}{45}\pi^2\mu Pn(R^3 - r^3)$$

where

ω : Angular velocity (rad/sec)

n : Rotational speed(rpm) $P = \frac{F}{A}$

The following assumptions are considered:

Friction coefficient (μ) = 0.4

Axial force (F) = 2000 N

$A = \pi(R - r)^2 \text{ mm}^2$

Shoulder radius (R) = 12.5 mm

Pin radius (r) = 4 mm

Since the friction coefficient, axial force, shoulder radius and pin radius are constants, changing the rotational speed values results in changed heat flux values leading to a change in the temperature distribution. Then, $Q = 2.5 \times 10^6 \text{ W/m}^2$ (at 400 rpm).

Figure 1 shows both boundary conditions and load subjected to the part.

Meshing: The element type is heat transfer DCC3D8 with 8-node convection/diffusion brick. Figure 2 shows the meshing of the part.

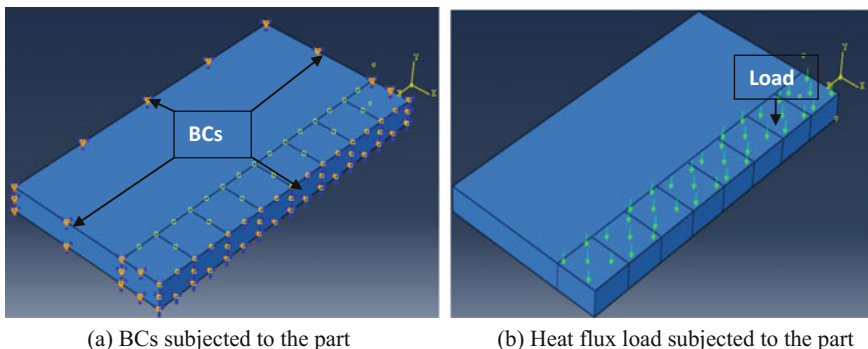
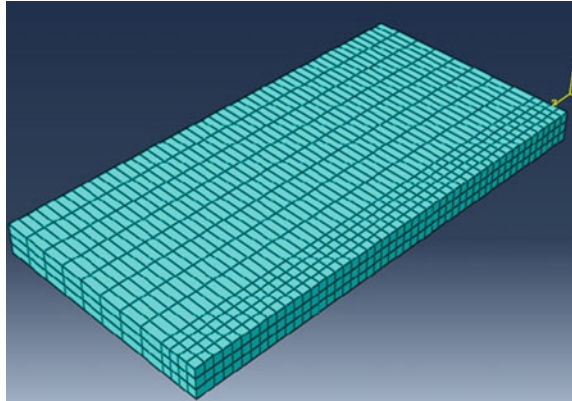


Fig. 1 BCs and load on the part

Fig. 2 Meshing of the part

2.2 *Welding Process and Operation Conditions*

The tool material is **K720** with **57 HRC**. Two tools with two different pin profiles, cylindrical threaded and tapered smooth pin profiles, were used. Figure 3 shows the schematic drawing of each tool. The work piece material is **AA5083-O** with dimensions of $100 \times 50 \times 6$ mm which is half of the welded joint. Tables 2 and 3 show the material chemical composition and mechanical properties respectively.

A universal milling machine was used to perform the friction stir welding process. The work piece was fixed on the machine by a mechanical vice as shown in Fig. 4. Table 4 shows the FSW parameters. **Fluke infra-red** thermal image camera shown in Fig. 5 was used to measure the temperature at each operation condition.

2.3 *Material Characterization*

A rectangular specimen was cut out from each friction stir welded joint perpendicular to the welding line. The samples were grinded using emery papers down to 2500 grade followed by polishing using $0.3 \mu\text{m}$ alumina suspension solution. The surfaces of the specimens were etched using Poulton's reagent [2 ml HF, 3 ml HCl, 20 ml HNO_3 , 175 ml H_2O]. The microstructure examination was carried out using an OLYMPUS optical metallurgical microscope, equipped with a high resolution digital camera for the investigation of the microstructure.

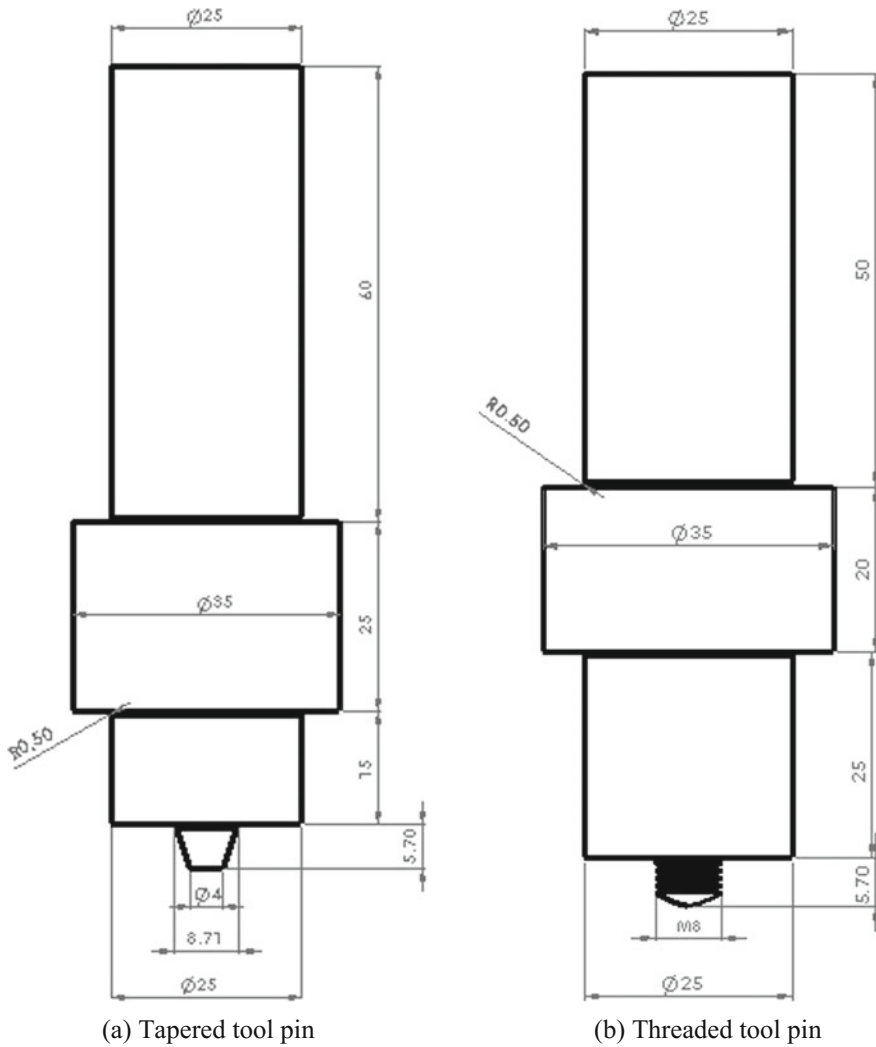


Fig. 3 Tools geometry

Table 2 The chemical composition of AA5083-O

Si	Fe	Cu	Mn	Mg	Zn	Ni	Pb	Sn	Al
0.1737	0.2867	<0.0010	0.4623	4.298	0.0075	<0.005	<0.002	<0.002	Balance

Table 3 The mechanical properties of AA5083-O

Ultimate tensile strength (σ_u)	Yield strength (σ_y)	Elongation (%)	Vickers Hardness (HV)
272	176	14	75

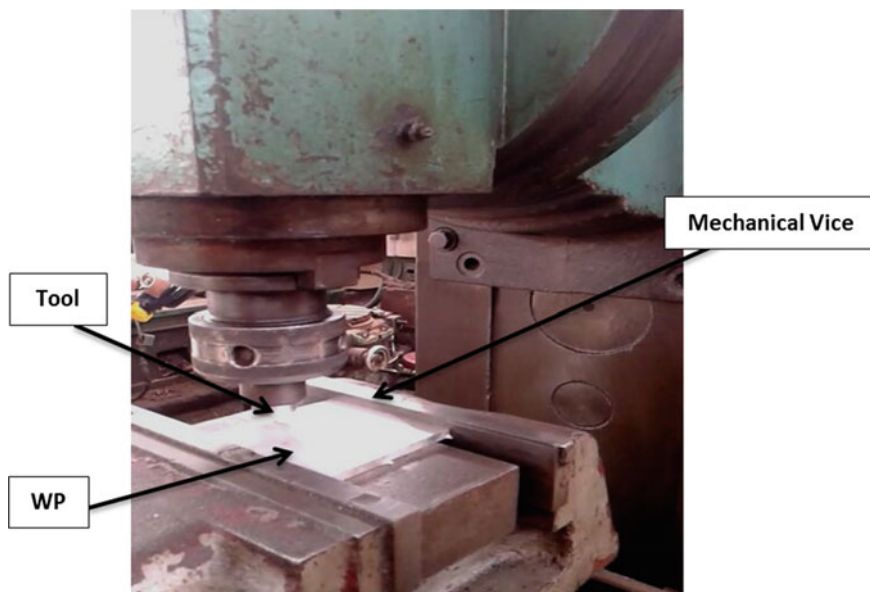


Fig. 4 Machine set-up

Table 4 FSW parameters

Process parameters	Tool pin profile	Welding speed (mm/min)	Rotational speed (rpm)	Plunge depth (mm)	Tool tilt angle (°)
Value	Cylindrical threaded and tapered smooth	50, 100 and 160	400	0.2	0

Fig. 5 Fluke IR thermal image camera



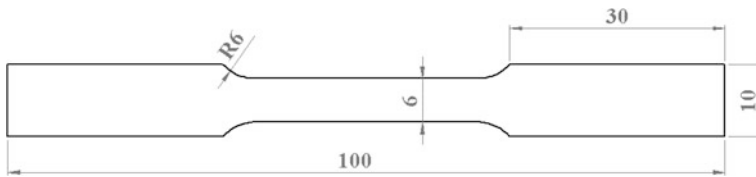


Fig. 6 Schematic drawing of tension test specimen (Thickness = 6 mm)

2.4 Mechanical Properties

The mechanical properties, mainly tensile strength and hardness, were measured for each sample.

2.4.1 Tensile Strength

Three tension test samples were taken from each welded joint and cut according to ASTM standard dimensions as shown in Fig. 6, tested on a universal testing machine and the average values were calculated for each case.

2.4.2 Microhardness Test

A rectangular specimen was cut out from each friction stir welded joint perpendicular to the welding line. The microhardness tests were conducted on a Zwick/Roell hardness testing machine.

3 Results and Discussions

3.1 Numerical Simulation and Temperature Distribution

After running the job of the model, the simulation is obtained and a path is taken along the line perpendicular to welding line to graph the temperature distribution. Figure 7a shows the temperature profile during simulation and Fig. 7b shows the temperature distribution curve obtained from simulation. It is observed that the peak temperature obtained from simulation in welding area is 448.8 °C and the temperature at 50 mm far from weld centre line is about 69.5 °C.

Figure 8 shows the variation of peak temperature at different welding speeds. It is observed from the graph that the highest peak temperature is at **50 mm/min** welding speed and the lowest one is at **150 mm/min** for the same tool pin profile. It is noticed that the tool pin profile does not strongly affect the peak temperature of the joints during welding process.

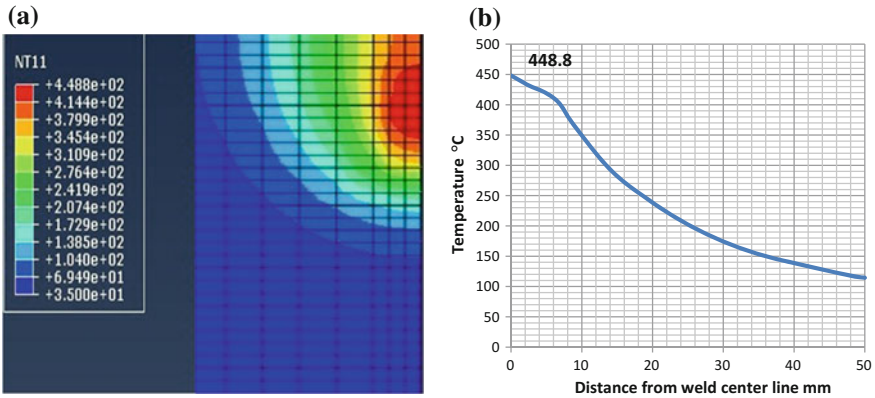


Fig. 7 a Temperature profile. b Simulated temperature distribution

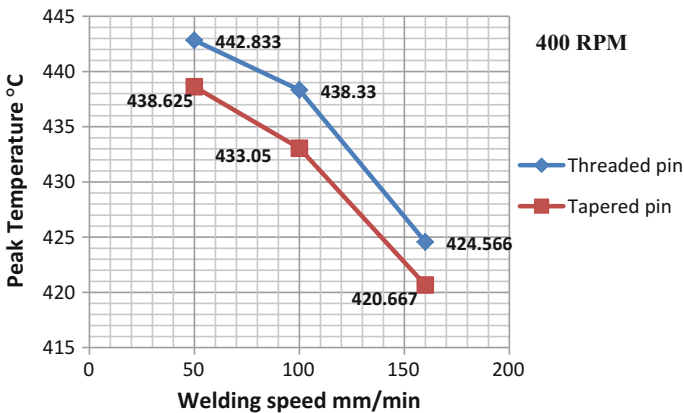


Fig. 8 Variation of peak temperature due to variation of welding speed and tool pin profile at 400 rpm

Figure 9 shows the comparison between the simulated temperature distribution obtained by the Abaqus software and the measured temperature distribution obtained by IR camera at 400 rpm rotational speed and 50 mm/min welding speed.

3.2 Surface Morphology

The upper surface macrographs of the welded joints at different welding conditions are shown in Fig. 10. It is observed from figure that the welded joints by threaded and tapered tool pin profile have an accepted surface appearance at all welding speeds where there are no grooves or surface-open tunnel defects.

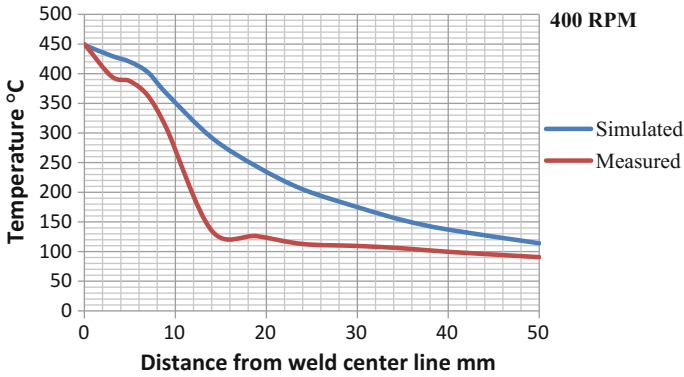


Fig. 9 Simulated and experimental temperature distribution

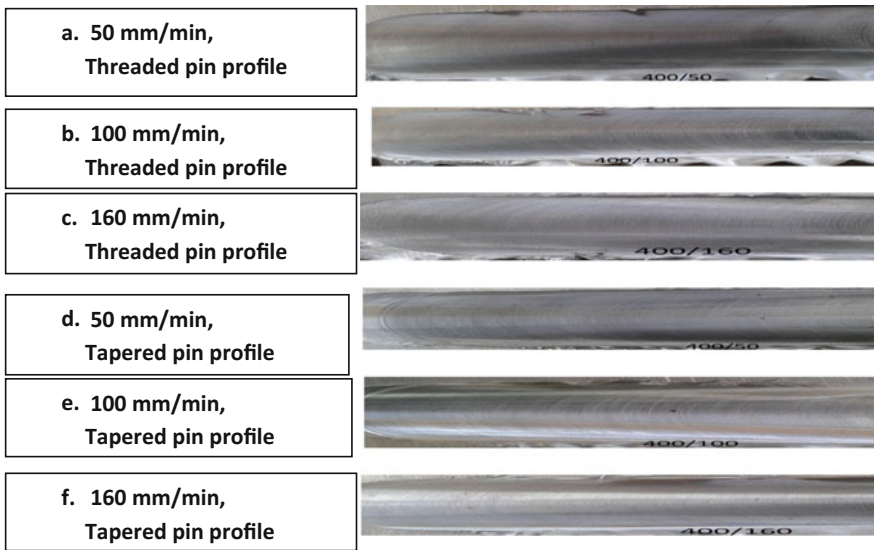


Fig. 10 Surface morphologies at different operating conditions

3.3 Macrostructure and Microstructure Evolutions

Figure 11 shows the macrostructure and microstructure observation for each sample. As observed from this figure, the defect free welds are obtained when welding process is performed using cylindrical threaded tool pin profile at all welding speeds values. While tunnel defects appeared when using smooth tapered pin

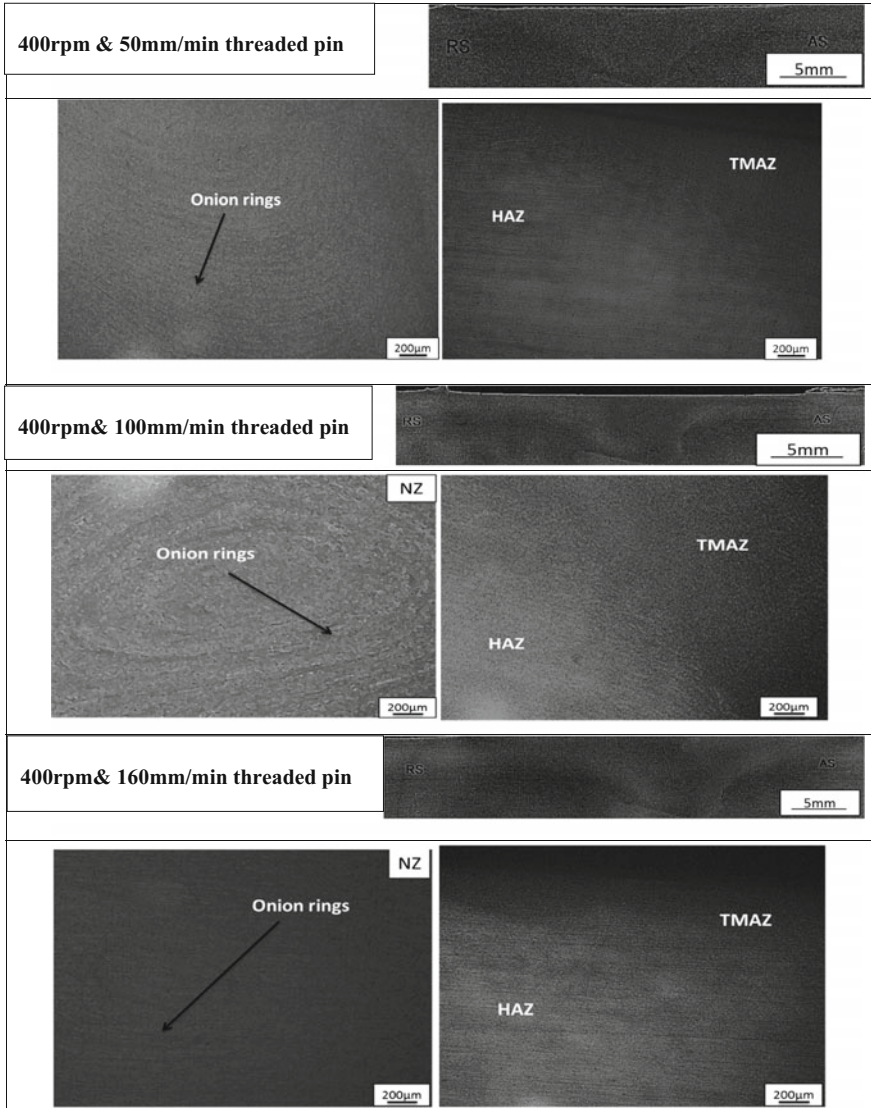


Fig. 11 Macrostructure and microstructure evolutions at different operation conditions

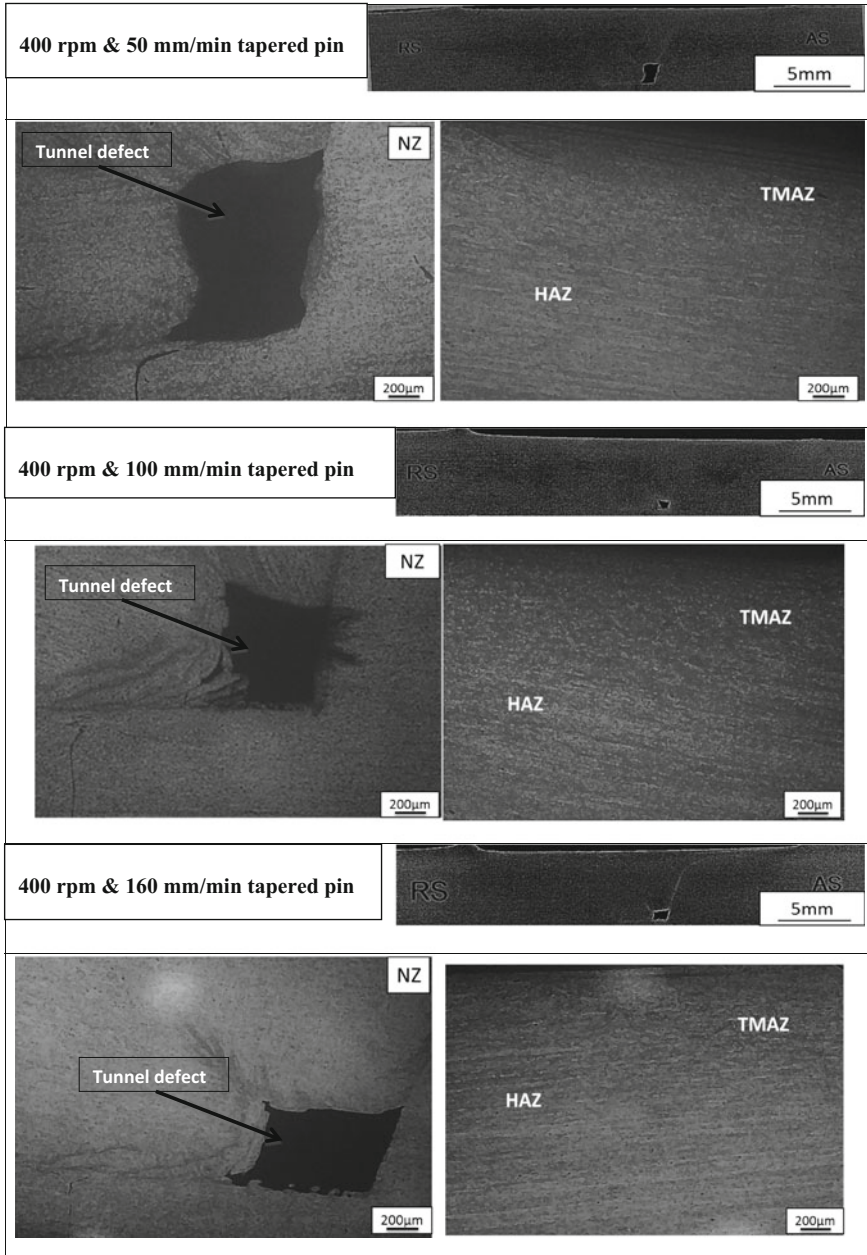


Fig. 11 (continued)

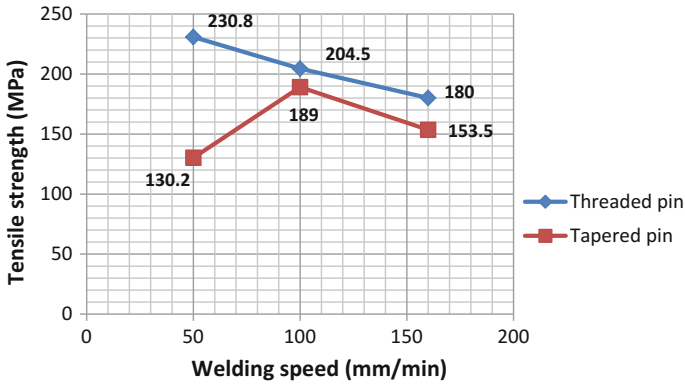


Fig. 12 The variation of TS with welding speed and pin profile at 400 rpm

profile tool at all welding speeds where, the largest tunnel defect size is at 50 mm/min welding speed and the smallest one is at 100 mm/min.

3.4 Mechanical Properties

The tensile strengths of the welded joints were obtained and plotted against welding speed for both types of tool pin profiles. As shown in Fig. 12 the best values of tensile strength are when using the threaded pin profile, especially at 50 mm/min welding speed; it is the best one. In comparison, using the tapered pin profile gives lower tensile strength values especially at 50 mm/min welding speed. It seems that the change in tool pin profile at 100 mm/min welding speed has a small effect on the tensile strength values.

Figure 13 shows the Vickers microhardness distribution along line perpendicular to the welding line at different FSW parameters. It is clear from graphs that for threaded cylindrical tool pin profile, the hardness values in nugget and thermo mechanically affected zones are greater than of base material at 50 and 100 mm/min welding speeds. The same is at 100 and 160 mm/min for tapered pin profile. This is due to finer grains in the welding zone. On the other hand, the hardness values are smaller than that of the base material 50 mm/min for tapered smooth tool pin profile and at some values for threaded pin profile at 160 mm/min welding speed. This action is due to coarsening of grains in the welding zone.

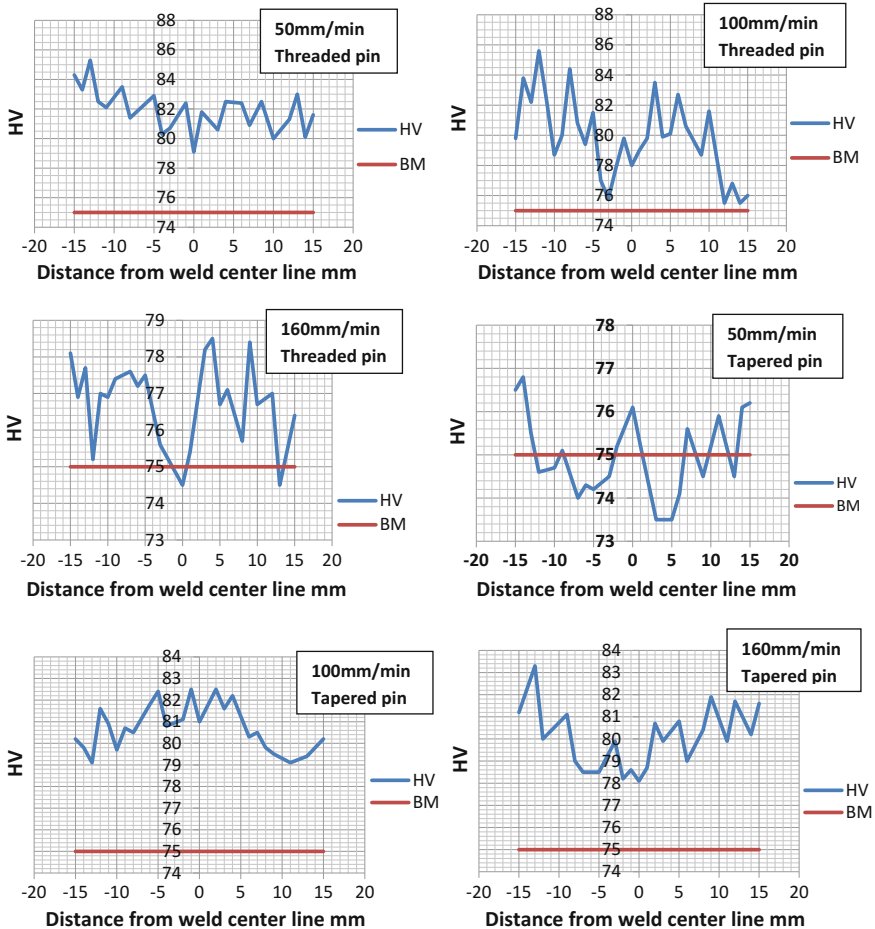


Fig. 13 Vickers microhardness distribution of the welded joints

4 Conclusions

Based on the present study, the following conclusions are obtained:

1. The peak temperature obtained from simulation is approximately near the measured one. Therefore, this heat transfer model can be used to predict the temperature distribution during the FSW process.
2. The peak temperature of the welded joints decreases by increasing the welding speed for the same tool pin profile and rotational speed.
3. Tool pin profile has a small effect on the peak temperature of the welded joints at the same welding speed.

4. The macrostructure and microstructure evolutions are affected by changing tool pin profile at the same welding speed.
5. Tensile strength values are affected by variations of the tool pin profile at the same welding speed.
6. Tensile strength values decrease by increasing welding speed for the joints welded by threaded tool pin profile.
7. The welded joints by threaded tool pin profile have an average hardness values in the welding zone greater than base material at all welding speed values.
8. The welded joints by tapered pin profile have an average value in the welding zone greater than base material at 100 or 160 mm/min welding speeds. While these values are lower than base material at 50 mm/min.

References

1. FSW-Technical-Handbook, ESAB, Welding Automation (2002) LAXÅ, Sweden
2. Thomas WM, Johnson KI, Wiesner CS (2003) Friction stir welding-recent developments in tool and process technologies. *Adv Eng Mater* 5:485–490
3. Mishra RS, Ma ZY (2005) Friction stir welding and processing. *Mater Sci Eng* 50:1–78
4. Rao MS, Prakash KJ, Kumar BVR (2013) A review of friction stir welding process and its variables. *Int J Sci Res (IJSR)* 2:375–379
5. Prasanna P, Penchalayya Ch, Rao DA (2013) Effect of tool pin profiles and heat treatment process in the friction stir welding of AA 6061. *Am J Eng Res (AJER)* 2:7–15
6. Threadgill PL, Leonard AJ, Shercliff HR, Withers PJ (2009) Friction stir welding of aluminum alloys. *Int Mater Rev* 54:49–93
7. Khodir SA, Shibayanagi T, Naka M (2006) Microstructure and mechanical properties of friction stir welded AA2024-T3 aluminum alloy. *Mater Trans* 47:185–193
8. Mao Y, Ke L, Liu F, Huang C, Chen Y, Liu Q (2016) Effect of welding parameters on microstructure and mechanical properties of friction stir welded joints of 2060 aluminum lithium alloy. *Int J Adv Manufact Technol* 81:1419–1431
9. Lim S, Kim S, Lee C, Kim S (2004) Tensile behavior of friction-stir-welded Al 6061-T651. *Metall Mater Trans* 35A:2829–2835
10. Habba MIA, Ahmed MMZ, Mohamed AYA, EL-Nikhaily A (2014) Effect of friction stir welding parameters on the mechanical properties of AA5083-H111. In: *Proceedings of the 10th international friction stir welding symposium, Beijing, China*
11. Chandrashekar A, Reddappa HN, Ajaykumar BS (2016) Influence of tool profile on mechanical properties of friction stir welded aluminum alloy 5083. *Int J Chem Mo Nucl Mater Metall Eng* 10:8–14
12. Schmidt H, Hattel J, Wert J (2004) An analytical model for the heat generation in friction stir welding. *Modell Simul Mater Sci Eng* 12:143–157
13. He X, Gu F, Andrew DB (2014) A review of numerical analysis of friction stir Welding. *Prog Mater Sci J* 65:1–66

Artificial Neural Networks Prediction of Rubber Mechanical Properties in Aged and Nonaged State

Ivan Ružiak, Pavel Košťal, Zora Jančíková, Milada Gajtanska, Luboš Krišťák, Ivan Kopal and Peter Polakovič

Abstract Artificial neural networks (ANN) have been used for characterization of rubber blend mixtures ageing and for prediction of mechanical properties according to chemical composition. Strength R_m and modulus M_{100} have been evaluated. The ANN application was tested by statistical function RMSE (root mean square error) and R^2 (coefficient of determination) which value for all predictions was higher than 0.93.

Keywords Rubber blends · Mechanical properties · Artificial neural networks

I. Ružiak (✉) · M. Gajtanska · L. Krišťák
Wood Sciences and Technology, Technical University of Zvolen, T. G. Masaryka 24,
96053 Zvolen, Slovak Republic
e-mail: ruziak@tuzvo.sk

M. Gajtanska
e-mail: gajtanska@tuzvo.sk

L. Krišťák
e-mail: kristak@tuzvo.sk

P. Košťal · Z. Jančíková
Metallurgy and Material Engineering, VŠB—Technical University of Ostrava,
17. Listopadu 15, 70833 Ostrava, Czech Republic
e-mail: pavel.kostial@vsb.cz

Z. Jančíková
e-mail: zora.kostialova.jancikova@vsb.cz

I. Kopal
Institute of Physics, Mining and Geology, VŠB—Technical University of Ostrava,
17. Listopadu 15, 70833 Ostrava, Czech Republic
e-mail: ivan.kopal@vsb.cz; ivan.kopal@fpt.tnuni.sk

1 Introduction

Several properties of rubber mixtures are strongly influenced by technology treatment and agents or fillers added to the rubber. Carbon black is an active filler which is used to increase the electrical and thermal properties because of its strong interactions with natural rubber. Plasticizers play an important technological role in rubber industry. Rubber is a multicomponent material, which is very sensitive to a lot of chemical species and mainly their technological treatment. For a multicomponent system inputs and outputs connected with optimization of chemistry or technological processes is useful to use an artificial neural network (ANN).

The study [1] proposed a novel approach to determine the fibre volume fraction in composites using vibration based on a non-destructive technique with a neural network. Currently, the volume fraction of a glass fibre/matrix based composite material is assessed using destructive techniques. Instead of changing or destroying the structure, a new non-destructive approach based on vibration analysis is proposed. Complete experimental protocols were developed to capture the vibration pattern. An auto-regressive model was developed as a feature extraction tool to classify the fibre volume fractions and as a pole tracking algorithm. The classification performances were within the range of 90–98%.

In [2] a back-propagation neural network was employed to conduct an approximation of a true stress-strain curve using the load-displacement experimental data of DP590, a high-strength material used in automobile bodies and chassis. The optimized interconnection weights are obtained with hidden layers and output layers of the BPN through intelligent learning and training of the experimental data; by using these weights, a mathematical model of the material's behaviour is suggested through this feed-forward neural network.

A decoupled computational homogenization method for nonlinear elastic materials was proposed using neural networks in [3]. In this method, the effective potential is represented as a response surface parameterized by the macroscopic strains and some microstructural parameters. The discrete values of the effective potential are computed by the finite element method through random sampling in the parameter space, and neural networks are used to approximate the surface response and to derive the macroscopic stress and tangent tensor components.

The article [4] deals with the experimental modal analysis of glass laminates plates with different shape and these results are compared with those obtained by applications of artificial neural networks (ANN) and the finite element method

P. Polakovič

Department of Informatics, Slovak University of Agriculture in Nitra, Tr. A. Hlinku 2,
94976 Nitra, Slovak Republic
e-mail: polakovic@is.uniag.sk

I. Kopal

Industrial Technologies in Puchov, Alexander Dubcek University of Trencin, I. Krasku 491,
02001 Puchov, Slovakia

(FEM). It is presented the dependence of the generated mode frequency as a function of sample thickness as well as the sample shape (rounding) of glass laminate samples. The coincidence of both experimental and simulated results is very good.

In the paper [5] an application of artificial neural networks (ANN) on the relation between glass composition versus optical transmittance of the chosen glass systems is described. The excellent prediction ability of the ANN program shows a possibility to influence the glass composition to obtain the required optical properties.

The objective of the paper [6] is to classify each layer as coal, shale coal and shale depending upon the content of ash % and moisture % of the corresponding layer in coaly horizon. Hierarchical cluster analysis (HCA) is applied to classify the non-coal horizons and bands of identified coal seams of each well under the study area based on geophysical log responses: natural gamma ray (NG), high resolution density (HRD) and single point resistance (SPR). Hierarchical clustering separates the zones in a particular coal seam from five wells using the nature of the curve. These zones/clusters are further identified as coal, shale coal, shale in three wells using regression and a multilayer feed forward neural network.

In the study [7], an artificial neural network (ANN) and adaptive neuro-fuzzy inference system (ANFIS) models were used to predict the average permeate fluxes and sodium chloride rejection of waste brine nanofiltration process. A hybrid method was used as the training method of the ANFIS. The overall agreement between the ANFIS predictions and experimental data was excellent for both permeate flux and salt rejection ($r = 0.96$ and $r = 0.94$, respectively).

The aim of the work [8] is to develop a prediction method for renewable energy sources in order to achieve an intelligent management of a microgrid system and to promote the utilization of renewable energy in grid connected and isolated power systems. The proposed method is based on the multi-resolution analysis of the time-series by means of wavelet decomposition and artificial neural networks.

In the paper [9], authors investigated the ensemble of deep neural networks (DNNs) by using an acoustic environment classification (AEC) technique for the statistical model-based voice activity detection (VAD). From an investigation of the statistical model-based VAD, it is known that the traditional decision rule is based on the geometric mean of the likelihood ratio or the support vector machine (SVM), which is a shallow model with zero or one hidden layer. The approach for VAD was evaluated in terms of objective measures and showed significant improvement compared to the conventional algorithm.

The study [10] describes the application of TiO_2 , ZnO , TiO_2 - ZnO -based systems modified with 1.5 and 2.5% wt. Fe using the impregnation method for the maxilon blue 5G dye discoloration. Specific surface area (BET method), X-ray diffraction, thermogravimetric analysis, and photoacoustic spectroscopy characterization techniques were used in this work. A neural model was developed for each studied catalyst with three intermediate layers, backpropagation learning algorithm, and sigmoid activation function implemented in FORTRAN. The three models presented the best results with three neurons in the intermediate layer. Therefore, the neural networks can be successfully employed to model the discoloration process involving the synthesized catalyst (R^2 varying between 0.98 and 0.99).

In this paper we solve by ANN the optimization of plasticizer amount on chosen mechanical properties such as strength R_m and modulus M_{100} before and after aging on air.

2 Theoretical Assumptions

Artificial neural networks are used for materials properties prediction when analytical mathematical approximation cannot be found. From this very robust mathematical tool material properties can be predicted.

Artificial neural networks use different topologies that in most cases consist with three or four layers. In these networks three types of neurons occur that are:

- input neurons
- hidden neurons
- output neurons.

Input neurons have the information about parameters that change in our data-sheet such as material composition, thermal treatment information and others.

Output neurons correspond to material properties that we want to predict.

Some part of the input neurons is used for training and another part for generalizing.

Advantages of neural networks are as follows:

- Neural network can teach
- Neural network can generalize.

Disadvantages are as follows:

- Neural networks need very much values of one or more parameters that change in every dataset as input.

The ANN usage is tested by statistical parameters RMSE and R^2 which are defined by Eqs. (1) and (2)

$$RMSE = \sqrt{\frac{\sum_{i=1}^n (y_i - o_i)^2}{n \cdot (n - 1)}}. \quad (1)$$

$$R^2 = \left(\frac{E(y) \cdot E(o)}{E(y \cdot o)} \right)^2 \quad (2)$$

where y_i represent i -th measured value of selected parameter, o_i represent i -th predicted value of selected parameter corresponding to i -th measured value, n is the total number of input values, $E(y)$ represent statistical mean value of inputs, $E(o)$ is the statistical mean value of predicted values and $E(y \cdot o)$ is the mean value of multiplication of predicted and measured values in the same point.

3 Experimental Procedures

3.1 Used Samples

Chemical composition of standard rubber mixture in DSK (one part of component per 100 part of rubber) is shown in Table 1.

3.2 Ageing Conditions

Conditions of ageing are shown in Table 2.

3.3 Experimental Values

3.3.1 Measured Properties

Measured values of tensile strength and moduli M100 of samples with 1DSK oleic acid and surfactant Etoxon are shown in Table 3.

The measured values of tensile strength and moduli M100 versus Etoxon amount for the rubber blend with 3DSK oleic acid and non-aged state are shown in Table 4.

The measured values of tensile strength and moduluses M100, versus Etoxon amount with 1DSK oleic acid after ageing are shown in Table 5.

The measured values of tensile strength and moduluses M100 versus Etoxon amount of samples with 3DSK oleic acid after ageing are shown in Table 6.

Table 1 Chemical composition of standard rubber mixture

Ingredient	DSK contain
SMR	100
Sulphur	2
ZnO	5
Stearine	2
Sulfenax	2
N339 CB	50
Gumodex	10

Table 2 Ageing conditions of samples

Environment	Time
Air	1 month

Table 3 Measured values of R_m and M100 versus Etoxon amount for 1 DSK oleic acid mixtures (non-aged state)

Etoxon amount (%)	R_m (MPa)	M100 (MPa)
0	17	3.60
2	18.01	3.80
4	18.71	4.10
6	19	4.20
8	19.28	4.30
10	19.83	4.60
20	20.50	5.10
30	21.90	5.50

Table 4 Measured values of R_m and M100 versus Etoxon amount for 3 DSK oleic acid mixtures (non-aged state)

Etoxon amount (%)	R_m (MPa)	M100 (MPa)
0	18.50	3.90
2	18.72	4.10
4	18.90	4.20
6	19.16	4.30
8	19.85	4.70
10	20.50	5.10
20	21.42	5.40
30	22.49	5.70

Table 5 Measured values of R_m and M100 versus Etoxon amount for 1 DSK oleic acid mixtures (aged state)

Etoxon amount (%)	R_m (MPa)	M100 (MPa)
0	14.21	4.20
2	15.50	4.50
4	15.81	4.70
6	16.90	5.30
8	17.35	5.50
10	17.50	5.60
20	17.80	5.70
30	17.86	6.10

Table 6 Measured values of R_m and M100 versus Etoxon amount for 3 DSK oleic acid mixtures (aged state)

Etoxon amount (%)	R_m (MPa)	M100 (MPa)
0	17	5
2	17.21	5.10
4	17.44	5.30
6	17.66	5.50
8	18	5.70
10	18.16	5.70
20	18.55	6.20
30	19.12	6.40

3.3.2 ANN Prediction

The ANN prediction was performed by the Statistica 7 software. DSK content of oleic acid and ETOXON have been used as input neurons.

Functions of predicted tensile strength as function of measured tensile strength are shown in Figs. 1 and 2. Functions of predicted M100 value as function of measured M100 value are shown in Figs. 3 and 4.

Figures 1, 2, 3 and 4 show very good correlation between measured and ANN predicted values. Statistical parameters of ANN predictions for tensile strength R_m , moduli M100 are shown in Tables 7 and 8.

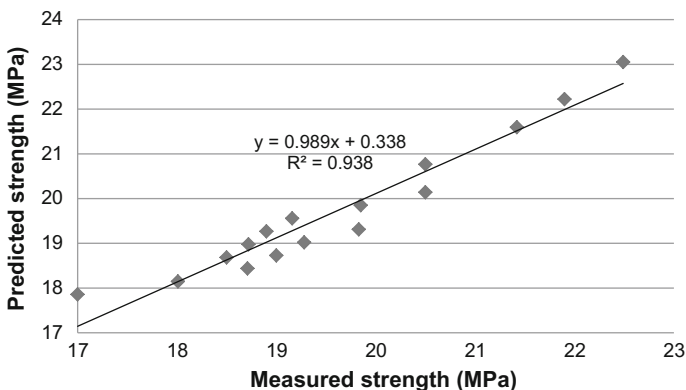


Fig. 1 Predicted versus measured values of R_m for oleic acid mixtures before ageing process

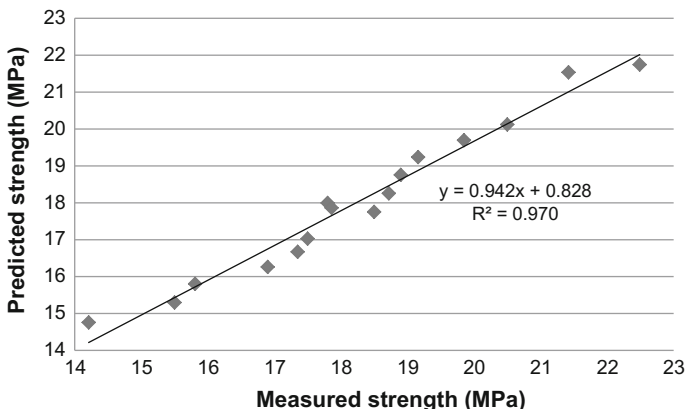


Fig. 2 Predicted versus measured values of R_m for oleic acid mixtures after ageing process

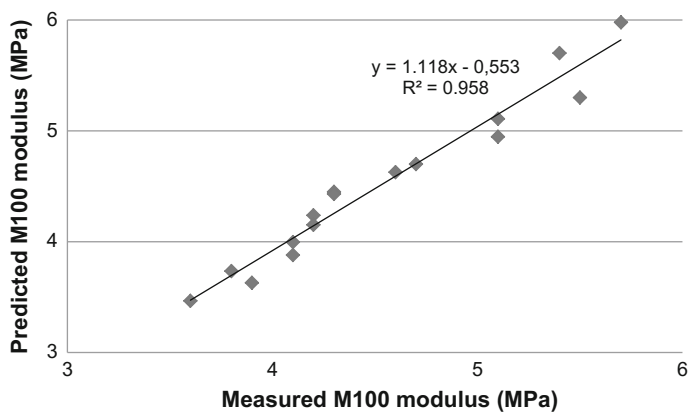


Fig. 3 Predicted versus measured values of M100 for oleic acid mixtures before ageing process

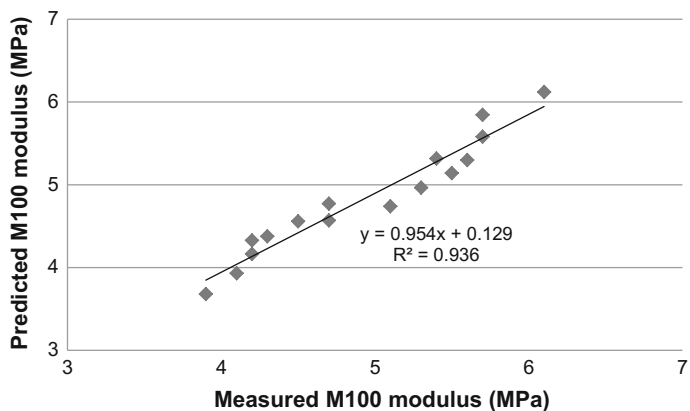


Fig. 4 Predicted versus measured values of M100 for oleic acid mixtures after ageing process

Table 7 Statistical parameters of ANN predictions for tensile strength R_m

State	RMSE	R^2
Before ageing	0.080	0.938
After ageing	0.112	0.970

Table 8 Statistical parameters of ANN predictions for modulus M100

State	RMSE	R^2
Before ageing	0.042	0.958
After ageing	0.051	0.936

4 Conclusions

From presented results of ANN prediction we can draw following conclusions.

- ANN can predict chosen mechanical values of rubber mixtures with combination of both plasticizer and ETOXON surfactant amount,
- ANN can predict values also after ageing process.

Acknowledgements Selected work has been created with help of Slovakian grants VEGA1/0538/14, VEGA1/0213/15, ITMS 26210120024 and the Slovak Research and Development Agency under the contract No. APVV-14-0506 “ENPROMO”.

References

1. Farhana NIE, Majid MSA, Paulraj MP et al (2016) A novel vibration based non-destructive testing for predicting glass fibre/matrix volume fraction in composites using a neural network model. *Compos Struct* 144:96–107
2. Doh J, Lee SU, Lee J (2016) Back-propagation neural network-based approximate analysis of true stress-strain behaviors of high-strength metallic material. *J Mech Sci Technol* 30:1233–1241
3. Le BA, Yvonne J, He QC (2015) Computational homogenization of nonlinear elastic materials using neural networks. *Int J Numer Meth Eng* 104:1061–1084
4. Seidl D, Košťál P, Jančíková Z et al (2011) Modal analysis—measurements versus fem and artificial neural networks simulation. *Commun Comput Inf Sci* 188:170–175
5. Jančíková Z, Minárik S, Bošák O et al (2014) The neural network analysis of optical glasses transmittance. In: *International carpatian control conference, IEEE*, 345 E 47th St, New york
6. Ghosh S, Chatterjee R, Shanker P (2016) Estimation of ash, moisture content and detection of coal lithofacies from well logs using regression and artificial neural network modelling. *Fuel* 177:279–287
7. Salehi F, Razavi SMA (2016) Modeling of waste brine nanofiltration process using artificial neural network and adaptive neuro-fuzzy inference system. *Desalin Water Treat* 31:14369–14378
8. Doucoure B, Agbossou K, Cardenas A (2016) Time series prediction using artificial wavelet neural network and multi-resolution analysis: application to wind speed data. *Renew Energy* 92:202–211
9. Hwang I, Park HM, Chang JH (2016) Ensemble of deep neural networks using acoustic environment classification for statistical model-based voice activity detection. *Comput Speech Lang* 38:1–12
10. Lenzi GG, Evangelista RF, Duarte ER et al (2016) Photocatalytic degradation of textile reactive dye using artificial neural network modeling approach. *Desalin Water Treat* 30: 14132–14144

Semi-automated Gating System Design with Optimum Gate and Overflow Positions for Aluminum HPDC

Mohamed Refaat Abo El-Fotouh, Ahmed Yehia Shash
and Mohamed Hasan Gadallah

Abstract Die casters usually carry out a die casting test before producing new castings. At the die-casting test stage, the runner and gate parts are always repeatedly corrected, which lead to a lengthened processing time and increased processing cost. In this study, a computer software was developed to calculate the gating system design with optimum gate and overflow positions for cold chamber High Pressure Die Casting (HPDC) die design by getting the part dimensions and choosing the suitable machine from a pre-defined database in the software. A design of experiment is used to formulate the objective function of the gate and overflow optimum position. At the end of this paper, a case study was developed as part of the software validation. The results show that the developed software can calculate the gating system design and eliminate the correction in the test stage.

Keywords HPDC · Die casting · Gating system · Die casting design

1 Introduction

Die-casting is similar to permanent mold casting except that the metal is injected into the mold under a high pressure of 10–210 MPa (equiv. to 1450–30,500 psi). This results in a more uniform part with a generally good surface finish and good dimensional accuracy, as well as 0.2% of the casting dimension. For many parts, post-machining can be totally eliminated, or very light machining may be required to bring dimensions to size.

M.R.A. El-Fotouh · A.Y. Shash (✉) · M.H. Gadallah
Mechanical Design and Production Engineering Departement, Cairo University,
12316 Giza, Egypt
e-mail: ahmed.shash@cu.edu.eg

M.R.A. El-Fotouh
e-mail: abo.elfotouh@ymail.com

M.H. Gadallah
e-mail: m_gadallah@hotmail.com

However, because of the high injection speed, die-casters usually carry out a die-casting test before producing new castings to eliminate part defects. In this stage the runner and gate parts are always repeatedly correctly, which leads to a lengthened processing time and increased processing cost.

In this area, some researches study the gating system only, while others only study the runner system and its effects of product defects. In this research developing a software, using visual basic that give a recommended gate and runner design (Gating system) related to the product's dimensions and machine used. This will minimize the part defects/porosity. Moreover, the software lets the user choose from the different machines and its plunger diameter from a pre-defined database to get a desired number of cavities for the user's case.

Mentioned, some researches only study the runner system, such as Tai and Lin [15] which use a simulated annealing optimization algorithm with a performance index to get the optimum runner network. Weishan et al. [17] developed a CAD/CAE system for die casting. By using the CAD package, die designers can determine the location, the shape and the dimension of the runner and gating systems of die castings according to the characteristics of the die-casting machine, the geometry of the casting, and the properties of the alloy. Through the interactive process of CAD/CAE, and an ideal design can be provided with the best filling pattern and the optimal thermal conditions for both the die and the die casting. Lee and Lu [11] proposed a new mathematical model for the calculation of the back pressure in a die cavity. Fuh et al. [3] described a prototype system structured by several functional modules as specific add-on applications on a commercial CAD system for die casting die design. These modules include data initialization, cavity layout, gating system design, die-base, parting, standard components design, among others. The focus of the development was placed on gating, runner and die-based design. Yue et al. [19] established a CAD/CAE/CAM integrated system dies for application in the primary stage. The use of this integrated system can shorten the cycle of die design and manufacturing, as the lead-time of die castings is shortened greatly. Shehata and Abd-Elhamid [14] presented main die designing procedures and related equations in logical way. A computer program is developed to estimate the main die elements based on the geometry input of casting shape. After the initial inputs given, the system does full calculations, optimizes selections, and lists main die element sizes. The program can present die characteristics and casting machine characteristics. Cleary et al. [2] explored the effects of die temperature, metal super-heating and volume filling on the short shots for the casting of a simple coaster. The research used simulation methods that proved particularly suited to modeling HPDC is Smoothed Particle Hydrodynamics (SPH). SPH was used to study three industrial case studies. Hangai and Kitahara [5] proposed a fractal analysis by comparing the porosity in two types of aluminum alloy die casts manufactured by different die-casting processes, and to confirm that the fractal analysis of the spatial distribution of pores can quantitatively characterize the porosity. The same researchers [6] proposed another two types of fractional analysis to characterize the porosity in terms of the shape of individual pores and the spatial distribution of multiple pores. Their analysis shown that these are indicators of whether the predominant cause of the porosity is shrinkage or gas. these parameters are

expected to indicate the action that should be taken to manufacture pore-free die castings. Park and Yang [12] proposed a linear programming (LP) model that maximizes the average efficiency of processing time for casting in real foundries. Lee et al. [10] presented a methodology for obtaining optimal designs of 4-cavity thin electronic component housings. Their study analyzed the fluid behavior and amount of air entrainment caused by the overflows and air vent using a computer fluid dynamics (CFD) simulation. Furthermore, the effect of vacuum systems on the porosity and mechanical properties of the castings was studied in their work. Queudeville et al. [13] modularized a proven instrument in reducing costs in manufacturing processes. Their methodology tries to assist design engineers throughout the development of new dies, helping to choose an appropriate set of modules based on technical as well as economic criteria. Gulagoudar et al. [4] developed a robust design approach to analyze casting defects in foundry. Thus process parameters are set in order to reduce the rejection of castings. Kittur et al. [9] determined the optimal process parameters by using the desirability function. The process parameters, namely, fast shot velocity, injection pressure, phase changeover point, and holding time, have been considered as the input to the model. Porosity, surface roughness, and hardness are measured and represented as the responses. Wu et al. [18] developed a parametric design software for die-casting die gating system, so the designing and modification will be more easy to maintain by using parametric design.

2 Framework of the Gating System

Gating system dimensions directly affect part quality. This requires designer to have detailed information for the part and the machine, so that accurate dimensions for gating system elements as runner, gate overflow and air vent can be achieved, see Fig. 1.

2.1 Part Details/Dimensions

The part details as width, length and height also its thickness and angles, are important to take into account in the designing stage. In this study a standard parallelogram is taken to study the part details with gating system dimensions/details.

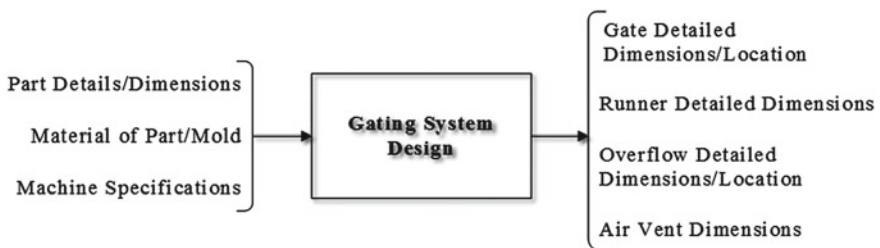


Fig. 1 Gating system design flow chart

2.2 Material of Part/Mold

The material of the part and the mold also affect the design parameters. The study uses the popular part material (Al 306) as seen in Table 1, and also mold material (H13), see Table 2. So designers can cover large variant of part application.

2.3 Machine Specifications

For the material selected, the designer has to follow the specification of the cold chamber HPDC machines. Machine tonnage and casting volume identifies the number of cavities used, also plunger diameter and position affect the runner dimensions and mold design. In this study a pre-defined machine database is created to cover parts details as much as possible. These machines database collected from those in market and compared with many others to be sure that the deviation between machines in the same type almost none see Table 3.

2.4 Gate Detailed Dimensions/Location

“The gate is a narrow opening into the cavity from the gate runner” [18]. Its area is related to casting volume and thickness. The detailed dimensions of the gate can be calculated using functions and rules from handbooks and textbooks ([1], [7], [8], [16]), but the study add experts’ reviews to smoothing the gate details for better efficiency. Table 4 show functions used in gate details.

The gate detailed dimensions are given by 8 sections so it can be drawn along the gate path on any CAD modeling software i.e., SolidWorks. Figure 2 shows how sections are drawn with the required smoothness.

The gate location is identified using an experimented model developed using the design obtained by the experimental methods so that the gate location can be related to part dimensions and details.

Table 1 Al 306 (AlSi12) chemical composition

Si %	Fe %	Cu %	Mn %	Mg %	Ni %	Pb %	Sn %	Ti %	Zn %	Al %
10.5–13.5	0.55	0.05	0.35	–	–	–	–	0.15	0.1	Rest

Table 2 H13 1.2344 (X40CrMoV5-1) chemical composition

C %	Si %	Mn %	P %	S %	Cr %	Mo %	V %	Fe %
0.35–0.42	0.8–1.20	0.25–0.50	0.03	0.02	4.80–5.50	1.20–1.50	0.85–1.15	Rest

Table 3 Machines database

Machine/Specs.	Unit	150 TON			250 TON		
Locking force	kN	1500			2500		
Plunger diameter	mm	45	50	60	50	60	70
Injection speed	m/sec	0.1–7.0			0.1–7.0		
Injection force	kN	182			270		
Injection stroke	mm	340			420		
Injection volume	cm ³	362	447	644	540	777	1058
Cast area	cm ²	239/118	296/146	426/210	363/181	524/262	714/357
Machine/Specs.	Unit	420 TON			500 TON		
Locking force	kN	4200			5000		
Plunger diameter	mm	60	70	80	70	80	90
Injection speed	m/sec	0.1–7.0			0.1–7.0		
Injection force	kN	350			520		
Injection stroke	mm	500			630		
Injection volume	cm ³	904	1230	1607	1788	2336	2956
Cast area	cm ²	584/292	794/397	1036/518	919/459	1201/599	1522/775
Machine/Specs.	Unit	650 TON			Machines database		
Locking force	kN	6500					
Plunger diameter	mm	70	80	90			
Injection speed	m/sec	0.1–7.0					
Injection force	kN	545					
Injection stroke	mm	630					
Injection volume	cm ³	1788	2336	2956			
Cast area	cm ²	919/459	1201/599	1522/775			

2.5 Runner Detailed Dimensions

Runner is responsible to feed the gates from the machine sleeve. It is composed of the main runner and branch runners. Branch runners are connected to the main runner and the part, its cross sectional area is equal to that of the gate at Sect. 8. The main runner has a different cross sectional area, depending on the branch runners connected. For every two branches runners connected the main runner area must be more than 1.1 times the sum of their areas.

2.6 Overflow Detailed Dimensions/Location

The overflow is a volume of aluminum that is responsible for reducing non-metallic inclusions (porosity) and air entrapment, localized after the part. The size of the

Table 4 Gating system equations

Equation	Parameters
$t = k \left[\frac{T_i - T_f + S \cdot Z}{T_f - T_d} \right] T$ [16]	<p>k = Empirically derived constant related to the die steel T = Wall thickness (mm) t = Max. filling time (sec) T_f = Min. flow temperature of the metal alloy (°C) T_i = Metal temperature at the ingate (°C) T_d = Die surface temperature just before the metal arrives (°C) S = Percent solids at the end of fill Z = Solids units conversion factor, degree to %</p>
$Q_i = \frac{V_i}{t}$	<p>Q_i = Flow rate of a segment (mm³/sec) V_i = Volume of a segment volume (mm³) t = Cavity filling time (sec)</p>
$A_{appi} = \frac{Q_i}{v_g}$	<p>A_{appi} = Apparent ingate area of a segment (mm²) Q_i = Flow rate of a segment volume (mm³) v_g = Ingate velocity (mm/sec)</p>
$v^{1.71} \cdot T_g \cdot \rho \geq J$	<p>v_g = The ingate velocity (mm/sec) T_g = The ingate thickness (mm) ρ = The density of the metal (N/mm³) J = The atomization factor</p>
$A_v = \frac{A_{gapp}}{4}$ [16]	<p>A_v = The min. area of the vent (mm²) A_{gapp} = Apparent area of the ingate (mm²)</p>
$V_c = (V_p + V_o) \cdot 1.2$	<p>V_c = Cast volume (mm³) V_p = Part volume (mm³) V_o = Overflow volume (mm³)</p>
$A_c = A_p \cdot 1.5$	<p>A_c = Cast projected area (mm²) A_p = Part projected area (mm²)</p>

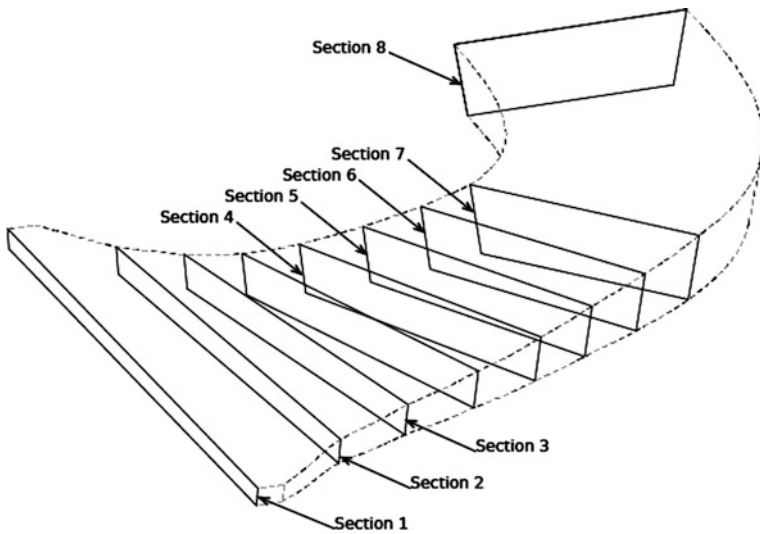


Fig. 2 Gate detailed sections

overflow is depending on the part volume and thickness. The rule of overflow volume selection was implemented by the IF/THEN rule. Overflow location is identified via the same experimental model used for gate location.

2.7 Air Vent Dimensions

Air vent is just a narrow area that enables air to escape without letting aluminum out. It helps the air entrapment of the gating system. Its area can be calculated from the gate area Table 4.

3 Experimental Model

The study developed an experimental model to study the effect of the part factors on the its porosity. Also creates an objective function for porosity percentage so it can minimize. These factors are related to part dimensions i.e., Width, length, height, angle and thickness. Furthermore, there are two factors that have been created to study gate and overflow positions effect. GSS (Gate Shift Scale) and OSS (Overflow Shift Scale) are the factors responsible for gate and overflow positions, see Fig. 3.

The study used Box-Behnken experimental design to study the effect of the factors Table 5 on the porosity percentage. A simulation model was developed for

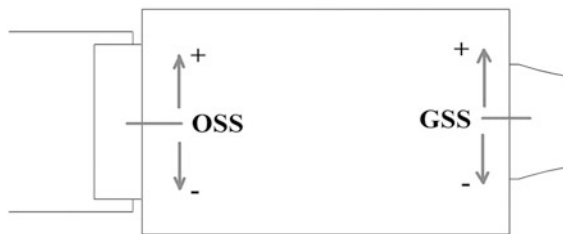


Fig. 3 GSS and OSS factors

Table 5 Box-Behnken design factors

#	Factor	Description	Units	Range	
				From	To
1.	Width	Part width	mm	20	200
2.	Length	Part length	mm	25	250
3.	Height	Part height	mm	10	100
4.	Angle	Part angle	degree	50	90
5.	Thickness	Part thickness	mm	0.3	3
6.	GSS	Gate shift scale	ul	-1	1
7.	OSS	Overflow shift scale	ul	-1	1

Table 6 Simulation model parameters

Parameter	Units	Value
Atmospheric temperature	°C	35
Die temperature	°C	280
Molten aluminum temperature	°C	650
Incoming velocity	m/sec	1

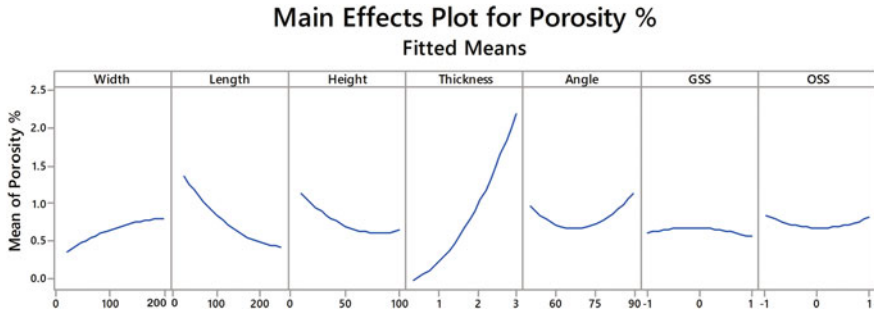


Fig. 4 Main effects plot for porosity %

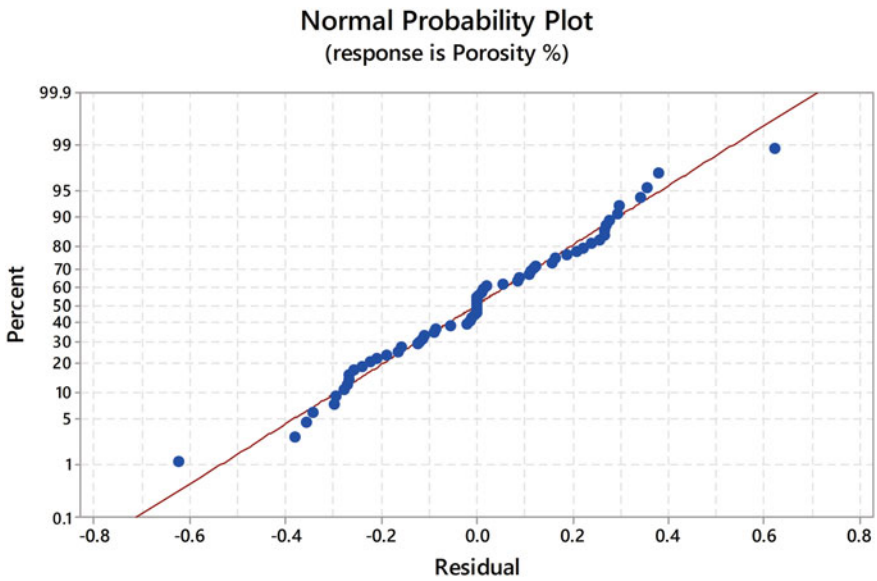


Fig. 5 Normal probability plot

this experiment using ProCAST¹ software. To study the effect of the 7 factors only the other parameters must be fixed, Table 4 shows simulation parameters used (Table 6).

The experiment shows how the porosity affected from the part shape specially the thickness and also that GSS and OSS affect it, see Fig. 4. The experiment also built a model that described the effect of all the seven factors on the porosity percentage, see Fig. 5. Once the all 5 factors are known from equations from handbooks and experts' reviews it will be easy to get the values of GSS and OSS that gets the minimum porosity for the chosen part, see Eq. (1).

Equation (1)—*Describes the relation between Width, Length, Thickness, Angle, GSS and OSS factors and the part Porosity % as an output from the experimental design*

$$\begin{aligned}
 \text{Porosity \%} = & 5.75 - 0.00009 \cdot \text{Width} - 0.00953 \cdot \text{Length} - 0.0195 \cdot \text{Height} + 0.208 \\
 & \cdot \text{Thickness} - 0.1313 \cdot \text{Angle} - 0.327 \cdot \text{GSS} - 0.456 \cdot \text{OSS} - 0.000012 \\
 & \cdot \text{Width}^2 + 0.000017 \cdot \text{Length}^2 + 0.000106 \cdot \text{Height}^2 + 0.2283 \\
 & \cdot \text{Thickness}^2 + 0.000946 \cdot \text{Angle}^2 - 0.0934 \cdot \text{GSS}^2 + 0.1598 \cdot \text{OSS}^2 \\
 & + 0.000028 \cdot \text{Width} \cdot \text{Length} - 0.000068 \cdot \text{Width} \cdot \text{Height} + 0.0017 \text{Width} \\
 & \cdot \text{Thickness} + 0.000031 \cdot \text{Width} \cdot \text{Angle} - 0.00003 \cdot \text{Width} \cdot \text{GSS} \\
 & + 0.00008 \cdot \text{Width} \cdot \text{OSS} + 0.000058 \cdot \text{Length} \cdot \text{Height} - 0.002092 \\
 & \cdot \text{Length} \cdot \text{Thickness} - 0.000031 \cdot \text{Length} \cdot \text{Angle} + 0.00077 \cdot \text{Length} \\
 & \cdot \text{GSS} + 0.00072 \cdot \text{Length} \cdot \text{OSS} - 0.00148 \cdot \text{Height} \cdot \text{Thickness} \\
 & + 0.000064 \cdot \text{Height} \cdot \text{Angle} + 0.00179 \cdot \text{Height} \cdot \text{GSS} + 0.00015 \\
 & \cdot \text{Height} \cdot \text{OSS} + 0.00053 \cdot \text{Thickness} \cdot \text{Angle} + 0.0020 \text{Thickness} \cdot \text{GSS} \\
 & + 0.0191 \cdot \text{Thickness} \cdot \text{OSS} + 0.00136 \cdot \text{Angle} \cdot \text{GSS}
 \end{aligned} \tag{1}$$

4 Validation

The study validating of the developed software and the model output was performed by creating two HPDC aluminum dies designs. The part dimensions in the two models are the same but the first model has one cavity and the other has two cavities. The validation uses two methods, first by ProCAST simulation software and the other by built the mold itself with all its stages, beginning from full design using SolidWorks CAD software through manufacturing and injection on cold chamber HPDC machine.

The software is developed to be as simple as possible to meet user needs. The following steps are the steps used in the software:

1. The user inputs the dimensions and the thickness of the shape as shown in Fig. 6.

¹ProCAST: is software used for foundry simulation for all casting processes.

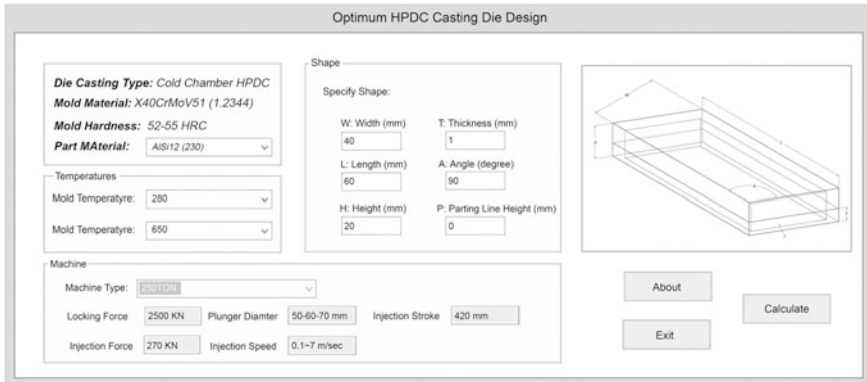


Fig. 6 User input

2. The user also selects the type of machine and temperature used for his application.
3. The software calculates from the data input and machine database the maximum number of cavities can be used in this die design. It is calculated from the minimum number of cavities gets from the maximum number of cavities calculated from the machine volume, machine plunger speed and machine locking force.
4. User again chooses the plunger and selects the number of cavities needed or presses back to select another machine if this machine not suitable for his application as in Fig. 7.
5. The software calculates the plunger speed of the machine as an output for the user.
6. It also calculates the gate area and dimensions with all its sections.

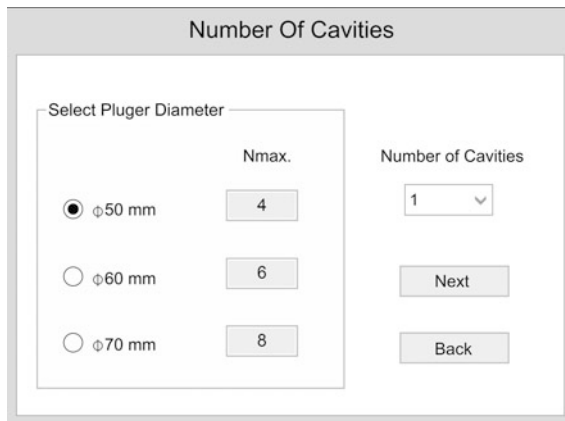


Fig. 7 Number of cavities

7. Moreover, the software calculates the overflow and vent area with detailed dimensions.
8. Finally, it calculates the optimum gate and overflow positions.
9. After these calculations, the software gives the output calculations with a simple form as viewed in Fig. 8.

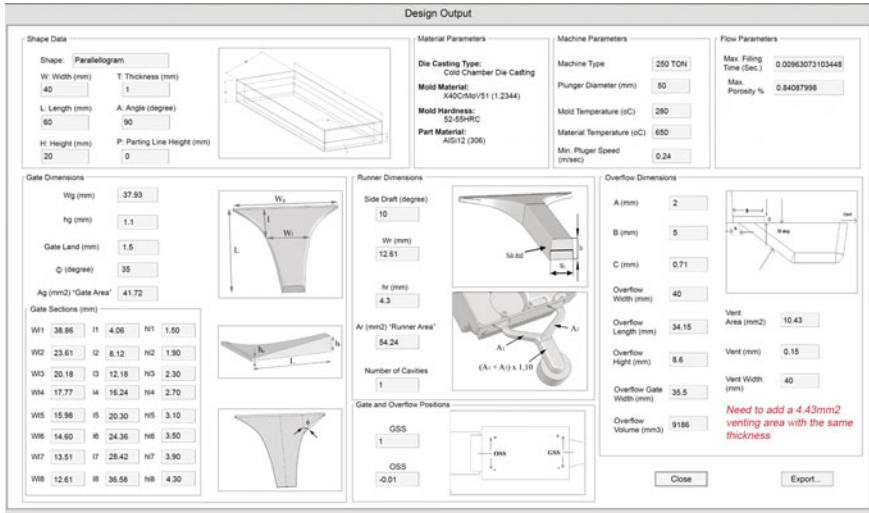


Fig. 8 Design output

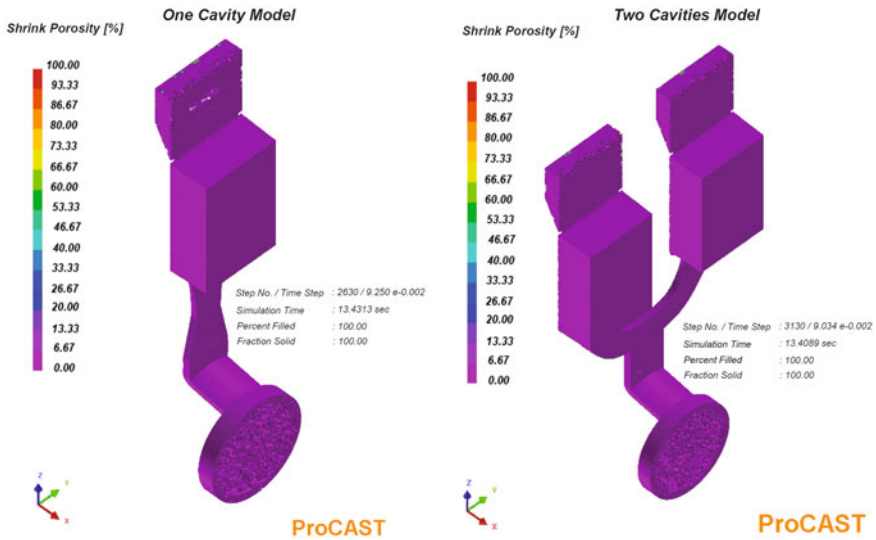


Fig. 9 The two ProCAST validation models, one cavity model on the left and two cavities model on the right

In Fig. 8 the developed software gives that the maximum porosity of 0.8% with this design. And that was the same results obtained from ProCAST simulation model in Fig. 9.

The other validation for the developed software is done by manufacture two molds. Figure 10 shows the design of the two molds. Figure 11 shows the 2 molds after manufacturing.

After manufacturing the molds, it has been tested on a HPDC cold chamber machine 250TON. Figure 12 presents validation parts after testing the molds on the HPDC machine.

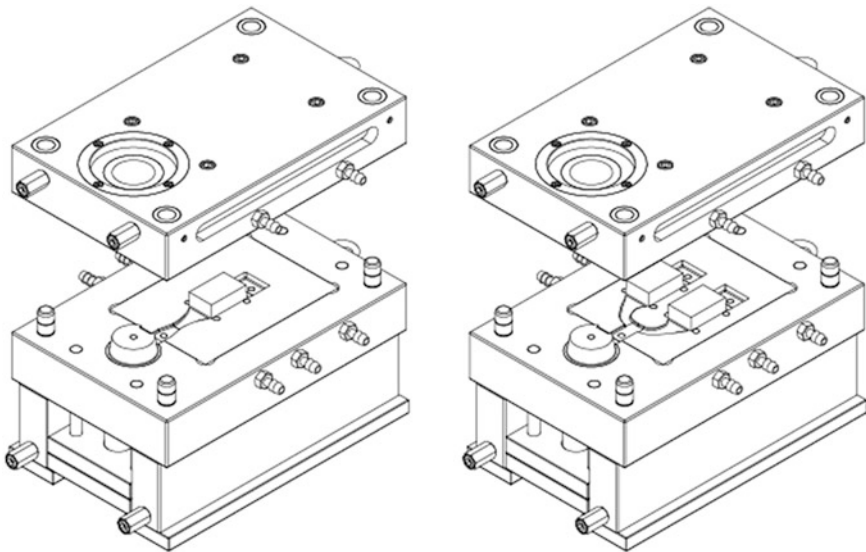


Fig. 10 The two validation molds design, one cavity model on the *left* and two cavities model on the *right*

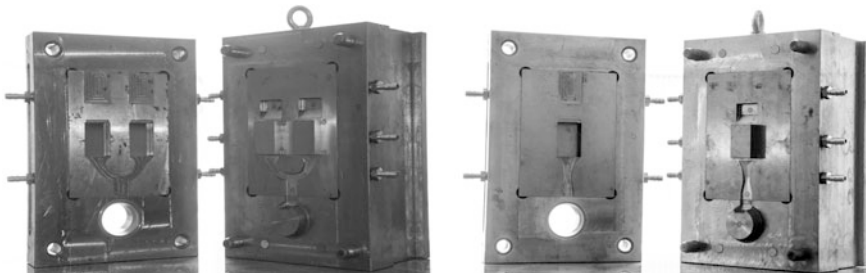


Fig. 11 The two validation molds after manufacturing, one cavity model on the *right* and two cavities model on the *left*

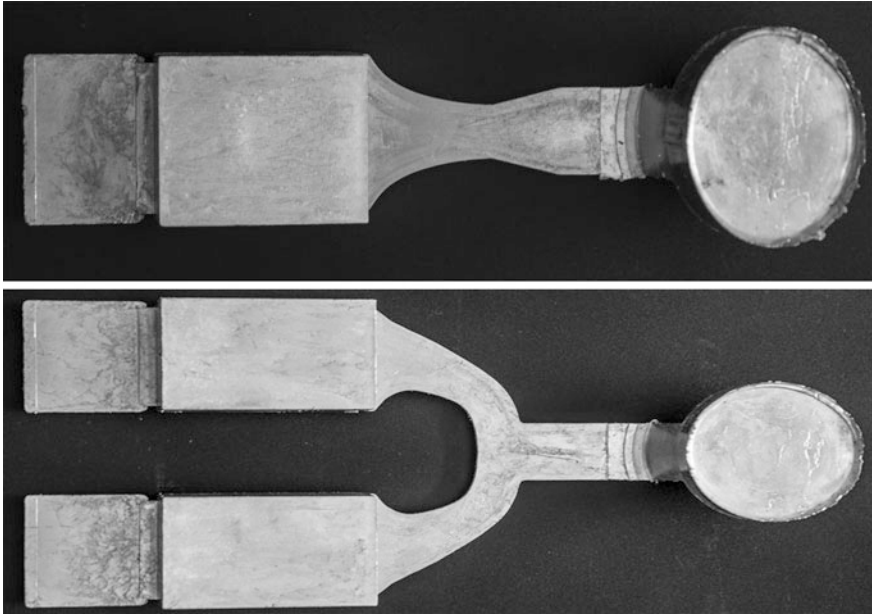


Fig. 12 The two validation parts, one cavity validation model on the *top* and two cavities validation model on *bottom*

The components have been sectioned in random sections to show if there is any porosity in the component or not. Figure 13 shows that there is no porosity in the components even after polishing the sectioned surface.

5 Discussions and Conclusions

In this work, a computer software has been developed to help cold chamber HPDC die designers by generating a detailed design for the gating system with optimum gate and overflow positions, which traditionally require a long time to design. The software also is validated, which will guarantee the user that the software output eliminates further corrections and adjustments in the gating system testing stage.

The experimental design done in this study gives an equation to relate all the 7 factors to the porosity percentage, it also concludes the following:

1. Part thickness is the most effective parameter for part porosity %.
2. The best gate location is to be shifted to the right side of the part ($GSS = 1$), regardless to all parallelogram parameters including its angle.
3. Also the best location for the overflow is around the center depending on the angle of the part.

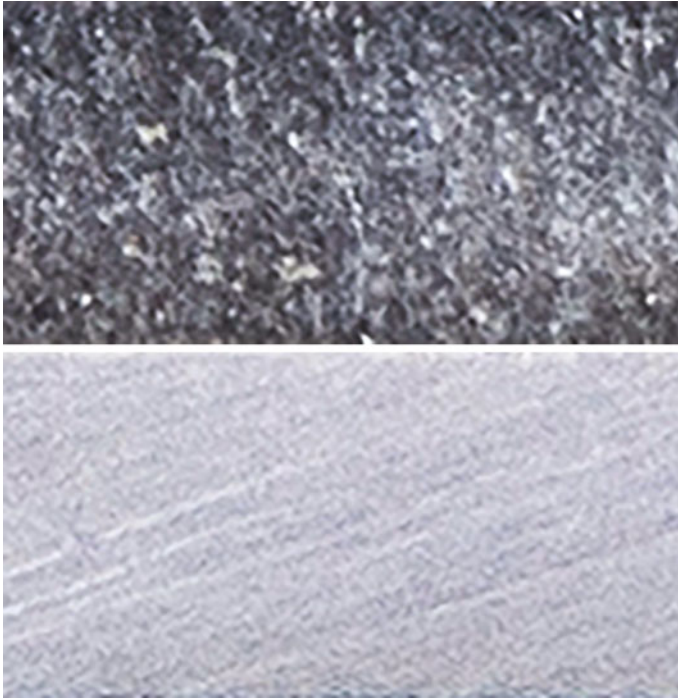


Fig. 13 Part sections with no porosity, polished section on *bottom* and without polishing on *top*

This study recommends the following:

1. Extend the study to cover the injection process with its factors.
2. Study more complex shapes.
3. Make the cooling rate and its parameters a part of the model.

References

1. Butler B (ed) (2001) Die casting handbook (2nd ed). NADCA, USA
2. Cleary PW, Ha J, Prakash M, Nguyen T (2008) Short shots and industrial case studies: understanding fluid flow and solidification in high pressure die casting. *Appl Math Model* 34:2018–2033
3. Fuh JY, Wu SH, Lee KS (2002) Development of a semi-automated die casting design system. *J Eng Manuf* 216:1575
4. Gulagoudar A et al (2015) Robust design approach to analyze casting defects in foundry industry. *Adv Eng Appl Sci: An Int J* 5(3):53–58
5. Hangai Y, Kitahara S (2008) Quantitative evaluation of porosity in aluminum alloy die castings by fractal analysis of spatial distribution of area. *Mater Des* 30:1169–1173

6. Hangai Y, Kitahara S (2008) Quantitative evaluation of porosity in aluminum die castings by fractal analysis of perimeter. *Jpn Inst Met* 49(4):pp 782–786
7. Herman EA (1992) Designing die casting dies. NADCA, USA
8. Herman EA (1996) Gating die casting dies. NADCA, USA
9. Kittur JK, Choudhari MN, Parappagoudar MB (2015) Modeling and multi-response optimization of pressure die casting process using response surface methodology. *Int J Adv Manuf Technol* 77:211–224
10. Lee BD, Baek UH, Han JW (2012) Optimization of gating system design for die casting of thin magnesium alloy-based multi-cavity LCD housings. *J Mater Eng Perform* 21:1893–1903
11. Lee WB, Lu HY (1999) Modeling of air back pressure in die-casting dies. *J Mater Process Technol* 91:264–269
12. Park YK, Yang J-M (2011) Maximizing average efficiency of process time for pressure die casting in real foundries. *Int J Adv Manuf Technol* 53:889–897
13. Queudeville Y, Vroomen U, Bührig-Polaczek A (2014) Modularization methodology for high pressure die casting dies. *Int J Adv Manuf Technol* 71:1677–1686
14. Shehata F, Abd-Elhamid M (2003) Computer aided foundry die-design. *Mater Des* 24:577–583
15. Tai CC, Lin JC (1998) A runner-optimization design study of a die-casting die. *J Mater Process Technol* 84:1–12
16. Ward M (2006) Gating manual. NADCA, USA
17. Weishan Z, Shoumei X, Baicheng L (1997) Study on a CAD/CAE system of die casting. *J Mater Process Technol* 63:707–711
18. Wu SH, Fuh JY, Lee KS (2007) Semi-automated parametric design of gating systems for die-casting die. *Comput Ind Eng* 53:222–232
19. Yue S et al (2003) Application of an integrated CAD/CAE/CAM system for die casting dies. *J Mater Process Technol* 139:465–468

Dielectric Material Selection Optimization Based on Relative Dielectric Constant Dependencies in Operating Environment

Ivica Kuzmanić, Igor Vujović and Joško Šoda

Abstract Selecting suitable material is an important issue in applied engineering. In this paper, an algorithm for optimum dielectric material identification is developed. Its scope covers general and specific requirements for the marine environment, using the parameters of influence to test whether the chosen material is suitable for use in the range of the parameters. The design of a parameter's range is determined by the designer, and should be suited to the exact field of the specific application. The proposed algorithm is also location/application-dependent. It provides a framework for further development of self-turning devices, correcting itself by calculating the influence of environmental conditions.

Keywords Selection algorithm · Relative dielectric constant (permittivity) · Operating conditions · Dielectric materials · Structural characterization

1 Introduction

Dielectric materials are a broad and rapidly growing group of materials used to insulate electrical currents, in LCD monitors, fiber optic communication cables, packaging of electronic and electrical products and devices, casings, among others. Owing to their wide range of applications, optimizing the selection of suitable materials is difficult. Since the definitions of “suitable” are inadequate, a more precise term should be used to describe the problem. We explore an approach to

I. Kuzmanić (✉) · I. Vujović · J. Šoda
Signal Processing, Analysis and Advanced Diagnostics Research
and Education Laboratory (SPAADREL), Faculty of Maritime Studies,
University of Split, Ruđera Boškovića 37, 21000 Split, Croatia
e-mail: ikuzman@pfst.hr

I. Vujović
e-mail: ivujovic@pfst.hr

J. Šoda
e-mail: jsoda@pfst.hr

finding the optimum material, reliable in the aggressive marine environment, suitable for use in shipbuilding, maritime traffic and industry.

Since the choice of dielectric materials is vital for the operation and performance of systems partly consisting of dielectrics, the selection of materials is highly important for a system's design. However, it has not been extensively researched. For example, guidelines for marine applications are given in [1]. To make matters more complex, in addition to traditional materials, there are now new synthetic materials, nanomaterials, and metamaterials with artificially created properties in use. The sheer quantity of materials aggravates the selection of a material best suited for any application. Furthermore, a designer or an engineer must take into consideration not only the best characteristics, but economic efficiency, the supply chain and a variety of other factors as well. There is also the question of what the best characteristics are. Characteristics can either be a reflection of general requirements, or of what is specifically desired in a given application, for example, in [2] the optical material (dielectric) refractive index is considered. Hence, material selection algorithms are in unprecedented demand.

Since the consequences of choosing an inappropriate material may range from minor deviations from normal operation to fatal failures (ranging from material damage to loss of lives or environmental pollution), the research in this area can be motivated by the need to prevent environmental accidents, save human lives and marine organisms. For example, if toxic material is used and there is danger of its release into the environment, it should be treated as an environmental threat. Finally, operating characteristics (cross-resistance to punctures, surface, etc.) and function of structural elements (e.g. an insulating element must simultaneously be sufficiently hard and elastic) play a vital role in write-off (economy), preventive measures against degradation processes (maintenance), breakdown and mechanical fractures [3], and so on.

This paper builds on papers in [2, 4, 5] and presents an upgraded material selection algorithm as a part of a broader material selection process.

Although there are only a limited number of references pertaining to the selection of dielectric materials, references relating to various dependencies of dielectrics i.e. [6–13] abound.

This paper is organized as follows. The second section provides necessary definitions, the mathematical background, and preliminary considerations. The third section describes the proposed algorithm and the broader optimum material selection scheme. A case example is given before the last section. Conclusions are given in the last section.

2 Background and Preliminaries

Determining the dependencies of any given physical phenomena or constant can be viewed from different perspectives: theory of sets, stochastic processes with covariances, or as functions.

Covariances can be separable in processes lacking any known analytical or other law (determining their mutual dependencies).

Definition 1 Consider $\{Z(\mathbf{s}; t) : \mathbf{s} \in D \subset \mathfrak{R}^d; t \in Z\}$ a spatial temporal zero-mean process observed at N space–time coordinates $(\mathbf{s}_1; t_1), \dots, (\mathbf{s}_N; t_N)$. Assuming that the covariance function is stationary in space and time, we can write:

$$\text{cov}(Z(\mathbf{s}_1; t_1), Z(\mathbf{s}_2; t_2)) = C(\mathbf{h}; u) \quad (1)$$

for $\mathbf{h} = \mathbf{s}_1 - \mathbf{s}_2, u = t_1 - t_2$. If C is a separable covariance:

$$C(\mathbf{h}; u) = C_1(\mathbf{h})C_2(u) \quad (2)$$

where C_1 is a positive-definite function in \mathfrak{R}^d , and C_2 is a positive-definite function in \mathfrak{R} (see [14]).

Although temperature and similar dependencies can be described as processes, this would not facilitate the selection of the optimum material at the macroscopic level. If dependencies are based on functions, they can be separated if general separability conditions are met as in Theorem 1 (see [15]).

Theorem 1 For $m, s \in N$ such that $m \leq s$, let u_1, \dots, u_m be m disjoint subsets of $[1: s]$. Function $f(x) \in F$ is separable with respect to x_{u_1}, \dots, x_{u_m} if and only if the following equation holds for any $x \in D$:

$$\left(\prod_{j=1}^m (I - P_{-u_j}) \right) (f)(x) = 0. \quad (3)$$

Definition 2 A topological space is called separable if it contains a countable, dense subset; that is, there exists a sequence $\{x_n\}_{n=1}^{\infty}$ of elements of space such that every nonempty open subset of the space contains at least one element of the sequence [16].

Definition 3 A metric space Z is separable if it contains a countable subset $\{z_n\}_{n=0}^{\infty}$ which is dense in Z (i.e., for all $z \in Z$ and all $\varepsilon > 0$, there exists z_n such that $d_Z(z; z_n) < \varepsilon$) [17].

Definition 4 A and B are separated in X if each is disjoint from the other's closure. The closures themselves do not have to be disjoint from each other; for example, the intervals $[0, 1)$ and $(1, 2]$ are separated in the real line R , although point 1 belongs to both of their closures. More generally in any metric space, two open balls $Br(x_1) = \{y: d(x_1, y) < r\}$ and $Bs(x_2) = \{y: d(x_2, y) < s\}$ are separated whenever $d(x_1, x_2) \geq r + s$. Note that any two separated sets must automatically be disjoint [18].

The theory of sets offers an approach to finding an optimum solution. Sets of possible candidates are formed based on the value of the relative dielectric constant. The intersection of sets has to be established to arrive at a possible solution.

Proposition 1 (separability condition) *Suppose there is phenomenon with characteristics which are described as a function dependent on several parameters described as variables. If function has separability property, it is allowed to express different dependencies (i.e. independent variables) separately as:*

$$f(x_1, x_2, \dots, x_n) = g_1(x_1) \cdot g_2(x_2) \cdot \dots \cdot g_n(x_n) \quad (4)$$

whose dependencies can be described and analyzed separately.

The problem with Proposition 1 is that while some dependencies have been explored, cross-dependencies have not. For example, if both temperature and moisture increase, should synergic effects be observed? Since neither theoretical nor experimental studies of this kind exist, this seems to be a new field of research.

After accepting an assumption about separability, corrections of the relative dielectric constant can be made. For example, if the operating temperature range is from T_1 to T_2 , then i.e. capacitance, C , should be in tolerable range.

We propose the identification of specific optimum materials by simply looking them up in a table indicating materials and the values of their dielectric constant under referent conditions. Other conditions should be normalized to referent after checking whether the given range produces a tolerable change of final characteristics, i.e. current, breakdown voltage or others.

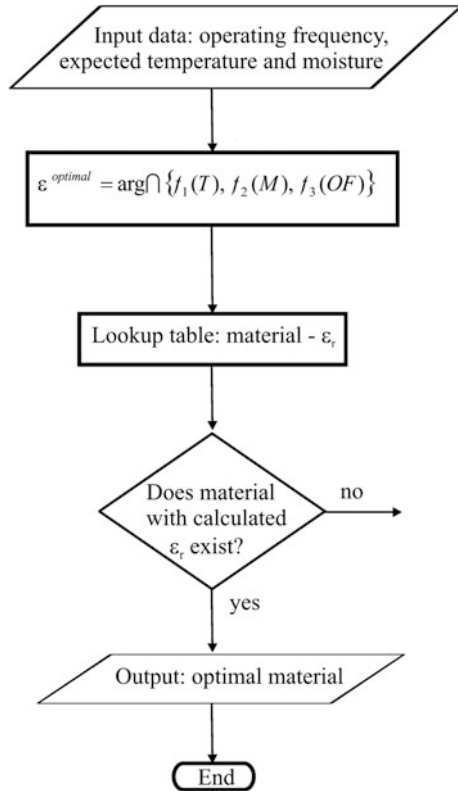
Lookup tables contain relative permittivity data for all available materials and equations for calculating dependencies from various parameters (allowing realistic cases to be designed, instead of assuming ideal laboratory operating conditions).

3 Development of the Proposed Method

An algorithm for optimum dielectric material selection is proposed in this paper, which covers general and specific influencing factors in the marine environment. In [4], general conditions were considered, such as operating frequency, moisture or temperature. In this paper, we also consider specific parameters, such as deck salinity, oil and fuel impact, dust, fumes, cross-resistance to punctures, among others. These parameters are specific ship requirements, which introduce more complex divisions, taking into account the place of work. For example, deck operations increase salinity. In the power compartment, the impact of oils and fuels is of interest. Aggressive holds-impact dust and fumes, and other factors, are also of interest in the engine room. Operating characteristics (cross-resistance to punctures, surface, among others) and functions of structural elements (e.g. an insulating element must simultaneously be sufficiently hard and elastic) play a vital role in write-off (economic efficiency), preventive measures against degradation processes (maintenance), breakdown and mechanical fractures [3], among others.

Figure 1 shows an algorithm for dielectric material selection based on general requirements, such as operating frequency of the product, anticipated temperature

Fig. 1 General dielectric requirements



and moisture. The algorithm is based on set intersection and implements the intersection of various dependencies which should be used to identify the optimum material [5, 19]. Relative permittivity is used for material characterization. Similarly, other characteristics, as well as a combination of several characteristics can be used for characterization. After establishing optimum relative permittivity, lookup table should be consulted to identify the appropriate material, since it can not be determined by other means.

Figure 2 illustrates a general scheme for the integration of specific requirements of an application into the general requirements for a given operating condition. If an intersection between these groups of requirements can not be determined, all requirements can not be met and the optimum material does not exist. Another possible failure in finding the optimum material is to not find it in the lookup table, because no material with calculated relative permittivity exists.

Figure 3 shows the inclusion of specific requirements into the selection process. Two cases are taken into account: power compartment and deck. Additional cases can be added as parallel branches (inclusion of the power compartment and deck as places of work). It is not plotted, because it would not be clear for examinations to include more branches. These branches reduce the number of possible materials by

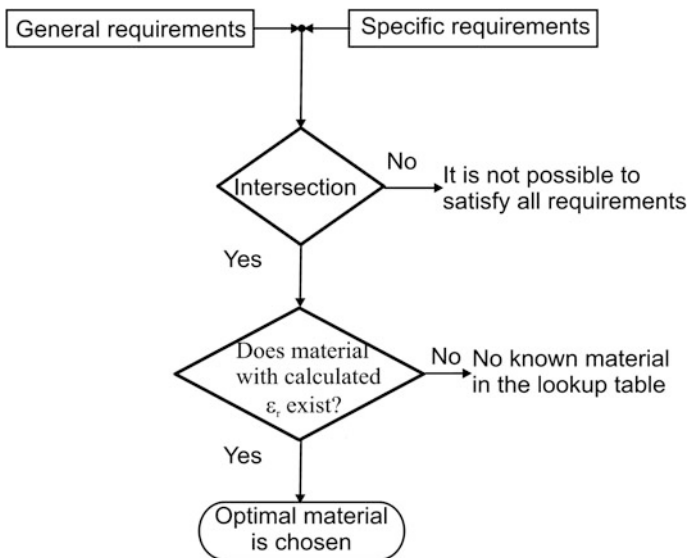


Fig. 2 General and specific requirements

excluding particular materials from the reduced lookup table used in further steps. Blocks “Include: ...” mean dependencies indicated in the block are taken into consideration. For example, “Include: deck salinity, atmosphere influences” means that mentioned dependencies are taken into account. Block “Exclude from lookup table” means that materials which do not comply with the above are excluded from further consideration.

If more than one material is in the optimum range of characteristics, other considerations can be taken into account, such as price, mechanical, technological and other factors.

4 Case Example of Consequences

As can be calculated, in the case of polyethylene, a 10% change in moisture would mean an increase in the relative dielectric constant from the referent 2.25 to 2.977, or, an increase by 32.31%. However, since moisture is only one parameter, the changes in other parameters should also be taken into account, since it could make the change in the relative dielectric constant deviate downwards or even upwards from 32% (see [20]).

If $\epsilon_r = 5$ (PVC), a 10% change in moisture gives a new value of 5.4521, i.e. implies a 9% change in the relative dielectric constant.

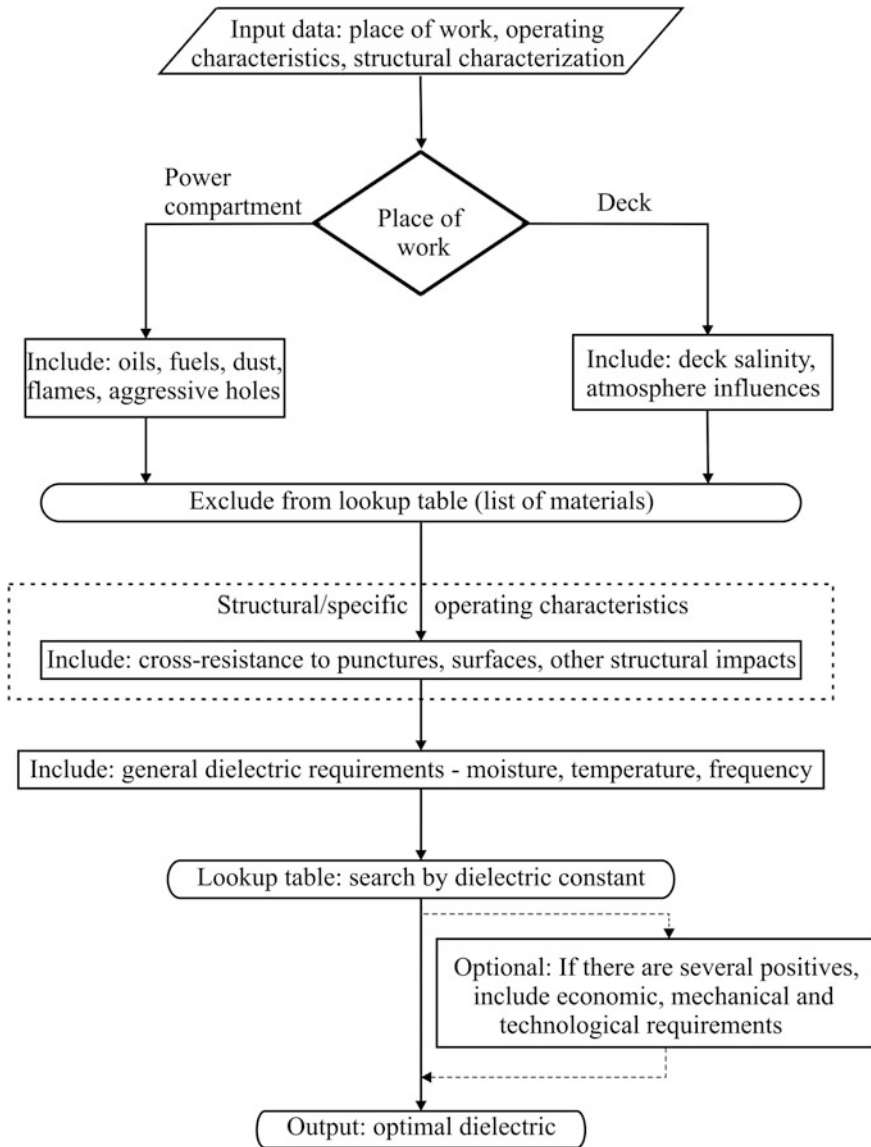


Fig. 3 Proposed algorithm (include general requirements means that the entire Fig. 1 is included)

$$C = \epsilon_0 \epsilon_r \frac{S}{d} \tag{5}$$

$$\frac{C}{C_0} = \frac{\epsilon_0 \epsilon_{rnew} \frac{S}{d}}{\epsilon_0 \epsilon_r \frac{S}{d}} = \frac{\epsilon_{rnew}}{\epsilon_r} \tag{6}$$

$$\frac{C}{C_0} = \frac{5.4521}{5} = 1.09042$$

or a 9.042% increase. For example, suppose this capacitor is used to tune a radio in a simplified circuit. The chosen frequency is changed by:

$$\frac{f_{new}}{f_0} = \frac{1/\sqrt{LC_{new}}}{1/\sqrt{LC_0}} = \sqrt{\frac{C_0}{C_{new}}} = 0.95764 \quad (7)$$

If we intended to tune the radio to 100 MHz, we would actually listen to 95.764 MHz, which is a tremendous error. In the case of digital modulation, the error is approx. 5% of the entire digital frequency range.

5 Conclusions

Since the influence of specific and structural impacts on the relative dielectric constant is not well researched, further research is required. Although further research is anticipated to be most beneficial for the shipbuilding industry, analogous research can benefit other industries, such as electronic, electrical, or machine industries as well.

This research can be used to test the sensitivity and robustness of systems containing dielectrics, and in the development of self-tuning devices.

References

1. Woodruff J (2012) Harsh environment connector material selection guide. Amphenol Fiber Systems International, Allen
2. Novkinić B, Vujović I, Šoda J (2015) Marine environment influence on fiber optic systems operation. *Trans Marit Sci.* doi:[10.7225/toms.v04.n01.003](https://doi.org/10.7225/toms.v04.n01.003)
3. Haddour L, Mesrati N (2014) Wear resistance of aluminas—dielectrical approach. In: Abstracts of 8th international conference on advanced computational engineering and experiment, Paris, 30 June–3 July 2014
4. Vujović I, Kulenović Z, Kuzmanić I (2015) New algorithm for optimum dielectric material selection in marine environment. *Brodogradnja (Shipbuilding)* 66:39–48
5. Vujović I, Kulenović Z, Vujović Kežić S (2014) Proposal of new method for dielectric materials selection in ship system applications. *Naše more* 61:28–32
6. Cheng YL, Leon KW, Huang JF, Chang WY, Chang YM, Leu J (2014) Effects of moisture on electrical properties and reliability of low dielectric constant materials. *Microelectron Eng.* doi:[10.1016/j.mee.2013.08.018](https://doi.org/10.1016/j.mee.2013.08.018)
7. Guo J, Zhou D, Wang L, Wang H, Shao T, Qi ZM, Yao X (2013) Infrared spectra, Raman spectra, microwave dielectric suitabilities and simulation for effective permittivity of temperature stable ceramics $\text{AMoO}_4\text{-TiO}_2$ (A = Ca, Sr). *Dalton Trans* 42:1483–1491

8. Kaiser DR, Reinert DJ, Reichert JM, Minella JPG (2010) Dielectric constant obtained from TDR and volumetric moisture of soils in Southern Brazil. *Rev Bras Cienc Solo* 34:649–658
9. Li HM, Ra CH, Zhang G, Yoo WJ (2009) Frequency and temperature dependence of the dielectric suitabilities of a PCB substrate for advanced packaging applications. *J Korean Phys Soc* 54:1096–1099
10. Molberg M, Leterrier Y, Plummer CJG, Walder C, Löwe C, Opris DM, Nüesch FA, Bauer S, Månson JAE (2009) Frequency dependent dielectric and mechanical behavior of elastomers for actuator applications. *J Appl Phys*. doi:10.1063/1.3211957
11. Silans TP, Maurin I, Segundo PCS, Saltiel S, Gorza MP, Ducloy M, Bloch D, Meneses DS, Echegut P (2009) Temperature dependence of the dielectric permittivity of CaF₂, BaF₂ and Al₂O₃: application to the prediction of a temperature dependent van der Waals surface interaction exerted onto a neighbouring Cs (8P_{3/2}) atom. *J Phys-Condens Mat*. doi:10.1088/0953-8984/21/25/255902
12. Zhou J, Zhou H, Hu C, Hu S (2013) Measurements of thermal and dielectric suitabilities of medium density fiberboard with different moisture contents. *BioResources* 8:4185–4192
13. Gadani DH (2010) Dielectric suitabilities of soils in microwave region. The Gujarat University. <http://shodhganga.inflibnet.ac.in/handle/10603/3872?mode=full>. Accessed 12 Feb 2016
14. Fuentes M (2006) Testing for separability of spatial–temporal covariance functions. *J Stat Plan Infer* 136:447–466
15. Goda T (2013) On the separability of multivariate functions, arXiv:1301.5962v1 [math.NA]. <http://arxiv.org/abs/1301.5962v1>. Accessed 12 Dec 2015
16. Heinonen J (2003) Geometric embeddings of metric spaces. Lectures in the Finnish Graduate School of Mathematics, University of Jyväskylä, Jyväskylä
17. Application of the Stone-Weierstrass Theorem: Separability. <http://www.maths.manchester.ac.uk/~nikita/31002/separability.pdf>. Accessed 3 Nov 2015
18. Willard S (2004) General topology. Dover Publications, New York
19. Kulenović Z, Vujović I, Vujović Kežić S (2014) Simulation of important factors' impact in the choice of dielectric material for marine applications. In: Proceedings of International Maritime Science Conference, University of Split, Faculty of Maritime Studies, Solin, Croatia, 28–29 April 2014
20. Vujović I, Kuzmanić I, Matic P (2017) Environmental influence on the safety and reliability of electrical and communication systems. *Eng Rev* (in print)

New Morphology of a Silver Chloride Surface Grown on Silver Wires

Salah Seghir Mechaour, Akila Derardja, M. Jamal Deen
and Ponnambalam Ravi Selvaganapathy

Abstract Here in, we present an experimental investigation using a very simple and low cost technique to provide new properties of AgCl classical materials at the nanometer scale. Indeed, nano-devices, like nano-sensors for example, require miniaturized reference electrodes with high stability. Miniaturization of the reference electrode has a detrimental effect on its desired characteristics, namely on the potential and lifetime. In this work, the Silver chloride wire, also known as a reference electrode, have been produced using the AC mode by electroplating. We analyze the properties of the surface of the wire by changing the applied potential while the other parameters of electrodeposition are kept the same. Then the morphology of the surface is explored at the microscopic scale with SEM. We found that when the potential applied is under 1 V, the morphology of the surface is a globular one, but this surface is also covered by AgCl crystals which grow in spiral fashion from a screw dislocation. This means that the surface is not completely relaxed even if the electric stability of the wire has been shown. If the potential is increased up to 1 V, the surface is covered by nanosheets. Thus, the surface is entirely relaxed and produces a more stable potential. In addition to increased stability of the wire, nanosheets allow to obtain two-dimensional surfaces which could be increased while the thickness still unchanged.

Keywords Growth of AgCl · Electrodeposition · Screw dislocation · Nanosheets surface

S.S. Mechaour · A. Derardja (✉)
Laboratoire de Mécanique Des Structures et Matériaux, Faculté de Technologie,
Université Batna II, Batna, Algeria
e-mail: akila.derardja@univ-batna.dz; derarakila@hotmail.com

S.S. Mechaour
e-mail: seghirs@hotmail.fr

M.J. Deen · P.R. Selvaganapathy
McMaster University, Hamilton L8S 4L8, ON, Canada
e-mail: jamal@mcmaster.ca

P.R. Selvaganapathy
e-mail: selvaga@mcmaster.ca

1 Introduction

Over the past century, there has been a dramatic increase in the production of very small devices for use in nanotechnology. These devices are made from materials which should have specific properties, especially at the nanometer scale. The properties of such materials depend on the technique used to produce them and the growth mode which may include different interaction parameters. Among these techniques, electrodeposition is starting to be regarded as a viable process for nanofabrication, and even though electrocrystallisation has received considerable attention from both the theoretical and experimental viewpoints [1–5]. This technique is typically low-cost and has the possibility to grow nanoscale structures over large areas with fine temporal control [6]. Also, this method has been widely used to create various mesostructures and constrain their shape by modifying the electrochemical growth conditions [7–11]. The growth mechanisms of such structures are still under investigation; however, the capping effect at high growth rates or an oscillatory behavior in nucleation kinetics has been postulated as the possible reasons for shape modification [12, 13].

Recently, using the electrodeposition technique, a crystalline growth of silver nanodiscs was obtained on a sacrificial copper cathodic substrate [14]. The anisotropic growth was attributed to the higher concentration of the copper ions close to the surface due to their sacrificial release from the cathode. Nanostructures such as nanorods [15], nanosheets [16] and nanotubes [17] typically have a high-aspect ratio and can provide this fractal-like topology. Several methods such as chemical vapor deposition, epitaxy and plasma processing or cluster growth have been developed to create these kinds of nanostructures [18–20].

However, few studies have been focused on developing this type of structure based on the presence of dislocations at the interface [21, 22]. Some works are limited to buried dislocation networks at the interface and to modeling the surface obtained by epitaxy [23–25].

In this paper, we investigate the growth of silver chloride on silver wires under low AC potential. The AC potential provides a more elegant control over the parameters that govern the growth process and helps in understanding the dynamics of this process better. We noted that when the potential applied is under 1 V, AgCl grows in spiral fashion from a screw dislocation. The mixture of globular and spiral aspects means that the surface of silver chloride is not completely relaxed. If the potential exceeds 1 V, the globular form disappeared and two-dimensional growth takes place leading to nanosheets. Then, the surface is completely relaxed. Furthermore, the surface of the wire could be increased by this process and new properties should be identified to make the most of in some applications of nanotechnology.

2 Experimental Details

In our beautiful experimental AC anodization, we use a function generator (Tektroix AFG 3022B) which can generate rectangular potential waveforms of various frequencies and duty cycles. The power source is connected to an electrochemical cell, which contains a cathode platinum wire (diameter of 250 μm) and Ag anode wire (diameter of 200 μm). The two electrodes are immersed in 1 M KCl and the distance between them is 1 cm.

Prior to the deposition, the Ag wire was rinsed with acetone, then DI water, followed by diluted HCl and then DI water again. The rinse is used to remove organic and inorganic residues on the wire's surface. The electrochemical conversion of the Ag to AgCl was carried out on a predefined portion of the Ag wire (1 cm) dipped in KCl at room temperature using asymmetric square waveforms of 50% duty cycle with various frequencies and amplitudes (AC mode).

3 Results and Discussion

The first stage of electrodeposition on an extraneous substrate is of course the formation of a thin film of the metal being deposited. The crystallographic nature, the thickness and the continuity of this layer is a function of the plating system. The exchange current density is actually the main reason for grain growth, also driving the growth of larger grains at the expense of smaller ones. Our measured lattice parameters are respectively 5.5494 \AA for AgCl [26] and 4.086 \AA for Ag. AgCl and Ag have FCC structure. The lattice mismatch between the two crystals is high which explains the presence of dislocations at the interface. The presence of dislocations may be the controlling factor in crystal growth. In FCC cubic metals, the screw dislocations move in $\{111\}$ type planes, but can switch from one $\{111\}$ type plane to another. It is well known that a large lattice mismatch expresses the difficulty of nucleating a new monolayer on a completed surface of an ideal crystal. But if a screw dislocation is present, it is never necessary to nucleate a new layer; the crystal will grow in spiral fashion at the edge of the discontinuity as shown in Fig. 1. An atom can be bound to a step more strongly than to a plane. If the growth rate is independent of the direction of the edge in the plane of the surface, the growth pattern is an Archimedean spiral:

$$r = a\theta \tag{1}$$

where a is a constant

If the radius of curvature r is too small, atoms on the curved edge move until the equilibrium curvature is attained (see Fig. 2). Away from the origin, each part of the step acquires new atoms at a constant rate, so that:

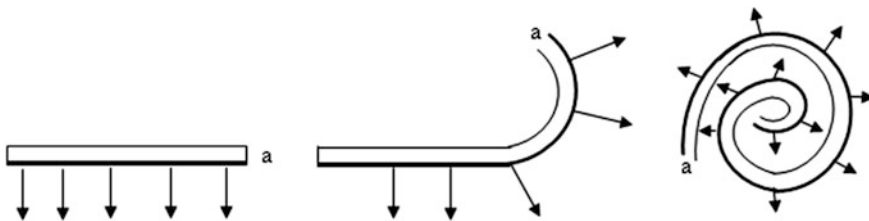


Fig. 1 Development of a spiral step produced by intersection of a screw dislocation with the surface of a crystal

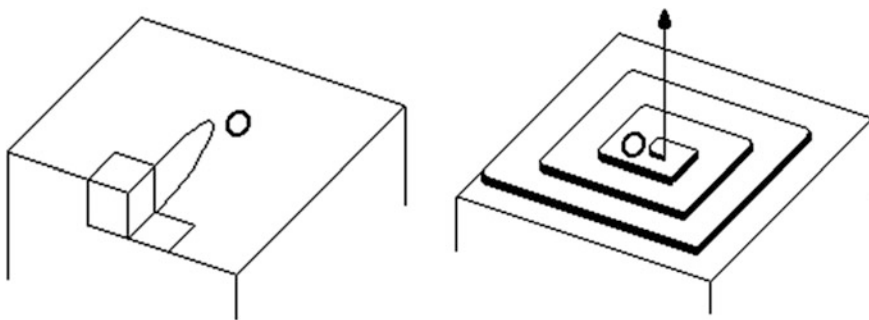


Fig. 2 Spiral growth on the strength of a dislocation emerging on the surface at point O

$$dr/dt = \text{Constant} \quad (2)$$

SEM images (see Fig. 3) show that the AgCl film contains a low density of axial screw dislocations that helps their essentially one-dimensional growth. Their density is so low that the crystal retains its theoretical elastic properties. From the absence of dislocations we would expect this AgCl film to have high yield strengths. That is, the stress is not in a direction that can cause slip but the stress caused by the electric field is the force under which the process of growth begins. A particular crystalline growth has been observed when using a potential of about 0.7 V (see Fig. 4).

The chemical composition of AgCl crystals (black in Fig. 4) is reported on Table 1. It is clear that once the dislocations are formed, the tabular growth of the crystals proceeds. The direction of the dislocations does not change very much, except for a few short segments. The origin of these dislocations is related to the addition of chloride after the nucleation phase, which induces lattice strains. The growth process occurs under a potential ≤ 0.5 V. Unfortunately, there is no mean to correlate the potential applied more firmly with the helicoidally growth and there is no theoretical evidence of this phenomena up to now; moreover, it is not so easy to exactly control the growth process with different parameters.

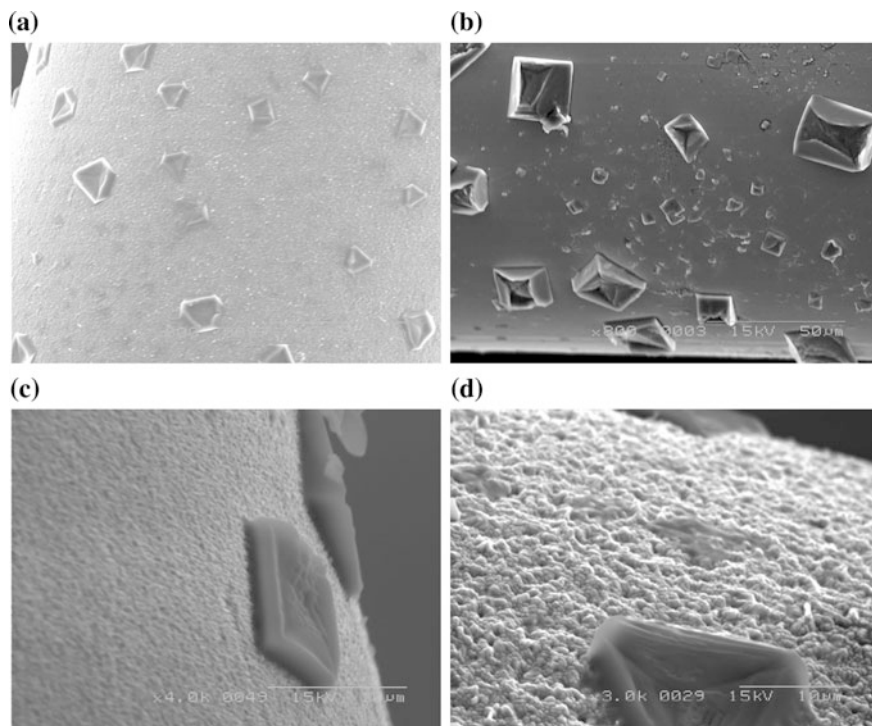


Fig. 3 SEM images of anodically grown AgCl on Ag wire in 1 M KCl for 15 min by applying an anodic potential of 0.1 V **(a)**, **(b)** and 0.5 V **(c)** and **(d)** while frequency was 0.5 MHz (The scale bar in image **(b)** applies to image **(a)**)

On the other hand, we think that the application of a potential which is over 1 V introduces a quick depletion of the chlorine concentration close to AgCl surface wire. The helical crystalline form disappears completely and the film seems completely relaxed.

At 1.5 V anodic potential, the silver wire is covered mostly by the nanosheets which are 300–400 nm thick, 5–10 μm high and 10–20 μm long (see Fig. 5b). These results indicate that the growth of the nanosheet AgCl structure over the conventional globular structure is increasingly preferred at higher anodic potentials.

As it demonstrated in a previous work [27], increasing the anodic potential results in increases in the length and height of the nanosheet, while the thickness remains constant (see Fig. 5). We note that when the potential exceed 1 V, the atoms Cl^- arrive from NaCl solution with a high rate which could be expressed in mono layers. For simplicity, we assume that the surface temperature is low enough so that only Cl^- diffuse on the surface and that Ag remain immobile. As deposition proceeds, the number of Ag^+ cations will increase roughly linearly until their concentration becomes comparable to the density of Cl^- .

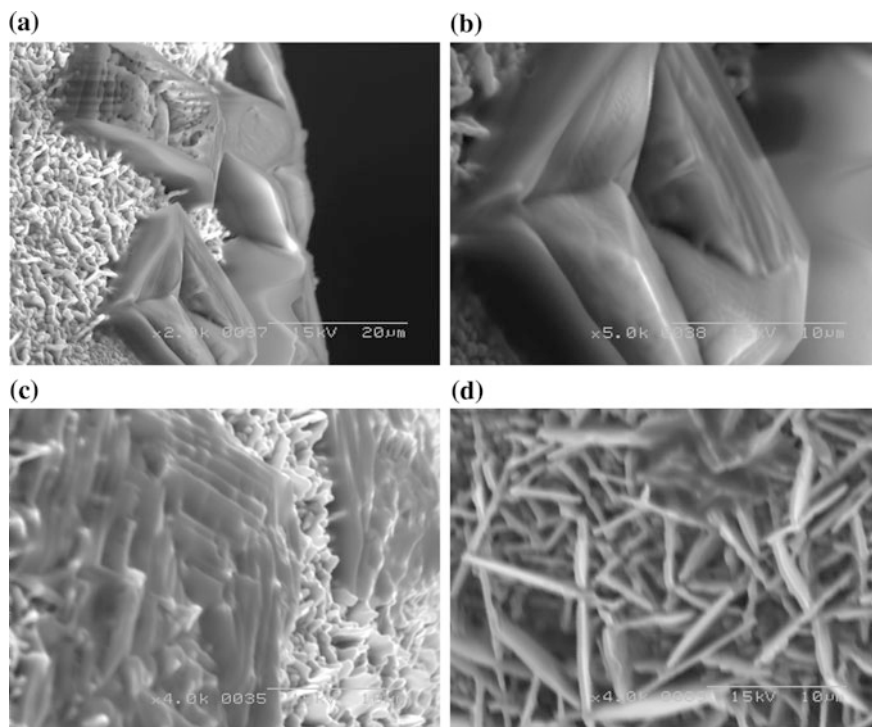


Fig. 4 SEM images of anodically grown AgCl on Ag wire in 1 M KCl for 15 min by applying anodic potential of 0.7 V (a), (b) and (c) and 1.5 V (d) while frequency was 0.5 MHz

Table 1 Chemical composition of black crystals on AgCl surface

Weight%	Atom%	Appl. Conc. %
Cl: 71.98	86.61	79.16
Ag: 26.12	10.33	19.31

From there on, the probabilities of a diffusing Cl^- anions to encounter one of its own or an Ag^+ cation become comparable and sheet growth competes with the creation of new stable nuclei. At the saturation nanosheets density, the frequency influences the diffusion of atoms until the size of grains is equal to the mean sheet separation and grains will attach themselves with much higher probability to existing grains than to create new ones. If the deposition continues the nucleation centers become more numerous and coalescence of 2D nanosheets occurs.

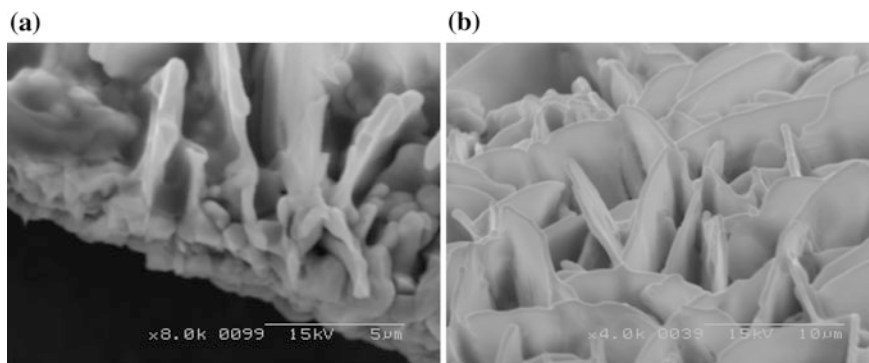


Fig. 5 SEM images of AgCl obtained under 2 V (a) a section of AgCl film (b) morphology of the AgCl surface

4 Conclusions

Silver chloride wires are commonly used as reference electrode, which is why research to date has tended to focus on the stability of AgCl rather than its morphology. Nevertheless, few papers have consistently shown that the morphology of the AgCl surface produced in general is a globular one. This work is an attempt to analyze the new morphology of silver chloride surfaces obtained through an electrochemical process at room temperature. To achieve this aim, wires of AgCl are produced under low potentials in AC mode and the growth is tested under different applied potential.

Microscopic investigations by SEM reveal clearly a new morphology of the silver chloride surface which may be described as random nanosheets. This morphology related to new properties depends on the potential applied and allows to increase the surface wire at nanometer scale. When the potential is under 1 V, the surface of AgCl has a mixture aspect; globular and in spiral fashion. If the potential exceed 1 V, the mosaic appearance of nanosheets is obtained and it would have remained unchanged during the major period of layer growth. In this case, we could confirm that the AgCl surface is completely relaxed and produces a more stable potential.

References

1. Yu Huang I, Huang Ruey-Shing (2002) Fabrication and characterization of a new planar solid-state reference electrode for ISFET Sensors. *Thin Solid Films* 406:255–261
2. Ardizzone I S, Cappelletti I G, Mussini I PR, Rondinini I S, Doubova LM (2003) Electrodeposited polycrystalline silver electrodes: Surface control for electrocatalysis studies. *Russ J Electrochem* 39(2):170–176

3. Bozzini Benedetto, Giovannelli Giuseppe, Mele Claudio (2007) Electrochemical dynamics and structure of the Ag/AgCl interface in chloride-containing aqueous solutions. *Surf Coat Technol* 201:4619–4627
4. Jin X, Lu J, Liu P, Tong H (2003) The electrochemical formation and reduction of a thick AgCl deposition layer on a silver substrate. *J Electroanal Chem* 542:85–96
5. Tiwari JP, Rao Chepuri RK (2008) Template synthesized high conducting silver chloride nanoplates. *Solid State Ion* 179:299–304
6. Gurrappa I, Binder L (2008) Electrodeposition of nanostructured coatings and their characterization. A review *Sci Technol Adv Mater* 9:043001
7. Pradhan D, Kumar M, Ando Y, Leung KT (2008) One-dimensional and two-dimensional ZnO nanostructured materials on a plastic substrate and their field emission properties. *J Phys Chem C* 112:7093–7096
8. Cao BQ, Teng XM, Heo SH, Li Y, Cho SO, Li GH, Cai WP (2007) Surfactant-assisted in situ chemical etching for the general synthesis of ZnO nanotubes array. *J Phys Chem C* 111: 2470–2476
9. Sajanlal PR, Sreeprasad TS, Samal AK, Pradeep T (2011) Anisotropic nanomaterials: structure, growth, assembly, and functions. *Nano Rev* 2(1):5883
10. Xu LF, Guo Y, Liao Q, Zhang JP, Xu DS (2005) Morphological control of ZnO nanostructures by electrodeposition. *J Phys Chem B* 109:13519–13522
11. Martin-Gonzalez M, Snyder GJ, Prieto AL, Gronsky R, Sands T, Stacy AM (2003) Direct electrodeposition of highly dense 50 nm Bi₂Te₃-y Se y nanowire arrays. *Nano Lett* 3: 973–977
12. Xiao ZL, Han CY, Kwok WK, Wang HW, Welp U, Wang J, Crabtree GW (2004) Tuning the architecture of mesostructures by electrodeposition. *J Am Chem Soc* 2316–2317:126
13. Fleury V (1997) Branched fractal patterns in non-equilibrium electrochemical deposition from oscillatory nucleation and growth. *Nat* 390:145–148
14. Zhu YC, Geng WT (2008) Three-dimensional self-assembly of Ag nanodisks in crystallography orientations by modified electrochemical deposition. *J Phys Chem C* 112:8545–8547
15. Xia YN, Yang PD, Sun YG, Wu YY, Mayers B, Gates B, Yin YD, Kim F, Yan YQ (2003) One-dimensional nanostructures: synthesis, characterization, and applications. *Adv Mater* 15:353–389
16. Law M, Goldberger J, Yang PD (2004) Semiconductors nanowires and nanotubes *Annu. Rev Mater Res* 34:83–122
17. Wu YH, Yu T, Shen ZX (2010) Two-dimensional carbon nanostructures: Fundamental properties, synthesis, characterization and potential applications. *J Appl Phys* 108:071301
18. Knez M, Niesch K, Niinisto L (2007) Synthesis and surface engineering of complex nanostructures by atomic layer deposition. *Adv Mater* 19:3425–3438
19. Gonzalez-Aguilar J, Moreno M, Fulcheri L (2007) Carbon nanostructures production by gas-phase plasma processes at atmospheric pressure. *J Phys D Appl Phys* 40:2361–2374
20. Jensen P (1999) Growth of nanostructures by cluster deposition: experiments and simple models. *Rev Mod Phys* 71:1695
21. Morin SA, Forticaux A, Bierman MJ, Jin S (2011) Screw dislocation-driven growth of two-dimensional nanoplates. *Nano Lett* 11:4449–4455
22. Hacialioglu Salih, Meng Fei, Jin Song (2012) Facile and mild solution synthesis of Cu₂O nanowires and nanotubes driven by screw dislocations. *Chem Commun* 48:1174–1176
23. Derardja A (2010) Anisotropic elastic distortions of a buried dissociated hexagonal network of dislocations in a Nickel based superalloys. *Adv Mater Res* 83–86:289–294
24. Lashmore DS, Thompson R (1992) Cracks and dislocations in face-centered cubic metallic multilayers. *J Mater Res* 7:2379
25. Bonnet R (2000) Evaluation of surface strain due to the reconstruction of atomically close-packed crystalline surfaces. *Phys Rev B* 61:14059–14065

26. Plendl JN, Mansur LC (1972) Anomalous thermal expansion with infrared spectroscopy. *Appl Opt* 11:1194–1999
27. Safari S, Selvaganapathy PR, Derardja A, Deen MJ (2011) Electrochemical growth of high-aspect ratio nanostructured silver chloride on silver and its application to miniaturized reference electrodes. *Nanotechnol* 22(31):315601–315608

Development of Highly Effective Multiplex Integration Electric Charging Module for Range Extension of Hybrid Type Refrigeration Truck

Kee Joo Kim

Abstract In present study, a refrigeration truck cooling device for efficiently driving a compressor of a cooling engine was developed. For this purpose, an electric refrigeration system and the alternator from a solar charging system was added to an existing hydraulic engine refrigeration system in order to maintain continuous charging. Technologies to be developed in this study are related to the refrigeration vehicle cooling system to power the compressor for cooling with the electric current generated from a variety of electric sources. In addition, the solar cell was connected to the power supplies which were charging the battery pack as well as to operate the drive motor by using the voltage generated by the solar cell. In this case, the solar cell was installed to the top freight loading part to generate a direct electric current from the sun-light generating electricity. From this system, the new refrigeration truck was successively developed which was equipped with solar cell modules to extend the mileage of the existing refrigeration vehicle and to improve fuel efficiency.

Keywords Electric charging module · Motor · Solar cell · Hybrid · Refrigeration truck

1 Introduction

In the case of the battery installed inside the vehicle, battery power is wasted because it is used to start up the electric starter motor, therefore, the power supply is sufficient to turn the vehicle on. From this, in order to increase the amount of power while driving and the freezer is running, there is a need for a method for regenerating electricity by using a hybrid model and increase the size and capacity of the battery. In addition, for a constant (continuous) power charge, it is helpful to use the electric power in the refrigeration truck after it is equipped with the ability to

K.J. Kim (✉)

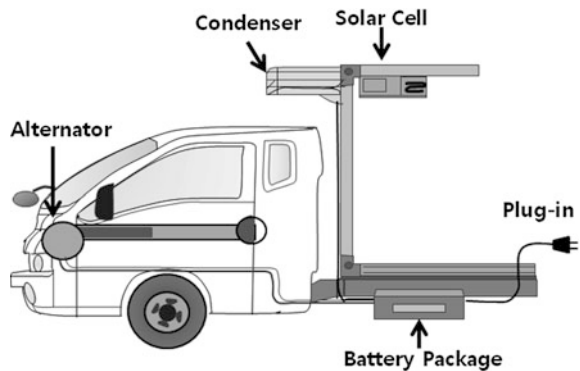
Department of Mechatronics Engineering, Tongmyong University, Busan 48520, Korea
e-mail: kjkim@tu.ac.kr

recharge at home or in the company from the “plug-in hybrid” type. These days, one of the main issues of the automobile industry is exhaust gas emissions and fuel efficiency. Therefore, improving the refrigeration (freezer) running in the truck, can contribute to reduce gas exhaustion and improve fuel economy when stopped or even when the city. By providing the power required for operating the refrigeration to automatically or manually select possible, it is necessary to design a solution which addresses the noise problem. In the case of electric vehicles as well as refrigeration trucks, it is noteworthy that even the running distance (range) is significantly reduced when running the heater or air conditioning. Especially, in case of the MiEV vehicle made by Missibissi Co., the maximum driving distance (range) was reduced from 160 to 108 km (reduction of 32.5%) when running the air conditioning system and it was reduced by 37.5% when running the heating system [1–3]. In the present study, in order to improve the generation method of the cooling system for the refrigeration truck, lithium-ion battery charging systems, as well as photovoltaic (PV) module renewable energy conversion systems were developed and equipped with and energy-saving type refrigeration truck used for driving a cooling system. Because these charging systems increase battery life, the driving range extension and fuel saving can be achieved from the successful development of an energy-saving type refrigeration truck equipped with a PV module.

2 Development Method

In the present study, the conventional refrigeration truck operated only with an engine that was modified by attaching the auxiliary power generation system with the electric motor and the battery module and the PV module charging device. From this, a system was developed that can increase the running distance of the conventional refrigeration truck by more than 20%. Figure 1 shows the schematic of the electric charging module system. As shown in Fig. 1, it was developed as a

Fig. 1 Schematic of electric charging module system of hybrid type refrigerator truck for range extension



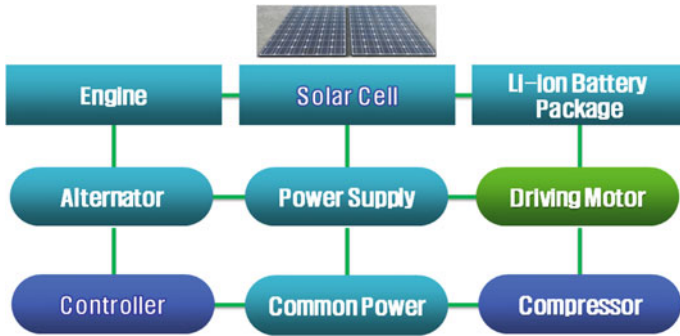


Fig. 2 Block diagram of power supply for cooling module driving

multi-integrated electricity module equipped with alternator (generator), solar cell and battery pack.

Figure 2 shows the block diagram of the power supply. The alternator that is connected to the engine power is a generator (generating a direct current voltage) in a broad sense that converts the mechanical energy of the engine into electrical energy. The power supply is connected to the alternator, and operates the driving motor with a voltage generated by the alternator. In addition, the motor can be operated through the battery pack from the power supply unit to charge it. The motor is connected to the compressor which is operated by the drive motor to drive the cooling cycle.

The solar cells are connected to the power supply and the power supply using the voltage generated from the solar cell operates the motor for the cooling module. In addition, the motor can be operated through the battery pack in the engine stop state by solar cells to charge the battery pack. The solar cells convert solar energy into electric energy and then generates a voltage through a photoelectric effect. The solar cells are designed to produce a DC voltage and be installed in the refrigeration truck to the upper portion of the vehicle cargo area.

The total energy consumed during driving can be calculated from Eq. (1). Equation 1 is a key to solve the formula to calculate the target value for this study. After all, the ultimate goal of this study was to enhance the driving range by attaching the auxiliary power generation system with the electric motor and the battery module and the PV module charging device.

$$\begin{aligned}
 \text{Energy}[\text{kJ}] &= \left\{ \frac{f_{road}[\text{N}] \cdot r_{tire}[\text{m}]}{FDR[-] \cdot \eta_m[-]} + \frac{V_m[\text{kg}] \cdot a[\text{m/s}^2] \left(= \frac{dv[\text{kph}] \cdot 1000}{3600 \cdot dt[\text{s}]} \right) \cdot r_{tire}[\text{m}]}{FDR[-] \cdot \eta_m[-]} \right\} \\
 &\cdot S[\text{m}] \\
 f_{road} &= \mu \cdot m[\text{kg}] \cdot g + 0.5 \cdot C_d \cdot \rho \cdot A \cdot v^2 \tag{1}
 \end{aligned}$$

here,

- v vehicle velocity, km/h,
- V_m vehicle total mass, kgf,
- a acceleration, m/s^2 ,
- r_{tire} tire radius, m
- dt time increment,
- dv velocity increment,
- η_m efficiency,
- u friction coefficient,
- m vehicle mass, kgf
- g gravity, m/s^2 ,
- C_d air resistance coefficient,
- ρ density, g/cm^3 ,
- A vehicle projected area, m^2 .

3 Fabrication of Photovoltaic Electric Module

Table 1 shows the specification of the target system.

Figure 3 shows the picture of a hybrid type PV electric module and a BLDC motor for the refrigerator and compressor mounted to a refrigeration truck. As shown in Fig. 3, the PV modules were installed to the upper portion of the cargo compartment on a flat surface and connected to 3 number of solar plate having 250 W (total 750 W). The controller capacity of the PV electric modules are given by input values of DC 72 ~ 144 V, 15.2 A and output values of 51.5 V, 21 A.

Table 1 System specification

Compressor	138 cc Piston
Compressor RPM	1500 rpm
All in one charging module	DC 12 ~ 140 V to DC 51.5 V AC 220 V to DC 51.5 V
Battery package system weight	100 kg ↓
Operating time	Max. 8 h
Refrigerator/freezer Temperature	+20 °C to -20 °C
Capacity of truck	1 Ton

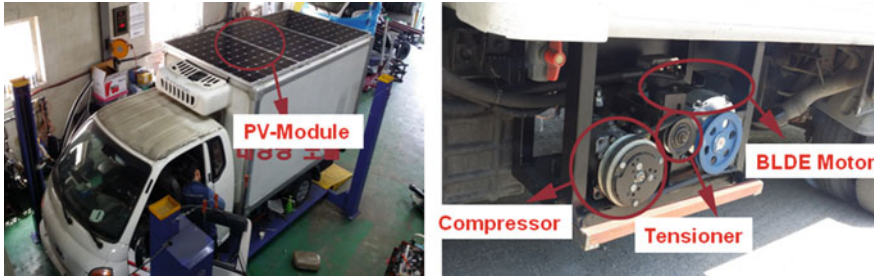


Fig. 3 Solar cell module, operating motor and compressor installation place in refrigerator truck

4 Experimental Results and Discussion

The optimal rotation speed and power consumption for cooling were measured by operating the compressor from the motor. For this, the test jig was manufactured as shown in Fig. 4. The battery voltage and the current were measured when the compressor was driven by the motor at 3000 rpm.

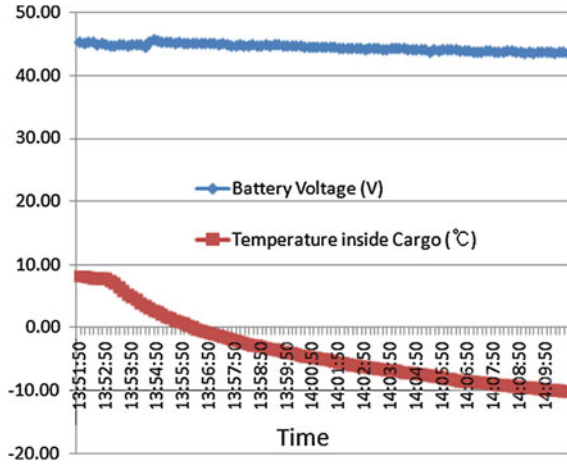
Figure 5 shows the battery voltage and temperature following as the time change measured through the testing jig.

As shown in Fig. 5, it took 4 min and 30 s to go from 8.3 to 0 °C and 13 min and 40 s to reach to -10 °C from 0 °C inside the cargo temperature. The battery voltage was dropped to 1.78 V to reach the temperature of -10 °C. From this experiment, it was found that the electric consumption increased because of the high speed of the motor and the motor overheating due to overload occurring due to the increased motor rotation speed. The cooling performance of the refrigeration truck was setting from this experiment. For this, the temperature was measured by attaching the temperature sensor on the inside and outside of the refrigeration truck. After initially setting the temperature at -10 °C, it was measured by operating the

Fig. 4 Test jig for measuring rotating speed and electric power consumption



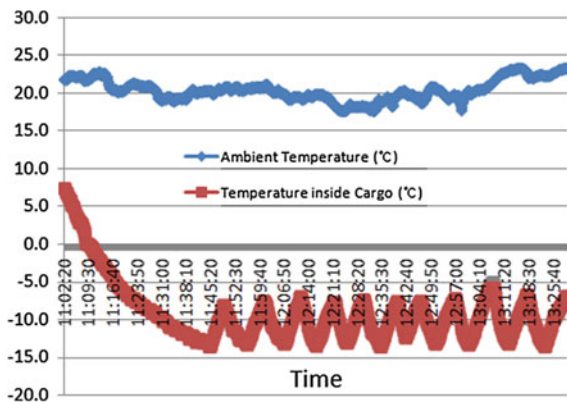
Fig. 5 Measurement of time versus battery voltage and temperature



cooler. Figure 6 shows the experimental results of the cooling performance of the refrigeration truck following as the time.

As shown in Fig. 6, the temperature from 7.6 to 0 °C was falling rapidly and it took for about 7 min. However, it took about 35 min from 0 to -13 °C. Again, it took about 4 min and 40 s to raise the temperature to go -7.9 °C from -13 °C and it took 6 min and 50 s to fall back from -7.9 to -13 °C. Therefore, it was found that the time for raising the temperature was faster than the time for lowering the temperature. The controller proved to operated correctly as a temperature controlled operation. In addition, sufficient time was needed until the internal insulation material achieved constant cooling. The motor overheating may be a problem because it requires a considerable amount of time to reach the -(minus) temperatures from +(plus) temperatures. However, in the initial time, it needs a lot of power to reach the -(minus) set temperature. After that is not expected to have a high power consumption, because less time is spent. In order to prevent the initial motor

Fig. 6 Measurement of time versus ambient temperature and room temperature in refrigerator truck



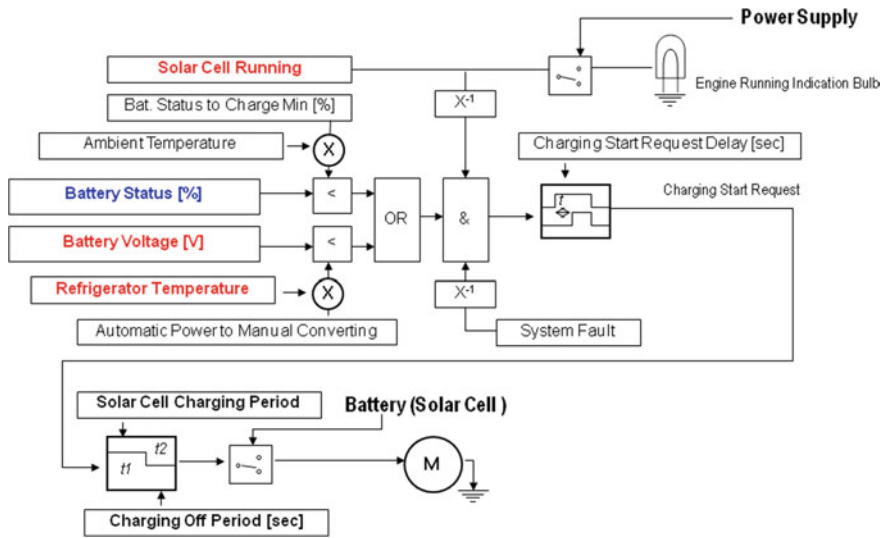


Fig. 7 Control logic of system module

overheating, it was equipped with a separate cooling motor fan. Adjusting the rotational speed of the motor can shorten the time to reach the set freezing temperature. However, the motor overheating is expected due to the fast motor rotation speed for freezing. Through the repetition of the experiment above, the control logic of the refrigeration truck could be set as shown in Fig. 7. The refrigeration truck was fabricated from the established control logic as shown in Fig. 7. From this, the cooling module for refrigeration truck that the fuel efficiency was considerably improved was successively developed.

In the case of the refrigeration truck developed in the present study, the main uses of the refrigeration system was to achieve cooling while driving. However, if the battery level drops below a critical level, it automatically switches to the existing refrigeration system (using an engine hydraulic driving system) and if the battery level reaches a certain level or higher through continuous charging, it converts to the electric refrigeration system automatically. Apart from a battery mounted on current vehicles, the high capacity (8 kWh) Li-ion battery controlled by BMS (battery management system) was also installed. The motor for the operation of the cooling system can be driven through this high capacity battery by continuously charging into the electricity collected by electricity which was generated during vehicle operation or solar power generated from solar system. After successful development of this system, the fuel efficiency of the refrigeration truck should be improved than in conventional refrigeration truck which are operated by a hydraulic type.

Table 2 Results after fuel consumption test

	Without refrigerator operation	With refrigerator operation (using vehicle power)	With hybrid type refrigerator operation (using PV module)
Average Fuel Efficiency	13.4 km/l	11.4 km/l	12.2 km/l
Fuel Consumption	3.46l l	4.07l l	3.82l l

The fuel consumption test of the hybrid type refrigeration truck equipped with electric charging module was conducted. The fuel consumption measurement was commissioned by KIMM (Korean Institute of Machinery and Materials). Table 2 shows the measuring results of average fuel efficiency and consumption.

After the engine stopped, the refrigeration freezer driving time (after setting the controller to maintain the temperature within the refrigeration truck to 10 °C) was measured. From this results, it was found that the refrigeration freezer was operating smoothly for a total of 3 h 42 min including pre-cooling time (about 11 min) with pure electricity driving supplied by high capacity Li-ion battery.

5 Conclusions

- (1) From the experimental results of the fuel efficiency and fuel consumption studies for refrigeration truck, the fuel efficiency of the refrigeration truck which was operated with the hybrid type refrigeration freezer equipped with a PV generation module with an efficiency of 12.2 km/l. However, the consumption of the refrigeration truck which was operated with only vehicle engine power was about 11.4 km/l. Therefore, the fuel efficiency was improved about 7% and the fuel consumption was also improved by about 6.5% (from 4.071 l to 3.821 l).
- (2) After the engine stopped, the refrigeration freezer was operating for over 3 h. Through these results, it was a successful that the refrigeration freezer could be operated with engine stop. Therefore, it is possible to get off cargo with engine stop even though the refrigeration truck is parked inside the building parking lot and it is possible to reduced exhaust emissions concerns.
- (3) In case of the refrigeration truck driven by electric power, fuel consumption and emissions do not occur at all, and noise problems were also solved.

Acknowledgements This work (Grants No.C0346355) was partially supported by Business for Cooperative R&D between Industry, Academy, and Research Institute funded Korea Small and Medium Business Administration in 2015.

References

1. Kim KJ, Won ST (2008) Effect of structural variables on automotive body bumper impact beam. *Inter J Auto Tech* 9:713–720
2. Kim KJ, Park JH (2016) Development of automated electric snowplow by using clutch bobbin for improving durability. *Trans Korean Soc Mech Eng A* 40:947–952
3. Kim KJ, Lee YC, Park JH (2015) Fundamental research on power train systems for electric vehicles. *Mat-wiss Werkstofftech* 46:414–419

Experimental Numerical Model of Roughness in Finishing Face Milling of AISI 4140 Hardened Steel

Marco Stipkovic Filho, Marco Antônio Stipkovic,
Éd Cláudio Bordinassi, Sérgio Delijaicov
and Sérgio Luis Rabelo de Almeida

Abstract This work is based on the roughness analysis of a hardened steel, AISI 4140 quenched and tempered with 58HRC, during an end milling process executed with a CBN (cubic boron nitride) tool, obtained by varying three basic cutting parameters (cutting speed, feed and cutting depth). It was decided for the experimental planning, to use a central composite design, widely applied in research related to machining experiments. The results were statistically processed by the software “Statistica”, enabling the generation of a mathematical equation to predicted the surface roughness value due to the optimization of the three cutting parameters adopted. The surface roughness results are in the range of 0.16–0.4 R_a . Two numerical models were created using the NLREG software confirming the interaction of the cutting parameters with the roughness. The cutting parameter with the most influence on the surface integrity during the end milling process was the feed per tooth.

M.S. Filho (✉) · S.L.R. de Almeida
Escola de Engenharia, Universidade Presbiteriana Mackenzie, Rua Da Consolação, 930,
01302-090 São Paulo, SP, Brasil
e-mail: mstip@uol.com.br

S.L.R. de Almeida
e-mail: slrabelo@terra.com.br

M.A. Stipkovic · É.C. Bordinassi · S.L.R. de Almeida
Instituto Maua de Tecnologia, Centro Universitário, 01–09580.900 São Caetano Do Sul, SP,
Brasil
e-mail: marco.stipkovic@schuler.com

É.C. Bordinassi
e-mail: ecb@maua.br

M.A. Stipkovic · É.C. Bordinassi · S. Delijaicov
Faculdade de Engenharia Industrial, Centro Universitário, 3972–09850.901 São Bernardo Do
Campo, SP, Brasil
e-mail: sergiode@fei.edu.br

Keywords End milling · Roughness · Numerical model · Cutting parameters · Hardened steel

1 Introduction

Development of a numerical model able to predict the value of roughness in machining AISI 4140 hardened steel according to the main cutting parameters and thus help to assist the machinist in the correct selection of these parameters.

Given the constant search to reduce manufacturing costs of mechanical components in the segment of machinery and equipment, there is a growing tendency to replace the grinding process hardened steel (in the range 45–65 HRC), by turning and milling processes and with cubic boron nitride CBN tools.

2 Materials and Methods

The material used was a wrought AISI 4140 steel.

It was quenched and tempered with a hardness of 58 ± 2 HRC and a depth of 3 ± 1 mm with the following chemical composition attested by trial: C-0.413; Mn-0.842; Si-0.241; P-0.013; S-0.012; Cr-0.904; Ni-0.045; Mo-0.181; Al-0.030; Cu-0.063; Ti-0.002; V-0.004.

The specimens were of prismatic format with $140 \times 110 \times 20$ mm previously roughed, according to Fig. 1.

The tool used was a face milling head with $\phi 63$ mm provided with 5 cutting edges in a straight path through the center of the part and the whole diameter in touch and no refrigerant. The insert code CBN used was R245 12T3 E CB50. Figure 2 shows one specimen during the end milling process.

The milling machine employed was manufactured by Sanches Blanes, model FU-1, ISO cone 40, with a maximum rotation of 6000 rpm and $V_{\text{fmax}} = 1500$ mm/min with good rigidity.

The cutting parameters were chosen with the intent to explore the limits of the CBN tool, representing a wide variation of 400% per cutting parameter.

The statistical analysis was performed based on a composed central design. It fits very well to machining tests, due to the good repeatability in relation to the cutting parameters and concentrates the necessity of some replicas only in the central points to assure the stability of the process.

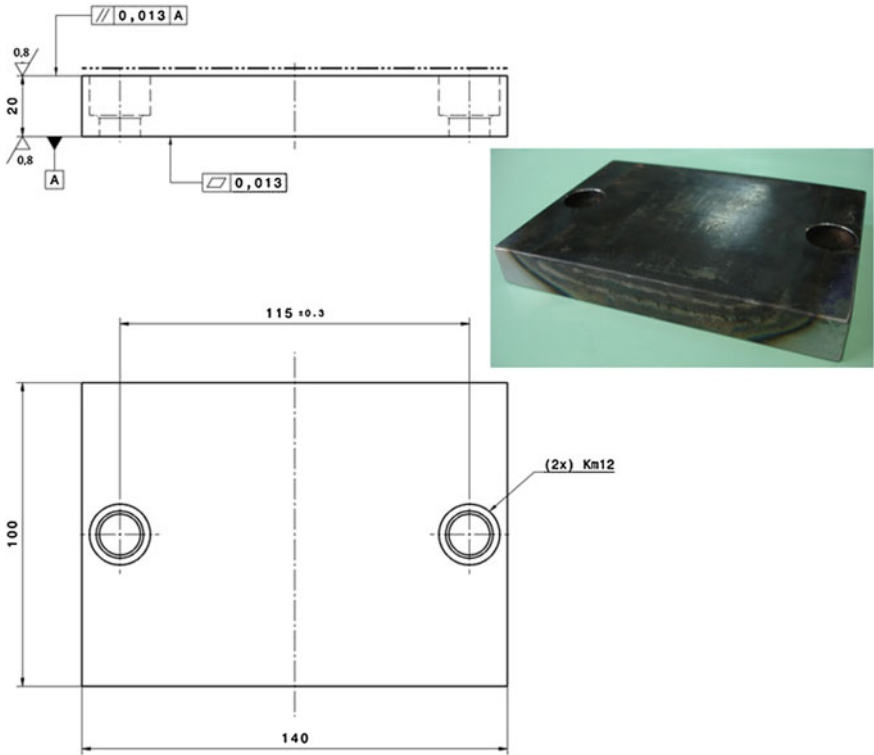


Fig. 1 Specimen’s drawing and photo of wrought AISI 4140

Table 1 gives a clear vision of the cutting parameters variation and the defined central point at the cutting speed V_c of 225 m/min, feed per tooth f_z of 0.1 mm/rev and depth penetration a_p of 0.15 mm to confirm process repeatability.

Specimens’ roughnesses were measured with a portable Mitutoyo rugosimeter model SJ-301, adjusted to a cut off length of 0.8 mm. Roughness measures were displaced in the feeding direction. For each point, the roughness adopted was an arithmetic mean of three consecutive measures. Figure 3 illustrates the equipment measuring one specimen.



Fig. 2 Specimen during end milling machining

Table 1 Defined cutting parameters by the use of an experimental composed central design (CCD)

Test	V_c (m/min)	f_z (mm/rev)	a_p (mm)
1	150	0.05	0.1
2	150	0.05	0.2
3	150	0.15	0.1
4	150	0.15	0.2
5	300	0.05	0.1
6	300	0.05	0.2
7	300	0.15	0.1
8	300	0.15	0.2
9	98.9	0.1	0.15
10	351.1	0.1	0.15
11	225	0.016	0.15
12	225	0.187	0.15
13	225	0.1	0.07
14	225	0.1	0.23
15	225	0.1	0.15
16	225	0.1	0.15
17	225	0.1	0.15
18	225	0.1	0.15
19	225	0.1	0.15
20	225	0.1	0.15

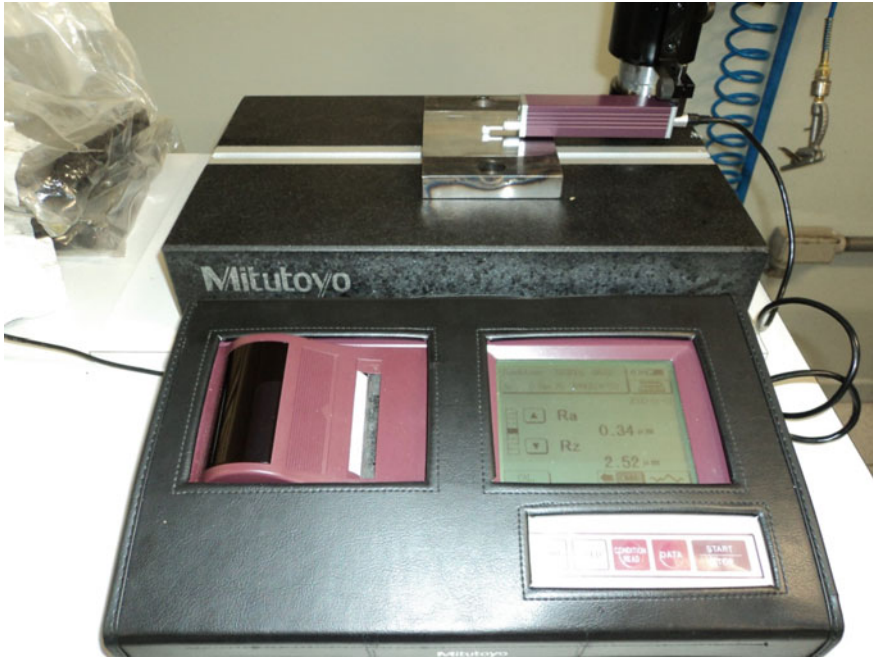


Fig. 3 Roughness tester Mitutoyo SJ-301 used to measure specimens roughness

3 Results

The roughness values obtained for the various tests revealed an appropriate roughness for finish machining processes, with an R_a ranging from 0.16 to 0.41 μm illustrated in Table 2.

The data was analyzed using the STATISTICA statistics software with a 95% confidence level. The roughness R^2 correlation factor was 0.81 and 0.64 R_{aj}^2 .

The roughness was influenced by two of the three studied cutting parameters, the feed per tooth f_z (most representative) and the depth a_p . Figure 4 shows the relevance of the feed per tooth in comparison with others cutting parameters and their interactions.

The influence of feed in the surface roughness was evident through the graphics showed in Fig. 5, indicating the behavior of the feed as a function of cutting speed ($f_z \times V_c$), and the feed as the function of depth of cut ($f_z \times a_p$).

Numerical Model 1

A non-linear regression was performed using the NLREG software, with the equation of form (Fig. 6):

Table 2 Roughness measurements with different cutting parameters

Cutting parameters—End milling (AISI 4140, Hardened)				
	Cutting speed	Feed per tooth	Depth penetration	Roughness
Exp.	V_c (m/min)	f_z (mm/rev)	a_p (mm)	R_a (μm)
1	150	0.05	0.1	0.18
2	150	0.05	0.2	0.19
3	150	0.15	0.1	0.22
4	150	0.15	0.2	0.41
5	300	0.05	0.1	0.19
6	300	0.05	0.2	0.25
7	300	0.15	0.1	0.25
8	300	0.15	0.2	0.29
9	98.9	0.1	0.15	0.3
10	351.1	0.1	0.15	0.19
11	225	0.016	0.15	0.16
12	225	0.187	0.15	0.3
13	225	0.1	0.07	0.2
14	225	0.1	0.23	0.25
15	225	0.1	0.15	0.21
16	225	0.1	0.15	0.24
17	225	0.1	0.15	0.25
18	225	0.1	0.15	0.23
19	225	0.1	0.15	0.22
20	225	0.1	0.15	0.23

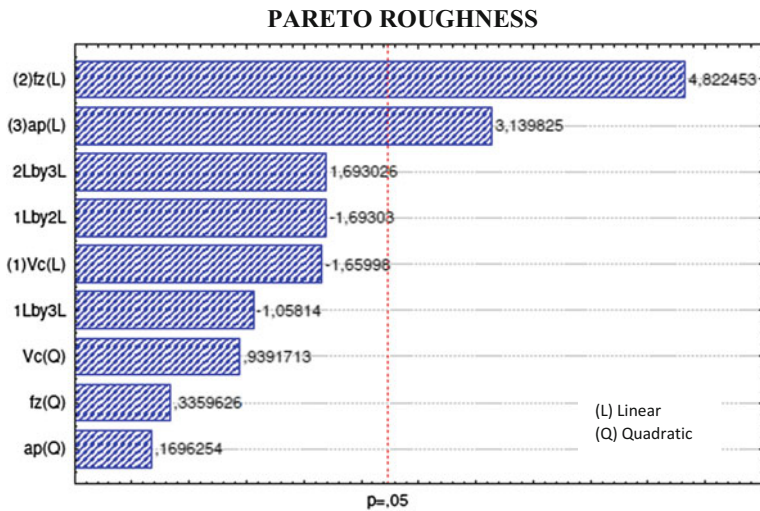


Fig. 4 Pareto diagram of cutting parameters influence on surface roughness

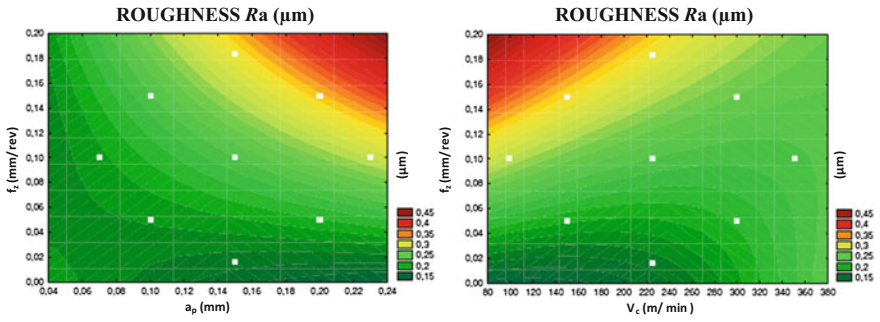


Fig. 5 Roughness graphics ($a_p \times f_z$) with $V_c = 225$ m/min and ($f_z \times V_c$) with $a_p = 0.15$ mm

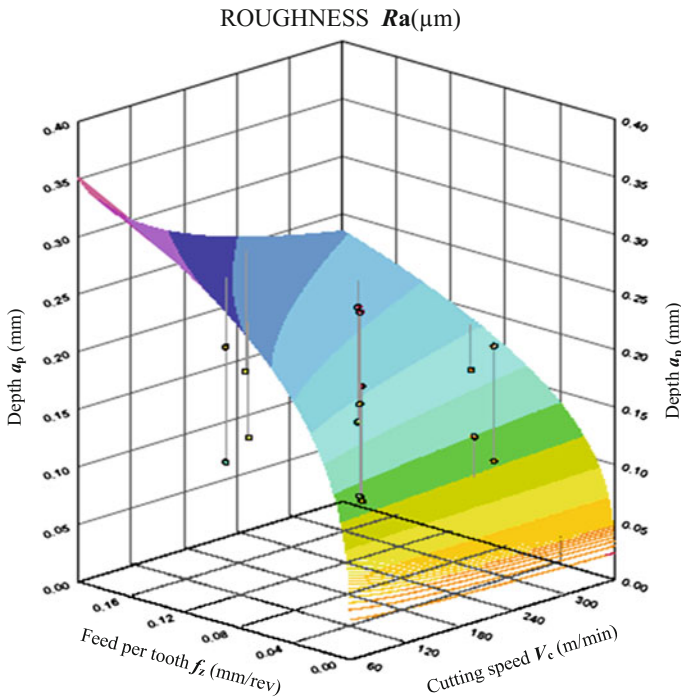


Fig. 6 Model 1, NLREG graphic, non linear regression of roughness based on cutting parameters $a_p, f_z \in V_c$

$$Ra = k \cdot v_c^a \cdot f_z^b \cdot a_p^c \tag{1}$$

As a result, the following equations were obtained:

$$Ra = 3.48 \cdot V_c^{-0.228} \cdot F_z^{0.320} \cdot A_p^{0.373} \tag{2}$$

$$R^2 = 69.44\% \left(R_{aj}^2 = 63.7\% \right) \tag{3}$$

Numerical Model 2

A linear regression was performed, using the NLREG software, with an equation of the form (Fig. 7):behavior of the feed as a function

$$Ra = a \cdot V_c + b \cdot f_z + c \cdot a_p + k \tag{4}$$

As a result, the following equation was obtained:

$$Ra = -0.002 \cdot V_c + 0.872 \cdot f_z + 0.579 \cdot a_p + 0.1089 \tag{5}$$

$$R^2 \text{ de } 66.8\% \left(R_{aj}^2 = 60.1\% \right) \tag{6}$$

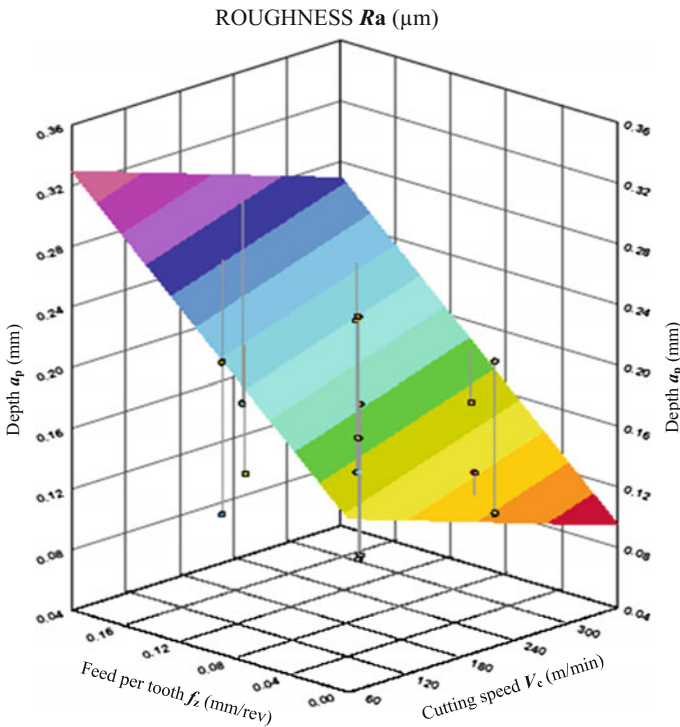


Fig. 7 Model 2, NLREG graphic, linear regression of roughness based on cutting parameters a_p , f_z e V_c

4 Conclusions

The roughness Ra values ranged from 0.16 to 0.41 μm .

The roughness interacted with the feed per tooth and the depth of penetration, so that greater feeds combined with greater depths of cut generated poorer surface finish.

Very low cutting speeds damaged the surface.

The milling machines used have demonstrated sufficient structural rigidity to not influence the roughness results within the range of the cutting parameters adopted.

It was possible to establish a numerical model relating, feed per tooth f_z , depth of cut a_p and cutting speed V_c , with the roughness through a non-linear and linear regression.

Based on the results obtained, it can be said that the finishing milling of hardened steels with CBN tool without the presence of lubricant, generates a surface finish as good as those found by the grinding process, with the advantage of being faster and less aggressive to the environment by eliminating the refrigerant.

References

1. Souza MS, Lauro CH, Brandão LC (2010) Análise de rugosidade em função da velocidade de avanço em operações de torneamento, VI *CONEM*
2. Lahiff C, Gordon S, Phelan P (2007) PCBN tool wear modes and mechanisms in finish hard turning. *Robot Comput-Integr Manuf* 23:638–644
3. Gaurav B, Choudhury SK (2012) State of the art in hard turning. *Int J Mach Tools Manuf* 53:1–14
4. Diniz A, Marcondes FC, Coppini NL (2001) *Tecnologia da usinagem dos materiais*, 3rd edn. Artliber Editora, São Paulo
5. Batalha GF, Rossi GC, Kanenobu AA (2005) Relação entre os parâmetros de corte e a rugosidade da superfície usinada numa operação de fresamento de topo. 3º Congresso Brasileiro de Engenharia de Fabricação, vol 3. Joinville, pp 1–10

A Flexible Numerical Framework for Engineering—A Response Surface Modelling Application

P. Viviani, M. Aldinucci, R. d'Ippolito, J. Lemeire and D. Vucinic

Abstract This work presents an innovative approach adopted for the development of a new numerical software framework for accelerating dense linear algebra calculations and its application within an engineering context. In particular, response surface models (RSM) are a key tool to reduce the computational effort involved in engineering design processes like design optimization. However, RSMs may prove to be too expensive to be computed when the dimensionality of the system and/or the size of the dataset to be synthesized is significantly high or when a large number of different response surfaces has to be calculated in order to improve the overall accuracy (e.g. like when using ensemble modelling techniques). On the other hand, the potential of modern hybrid hardware (e.g. multicore, GPUs) is not exploited by current engineering tools, while they can lead to a significant performance improvement. To fill this gap, a software framework is being developed that enables the hybrid and scalable acceleration of the linear algebra core for engineering applications and especially of RSMs calculations with a user-friendly syntax that allows good portability between different hardware architectures, with no need of specific expertise in parallel programming and accelerator technology. The effectiveness of this framework is shown by comparing an accelerated code to a

P. Viviani · M. Aldinucci
Dipartimento di Informatica, Università degli Studi di Torino, Turin, Italy
e-mail: aldinuc@di.unito.it

P. Viviani · R. d'Ippolito
Noesis Solutions, Leuven, Belgium
e-mail: roberto.dippolito@noessolutions.com

J. Lemeire · D. Vucinic
Department of Electronics and Informatics (ETRO), Vrije Universiteit Brussel,
Brussels, Belgium
e-mail: jan.lemeire@etro.vub.ac.be

D. Vucinic
e-mail: dean.vucinic@vub.ac.be

P. Viviani (✉)
Noesis Solutions srl c/o Ufficio 201, Corso della Vittoria 12b, 28100 Novara, Italy
e-mail: pviviani@unito.it

single-core calculation of a radial basis function RSM on some benchmark datasets. This approach is then validated within a real-life engineering application and the achievements are presented and discussed.

Keywords Response surface modelling · GPU computing · Linear algebra · Armadillo

1 Introduction

Response surface modelling (RSM) is a key tool when it comes to engineering design optimization: in most real-life use cases the engineer knows its domain of design parameters as a discrete dataset, namely as a black-box model, while most optimization strategies need a certain degree of continuity in order to be applied. Regression (i.e. approximation and interpolation) is then necessary to obtain a continuous or differentiable function that well represents the underlying model. Moreover, computing new points on an analytical regression function is significantly cheaper than obtaining new samples of the dataset, as they come from experimental data or expensive numerical simulations.

In this context, response surface modelling can address both the sparsity of the dataset and the expensiveness of producing new points, since it provides a continuous and analytical function that can be easily evaluated when performing optimization; however, there are a number of situations in which even the RSM can be too expensive computationally-wise to actually represent an advantage compared to numerical simulation. When the dataset is very large and its dimensionality is possibly high (in terms of inputs and outputs), then the time needed to obtain an accurate regression becomes not acceptable, so the response surface is not able anymore to fulfil its purpose of reducing the computational effort.

A possible solution to this issue comes from the recent development of new computational architectures, namely multicore and manycore platforms, which allow to speed up numerical calculation even on off-the-shelf workstation. Unfortunately, it is not straightforward to port existing code like sophisticated regression tools to such architectures, since specific expertise in parallel and GPU computing is needed. The aim of this work is hence to address this issue by introducing a numerical framework that can accelerate the most numerical intensive parts of well-known regression methodologies and needs no specific low-level coding expertise from the domain expert who uses it; the actual application of this framework within a response surface model is showed and validated, both from the performance point of view and from the usability point of view.

The paper is structured as following: Sect. 2 explains in detail the use case that drove the development of this work, Sect. 3 presents the main related work in terms of available and competing tools for high-performance linear algebra computations, Sect. 4 illustrates the architecture of the framework developed by the authors and Sect. 5 reports the experimental validation of such framework.

2 Industrial Use Case

The response surface modelling use case that served as benchmark for this work has been provided by Noesis Solutions NV, a simulation innovation partner to manufacturers in automotive, aerospace and other engineering-intense industries. Specialised in simulation process integration and numerical design optimization (PIDO), its flagship software Optimus leverages Noesis' experience in optimization and system integration methodologies to increase the efficiency of engineering practices and processes. Noesis research tracks include process integration, extraction and exploitation of engineering knowledge within multidisciplinary industrial processes, advanced methods for modelling and optimization of the behaviour of large engineering systems in the virtual prototype stage, parallelization of computational effort, and assessment of quality and robustness of the final product. The implementation of RSM in the context of design engineering and optimization is a well-known technique usually referred to as Metamodel Based Design Optimization [3].

One of the most significant functionalities of Optimus is indeed the calculation of response surface models related to arbitrarily complex engineering simulation workflows: this feature makes heavy use of linear algebra operations and performing such operations as fast as possible is a paramount in order to achieve the purpose of response surface modelling. The presented work is focused on a specific RSM: the *radial basis function interpolation* (RBF), but the techniques presented here are flexible enough to be applied to other models as well as completely different engineering fields, given that they require intensive linear algebra computations.

The calculation of the RBF involves the resolution of a linear system, which can be expressed as $Ax = b$ and where A is rank-deficient; this system can be solved by computing the *Moore-Penrose pseudoinverse* of A by means of a *singular value decomposition* (SVD) [5]. Accelerating the SVD represents the main requirement to the tool here presented since it is the most expensive operation of the whole interpolation process, accounting for more than the 95% of computing time. For this reason, the SVD represents the main benchmark function for the performance of this numerical library.

The main goal of this work is to provide a tool that allows engineers and domain expert to exploit the computing capabilities of modern architectures to perform numerical linear algebra; in this sense, given the use case and the industrial context where the tool is expected to be used, a number of requirements that drove the development of this work have been identified:

- State-of-the-art performance on heterogeneous CPU-GPU platforms.
- Support for advanced linear algebra operations like linear system solving and matrix decompositions.
- Easy incorporation into existing C++ code.

- Simple interface (possibly similar to MATLAB).
- Hidden parallelism and GPU specific operations (i.e. memory transfer).
- Capability to switch from CPU to GPU implementation at runtime.
- Minimal amount of code to be maintained.
- Licensing compatible with commercial use.
- Support for both Linux and Windows.

From here on we will show how the proposed library is compliant with such requirements and how it performs within the use case introduced above, both in terms of usability and performance.

3 Related Work

Given the large spectrum of applications for dense linear algebra, it is not surprising that several tools exist to perform such operations; a significant subset of such tools is also developed with performance in mind, but only recently heterogeneous architectures like CPU/GPU ones are being targeted by such tools. The *de facto*-standard for what concern linear algebra computations is the software stack composed of BLAS [4] and LAPACK [2]. The first library is focused on elementary operations like matrix-vector and matrix-matrix multiplications, while the second implements more complex functions like matrix decompositions (including the SVD), least squares and linear system solving. Both libraries are also implemented by third parties (either commercially or open-source) that preserve the API while they modify the internal mechanisms, possibly targeting different architecture like GPUs. Below we report the most notable implementations of BLAS and LAPACK:

BLAS

- Netlib BLAS, original implementation [4]
- Intel MKL
- OpenBLAS [14]
- NVidia cuBLAS, dedicated to CUDA GPUs [9]
- clBLAS, dedicated to OpenCL GPUs.

LAPACK

- Netlib LAPACK, original implementation [2]
- Magma, hybrid CPU-GPU implementation [1, 13]
- Plasma, multithreaded implementation [1]
- Intel MKL
- CULA Dense [7].

While most of these libraries provide very high-performance execution of the linear algebra operations that we are concerned about, there is a main drawback that

prevents their application in an engineering environment: their interface is so complex such that specific expertise is needed to be used directly. In this context a number of higher-level libraries have been developed in order to provide access to BLAS and LAPACK functionalities to domain experts and engineers. Such wrappers usually provide a large catalogue of functionalities that goes far beyond linear algebra (e.g. array slicing, sorting, cumulative summing), but for the scope of this work we are going to focus only to BLAS and LAPACK capabilities. A number of these tools have been evaluated for an application to the use case presented above, in particular we considered:

- Armadillo [11]
- Eigen [6]
- ArrayFire [15]
- ViennaCL [12]
- LAMA [8].

Armadillo and Eigen are not intended to be used on different platforms other than the CPU, while ArrayFire, ViennaCL and LAMA provide support for different back-end libraries to target both CPU and GPU.

With respect to our requirements, the last three tools listed above are good candidates, but there are drawbacks: LAMA and ViennaCL cannot switch from GPU to CPU at runtime, while ArrayFire, as will be shown in Sect. 5, presents significant performance issues when considering the SVD.

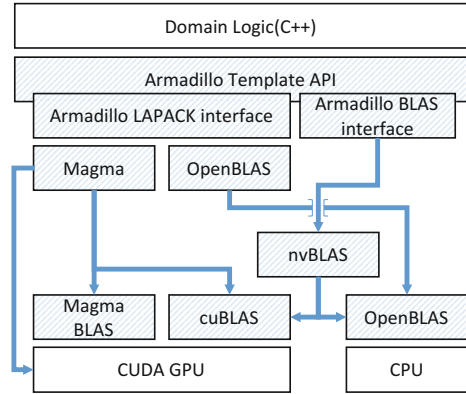
These limitations lead to a different implementation approach: given that is required to keep the amount of code to be maintained to a minimum, existing state-of-the-art tools have been reused as much as possible in order to build a software stack that actually complied with the industrial requirements. Section 4 will present the components used and will outline the architecture of such software stack.

4 Architecture and Usage

The presented software stack is structured as outlined in Fig. 1: a user friendly interface is provided to the domain expert, then the code of such interface is provided with mechanisms so it becomes possible to switch between different computing back-ends at runtime. In this way the state-of-the-art performance of existing BLAS/LAPACK implementations can be leveraged without burdening the user with a cumbersome API or with the need of taking care of the GPU specific mechanisms.

Below, the individual components are presented, along with the reasons that guided us in the choice.

Fig. 1 Proposed software stack



4.1 Armadillo

The interface exposed to the user is Armadillo, a C++ template library for linear algebra with a high-level API, which is deliberately similar to Matlab [11]. It provides a large number of functions to manipulate custom objects representing vectors, matrices and cubes (namely 3rd-order tensors); to perform the most intensive computations it provides an interface to BLAS and LAPACK implementations (hereafter we will refer to such implementation as the back-end). It employs a number of internal layers in order to translate simple function calls like

```
Solve(A,b); //Solves the linear system Ax=b
```

to more complex but equivalent LAPACK syntax

```
dgesv( &n, &nrhs, a, &lda, ipiv, b, &ldb, &info );
```

Armadillo is designed to support whatever library providing an API compliant with BLAS and LAPACK, such as MKL or OpenBLAS. It is also able to perform a few of the operations included in the back-end with its own implementation, but they are not designed for high performance. Its modularity and the simple and user-friendly interface guided our choice towards Armadillo as the API presented to the developer.

4.2 OpenBLAS

The default CPU back-end is OpenBLAS: an open-source implementation of BLAS which, given the benchmarks provided by the authors, can be compared to the best-in-class proprietary libraries like Intel MKL [14]. The standard distribution of OpenBLAS also provides LAPACK functions, some of which are further optimised by the authors. The interface is compatible with the standard distribution of

BLAS/LAPACK. The very easy build-and-deploy workflow, along with its solid performance, was the key point for the adoption of OpenBLAS as the reference CPU back-end.

4.3 *Magma*

The development of Magma is aimed to replace LAPACK on heterogeneous architectures, with the typical Multicore+GPU platform as a paradigmatic example [1, 13], in this sense we used it as the GPU back-end for the presented work. The Magma library employs Directed Acyclic Graphs (DAGs) in order to dispatch the different tasks related to a given computation to different cores/devices, taking data dependencies into account and aiming for the best exploitation of the available hardware.

The motivation that drove interest to Magma is twofold: it does not require the user to take care of data transfer between the host and the device, and, its API is only marginally different from the standard LAPACK interface. These two features make Magma a good candidate for a *drop-in* replacement of LAPACK on heterogeneous platforms.

4.4 *NVidia nvBLAS*

Direct BLAS calls from Armadillo would normally be handled by OpenBLAS, in this case the nvBLAS library [9] provided by NVidia has been leveraged in order to offload the operation to a GPU when available. nvBLAS intercepts standard BLAS calls and, when available, performs the operation on the GPU using the cuBLAS implementation from NVidia. The use of nvBLAS allowed us to leverage the GPU for what concern the BLAS operations, while keeping Armadillo code unchanged.

4.5 *Usage*

As already stated, we provided Armadillo with mechanisms to handle multiple back-ends while keeping the code to be maintained to a minimum, in this sense we also tried to modify Armadillo's interface as little as possible. Given a user code written using the Armadillo syntax, only a few more lines are needed in order to take advantage of the Magma GPU back-end, the typical usage is showed below:

```
// Check supported CUDA device, then initialises Magma
arma::arma_magma_init();
// Set the Magma back-end at runtime
```

```
arma::arma_set_backend(1);  
// User code  
// ...  
// Finalises Magma back-end for a clean exit  
arma::magma_finalize();
```

While details will be provided in the next section, this architecture satisfied all the requirements listed in Sect. 2.

5 Validation

As stated in Sect. 2, the goal of this work is to provide a tool that allows developers to easily leverage modern computing architectures to perform intensive linear algebra operations. As a part of the experimental validation, the Optimus Radial Basis Function interpolation has been re-implemented using Armadillo. Both the usability of the framework and its performance in comparison to the original implementation, where the SVD is largely based on [10], have been assessed. At last, even if the tools implemented are very well-regarded, the numerical accuracy of the framework with respect to the RBF interpolation has been assessed too.

For what concern the usability, positive feedback has been collected from industrial developers, in particular with respect to the very easy implementation of numerical algorithms and the very little effort required to port such algorithm on high-performance architectures; the productivity improvement can be roughly estimated to reduce development time by 50% with respect to writing plain C++ code from scratch.

5.1 Performance

On the performance side we carried out several tests to assess that: (1) the computation time required by the RBF significantly benefits from the new implementation; (2) the two back-ends are somehow complementary and there is a significant advantage given by the ability to switch between the two at runtime.

The first benchmark is performed on a variable-sized synthetic dataset produced by an analytical function, in order to identify the evolution of the model building time versus the size of the dataset.

The results presented in Fig. 2 highlight how the Armadillo's implementation becomes almost two orders of magnitude faster than the original one as the size of the dataset grows; let us remark that, for this range of dataset sizes, OpenBLAS outperforms Magma noticeably.

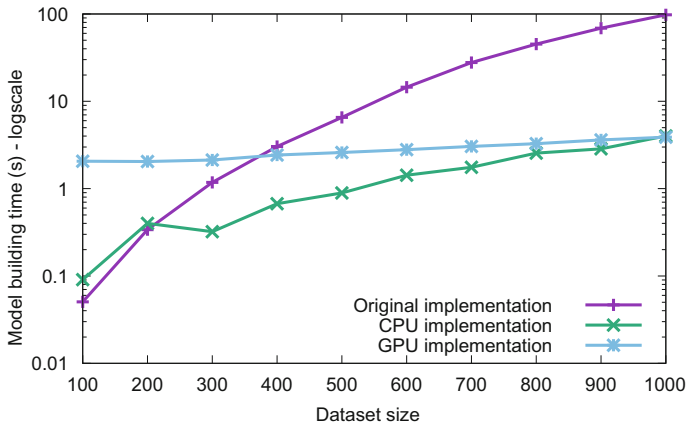


Fig. 2 Comparison of model building times for a variable-sized dataset. 2x Xeon E7-4820@2.00 GHz, NVidia Tesla K20c

This result becomes significant as we consider a real-life engineering problem: the following test has been performed on a large dataset (4149 samples) provided by a major manufacturer in the aerospace industry. Figure 3 shows, in a logarithmic scale, the model building times for the same three cases considered before.

Let us underline the advantage in terms of computing time provided by our framework: this result is consistent with the two orders of magnitude gap showed by the rightmost part of Fig. 2 and reduces the model building time from almost three hours to one and a half minute, restoring the feasibility of a response surface

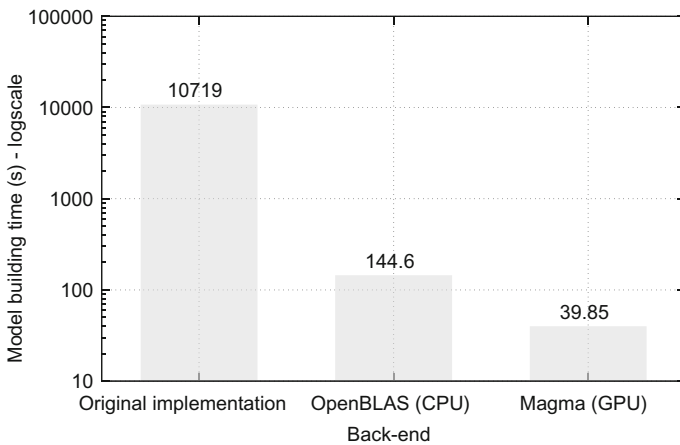


Fig. 3 Model building times for a large manufacturing dataset. 2x Xeon E7-4820@2.00 GHz, NVidia Tesla K20c

modelling approach. It is also important to note that, for such a large dataset, a visible gain by using the GPU back-end with respect to OpenBLAS has been experienced.

While above the comparison with the original implementation of the RBF has been considered, now the focus is put on comparing the two BLAS/LAPACK back-ends of this framework. The previous experiments showed a substantial advantage in favour of OpenBLAS for datasets of size up to a thousand of samples, while the real-life dataset showed how the GPU takes the edge for very large problems. In this sense it would be useful to understand the behaviour of the back-ends in the region between these two cases: Fig. 4 shows the break-even dataset size for which the GPU becomes actually faster.

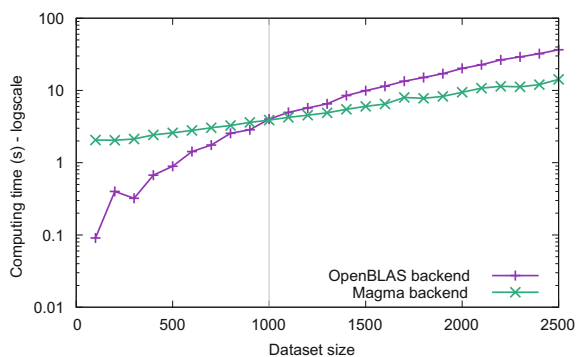
In fact, the expectation is that the fastest back-end depends on both, the problem size and the hardware configuration. To prove such assumption, experiments on different machines have been performed considering only the most expensive part of the RBF interpolation: solving the rank-deficient linear system $Ax = b$.

Figure 5 shows three different hardware configurations and the statement that there is not a back-end that is in principle faster than another holds true: different back-ends behave better based on the hardware configuration and the problem size and, above all, the break-even point for Magma to take the edge gets larger as the GPU gets more low-end, to the extreme case in which there is no break-even at all. In this sense the possibility to switch among the back-ends at runtime opens up the possibility to implement a policy that always chooses the fastest based on the problem and the platform.

As a final performance benchmark it is interesting to show how this framework significantly outperforms the only competing tool that possibly meets the requirements, when considering the calculation of the SVD on GPU. It has been stated in Sect. 3 that ArrayFire revealed a significant performance issue, so it was discarded despite being a good candidate. Figure 6 shows the comparison of computing times for ArrayFire and Armadillo+Magma. Let us note that ArrayFire leverages the cuSolver LAPACK replacement provided by NVidia in order to perform the SVD.

It is noticeable how Magma significantly outperforms cuSolver as the dimension of the dataset increases.

Fig. 4 Model building times for different dataset sizes. 2x Xeon E7-4820@2.00 GHz, NVidia Tesla K20c



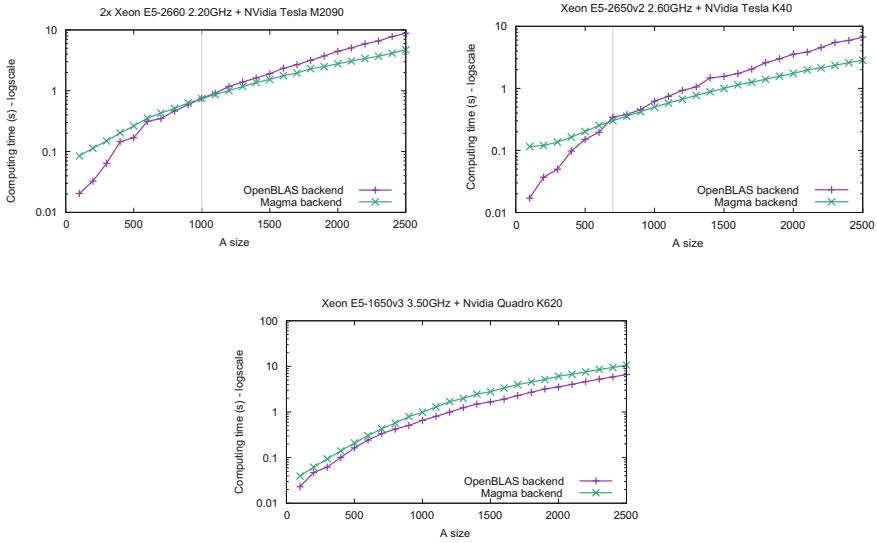
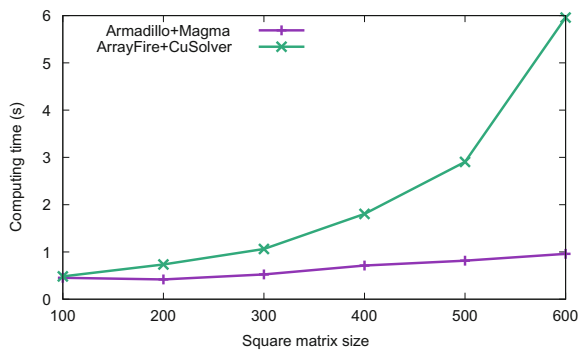


Fig. 5 Linear system $Ax = b$ solved on different machines with different hardware configuration

Fig. 6 Computing time for the SVD of a square matrix



5.2 Accuracy

In order to verify the numerical accuracy of the presented software stack, the interpolation results obtained on a test dataset by the original implementation and by both the back-ends leveraged by Armadillo have been compared. To produce a measure of accuracy we measured the errors on a different and dense validation dataset and we expected those errors to be at most equal in all the cases. Figure 7 shows how the Armadillo implementation produces a slightly more accurate implementation compared to the original one: this implies that the faster calculation does not affect final accuracy, which is possibly better than expected. Tuning of the

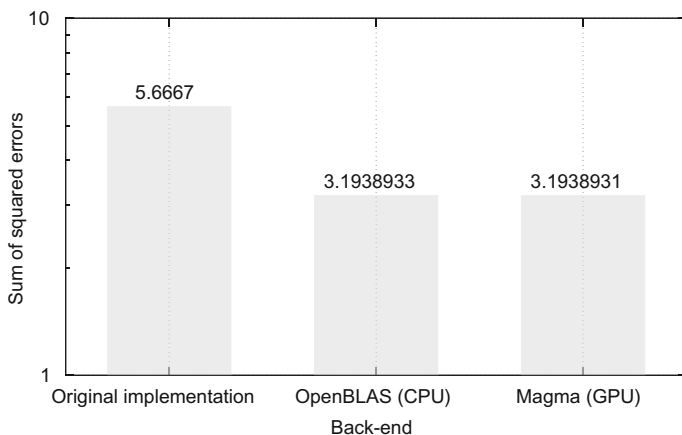


Fig. 7 Sum of squared errors calculated on a 1000 points validation dataset. RBF interpolation built on a 500 points synthetic dataset

tolerance parameter for the SVD is possible with Armadillo, but we did not consider such intervention as relevant, since under both the performance and accuracy point of view the framework proved itself to be fully satisfactory for the scope of this work.

6 Conclusion

Starting from the specific use case of response surface modelling, in this work we introduced a software stack designed to allow domain experts and engineers to exploit high-performance architectures in a transparent way while developing linear algebra intensive applications. To achieve such result, we carefully extended the Armadillo library, which provides a Matlab-like interface for linear algebra objects and operations, in order to both integrate it with different high-performance computing back-ends and to allow the user to transparently switch between such back-ends at runtime.

The resulting framework has been validated within the industrial context of the use-case provider, considering either the computing performance as well as the usability: the latter allowed for a code development time decrease of roughly 50%, while the former has largely outperformed the original implementation, as well a competing tool. In this sense we can state that the requirements listed during the analysis of the use-case are completely met by this framework, while providing fully satisfactory performance in both synthetic test cases as well as actual aerospace manufacturing problems.

6.1 Future Development

Since the main purpose of this work is to provide a general tool for developers, we expect that in the near future more Response Surface Models other than the RBF interpolation will benefit from the acceleration provided by this approach. Moreover, we also expect that new models will be implemented using Armadillo, significantly accelerating the coding process.

For what concern the architecture of the framework, we propose an improvement based on the results showed by Figs. 4 and 5: we observed that the performance is significantly dependent on the hardware configuration and the problem size, in this sense the idea is to implement a set on policies that, based on early performance evaluation, automatically selects the fastest back-end on which the given dataset should be processed.

At last, a possible development concerns the identification of a suitable BLAS/LAPACK back-end for OpenCL in order to target a wider range of accelerators like AMD and Intel GPUs.

Acknowledgements This work has been partially supported by ITEA2 project 12002 MACH, the EU FP7 REPARA project (no. 609666), the EU H2020 Rephrase project (no. 644235) and the “Nvidia GPU research centre” programme.

References

1. Agullo E, Demmel J, Dongarra J et al (2009) Numerical linear algebra on emerging architectures: the PLASMA and MAGMA projects. *J Phys: Conf Ser* 180:12037
2. Anderson E, Bai Z, Bischof C et al (1999) LAPACK users' guide, 3rd edn. Society for Industrial and Applied Mathematics, Philadelphia
3. Booker AJ, Dennis JE, Frank PD et al (1999) A rigorous framework for optimization of expensive functions by surrogates. *Struct Multidiscip Optim* 17:1–13
4. Dongarra J, Du Croz J, Hammarling S, Hanson RJ (1988) An extended set of FORTRAN basic linear algebra subprograms. *ACM Trans Math Softw* 14:1–17
5. Golub GH, Van Loan CF (1996) Matrix computations, 3rd edn. Johns Hopkins University Press, Baltimore
6. Guennebaud G, Jacob B (2010) Eigen v3
7. Humphrey JR, Price DK, Spagnoli KE et al (2010) CULA: hybrid GPU accelerated linear algebra routines. In: *Modeling and Simulation for Defense Systems and Applications V. {SPIE}-Intl Soc Optical Eng*
8. Kraus J, Förster M, Brandes T, Soddemann T (2012) Using LAMA for efficient AMG on hybrid clusters. *Comput Sci Res Dev* 28:211–220
9. NVIDIA Corporation (2016) CUDA Toolkit Documentation. <http://docs.nvidia.com/cuda/eula/index.html>. Accessed 25 Nov 2016
10. Press WH, Teukolsky SA, Vetterling WT, Flannery BP (2002) Numerical recipes in C
11. Sanderson C (2010) Armadillo: an open source C++ linear algebra library for fast prototyping and computationally intensive experiments. In: NICTA. Australia
12. Tillet P, Rupp K, Selberherr S, Lin C-T (2013) Towards performance-portable, scalable, and convenient linear algebra. In: 5th USENIX Workshop on Hot Topics in Parallelism. USENIX, Berkeley

13. Tomov S, Dongarra J, Baboulin M (2010) Towards dense linear algebra for hybrid GPU accelerated manycore systems. *Parallel Comput* 36:232–240
14. Wang Q, Zhang X, Zhang Y, Yi Q (2013) AUGEM: automatically generate high performance dense linear algebra kernels on x86 CPUs. In: *Proceedings of the International Conference on High Performance Computing, Networking, Storage and Analysis*. ACM, New York, pp 25:1–25:12
15. Yalamanchili P, Arshad U, Mohammed Z et al (2015) ArrayFire—a high performance software library for parallel computing with an easy-to-use API. AccelerEyes, Atlanta

Monitoring of the Thermal Properties of Cement Composites with an Addition of Steel Slag

Vojtěch Václavík, Milena Kušnerová, Tomáš Dvorský,
Vojtěch Šimíček, Jan Valíček, Lukáš Gola and Marta Harničárová

Abstract This article presents the results of an experimental research dealing with the preparation of cement composites with an addition of steel slag, in order to verify the possibility of using ground steel slag as a suitable admixture into cement composites. The samples of the cement composites were prepared with the following types of cements: Portland cement CEM I 42.5 R, Portland mixed cement CEM II/B-S 32.5 R, blast furnace cement CEM III/A 32.5 N, and mixed cement CEM V/A (S-V) 32.5 R. We have tested the effect of ground steel slag as an

V. Václavík (✉) · T. Dvorský · V. Šimíček
Faculty of Mining and Geology, Institute of Environmental Engineering,
VŠB-Technical University of Ostrava, 17. Listopadu 15/2172,
708 33 Ostrava-Poruba, Czech Republic
e-mail: vojtech.vaclavik@vsb.cz

T. Dvorský
e-mail: tomas.dvorsky@vsb.cz

V. Šimíček
e-mail: vojtech.simicek@vsb.cz

V. Václavík · V. Šimíček
Faculty of Mining and Geology, Institute of Clean Technologies for Mining
and Utilization of Raw Materials for Energy Use, VŠB-Technical University of Ostrava,
17. Listopadu 15/2172, 708 33 Ostrava-Poruba, Czech Republic

M. Kušnerová · J. Valíček · L. Gola · M. Harničárová
Faculty of Mining and Geology, Institute of Physics, VŠB-Technical University of Ostrava,
17. Listopadu 15/2172, 708 33 Ostrava-Poruba, Czech Republic
e-mail: milena.kusnerova@vsb.cz

J. Valíček
e-mail: jan.valicek@vsb.cz

L. Gola
e-mail: lukas.gola@vsb.cz

M. Harničárová
e-mail: marta.harnicarova@vsb.cz

admixture, which had been dosed in the amount of 20% of the weight of the cement dose, on the strength parameters (tensile flexural strength and compressive strength) and the thermal properties (coefficient of thermal conductivity λ , specific heat capacity c , and coefficient of thermal diffusivity a). The results of this experimental research have shown that the use of ground steel slag as an admixture in an amount of 20% of the weight of cement in the cement composite will reduce the values of the coefficient of thermal conductivity λ in cements CEM I 42.5 R, CEM II/B-S 32.5 R, and CEM V/A (S-V) 32.5 R and, at the same time, it will not cause a decrease in compressive strength.

Keywords Cement · Admixture · Ground steel slag · Compressive strength · Tensile flexural strength · Thermal properties · Coefficient of thermal conductivity

1 Introduction

At present, heavy industry produces enormous amounts of wastes, thus causing environmental burden. One of the main representatives of this burden is the metallurgical industry, which belongs to the largest producers of wastes, whether it is in the form of emissions or production wastes. Metallurgical wastes are more and more frequently in the scope of interest of research teams constantly trying to come up with new possibilities of their use. These teams very often focus their attention on other industrial sectors consuming huge amounts of natural resources used in building production. A number of researches deal with the incorporation of metallurgical wastes into building mixtures. These researches are focused, for example, on the use of fly ash as a partial substitution of cement in the production of concretes, mortars and copolymers [1–4] or on the use of finely ground blast furnace slag together with fly ash and powder from electronic equipment as a substitution of cement in mortars in order to improve their properties [5, 6]. Other research projects deal with finely ground blast furnace slag as an effective substitute of cement, depending on its properties [7, 8], or a partial substitution of Portland cement with blast furnace slag, and concrete whose filler (natural aggregate) is partially replaced by steel slag [9, 10]. Researches focused on the thermal and technical properties of materials are becoming prominent, in order to reduce emissions and to protect the climate. There are results of researches dealing with the impact of the ratio of cement and ground iron ore used as filler on the final thermal conductivity of mortar [11], respectively dealing with the study of the thermal conductivity and strength of cement sealants containing fly ash, slag, and silica powder [12]. The experimental researches in this area are focused on the factors influencing the thermal conductivity of concrete, mortar, or cement pastes, such as the water-cement ratio, the types of admixtures, the density of fractions, the temperature and humidity [13]. We can also find results of numerical simulations of

redevelopment material moisture based on cement composites [14] and the progress of the incorporation of moisture into a building with damaged waterproofing after the application of board insulation versus diffusion-open material based on calcium silicate [15, 16].

2 Materials and Methods

2.1 Composition of Cement Composite and Its Preparation

Cement. Four types of cement used for the production of cement composites have been tested to verify the possibility of the utilization of ground steel slag in the amount of 20% of the cement dose weight as an admixture: Portland cement CEM I 42.5 R and CEM V/A (S-V) 32.5 R from Cement Hranice, a.s. Company, as well as Portland mixed cement CEM II/B-S 32.5 R and blast furnace cement CEM III/A 32.5 N from Považské cementárny, a.s. All the tested cements meet the requirements of EN 197-1 [17].

Steel slag. It is an artificial aggregate which is produced during the metallurgical process, where active slag is used to separate adulterants. The basic components of steel slag are represented by the solutions of orthosilicates with the oxides of iron, manganese, aluminium and magnesium, which are chemically bound to calcium oxide. The chemical composition of the arising slag varies considerably, depending on the nature and the course of the technological process. The experimental research took advantage of converter slag fr. 0/8 from Třinecké železářny, a.s., which was ground to the specific surface area of 2356 cm²/g according to Blaine. The grinding procedure consisted of the following steps:

1. 3 passages through a twin-cylinder mill (cylinder diameter of 300 mm), 1200/1070 rpm; 1st passage 3 mm slit (maximum refinement coefficient of 5); 2nd passage 1 mm slit (refinement coefficient of 3); 3rd passage 0.3 mm slit (minimum refinement coefficient of 3).
2. The material refined below 0.3 mm was subjected to grinding using a high speed twin-engine (1.5 + 1.5 kW) counter pin mill DESI11 with three rows of working bodies on the rotors with the diameter of 170 mm and the maximum velocity at the outer row of bodies of 210 m/s.

The chemical composition of steel slag is shown Table 1.

Table 1 Chemical composition of steel slag

Parameter	Na ₂ O	MgO	Al ₂ O ₃	SiO ₂	P ₂ O ₅	SO ₃	K ₂ O	CaO	TiO ₂	MnO	Fe ₂ O ₃
Weight %	0.42	11.4	2.40	15.3	0.95	0.40	<0.05	32.2	0.28	4.76	32.5
Parameter	V	Cr	Zn	Sr							
mg/kg	560	5450	–	–							

Table 2 Grain size composition of standardized sand

Sieve with square mesh (mm)	2.00	1.60	1.00	0.50	0.16	0.08
Total remains on the sieve (%)	0	7 ± 5	33 ± 5	67 ± 5	87 ± 5	99 ± 1

Sand. Sand standardized according to EN 196-1 was used for the production of the cement composites [17]. The grain size composition of the standardized sand is shown in Table 2. The total dose of sand for one mixture was 1350 g.

Water. Water from water mains was used for the preparation of the mortar and the subsequent production of the cement composites.

Mortar composition. Each mixture for the 3 test specimens (beams with the dimensions of 40 × 40 × 160 mm) contained 450 g of cement, 1350 g of sand and 225 g of water (comparative mixture). This comparative mixture also contained added ground steel slag in the amount of 20% of the cement dose weight, i.e. 90 g. This mortar composition was used for the testing of the above presented types of cements.

Mortar mixing. The mortar was mixed in a laboratory cement paste mixer BS-MI-CM5A from Beton Systém, s.r.o. The mixing procedure was as follows:

1. Water was poured into the mixing container and cement was dosed.
2. Mixing was automatically triggered immediately upon the contact of water and cement at low speed (rotation around the whisk axis of $140 \pm 5 \text{ min}^{-1}$) and the mixing time was automatically measured at the same time. Sand was automatically and continuously added at equidistant time intervals of 30 s. After that, the mixing switched to high speed (rotations around the whisk axis of $285 \pm 10 \text{ min}^{-1}$) and the mixing continued for additional 30 s.
3. The mixing was stopped automatically after 90 s. The mortar sticking to the walls and bottom of the container was scraped during the first 30 s with a rubber blade.
4. The mixing continued for additional 60 s at high speed (rotations around the whisk axis of $285 \pm 10 \text{ min}^{-1}$).

Making of the test specimens. The test specimens in the shape of beams (composite cement), with the dimensions of 40 × 40 × 160 mm, were made immediately after the preparation of the mortar. The beam mould was always filled in two layers, while either of the layers was compacted with 60 surges on a compaction table ZSC 40. The excess mortar from the second layer was scraped off after the compaction using a metal ruler and the surface of the test specimens was horizontally smoothed out. The surface of each mould was covered with a glass plate and the mould was stored in a humid environment. After 24 h, the test specimens (beams) were demoulded and stored in water environment. The production process of the test specimens was in compliance with the procedure defined in the standard [17]. The test specimens produced in order to determine the thermal properties of the cement composite had the dimensions of 140 × 40 × 160 mm.

2.2 Methods

2.2.1 Determination of the Strength Characteristics

The strength properties of the cement composites (beams) were determined at the age of 28 days of the test specimens. The test specimens were tested for tensile flexural strength and compressive strength at the end of the beams according to a standardized procedure [17].

2.2.2 Determination of Thermal Properties

Effective thermal conductivity is significantly dependent not only on the chemical composition and structure of the material, but also on the effects of the external environment on the material, i.e. on moisture and temperature.

All the tested samples of the cement composites without and with the addition of ground steel slag were comparable in terms of the impact of humidity because they were measured in a dry state (steady-state weight). That is why their dependence on moisture was monitored.

The modelling of the thermal dependencies of the coefficients of thermal conductivity took advantage of conventional thermodynamic analytical relations (1, 2).

The coefficient of thermal conductivity λ in thermodynamics is generally defined by the Fourier's law

$$q = -\lambda \cdot \text{grad } t, \quad (1)$$

according to which the vector of the heat flow density q is directly proportional to the temperature gradient t and has the opposite direction.

In conventional thermodynamics, there is also a general physical rule that the higher material temperature increases the value of the coefficient of thermal conductivity approximately linearly in the narrow temperature interval, and quadratically in the wider temperature interval. The empirically verified dependence of the coefficient of thermal conductivity on temperature can be expressed analytically. The theoretical and practical thermodynamics uses the relation (2), especially for elementary temperature differences, such as the linear increase of material coefficient with temperature

$$\lambda = \lambda_0 \cdot [1 + \alpha_t \cdot (t - t_0)], \quad (2)$$

where λ is the value of the coefficient of thermal conductivity of the examined material at the temperature t , λ_0 is the value of the coefficient of thermal conductivity of the examined material at the temperature of t_0 , α_t is the linearized coefficient of the increase of the value of the coefficient of thermal conductivity with material temperature (using empirical and approximate evaluation for specific material).

The tested samples of the cement composites were well comparable in terms of their geometrical dimensions, they were also heated under the same operating conditions and measured using the same instruments, and the measurement results were evaluated by the same methodology.

ISOMET 2114 commercial device was used to measure the material parameters of the samples of the cement composites at a specific surface temperature. The measurements taking advantage of this device are based on an analysis of the course of the time dependence of the thermal response to pulses of heat flux into the analyzed material. The heat flux is created by scattered electric power in a probe resistor, which is thermally and conductively connected to the analyzed material. The temperature is sampled, and it is directly evaluated as a function of time by means of polynomial regression. The coefficients obtained by this regression are subsequently used to calculate the measured quantities.

The temperatures of opposite walls of the studied samples were measured using a prototype calorimetric computer-controlled chamber [18]. Excel spreadsheet processor was used to perform a graphical evaluation of the time development of the temperatures of the opposite walls of the examined samples, the evaluation of the temperature differences between the walls of the samples, the mean material core temperatures of the samples, and the coefficients of thermal conductivity of the samples, as well as graphical evaluations of the temperature development of the coefficients of thermal conductivity.

3 Measurement Results and Discussion

Figures 1 and 2 present the results of the strength characteristics of the cement composites.

The results of the strength parameter test clearly show that ground steel slag, which was used as an admixture in the production of cement composites and was dosed in the amount of 20% of the cement weight, does not significantly decrease the tensile flexural strength of the cement composites with various types of cements. When we compare the comparative samples and the samples with additions of ground steel slag, it is clearly visible that the change of the tensile flexural strength varies within the range of 0.06–0.51 MPa.

Figure 2 clearly shows that ground steel slag in the amount of 20% of the cement weight caused an increase in compressive strength of cement composites in cases where CEM II/B-S 32.5 R, CEM III/A 32.5 N and CEM V/A (S-V) 32.5 R cements were used. The highest increase (by about 5 MPa, app. 11%) was recorded in cement composites based on CEM II/B-S 32.5 R and CEM V/A (S-V) 32.5 R. On the other hand, the ground steel slag had no effects on the increase of the compressive strength of cement composites with CEM I 42.5 R.

Table 3 shows the results of the measurements of the thermal properties of the cement composites using commercial device ISOMET 2114.

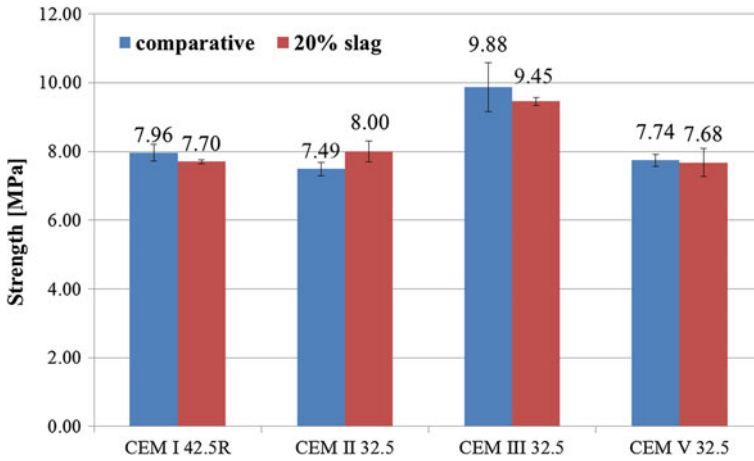


Fig. 1 Tensile flexural strength of cement composites after 28 days

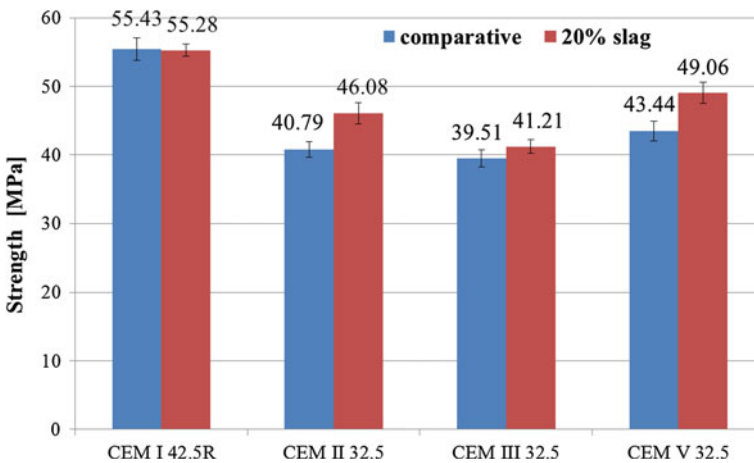


Fig. 2 Compressive strength of cement composites after 28 days

Table 3 shows that ground steel slag tested as an admixture in an amount of 20% of the cement weight is actively involved in the improvement of the thermal properties, especially in composites prepared from CEM I 42.5 R, CEM II/B-S 32.5 R and CEM V/A (S-V) 32.5 R.

Figures 3–6 present the results of the measurements of the thermal properties in a prototype calorimetric computer-controlled chamber within the temperature range of -5 – 50 °C. The measured results were used to model the dependencies of the coefficients of thermal conductivity λ on mean core temperature t_s of the examined samples.

Table 3 Thermal properties of cement composites measured using ISOMET 2114 device

Cement composite		Coefficient of thermal conductivity λ Ø (W/m K)	Volume-specific heat capacity $c \times 10^6$ Ø (J/m ³ K)	Coefficient of thermal diffusivity $a \times 10^{-6}$ Ø (m ² /s)
CEM I 42.5 R	Comparative	2.5218	1.8335	1.3754
	20% slag	2.4179	1.7815	1.3572
CEM II/B-S 32.5 R	Comparative	2.4941	1.8273	1.3650
	20% slag	2.3308	1.7367	1.3431
CEM III/A 32.5 N	Comparative	2.5046	1.8509	1.3532
	20% slag	2.5265	1.9056	1.3258
CEM V/A (S-V) 32.5 R	Comparative	2.6813	1.9231	1.3942
	20% slag	2.4602	1.8086	1.3603

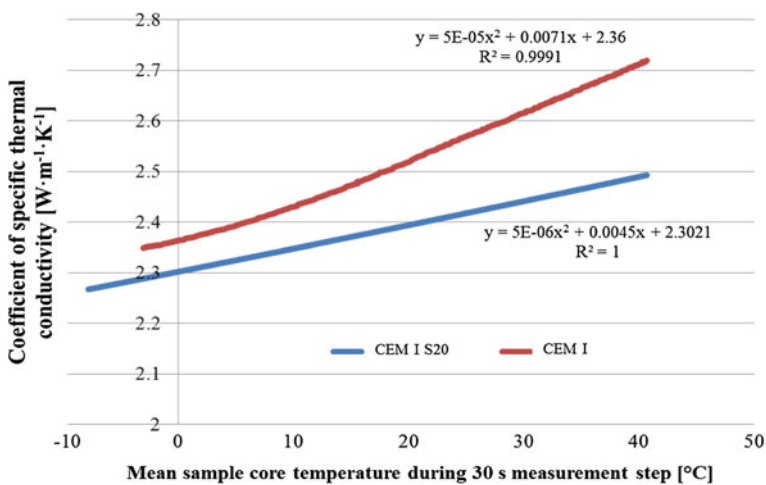


Fig. 3 Dependence of the coefficient of thermal conductivity λ on temperature for cement composite with CEM I 42.5 R

Direct measurements of the temperatures of opposite walls of the samples (250 sub-measurements of heating at temporally equidistant steps of 30 s) were performed during the experimental phase.

The evaluation phases involved indirect measurements, i.e. the measurement results were converted into an Excel spreadsheet processor. The evaluated factors included especially the mean material core temperatures t_s of the specimens during each sub-measurement in temporally equidistant steps of 30 s. The other modelled areas included the partial dependencies of $\lambda = \lambda(t_s)$ according to physical relations (1, 2) using an approximation and regression method (linear line, quadratic curve,

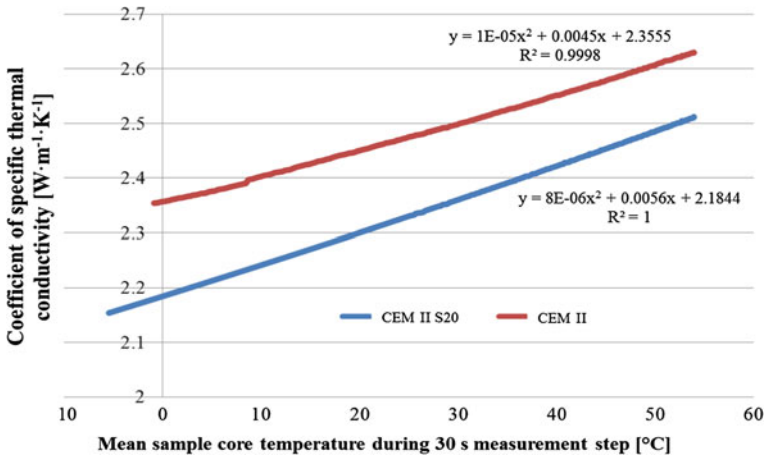


Fig. 4 Dependence of the coefficient of thermal conductivity λ on temperature for cement composite with CEM II/B-S 32.5 R

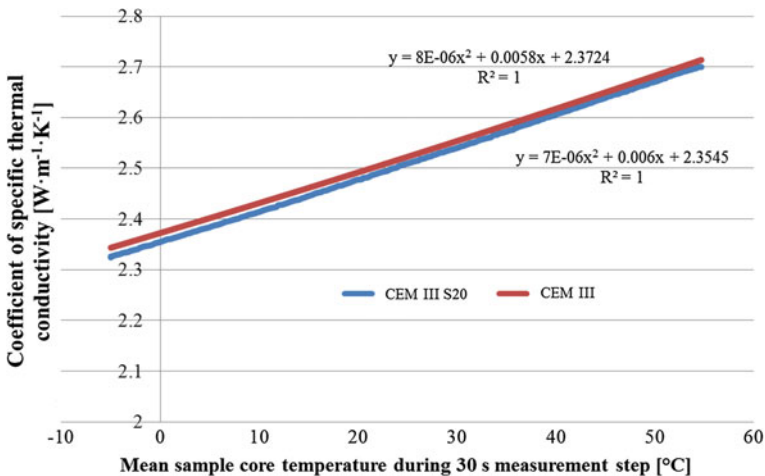


Fig. 5 Dependence of the coefficient of thermal conductivity λ on temperature for cement composite with CEM III/A 32.5 N

the courses were controlled by means of closeness of conformity). Finally, comparative charts of the dependencies of $\lambda = \lambda(t_s)$ of matching pairs of dependencies of the coefficients of thermal conductivity on mean sample material temperature with slag and the dependencies of the coefficients of thermal conductivity on the same mean material temperature without slag were performed for the purpose of the interpretation of the measurement results (see Figs. 3, 4, 5 and 6).

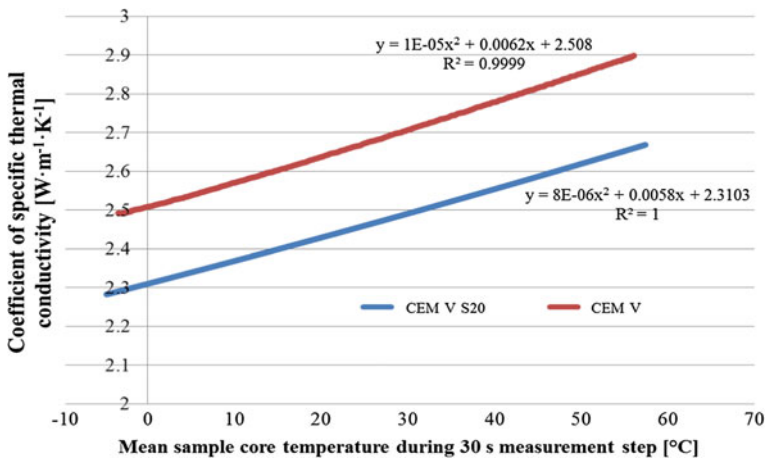


Fig. 6 Dependence of the coefficient of thermal conductivity λ on temperature for cement composite with CEM V/A (S-V) 32.5 R

It can be stated that in 2 presented cases of Portland cement CEM I 42.5 R and Portland mixed cement CEM II/B-S 32.5 R (Figs. 3 and 4), the dependencies of the coefficients of thermal conductivity on mean material core temperatures do not show entirely comparative development trends (in Fig. 3—the courses are slightly diverging, on the other hand, in Fig. 4—the courses are slightly converging). The admixture of slag is incorporated into the designed mixtures in such a way that the composites are not comparably “homogeneous” in their structure in comparison with the composites without the admixture of slag.

In 2 presented cases of blast furnace cement CEM III/A 32.5 N and mixed cement CEM V/A (S-V) 32.5 R (Figs. 5 and 6), it can be stated that the dependencies of the coefficients of thermal conductivity on the mean material core temperatures show well comparable development trends. The admixture of slag into the newly designed mixtures is incorporated in such a way that the composites are comparably “homogeneous” in their structure in comparison with the composites without the admixture of slag.

4 Conclusions

The results of the experimental research have confirmed that it is possible to use ground steel slag with a specific surface of 2350 cm²/g according to Blaine as an admixture in an amount of 20% of the cement weight, without any significant decrease in the tensile flexural strength after 28 days in case of cement composites produced from CEM I 42.5 R, CEM II/B-S 32.5 R, CEM III/A 32.5 N and CEM V/A (S-V) 32.5 R.

Ground steel slag in an amount of 20% of the cement weight in all cases of the presented measurements:

- increases the compressive strength of the cement composites after 28 days (when using cement CEM I 42.5 R, CEM II/B-S 32.5 R and CEM V/A (S-V) 32.5 R);
- slightly decreases the value of the coefficient of thermal conductivity, i.e. the insulation thermal properties of the cement composites improve (when using cement CEM I 42.5 R, CEM II/B-S 32.5 R and CEM V/A (S-V) 32.5 R).

As far as the informative value of the measurement results is concerned, the designed and examined materials of the cement samples with an addition of ground steel slag have exactly declared properties under exactly specified laboratory conditions.

Acknowledgements Project Institute of Clean Technologies for Mining and Utilization of Raw Materials for Energy Use. Reg. No. LO1406. SP2016/35—The Use of Steel Slag as an Admixture for the Preparation of Cement Composites.

References

1. Ondova M, Stevulova N (2011) Benefits of coal fly ash utilization in the area of a pavement building. *Environ Eng* 3:1156–1159
2. Junak J, Stevulova N (2011) Potential of selected industrial wastes in civil engineering applications. *SGEM* 2011. doi:[10.5593/sgem2011/s20.155](https://doi.org/10.5593/sgem2011/s20.155)
3. Svarla J, Sisol M, Botula J et al (2011) The potential use of fly ash with a high content of unburned carbon in geopolymers. *Acta Geodyn Geomater* 7:123–132
4. Yang KH, Song JK, Ashour AF et al (2008) Properties of cementless mortars activated by sodium silicate. *Constr Build Mater*. doi:[10.1016/j.conbuildmat.2007.07.003](https://doi.org/10.1016/j.conbuildmat.2007.07.003)
5. Xiang XD, Xi JC, Li CH et al (2016) Preparation and application of the cement-free steel slag cementitious material. *Constr Build Mater*. doi:[10.1016/j.conbuildmat.2016.03.186](https://doi.org/10.1016/j.conbuildmat.2016.03.186)
6. Tomkova V, Ovcacik P, Vlcek J et al (2012) Potential modification of hydration of alkali activated mixtures from granulated blast furnace slag and fly ash. *Ceram Silic* 56:168–176
7. Pal SC, Mukherjee A, Pathak SR (2003) Investigation of hydraulic activity of ground granulated blast furnace slag in concrete. *Cem Concr Res*. doi:[10.1016/S0008-8846\(03\)00062-0](https://doi.org/10.1016/S0008-8846(03)00062-0)
8. Vlček J, Drongová L, Topinková M et al (2014) Identification of phase composition of binders from alkali-activated mixtures of granulated blast furnace slag and fly ash. *Ceram Silic* 56:79–88
9. Václavík V, Dirner V, Dvorský T et al (2012) The use of blast furnace slag. *Metallurgy* 51:461–464
10. Stevulova N, Vaclavik V, Junak J et al (2008) Utilization possibilities of selected waste kinds in building materials preparing. *SGEM* 2008 2:193–200
11. Liu K, Wang Z, Jin C et al (2015) An experimental study on thermal conductivity of iron ore sand cement mortar. *Constr Build Mater*. doi:[10.1016/j.conbuildmat.2015.10.108](https://doi.org/10.1016/j.conbuildmat.2015.10.108)
12. Demirboğa R (2003) Influence of mineral admixtures on thermal conductivity and compressive strength of mortar. *Energy Build*. doi:[10.1016/S0378-7788\(02\)00052-X](https://doi.org/10.1016/S0378-7788(02)00052-X)
13. Kim KH, Jeon SE, Kim JK et al (2003) An experimental study on thermal conductivity of concrete. *Cem Concr Res*. doi:[10.1016/S0008-8846\(02\)00965-1](https://doi.org/10.1016/S0008-8846(02)00965-1)

14. Břenek A, Václavík V, Dvorský T et al (2016) Numerical moisture simulation of redeveloped structures using active materials based on cement composite. *Mater Sci Eng Technol*. doi:[10.1002/mawe.201600525](https://doi.org/10.1002/mawe.201600525)
15. Břenek A, Václavík V, Dvorský T et al (2014) Built-in moisture process in structure with damaged waterproofing after the application of thermal insulation boards. *Adv Mater Res*. doi:[10.4028/www.scientific.net/AMR.1020.591](https://doi.org/10.4028/www.scientific.net/AMR.1020.591)
16. EN 197-1 Cement—Part 1: Composition, specifications and conformity criteria for common cements
17. EN 196-1 Methods of testing cement—Part 1: Determination of strength
18. Kusnerova M, Valicek J, Harnicarova M (2014) Measurement of physical properties of polyurethane plaster. *Gradevinar* 66:899–907

Plywood Experimental Investigation and Modeling Approach for Static and Dynamic Structural Applications

Samara Jadi Cruz de Oliveira, Ophelia Bolmin, Michel Arrigoni and Christian Jochum

Abstract Although the mechanical behavior of various types of laminated wood has been already explored in the literature [1, 2], there is still a lack about static and dynamic testing and modeling approaches of the plywood. This study aims to describe a plywood composed of 10 layers of beech glued together with a melamine-urea-formaldehyde resin. Tests were performed on samples from two wood boards with different stacking sequences. The experimental data presented are provided from tensile tests performed in both fiber and transverse directions, out of plane compression tests, as well as dynamic tests in particular the Taylor gun test and the Hopkinson bar. This paper proposes three models based on composite theories to simulate the static behavior of plywood. An application to the finite element method to simulate the static tensile and compression tests is presented. The comparisons between experimental data and the models' results reveal that a plywood can be modeled as single block of a homogeneous anisotropic equivalent material whose properties are estimated following the rule of mixtures and classical laminate theory.

Keywords Plywood · Mechanical behavior · Modeling · Beech · Melamine-urea-formaldehyde

S.J.C. de Oliveira · O. Bolmin (✉) · M. Arrigoni · C. Jochum
Department of Naval and Offshore Structures, ENSTA Bretagne, FRE CNRS 3744,
IRDLE, 2 Rue F. Verny, 29806 Brest, France
e-mail: ophelia.bolmin@ensta-bretagne.org

S.J.C. de Oliveira
e-mail: samarajco@gmail.com

M. Arrigoni
e-mail: michel.arrigoni@ensta-bretagne.fr

C. Jochum
e-mail: christian.jochum@ensta-bretagne.fr

S.J.C. de Oliveira
CAPES Foundation, Ministry of Education of Brazil, Brasilia, DF 70.040-020, Brazil

1 Study Context

Wood is gaining popularity as a safe, environmentally sustainable and trustful material for structural purposes. For example, the strength to weight ratio of a structural plywood is about 4 times the ratio for structural steel [3] and ranks this material as a favorite one in the manufacturing of light green transportation equipment, such as bicycles and skateboards for instance.

As the most popular wood derivatives, laminated veneer lumber (LVL) and glued laminated timber (Glulam) are commonly used in several fields (civil engineering for example) and have already been the subject of several studies [1, 2].

However, plywood has not yet been widely investigated. Plywood is a wood derivative composed of thin layers of wood called veneers, with a 0.6 to 1.5 mm thickness, glued together. This material, mostly used to produce pieces of furniture and flooring, starts nowadays to gain popularity as raw material for sports items' manufacturing. Bekhta et al. [4] have already investigated compressed plywood made from birch and from alder and concluded that the use of this material can be an alternative method to improve both physical and mechanical properties of wood panels used in building applications.

The purpose of this study is to determine the static and dynamic mechanical behavior of a plywood composed of 10 layers of beech glued together with a melamine-urea-formaldehyde resin. Furthermore, it proposes a step-by-step procedure to simulate the static behavior of the plywood in the commercial finite element code Abaqus©.

The first part of this document introduces the material and provides some basic explanations for its better understanding. In this segment, a method aiming to analytically predict the plywood's mechanical properties is presented inspired by composite theories and, based on that, two approaches are proposed for the material's modeling. Afterwards, the results of these two approaches are compared with the experimental data to determine which approach represents the material at the best.

Secondly, the experimental procedures are exposed and the data provided by them are presented. The samples and their characteristics are defined and the experimental data obtained are discussed.

Finally, a technique is proposed to simulate the static behavior of plywood with a software based in the finite elements analysis (FEA), in this case, Abaqus©. To test the validity of this methodology, three models are proposed and each one of them is detailed and discussed in this study.

2 Plywood Material

This section discusses the plywood and provides a better understanding of the material and its microstructure. Taking into account the composite nature of the studied object, composite laminate theory is implemented to predict its mechanical

behavior. Two approaches are proposed and, afterwards, their results are compared with experimental data to determine the approach which best anticipates the real mechanical properties' values.

This study is a collaboration with the French company Cardineau, who provided two plywood boards differing themselves by their layers' direction. These boards are both composed of 10 beech veneers of a 1.2 mm thickness each, resulting in a 12 mm thickness of the plywood's stacking sequence.

2.1 Plywood Assembly

First of all, to build a plywood's stacking sequence, the wood must be chosen, beech in our case. Secondly, the subsequent step is to produce the veneer (thin layer of wood). As so, the Cardineau company has selected the "Unreeled technique", which consists in making the beech log rotate in its axis while a blade peel off the wood sheet, as illustrated in Fig. 1.

Secondly, these veneers proceed to the gluing stage: a melamine-urea-formaldehyde (MUF) resin is applied between the beech layers and, afterwards, they are all pressed. This procedure of pressing the stacking sequence prevents the layers from sliding one from another and helps to obtain a better quality glue joint. Nevertheless, as informed by the Cardineau company, compacting the stacking sequence can generate a 10% contraction in its thickness. This has to be taken into account for the final dimensions of the plywood.

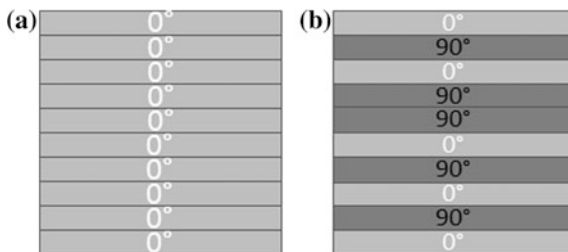
It should be noticed that wood is a porous material, and as so, it has the ability to absorb liquid [5]. Therefore, the liquid glue can penetrate into the wood layer and can change its properties. As a matter of fact, this observation is decisive for the analytical model presented.

The gluing stage is crucial to the final product, as it ensures the bonding between layers which will compose the stacking sequence and, most important, the direction of the layers. In this work, two types of stacking sequence were investigated:

Fig. 1 Illustration of the unreeled technique



Fig. 2 **a** Non-crossed beech (NCB) and **b** Crossed beech (CB)



1. Non-crossed beech (NCB): all the layers are oriented at 0° .
2. Crossed beech (CB): layers alternating their directions between 0° and 90° .

In Fig. 2, it can be observed that the crossed beech has two consecutive layers at a 90° direction. For aesthetic reasons of the manufacturer Cardineau, the first and the last layer have the same direction. That explains why, for the crossed stacking sequence, it is necessary to repeat two consecutive directions in some layers of the stacking. This can also be interpreted as a dislocated mirror symmetry. At this point, having already the wood boards manufactured, the final step is to cut the samples. They were cut in two directions: longitudinal and normal cut (as shown in Fig. 3). Both cut directions were guided by the top ply's fiber orientation.

The samples were cut in rectangular shapes for two reasons: the first is to reduce the risk of delamination and secondly because the main purpose of this study is to investigate the plywood's elastic behavior. For those reasons, it is neither worth to risk delamination nor mandatory for these samples to have a sophisticated shape, like a dumbbell shape.

Concluding, a set of 4 types of samples, as table presented in Table 1, is obtained and this will be the object of study during this investigation.

Since we work with an anisotropic material, each of these samples is associated to a 3D coordinate system, where axis 1 is along the wood fiber's direction belonging to the stacking sequence's top layer (Fig. 4), axis 2 is the transverse direction and axis 3 is the out of plane direction. In the same manner, a Young's modulus is assigned along each direction E_1 , E_2 and E_3 .

Fig. 3 Samples' cut direction

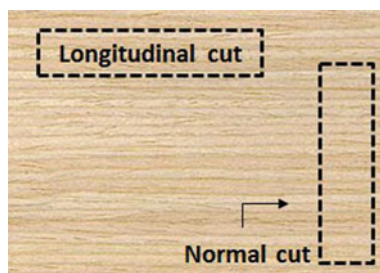
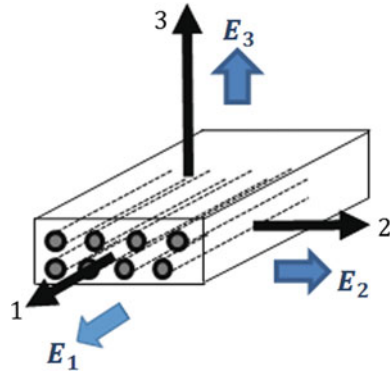


Table 1 Sample's range

	Stacking sequence	Cut direction	Abbreviation
1	Non-crossed beech (NCB)	Longitudinal	NCB-L
2	Non-crossed beech (NCB)	Normal	NCB-N
3	Crossed beech (CB)	Longitudinal	CB-L
4	Crossed beech (CB)	Normal	CB-N

Fig. 4 Axis coordinate system associated to a sample



2.2 Theoretical Modelling

Due to the wood's porous nature, the glue is absorbed into the wood. A cross section picture is shown in Fig. 5. It is possible to see that not all glue is absorbed, forming a thin glue layer between the wood plies.

This observation is the guiding principle for the two analytical approaches proposed in this study (as presented in Fig. 6):

- Approach 1: All ten layers are composed of 60% of wood and 40% of glue (Fig. 6a).
- Approach 2: The ten veneers are also modeled as a 60 and 40% glue mixture but with a layer of glue between them (Fig. 6b).

An estimated glue's thickness of 0.05 mm was considered.

2.2.1 Constitutive Mechanical Properties of Considered Materials

To predict the behavior of a composite material, it is crucial to know the mechanical properties of each component. These parameters are presented in Table 2.

As a matter of prudence, it was decided to work with the lowest beech properties' values for both E_1 and E_2 .

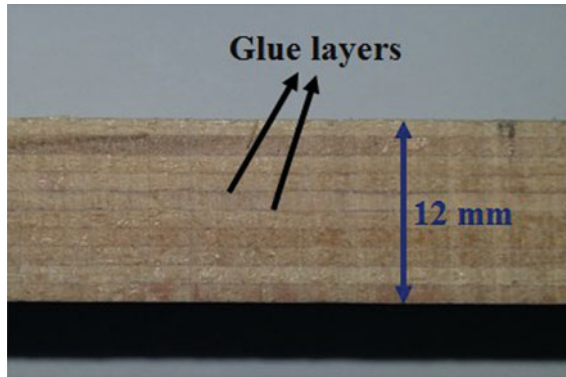


Fig. 5 Typical cross section of the plywood

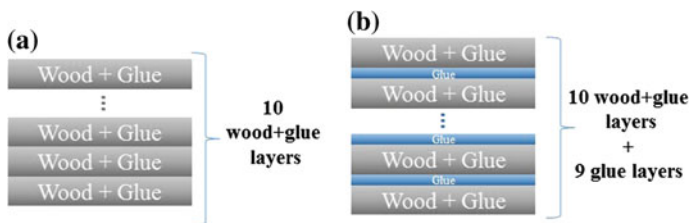


Fig. 6 a Approach 1 and b Approach 2

Table 2 Mechanical properties of the wood (beech) and the glue (MUF)

	E_1 (MPa)	E_2 (MPa)	ν_{12}	G_{12} (MPa) ^c
Beech [7–9]	14,100 ^a	807	0.46	482.9
Melamine-urea-formaldehyde [9, 10]	1800	1800 ^b	0.4	642

^aThe E_1 for beech is obtained from compression tests [7]

^bThe glue was supposed an isotropic material and, as such, the E_2 is considered as being equal to E_1

^cIn a framework of a linear elastic and isotropic material, the shear modulus G_{12} is estimated using Eq. 1

From the index board published by CIRAD [6], it can be noticed that the beech’s longitudinal modulus E_1 have a standard deviation around 6.8%. As such, the lower boundary for the interval considering a 6.8% deviation and an average value of an $E_2 = 867$ MPa [7], leads finally to $E_2 = 807$ MPa for the beech.

$$G_{12} = \frac{E_1}{2(1 + \nu_{12})} \tag{1}$$

Table 3 Elastic properties of a layer composed of 60% wood and 40% of glue

	E_1 (MPa)	E_2 (MPa)	G_{12} (MPa)	ν_{12}
60% wood and 40% glue layer	9180	1157	541.6	0.436

2.2.2 Rule of Mixtures and Classical Laminate Theory

This section aims to predict the mechanical properties of a layer composed of wood and glue, as well as the properties of a stacking sequence composed of these layers. As the properties of both glue and wood are well-known, a composite approach is employed.

To calculate the properties of the layer with 60% of wood and 40% of glue, the rule of mixtures is implemented. On the other hand, to estimate the properties for a stacking sequence (based on the layers' directions and eventual glue layers) it is made use of the Classical Laminate Theory (CLT). Both of these theories are widely applied in the composite materials' field.

2.2.3 Equivalent Anisotropic Material's Data Table

Thanks to the rule of mixtures and the CLT modeling approaches, the mechanical properties of a ply composed of 60% of wood and 40% of glue were estimated for the stacking sequences presented in approaches 1 and 2 (Table 4 and 5).

3 Static Experiments Analysis

During this investigation, two static tests were performed: tensile and compression tests. This section aims to describe the tests' procedures, to present the results and to discuss them.

All the sample's geometric characteristics can be consulted in Appendix 7.1.

3.1 Tensile Tests

In this experiment, 4 types of samples were tested as listed in Table 1. The tests were performed thanks to a tensile machine MTS 647 Hydraulic Wedge Grip for the samples in NCB-L and in a UTS 250 for the other samples. All tests were conducted displacement controlled with a 10 mm/min displacement rate.

It should be noticed that, when a sample with a longitudinal cut direction is tested, the slope of the stress-strain curve response is directly the Young's modulus E_1 . Similarly, for a sample with a normal cut direction, the property tested is the

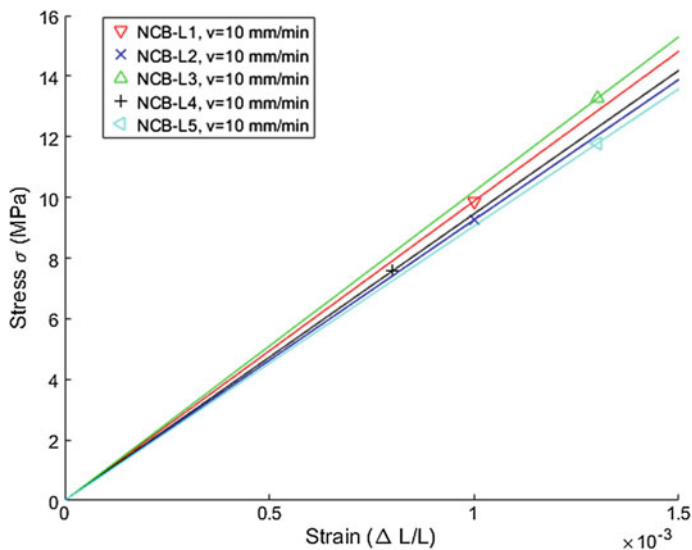


Fig. 7 Tensile test on NCB-L

Young's modulus E_2 . This is why, when presenting the results of the tensile tests, they will be announced and treated in terms of E_1 and E_2 .

3.1.1 NCB-L Tensile Tests' Results

NCB-L samples experimental results are gathered in Fig. 7 and Table 6. The samples tested are noted NCB-L1 to NCB-L5 and the tests' displacement rate is displayed at the chart's legend.

3.1.2 NCB-N Tensile Tests' Results

NCB-N samples experimental results are gathered in Fig. 8 and Table 6. The samples tested are noted NCB-N1 to NCB-N5 and the tests' displacement rate is displayed at the chart's legend.

It can be seen that the response in direction 1 is linear and the slope E_1 is about 9564 MPa in average with a standard deviation of 12%. This large deviation can be explained by the fact that wood is a natural material which carries irregularities in fibers alignment and porosity. The same conclusions can be inferred for the CB samples, where the average value of E_2 is 809 MPa with a standard deviation of 13%.

It is important to notice that a considerable amount of time has elapsed from the sample's fabrication to the moment where it was tested. Before performing the tests,

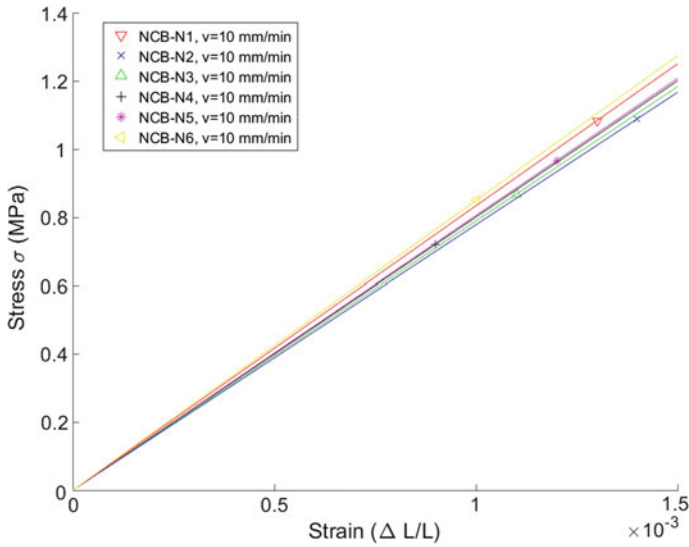


Fig. 8 Tensile test on NCB-N

it could be observed a slight bending in the NCB-N samples. This can suggest a residual stress state among the samples released by the cut and then a possible stress superposition during the E_2 's tensile tests.

3.1.3 CB-L Tensile Tests' Results

CB-L samples experimental results are gathered in Fig. 9 and Table 6. The samples tested are noted CB-L1 to CB-L5 and the tests' displacement rate is displayed at the chart's legend.

3.1.4 CB-N Tensile Tests' Results

CB-N samples experimental results are gathered in Fig. 10 and Table 6. The samples tested are noted CB-N1 to CB-N5 and the tests' displacement rate is displayed at the chart's legend.

Young's Modulus results (tensile slopes) obtained is presented in Table 6, as well as their relative errors compared to the properties predicted with the theoretical modeling approaches from Tables 4 and 5.

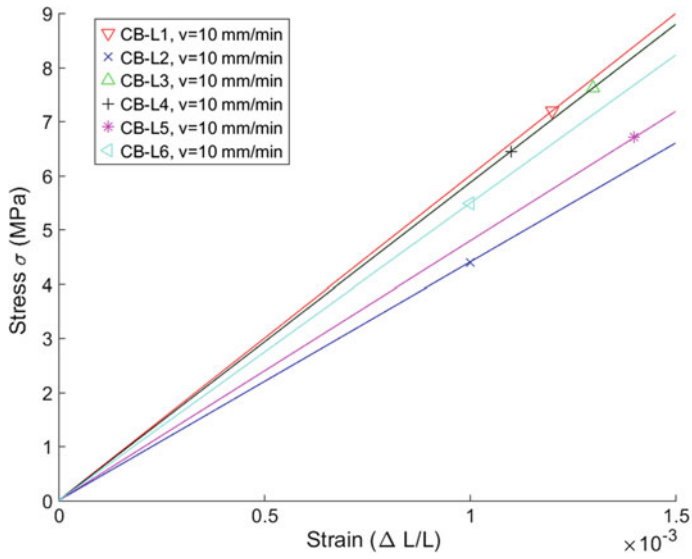


Fig. 9 Tensile test on CB-L

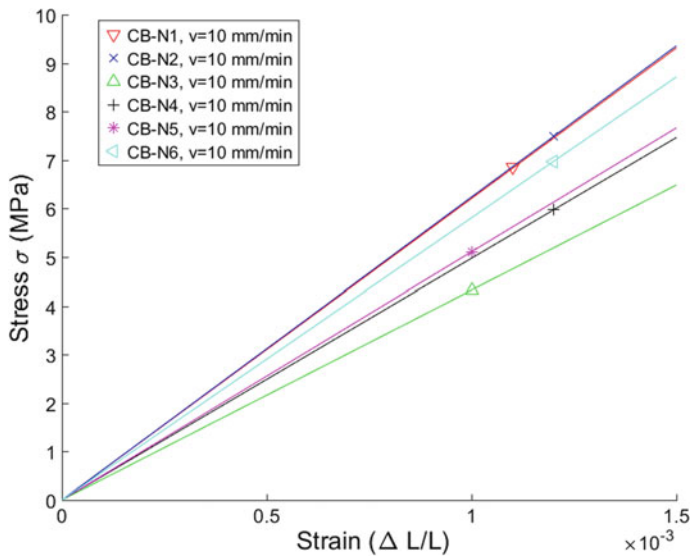


Fig. 10 Tensile test on CB-N

Table 4 Elastic properties of a stacking sequence following the approach 1

	E_1 (MPa)	E_2 (MPa)	G_{12} (MPa)	ν_{12}
NCB—Longitudinal cut	9180	1157	541.6	0.436
NCB—Normal cut	1157	9180	541.6	0.055
CB—Longitudinal cut	5242	5240	541.6	0.098
CB—Normal cut	5240	5242	541.6	0.098

Table 5 Elastic properties of a stacking sequences following the approach 2

	E_1 (MPa)	E_2 (MPa)	G_{12} (MPa)	ν_{12}
NCB—Longitudinal cut	8913	1189	545.2	0.434
NCB—Normal cut	1189	8913	545.2	0.058
CB—Longitudinal cut	5124	5123	545.2	0.102
CB—Normal cut	5123	5124	545.2	0.102

Table 6 Comparison between analytical Young Modulus prediction and experimental data results

Sample	E average (MPa)	Deviation (%)	Relative error Approach 1 (%)	Relative error Approach 2 (%)
NCB— E_1	9564	12	4	7
NCB— E_2	809	13	4	7
CB— E_1	5397	9	3	5
CB— E_2	5445	8	4	6

3.2 Compression Tests

The compression tests were conducted on cylindrical samples (Appendix 7.1). The machine used was an electromechanic compression machine ADAMEL LHOMARGY 100.

3.2.1 NCB Compression Tests' Results

Two displacement speed were imposed: 1 mm/min for tests 1 to 3 and 10 mm/min for samples 4 and 5. The maximum displacement was 5 mm for test 1 and 7 mm for the others.

During the tests, strain is deduced from displacement of the machine and the sample initial length. Force is measured with a 100 kN loaded cell force and the apparent stress is then deduced by dividing the force by the sample cross section.

The stress-strain curves obtained on these tests are presented in the Fig. 11.

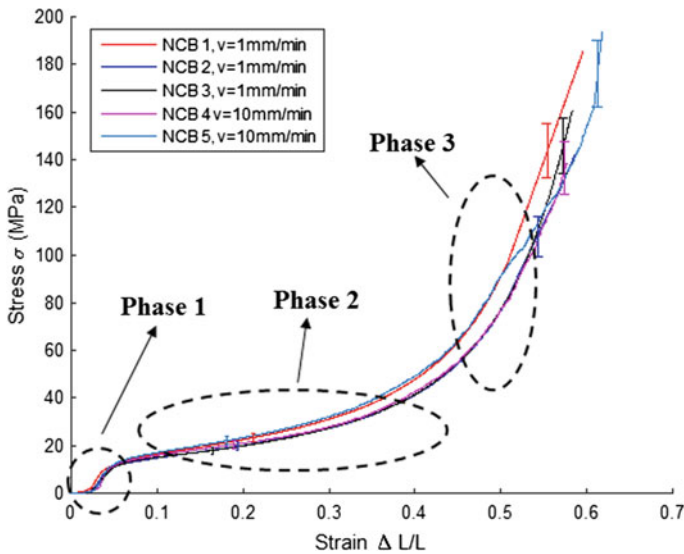


Fig. 11 Compression test on NCB

A typical and fairly reproducible “slide” like shape is obtained on NCB samples as well as on CB samples. An interpretation is proposed in the discussion paragraph.

3.2.2 CB Compression Tests’ Results

The curves obtained on these tests are presented in Fig. 12.

3.2.3 Compression Tests’ Discussion

Three linear phases can be observed in Figs. 11 and 12, which highlight three static responses of the material.

Phase 1 The first linear phase is the elastic response of the material. The phenomenon can be seen as an assembly in series of alternating springs of glue and wood and glue. As the wood is the less rigid component, i.e. the one which has the lowest modulus of elasticity, it is the first component to yield when compressed by the static load. Thus, phase 1 mainly corresponds to the elastic response of the wood and the slopes are presented in Table 7.

An inflection point can eventually be noticed within this phase. It can be due to the positioning face to face between the samples and the compression plates.

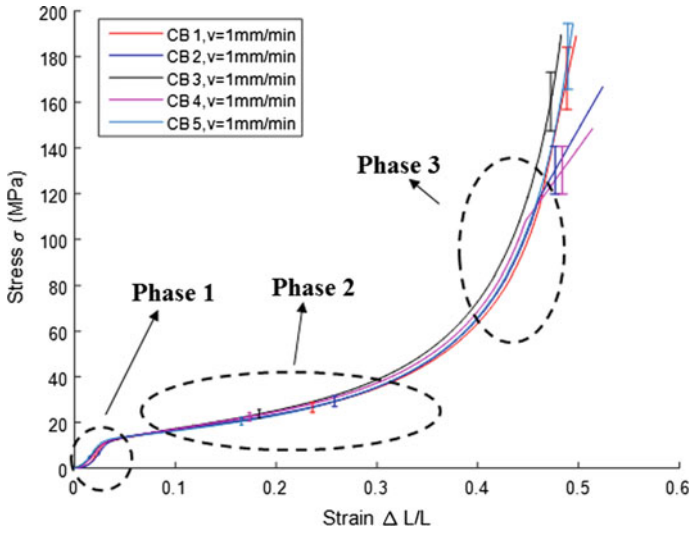


Fig. 12 Compression test on CB

Table 7 Compression slopes

Sample	Phase	E_3 average (MPa)	Deviation (%)
NCB	1	525	8
NCB	2	60	8
NCB	3	991	8
CB	1	552	8
CB	2	72	8
CB	3	2035	8

During phase 1, it seems that speed does not have any influence neither fiber orientation since NCB and CB tests gave similar values (E_3 equal to 525 MPa and to 552 MPa, respectively).

Phase 2 is characterized by a linear response, whose slope is lower than the slopes observed in phase 1 or 3. This phase shows the mechanical damage of the wood. When the force increases the sample cross section is also increasing since the wood is crushing.

Indeed, wood microstructure arrangement in the out of plane direction 3 can be reasonably considered as being the same as for the direction 2 (succession of lignite fiber and cellulose matrix). Consequently, the out of plane modulus E_3 could be considered of being in the same order of magnitude as for E_2 . Thus, assuming the same behavior in both direction 2 and 3 for tensile and compression, Table 2 clearly mentions that wood is much weaker than the MUF for a compression stress.

Phase 3 is, then, the compaction of the glue, which has already been damaged during the two compression tests' previous phases. The response of the non-crossed beech differs from the response of crossed beech (Table 7). One explanation of this

difference lies on the material's microstructure comprehension. The compression process causes the migration of rigid matter (the glue phase) into the soft part of the material (the wood-and-glue phase):

- In the case of NCB samples, wood fibers are mostly parallel, thus the microstructure allows the glue to penetrate the wood-and-glue (W-G) phases.
- In the case of CB samples, the grid of wood fibers (alternated 0° and 90° layers) stops the glue from entering the W-G phases, thus the modulus E_3 is more than twice as superior.

As an intermediate conclusion, we have determined an anisotropic quasi static behavior of NCB and CB beech samples. However, in real life, plywood manufactured devices also undergo shocks and vibrations. This is why we also focused our interest in the dynamic behavior of these samples.

4 Dynamic Experiments Analysis

The main goal of our investigation is to have sufficient knowledge of the plywood's behavior to apply it on objects such as bicycles and skateboards. Structures like those are submitted to dynamic loads, like impacts due to a hole on the road, for example. That is the importance to study also the plywood's dynamic behavior. This section is dedicated to describe the procedures during the Taylor Gun and Hopkinson bar tests, as results and conclusions are taken.

As said before, the sample's geometric characteristics can be consulted in Appendix 7.1.

4.1 Taylor Gun Test

Since this type of experiment tests the dynamic bending stiffness of a certain material, the purpose in performing the Taylor Gun tests on plywood is to find the greatest impact energy for which the material can resist. In other words, the samples are hit by a projectile and afterwards they are examined with an unaided eye to determine whether there is any macroscopic damage in it or not.

The Taylor gun facility had a 50 mm diameter with a 2 m long barrel. The projectile had a cylindrical shape, a diameter of 77 mm and a mass of 1.58 kg. A mass of 0.88 kg was used for two of the NCB-N samples in an attempt to reduce the impact level. The target was mounted in a holder with a central hole, as exposed in Fig. 13.

For this experiment, 4 types of samples were used, with the same characteristics as the tensile tests' samples presented in Sect. 3.1.

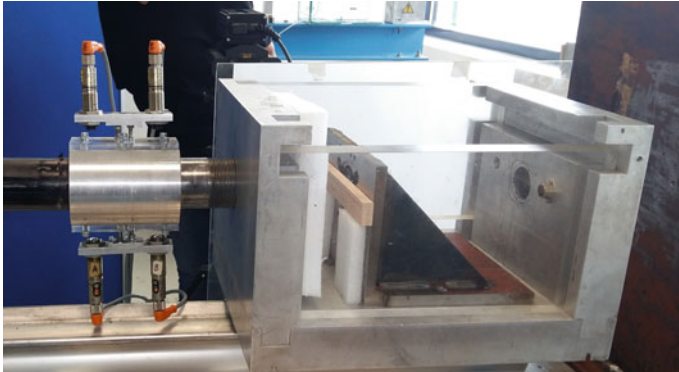


Fig. 13 Sample assembly for Taylor gun tests

4.1.1 Taylor Gun Tests' Results

The results for the Taylor Gun tests are illustrated in Fig. 14. In this image, the fulfilled squares represent the samples which resisted to the impact while the hollow squares symbolize the damaged samples.

Taylor gun tests' discussion It can be observed in Fig. 14, that the specimen which resists to the maximum impact energy is the NCB-L, as expected. Indeed, during the impact, all the fibers of the NCB-L are exposed to a bending stress, leading the NCB-L specimen to logically support far more than the NCB-N specimen where the fibers were not loaded.

As for the crossed beech, it is observed that the CB-L resists to a higher impact level than the CB-N. This is explained by the stacking sequence effect on the bending stiffness regarding CB-L and CB-N specimens. Indeed, the stacking is not symmetric and the upper plies are only loaded in the directions for the CB-L specimens, hence a higher level than for the CB-N specimen was observed.

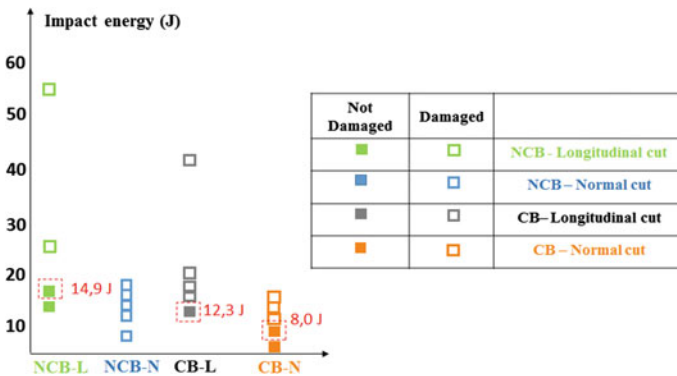


Fig. 14 Taylor gun results showing minimal impact energy that the samples can resist

4.2 Hopkinson Bar Tests

The aim of the Hopkinson bar test is to measure the samples' dynamic compression stiffness applying an out of plane impact stress and to obtain dynamic stress and strain curves. For that, the samples applied have the diameter reduced from 20 to 17 mm (in comparison with the static compression test samples) as required by the Hopkinson bar's set up where the bar used has a 20 mm diameter (Appendix 7.1).

Similarly to the static compression test, each stacking sequence (NCB or CB) was tested with different impact velocities. The qualitative results are presented in

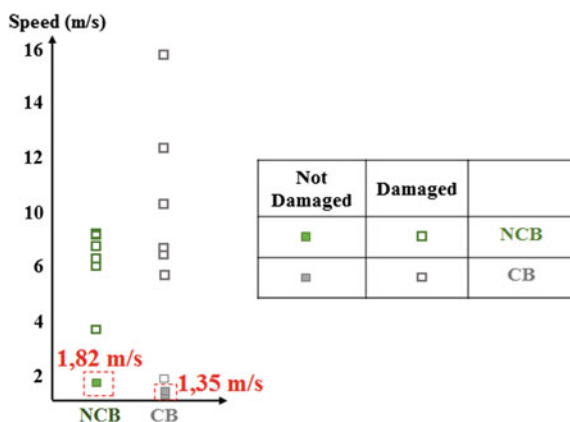


Fig. 15 Hopkinson bar qualitative results

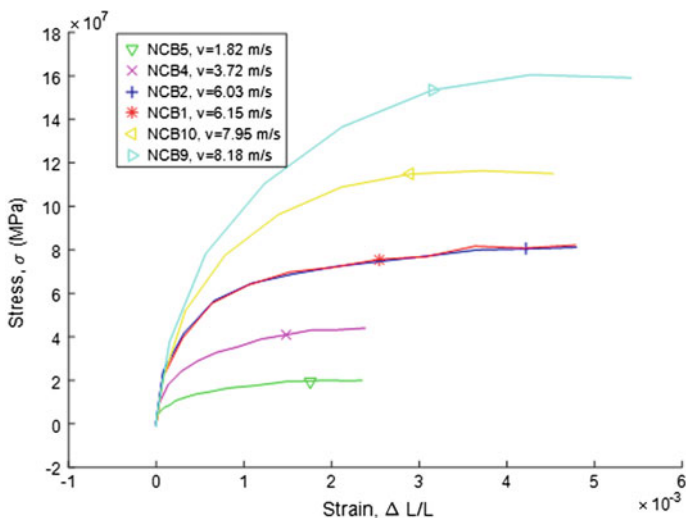


Fig. 16 Hopkinson bar test on NCB

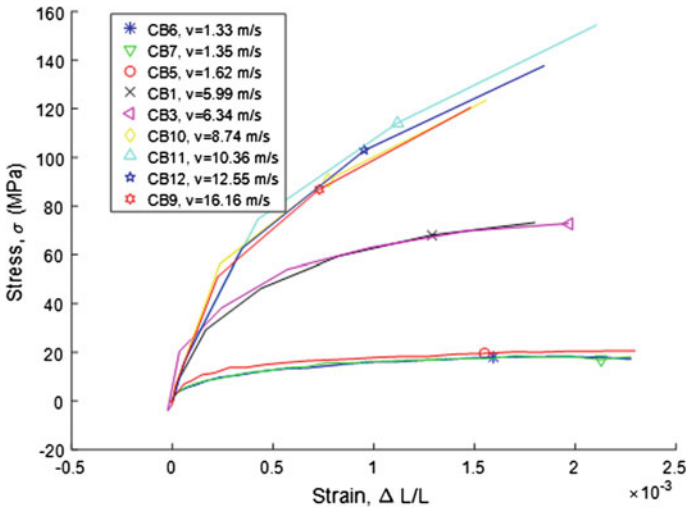


Fig. 17 Hopkinson bar test on CB

Table 8 Dynamic modulus out of plane of NCB and CB

	NCB	CB
E_3 dynamic (MPa)	2.54×10^5	2.32×10^5

Fig. 15 and as for the results of the Taylor gun tests, the fulfilled squares represents the samples which resisted to the impact while the hollow squares symbolize the damaged samples.

The stress-strain curves found with this procedures are exposed in Figs. 16 and 17. Notice that the only samples of NCB which resists to the impact is the NCB5 (impact speed = 1.82 m/s) while for the CB two samples are intact after the shock: the CB6 (impact speed = 1.33 m/s) and CB7 (speed impact = 1.35 m/s).

Discussion: The same dynamic response can be observed at the beginning of the impact of both NCB and CB, this suggests that they react similarly to a dynamic stress. The dynamic modulus were determined from the results curves Figs. 16 and 17 and are presented in Table 8.

5 FEA Simulation for Static Tests

For the modeling of the investigated plywood, a procedure to simulate the static behavior is proposed in this section based on a finite elements analysis (FEA) performed with the industrial software Abaqus©.

The leading idea is to simulate the static tests performed on the samples (tensile and compression tests) and to compare to the experimental data.

In this stage, three models are proposed and their results are discussed:

- Model 1: The sample is modeled as a homogeneous anisotropic equivalent block with the material properties of Approach 1 (Table 4), where all layers are composed of 60% of wood and 40% of glue.
- Model 2: The sample is modeled as a homogeneous anisotropic equivalent block with the material properties of Approach 2 (Table 5), where the stacking sequence is composed of wood + glue layers and glue layers.
- Model 3: The sample is modeled as a laminated stacking sequence with both glue layers and wood + glue layers. The mechanical properties of a wood and glue layer are exposed in Table 3 and the characteristics of glue alone are given by Table 2.

For the simulation of the tensile experiment following models 1 and 2, it was built a thick shell with a surface of 25 mm \times 200 mm and a 12 mm thickness with a linear quadratic element type S4. A 990 N/mm shell edge load was applied in each sample's boundaries, as represented in Fig. 18. The Young's Modulus was deduced from stress-strain simulation curves.

On the other hand, for the simulation of the compression experiment following the models 1 and 2, a 2D shell was built with a surface of 25 mm \times 12 mm, representing the cylindrical sample's transverse section. A 3 directions (x, y and z) constraint was created between a reference point and the sample's upper line. Finally, a displacement is imposed on the reference point. This procedure is illustrated in Fig. 19.

The major assumption made in this model is to take the plywood's out of plane modulus E_3 as being equal to the wood's transverse Young's modulus E_2 . This hypothesis is acceptable if we consider that not the whole veneer's thickness is infused with glue and that it remains a thin layer of pure wood in the middle of the

Fig. 18 Tensile sample modeled in Abaqus©

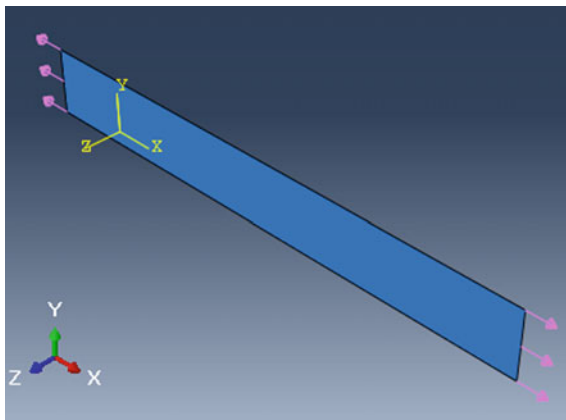
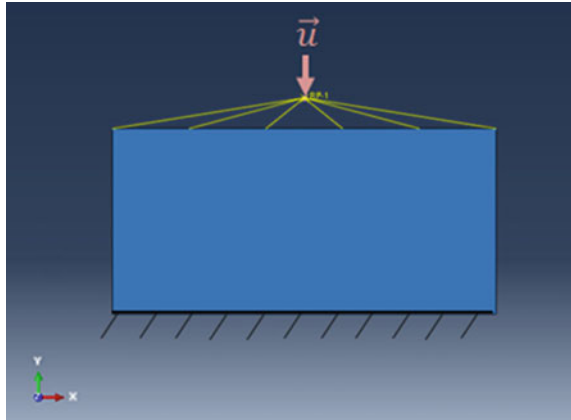


Fig. 19 Compression sample modeled in Abaqus©



vener’s thickness. In this case, with an out of plan compression stress, this phase is the weakest one in a serial arrangement and thus it would be the first to be damaged.

The procedure for the model 3 has many particularities, and for a matter of convenience, they will be all specified directly in the Sect. 5.3.

5.1 Model 1

In this first model, the subject is addressed from the most basic point of view: the sample is assumed as a homogeneous anisotropic equivalent block composed of 60% of wood and 40% of glue.

Tensile and compression results are exposed in Tables 9 and 10, respectively.

Discussion: Model 1’s results are almost satisfactory for tensile tests simulation except for the prediction of the NCB’s E_2 . However the prediction of the out on plane compression modulus E_3 led to significant difference of around 30%. This level of difference is also observed for the E_2 tensile model prediction.

One explanation of this overestimation might stay in the fact that glue layers are not taken into account in the first model. This now considered in model 2.

Table 9 Tensile test simulation: comparison between Model 1 and experiments’ results

	Experiment’s average (MPa)	Model 1 results (MPa)	Discrepancy (%)
NCB— E_1	9564	9180	4.18
NCB— E_2	809	1157	30
CB— E_1	5397	5242	2.95
CB— E_2	5445	5240	3.91

Table 10 Compression test simulation: Comparison between Model 1 and experiments' results

	Experiment's average (MPa)	Model 1 results (MPa)	Discrepancy (%)
NCB— E_3	525	807	35
CB— E_3	552	807	31.57

5.2 Model 2

The model 2 has a procedure very similar to the model 1, except for the fact that it applies the values calculated following the Approach 2 (Table 5), which considers layers of glue inserted between layers of wood and glue.

Tensile and compression results are shown in Tables 11 and 12, respectively.

Discussion: Although model 2 shows good prediction results for tensile tests, these are less accurate than those from those of model 1.

This is however in agreement with the physics of the samples since glue layers (0.05 mm thick) were inserted with a lower level of Young's modulus than the 60% of wood +40% glues layer (Tables 2 and 3). Consequently, the parallel assembly of layers composed in this tensile simulation for model 2 is affected by a slight decrease in Young's modulus prediction.

As for compression results, no changes were observed compared to model 1. This is consistent compared to model 1 since the weakest part of the serial assembly exposed to the compression test remains the wood and glue layer whose the E_3 modulus was taken as being the equal to 807 MPa (wood's E_2 , Table 2), assuming the existence of a glue free area.

Nevertheless, to check any structure effect on FEA simulations for compression, the stacking sequence was directly modeled as presented in model 3.

5.3 Model 3

In this third model, it is proposed to build, as usual as for previous models, a 2D shell part but this time with a surface area of 25 mm \times 12.45 mm. The additional 0.45 mm in the part's height is due to the introduction in the model of 9 glue layers

Table 11 Tensile test simulation: comparison between model 2 and experiments' results

	Experiment's average (MPa)	Model 2 results (MPa)	Discrepancy (%)
NCB— E_1	9564	8913	7.3
NCB— E_2	809	1189	31.95
CB— E_1	5397	5124	5.33
CB— E_2	5445	5123	6.29

Table 12 Compression test simulation: comparison between model 2 and experiments' results

	Experiment's average (MPa)	Model 2 results (MPa)	Discrepancy (%)
NCB— E_3	525	807	35
CB— E_3	552	807	31.57

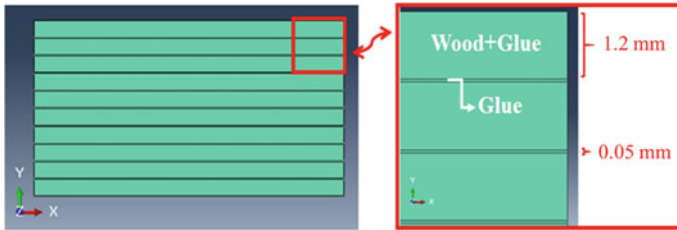


Fig. 20 Surface partition for model 3

with a 0.05 mm thickness. The aim of this model is to create 19 partitions to afterwards designate 9 of them as plies of glue alone (with a 0.05 mm thickness) inserted between 10 layers composed of wood and glue (with a 1.2 mm thickness), as illustrated in Fig. 20.

Boundary conditions and loads were applied in the same manner as the models 1 and 2 (see Fig. 18).

Compression tests simulation The results and comparison can be consulted in Table 13.

Discussion: Model 3 exhibits a slightly better result for the NCB's out of plane Young's modulus but a greater discrepancy for the CB. The gain compared to previous models is very limited, and Model 3 simulations require more time to be performed.

One might try 3D FEA modeling but this would be even more time consuming. Finally, it appears that model 1 can reasonably be considered as being accurate enough, especially for in plane elastic behavior predictions. However, when using model 1, one should be especially meticulous when simulating an out of plane elastic behavior, since E_3 modulus is overestimated by around 30%.

Table 13 Compression case: comparison between model 3 and experiments results

	Experiment average (MPa)	Model 3 results (MPa)	Discrepancy (%)
NCB— E_3	525	724	27.53
CB— E_3	552	819.34	32.60

The fact of having good results for the simulation of all tensile modulus, except for the NCB's E_2 denotes a possible weakness in the experimental set up for E_2 NCB. Whereas it worked fine for E_2 CB.

6 Conclusion and Future Plans

In this study, a step-by-step procedure was developed to determine the static and dynamic behavior of a plywood as well as a manner to simulate the static behavior of this material. A considerably complete material behavior map is provided, with real experimental data from tensile, compression, Taylor gun and Hopkinson bar tests.

It can be stated that, when creating a model of a plywood, it can be simulated as a single block of an anisotropic material with the properties previously calculated following a composite approach. However, special attention is required when simulating an out of plane behavior. Indeed, the assumption of considering the out of plane Young's Modulus (E_3) being the same as the transverse modulus of wood alone (E_2) led to an overestimation of around 30%. Nevertheless, the analytical modeling approach based on the CLT and rule of mixtures led to as good results as for FEA results.

For our future plans, it is intended to search for an improvement about the simulation of the out of plane Young's Modulus as to determine a procedure to simulate the plywood behavior under dynamic loading using the industrial software RADIOSS©.

Acknowledgements We would like to take this opportunity to warmly thank Mr. Boivineau from the Cardineau company, who very kindly provided the plywood samples and gave precious advices.

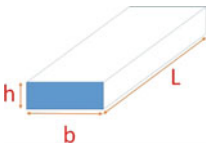
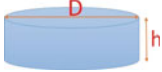
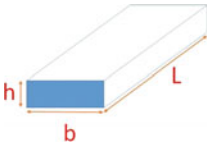
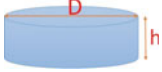
Authors are also grateful with ENSTA Bretagne, that supported this work and especially with Dr. Dhont and Demmouche and also the technical staff (Bernard Mazé, Fred Montel, Didier Pochard).

7 Appendix

7.1 Samples' Dimensions

See Table 14.

Table 14 Samples' dimensions

Experiment	Sample's shape	Sample's dimensions	
Tensile	Parallelepiped	Length (L) = 200 mm Width (b) = 25 mm Height (h) = 12 mm	
Compression	Cylinder	Diameter (D) = 25 mm Height (h) = 12 mm	
Taylor Gun	Parallelepiped	Length (L) = 200 mm Width (b) = 25 mm Height (h) = 12 mm	
Hopkinson bar	Cylinder	Diameter (D) = 17 mm Height (h) = 12 mm	

References

1. Kwon JH, Shin R-H, Ayrilmis N, Han TH (2014) Properties of solid wood and laminated wood lumber manufactured by cold pressing and heat treatment. In: Elsevier Ltd (ed) *Materials & design*, vol 62, Amsterdam
2. Issa CA, Kmeid Z (2005) Advanced wood engineering: glulam beams. In: Elsevier Ltd (ed) *Construction and building materials*, vol 61, Amsterdam
3. E. W. P. A. of Australasia (EWPAA) (2009) Plywood manufacture. In: Engineered wood products association of Australasia, Eagle Farm, QLD Australia
4. Bekhta P, Hiziroglu S, Shepelyuk O (2009) Properties of plywood manufactured from compressed veneer as building material. In: Elsevier Ltd (ed) *Materials & design*, vol 30, Amsterdam
5. Harding V et al (1997) Glues and gluing wood. In: LSU AgCenter (ed) Baton Rouge, Louisiana
6. CIRAD Unité de Recherche Biomasse bois énergie bioproduits (2012) Hêtre. *Tropix* 7. <http://tropix.cirad.fr/FichiersComplementaires/FR/Temperrees/HETRE.pdf> Accessed 17 Jan 2017
7. Forest Products Laboratory, U S Dept of Agriculture, Forest Service (2010) Wood handbook—wood as an engineering material. In: General Technical Report FPL-GTR-190, Centennial edn. Madison, Wisconsin
8. Guitard D (1987) Mécanique du matériau bois et composites. In: Cepadues-editions (ed) Collection Nabla, Toulouse
9. Gay D (2015) Matériaux composites. In: Lavoisier Hermes (ed) 6th edn. Paris
10. Cai X (2007) Wood modifications for valued-added applications using nanotechnology-based approaches. Ph.D. thesis, Université Laval

Monochrome Multitone Image Approximation on Lowered Dimension Palette with Sub-optimization Method Based on Genetic Algorithm

Rudolf Neydorf, Albert Aghajanyan, Anna Neydorf and Dean Vučinić

Abstract The problem of sub-optimum approximation of monochrome multitone images (MMI) by a palette with reduced amount of tones, called support palette (SP), is solved. The SP palette tones are defined with the images analysis, which arise in related scientific topics as: technical sight, recognition of images, etc. In this work the research objective was to assess the opportunity of using efficiently such analysis, by applying the genetic algorithms (GA) for sub-optimum approximation of MMI, considering the original big size tones palette [1]. The proposed approximation consists in replacing the original MMI pixels with the approximated pixels from a smaller size tone palette. This procedure is of importance in the synthetic vision approach, where image recognition procedures are expected to define the main contours within the image. The developed method reduces the amount of tones used to display an image, whose approximation approach is presented in this paper. In order to solve it, two alternative problems are considered: (1) minimization of losses in such image transformation, and (2) minimization of the SP size (for example, to simplify the image recognition process). The approximated MMI quality is defined as the mean square deviation of pixels brightness (original to approximated). The chromosome in GA is SP, where tones are represented as genes. Such approximations are resulting from the mutational variation of the MMI palette tones, within gene alleles, which are formed by applying the original palette tones. The palette is iteratively changing from

R. Neydorf (✉) · A. Aghajanyan · A. Neydorf
Don State Technical University, Rostov-on-Don, Russia
e-mail: ran_pro@mail.ru

A. Aghajanyan
e-mail: foralbert92@gmail.com

A. Neydorf
e-mail: neydan@yandex.ru

D. Vučinić
Vrije Universiteit Brussel, Brussels, Belgium
e-mail: dean.vucinic@vub.ac.be

generation to generation, where the reduction of the stop risks is done on the local extremum. This fact increases the available search opportunities, as provided by the multi-point crossing-over algorithm, whose parameters are able to mutate during such an evolution process. In addition, to demonstrate the result of this work, an appropriate software has been developed, having an easy-to-use user interface, enabling to show the highly efficient processing of the investigated algorithm. The presented solutions are validated with photo examples of several technical objects, on which the sub-optimum method has been applied.

Keywords Monochrome image · Image approximation · Optimization · Genetic algorithm · Gen · Chromosome

1 Introduction

The monochrome multitone image (MMI), called also “grayscale image”, is an array of different brightness pixels of the same tone, which are present in a picture. Quite often, the monochrome images are analyzed for technical sight needs, where the detection of the areas orientation forming the objects is used as support to the recognition process. There is a huge class of MMI’s approximations problems, which have significant difference in their realization and approach direction. For example they are: the image compression algorithms with minimal losses, image filtering or pre-processing for recognition algorithms, image converting to the device format with limited number of supported tones, and others [2–5]. However, many of them use different methods to lower the palette size, and which motivated the authors to research further this transformation, as till today and in their knowledge such approach has not been addressed. It is important to mention that this step in the image processing process has some underlying rules, and which is envisaged to be useful for solving different problems in image analysis. Therefore, the considered problem of MMI’s approximation, as the mapping of the image with a smaller palette, is expected to simplify the pattern recognition tasks, image defects detection and image transformation, for the variety of printing devices.

The proposed approximation consists in replacing the basic palette (BP) pixels of the original MMI (OMMI) with the approximated palette (AP) pixels, which contains less number of tones. This operation can be achieved by different algorithms, which have in common a pixels mapping from an original array $P_{parent} = \{p_i | i = \overline{1, n_p}\}$ of pixels, where n_p —is the size of BP, to a single pixel $p_{appr} \in \{p_j | j = \overline{1, n_a}\}$, where n_a —is the size of AP. The mapping rules have to follow some exact criteria, which evaluate the effectiveness of the approximated image. In case of major variations of the imposed criteria, resulting from the selected approximation methods, it is necessary to define the respective conceptual and mathematical models.

2 Image Approximation Model

In a general case, the quality of the approximation is set by a certain criteria. The most common criteria is the “root-mean-square deviation” (RMSD) of pixels brightness between approximated MMI (AMMI) and OMMI or “least square deviation”, defined as follows:

$$\Delta_2 = \frac{1}{n} \sum_{i=1}^n \frac{1}{m} \sum_{j=1}^m (A[i,j] - I[i,j])^2 \tag{1}$$

where A —is the matrix of AMMI; I —is the matrix of OMMI $n \times m = N$ —count of all pixels.

The performed research showed that for the considered problem it is more appropriate to use another criteria, which is the “least module of deviation” (LMD):

$$\Delta_m = \frac{1}{n} \sum_{i=1}^n \frac{1}{m} \sum_{j=1}^m |A[i,j] - I[i,j]| \tag{2}$$

The quality of the MMI approximation depends on the number of AP tones and their values, which are together called the support palette (SP) and the SP tones have to cover the range of OMMI tones (see Fig. 1).

One of the most important factors, which define SP, is to correctly choose the SP tones and their respective values. Often, the size of SP (number of tones) is the user prerogative. It is depends from different application area of approximation, which has different allowable error.

In the previous research [1], the SP covering range is defined by dividing BP in equal parts, where the number of parts, and the number of SP tones, is the same. Such homogeneous distribution was found quite effective for initializing such analysis.

However, the MMI Frequency Diagram of Brightness (FDB) is quite rare to be found equal (see Fig. 2).

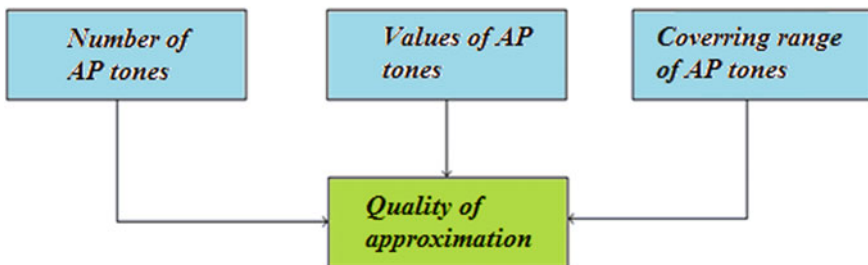


Fig. 1 Approximation parameters influencing the image quality

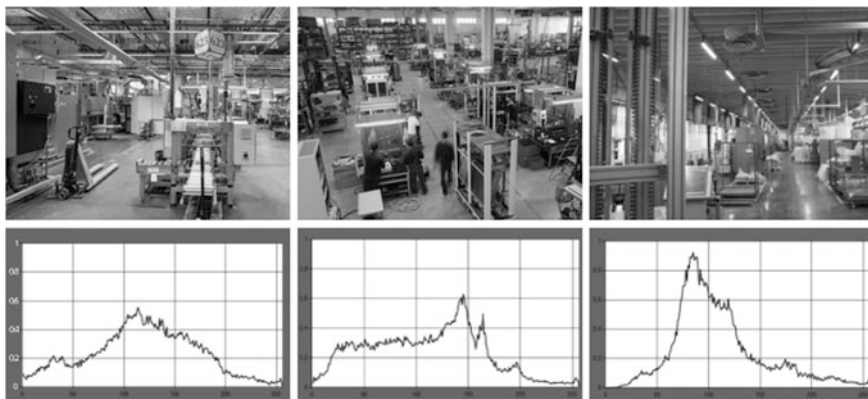


Fig. 2 Three different industrial workplace photos and their respective FDB

Thus, the strategy of maximal measured calculation of pixels number for each range was applied to define the SP covering range for this modified algorithm, which consists of the following steps:

1. determine the count of all tones N ,
2. find average count of the pixels N_c according the size of SP,
3. scan DFB by separating ranges, which have the full pixels number N_i of BP, and the minimal deviation from N_c .

Following such approach, the zones, which have smaller number of tones, receive the larger range, because their contribution to the MMI's correctness is less significant. The example of this strategy is present through the integral (accumulated) diagram of brightness, which is the analogue of the integral probability distribution (see Fig. 3).

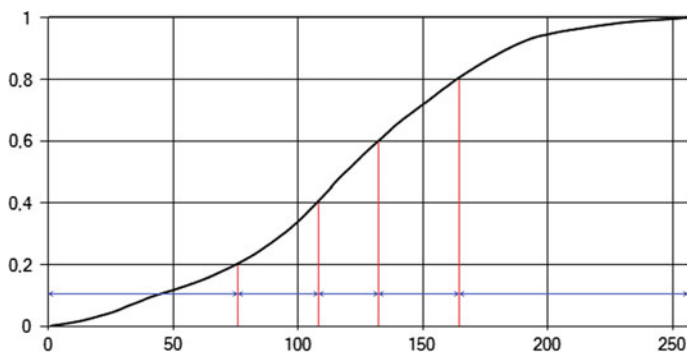


Fig. 3 The integral diagram of the 1st workplace photo

The above diagram shows, in the relative scale, the accumulated number of pixels for increasing brightness, where on Y-axis (number of pixels), shows the decomposition strategy between ranges. However, the follow up research has confirmed a good computational efficiency of this model in defining the covering range.

3 Image Approximation with Genetic Algorithms

The research decision was to use the genetic algorithm (GA) to optimize MMI's approximation, which modifications have been crucial to solve this problem.

The GA's modifications consider the individual to be AMMI and the chromosome to be SP. The genes are represented as separate elements of SP. The BP tones, which enter in a separate gene, are covering the range as gene alleles, which contain the genome of each gene. In the beginning, the chromosome model considers the like bitmap (matrix) of AMMI, but is influenced directly by the genetic operators on this matrix, undergoing a small change. The new created gene-chromosome structure simulates correctly the evolutionarily genetic field, because the chromosome contains the whole genetic information about each individual, so there is no need to push the matrix, which is only used for the chromosome estimation. The algorithm creates the matrix of individuals according to the genetic information contained within each chromosome, and which is evaluated by the optimization criteria. The simplified scheme of gene-chromosome structure is shown in Fig. 4.

The first step of the algorithm creates the initial population, which is based on the random variation of the SP pixels tones, and within the defined ranges limits, which allow creating different chromosomes within the developing population. The individuals of the initial population are estimated according the criteria (1) or (2). The evaluation results are used to perform "roulette" selection of the population. After selecting the evolved population happening under the influence of genetic operators "crossover" and "mutation", the new generation is created. The convergence of the

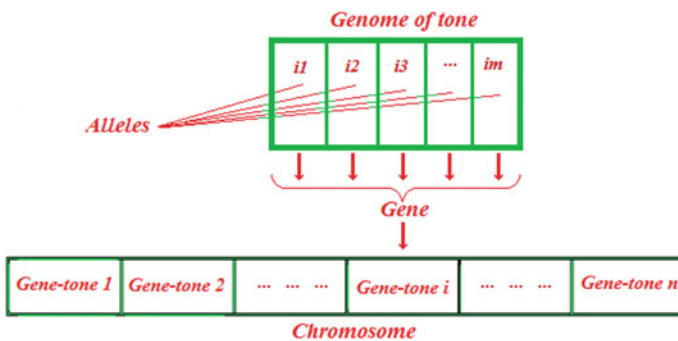


Fig. 4 Scheme of the gene-chromosome structure

algorithm is attainment for the last generation, and found quite simple and sufficient for motivating the current research.

The current research is aimed to understand the influence of the GA’s probability factors on the output results. Already stated in the previous work [1], the sub-optimal values of the quantity factors, from the standpoint of result/time has been reported. The algorithm modification, with quite predictable behavior of the quantity factors influence on the chosen values, is estimated to be sufficient, in order to validate the algorithm’s performance.

4 Image Approximation Based on Parametrical Sub-optimization of Genetic Algorithm

For the considered problem, the probabilistic component of modified GA consist of the four following parameters:

1. amplitude of initial SP— A_{sp} ;
2. crossover probability, defining the chromosomes gens recombination with probability P_{cross} ;
3. mutation probability, where each gene of chromosome changes with probability P_{mut} ;
4. amplitude of mutation— A_g , important in the case of mutation, where a gene changes in range of defined amplitude.

They are necessary to be defined in order to perform the full factorial experiment (FFE) with $n = 4$. The values and their level of variation have been chosen based on the experience acquired in the previous research on heuristic’s sphere, and are shown in Table 1.

The performed simulations consist of three experiments, which have different input OMMI for performing the image approximation, based on the industrial workplace pictures, called “Workplace-1”, “Workplace-2” and “Workplace-3”, having the resolution of 280×210 pixels (see Fig. 2).

Each experiment consists of 16 tests, where every test is repeated 30 times. The experiment’s structure is presented in Table 2.

Table 1 The factors value and their levels of variation

Factor	x1			x2			x3			x4		
	Variation of initial SP			Crossover probability			Mutation probability			Amplitude of mutation		
Level	max	mid	min	max	mid	min	max	mid	min	max	mid	min
Value	3	2	1	60	40	20	60	40	20	3	2	1
Symbol	+	0	–	+	0	–	+	0	–	+	0	–

Table 2 Matrix and results of optimization experiment of the Workplace-1 photo approximated with 2^4 pallet from 2^8 pallet

№	0	1	2	3	4	5	6	7	8
Factor	X1	-	-	-	-	-	-	-	-
	X2	-	-	+	-	-	-	+	+
	X3	0	-	+	-	+	+	-	+
	X4	0	-	-	-	-	+	+	+
Response	Y1	0.01528	0.01524	0.01526	0.01524	0.01527	0.01526	0.01539	0.01526
	Y2	0.01534	0.01525	0.01531	0.01526	0.01531	0.01530	0.01555	0.01530
	Y3	1.0E-09	3.8E-11	8.1E-10	1.0E-10	4.7E-10	5.2E-10	5.2E-09	4.4E-10
	Y4	3.2E-05	6.2E-06	2.8E-05	1.0E-05	2.1E-05	2.2E-05	7.2E-05	2.1E-05
№	0	9	10	11	12	13	14	15	16
Factor	X1	0	+	+	+	+	+	+	+
	X2	0	-	-	+	+	-	-	+
	X3	0	-	+	-	+	-	+	-
	X4	0	-	-	-	-	+	+	+
Response	Y1	0.01528	0.01524	0.01527	0.01524	0.01527	0.01525	0.01538	0.01526
	Y2	0.01534	0.01525	0.01531	0.01525	0.01532	0.01530	0.01556	0.01529
	Y3	1.0E-09	8.6E-11	6.0E-10	7.6E-11	5.7E-10	4.4E-10	8.0E-09	4.2E-10
	Y4	3.2E-05	9.2E-06	2.4E-05	8.7E-06	2.4E-05	2.1E-05	8.9E-05	2.0E-05

In the performed experiments evaluation for the graphic-approximation modification (GAM) of GA, the quality control is made in accordance to the following main parameters:

- y_1 —the best individual defined according the criteria (2), based on 30 parallel tests of the FFE line;
- y_2 —average value defined from the criteria (2), evaluated among the best individuals of FFE line;
- y_3 —dispersion of the best individuals based on the FFE line;
- y_4 —RMS of the best individuals based on the FFE line.

The above Table 2 with the performed experiment contains the output results for the Workplace-1 approximation. Under the same scheme the experiments for Workplace-2 and Workplace-3 are performed. The purpose of these experiments is to find out the influence of the FDB form on the GA parameters. The results of all three experiments are obtained in accordance to the main criteria (2), as shown in Table 3.

The FFE analysis, as shown in Tables 2 and 3, put in evidence that the best approximation (absolutely minimal deviation from OMMI), for the three quite different images, was obtained for T9 parameters (see Table 3, row 11). This represents a strong confirmation of the positive influence on the T9 parameters, which almost exclude the probability of the statistical error. For the point T9, the high level has only A_{sp} value. That has been predicted, because this parameter response directly to the genetic variety of the population, which according to the genetic point of view is always considered as one of the key factors indicating the successful population evolution.

Table 3 Results of experiments (minimal deviation from OMMI)

№ Test	$y_1(Workplace-1)$	$y_1(Workplace-2)$	$y_1(Workplace-3)$
T0	0.015288	0.015322	0.013876
T1	0.015249	0.015277	0.01382426
T2	0.015268	0.015302	0.013825
T3	0.015249	0.015277	0.013820
T4	0.015275	0.015317	0.013831
T5	0.015263	0.015278	0.013823
T6	0.0153930	0.0154540	0.014112
T7	0.0152630	0.0152740	0.01382452
T8	0.015383	0.015412	0.014370
T9	0.0152480	0.0152650	0.01382406
T10	0.0152760	0.0152810	0.013842
T11	0.0152480	0.0152750	0.013821
T12	0.0152730	0.0153000	0.013826
T13	0.0152580	0.0152800	0.013827
T14	0.015386	0.015473	0.014148
T15	0.0152600	0.0152800	0.013828
T16	0.0154030	0.0154800	0.014522

The other parameters of T9 are directed to the minimal side. Close to the accuracy of the T9 results, also characterized by the minimal value of the parameters p_{cr} , p_g and A_g . For the performed experiments, when considering the observed vector for these three parameters, it is required to perform an additional experiment, which has the center of plan close to T9. This modification will provide the possibility to find the sub-optimal parameters of the required probabilistic factors.

For all the three different images, the worsts results were obtained exactly in the same points of the experiment (T6, T8, T14 and T16), where the parameters p_{mut} and A_g are having their highest level. Therefore, this fact confirms the requirement that the search of the sub-optimal values of these factors has to be performed in their respective minimal value areas. In addition, this is influencing the stability of the designed algorithm, because these parameters are responsible for this common result in respect to the different images analyzed, and thus avoiding the absolutely random results.

For achieving a more concrete assessment on this influence for the approximation process optimization of the Workplace-1 we have obtained the mathematical model in the form of the regression equation $y(x_1, x_2, x_3, x_4)$:

$$\begin{aligned}
 y_{comp}(x_1, x_2, x_3, x_4) = & 0.0152934 + 0.00000056 \cdot x_1 + 0.00000081 \cdot x_2 \\
 & + 0.00003869 \cdot x_3 + 0.00003269 \cdot x_4 + 0.00000119 \cdot x_1 \cdot x_2 + 0.00000181 \cdot x_1 \cdot x_3 \\
 & + 0.00000006 \cdot x_1 \cdot x_4 + 0.00000056 \cdot x_2 \cdot x_3 + 0.00000031 \cdot x_2 \cdot x_4 \\
 & + 0.00002644 \cdot x_3 \cdot x_4 + 0.00000094 \cdot x_1 \cdot x_2 \cdot x_3 + 0.00000244x_1 \cdot x_2 \cdot x_4 \\
 & + 0.00000081x_1 \cdot x_3 \cdot x_4 + 0.00000006x_2 \cdot x_3 \cdot x_4 + 0.00000219x_1 \cdot x_2 \cdot x_3 \cdot x_4
 \end{aligned}
 \tag{3}$$

The above equation is for the experiment based on the OMMI Workplace-1 input. The regression equation of Workplace-2 and Workplace-3 has shown similar results. According to the regression equation, the largest influence was resulting from factors x_3 and x_4 , which is the confirmation of the conclusions early made.

Equation (3) is defined from the estimation of the response surface curvature created from the setting space parameters in order to find the minimum RMS area of AMMI from IMMI. This approach allows finding the antigradient direction (shortest path to minimum) from the partial derivatives in (3) according to the setting parameters x_j . The three additional steps, according to the antigradient direction, allow identifying the optimal area of the probabilistic factors, with the best RMS value around $3.05E-06$, for all the experiments. For that reason, the decision was taken to perform an additional experiment around this identified area.

In this additional experiment, the influence of A_{sp} , parameter will be fixed, by defining FFE with $n = 3$, as shown in Table 4.

This experiment is analogue to the previous one, except that there are 9 tests. As there is close results equality with the previous approximation for all the 3 images, only one experiment with the OMMI Workplace-1 input is performed.

The results analysis of this additional experiment shows that it is impossible to find the best point of the experiment with criteria y_j , because most of them have

Table 4 The factors value and their levels of variation

Factor	x_1			x_2			x_3		
	Crossover probability			Mutation probability			Mutation amplitude		
Level	max	mid	min	max	mid	min	max	mid	min
Value	20	15	10	20	15	10	2	1	1
Symbol	+	0	-	+	0	-	+	0	-

equal accuracy results estimated by the optimization criteria (2) as 0.015248. But according to criteria y_2 , y_3 and y_4 , the best point of the experiment is T8 (see Table 5, column 10). The analysis made, over all the experiments for OMMI Workplace-1, has shown that there no more accurate results are found. Thus, this one is considered as the extremum candidate, at least for the defined covering range of tones from SP.

By considering the found candidate for the extremum, it is required to add the new criteria for the GA’s search quality evaluation, as y_5 —the count % of results where $y_1 = 0.015248$. In addition, the new criteria shows that the best point of experiment is T8.

Based on the experiment results, the decision was to calculated the antigradient for the point T8 and perform the 2 steps for factors x_2 and x_3 , according to the received vector. The result of the calculation is the step with -1 for factor x_2 and 0 for x_3 .

The first step, according to y_5 has repeated the result of T8, but the second step has improved the percentage of extremum to 19% (see Table 6, column 6).

As mentioned before, every experiment is repeated 30 times. The analysis of the results from the implemented “steep descent” algorithm has shown that this algorithm is appropriate for finding the optimal (or possibly sub-optimal) solution of the OMMI approximation problem. Now, we can calculate the minimal number of parallel GA’s runs based on the found optimal parameters, which guarantee at least one optimal results with an acceptable probability (for example, three sigma).

The calculation of the required number of algorithm runs (every of them is independent) is defined according to the following formula:

$$N = \frac{\ln(1 - p_d)}{\ln(1 - p_o)} = \frac{\ln(1 - 0.9973)}{\ln(1 - 0.76)} \approx 4.1 \tag{4}$$

where p_d —is desired probability to find the extremum, p_o —probability to find extremum in the single run.

The number of parallel runs should be rounded up to a greater value, for example in our case $N = 5$, providing the high probability $P = 0.999204$.

For the validation of this algorithm 50 experiments have been conducted, where each of them was repeated 5 times. As expected, at least one optimum was found in all 50 of them. Overall, the number of repetitions (250) was negative 0.336%,

Table 5 Output results of additional experiment

N ^o	0	1	2	3	4	5	6	7	8	
Factor	X1	+	-	+	-	+	-	+	-	
	X2	+	+	-	-	+	+	-	-	
	X3	+	+	+	+	-	-	-	-	
Response	Y1	0.01524	0.01525	0.01524	0.015248	0.01524	0.015248	0.01524	0.01524	
	Y2	0.01525	0.01527	0.01527	0.015253	0.01525	0.015256	0.01525	0.01525	
	Y3	3.0E-11	2.7E-10	6.3E-10	2.77E-11	2.56E-11	7.05E-11	5.16E-11	1.01E-11	4.51E-12
	Y4	5.5E-06	1.6E-05	2.5E-05	5.26E-06	5.06E-06	8.39E-06	7.18E-06	3.18E-06	2.12E-06
	Y5	0.20	0.00	0.00	0.13	0.27	0.03	0.03	0.50	0.57

Table 6 Results of the additional steps

№ Step	y_1	y_2	y_3	y_4	y_5
SI	0.015248	0.0152507	1.57E-11	3.96E-06	0.57
S2	0.015248	0.0152494	9.08E-12	3.01E-06	0.76

indicating that the actual probability of obtaining a positive result after 5 repetitions for this experiment was 0.9957.

5 Conclusion

The proposed conceptual and mathematical model of the modified GA's has proven to be an extremely effective tool (when ranges are fixed) for the optimization of the MMI approximation process.

It is suggested to modify the model by including the number of variable settings in order to better cover the ranges of each separate gene.

There is an idea that such modification of GA will enable to have a solution when performing the “absolute” optimization process of AMMI, i.e. fulfilling the minimal deviation from OMMI.

References

1. Aghajanyan A, Neydorf R (2016) Optimization of monochrome multitone images approximation based on evolutionarily algorithm. Omega Science, Ufa, pp 11–17 <http://os-russia.com/SBORNIKI/KON-108-3.pdf>. Accessed 18 Dec 2016
2. Plonka G, Tenorth S, Rosca D (2010) A new hybrid method for image approximation using the easy path wavelet transform. IEEE Transactions on Image Processing. doi:10.1109/TIP.2010.2061861
3. Figueras R, Simoncelli E (2007) Statistically driven sparse image approximation. IEEE International Conference on Image Processing. doi:10.1109/ICIP.2007.4378991
4. Neydorf R, Derevyankina A (2010) The solution of multiextreme problems by the swarm sharing method. Vestnik DSTU. http://vestnik.donstu.ru/apex/f?p=381:39:1356694059628:::NO:P39_FILE_ID:2606925204771278. Accessed 28 Dec 2016
5. Neydorf R, Derevyankina A (2010) Solving the recognition problems with particle swarm method. Izvestia Sfedu. <http://izv-ti.tti.sfedu.ru/?p=13537>. Accessed 22 Dec 2016
6. Mitchell M (1999) An introduction to genetic algorithms. MIT Press, Massachusetts
7. Luke S (2014) Essentials of metaheuristics. Lulu, USA
8. Bäck T (1996) Evolutionary algorithms in theory and practice—evolution strategies, evolutionary programming, genetic algorithms. Wiley, New York
9. Lewin B (2012) Genes. Binom, Russia

“Cut-Glue” Approximation Method for Strongly Nonlinear and Multidimensional Object Dependencies Modeling

Rudolf Neydorf, Anna Neydorf and Dean Vučinić

Abstract The main difficulties in modeling a variety of technical systems are experienced when creating appropriate mathematical objects to simulate their behavior. It is well known that such inter-objects dependences are defined with their variable with strong nonlinear and multidimensional characteristics. The mathematical models (MM) dependences are approximated with advance numerical methods, such as polynomial decomposition, spline functions, etc., which are today still very time-consuming and laborious to be correctly created and applied, also considering their precision. In this paper, the authors have created and investigated the high-precision analytical approximation method to model the nonlinear MM dependences, which are defined only by appropriate analytical functions. These approaches have been already studied in details, where the Cut-Glue approximation method defines 1-dimensional dependences, and to 2-dimensional dependences were approximated with analytical functions of 2 arguments. The important advantage of the Cut-Glue method is that it well approximates the differentiability of the proposed MM dependencies, as its enables to investigate analytically the related modeling functions and thus, use them efficiently in applying MM in dynamical systems simulations. In this work, the Cut-Glue method has been further developed: (1) to prove its applicability by creating nonlinear models of any dimension, (2) to analyze its performance at all the stages, in which the “Cut-Glue” approximation is applied, and (3) to implement this formal algorithm, which allows numerical verification and validation of its applicability. The considered optimization criteria for both respective issues, accuracy and complexity, have been applied to the investigated MM-s. The proposed method is formalized by the optimal splitting of its experimental dependence into separate parts, which are then

R. Neydorf (✉) · A. Neydorf
Don State Technical University, Rostov-on-Don, Russia
e-mail: ran_pro@mail.ru

A. Neydorf
e-mail: neydan@yandex.ru

D. Vučinić
Vrije Universiteit Brussel, Brussel, Belgium
e-mail: dean.vucinic@vub.ac.be

numerically defined and implemented within the proposed software, developed in this work. In this paper, the different possibilities of applying the optimal multi-dimensional “Cut-Glue” approximation method are illustrated by examples. The achieved results represent a strong base to significantly expand the proposed method applicability, and further on, they indicate potential opportunities to improve the existing solutions. Especially, when solving a variety of problems, which requires mathematical modeling of any type of technical objects, to simulate overall systems dynamics.

Keywords Optimization · Approximation · Mathematical modeling · Experimental data · Heuristic methods · Particle swarm optimization

1 Introduction

The experimental creation of the mathematical models (MM) of various processes, objects, systems, etc. requires information on the involved research object, which are described with data having a certain structure. The general structure of the experimental data for the created MM is represented with the K records, containing 2 lists: (1) entrances (x_1, \dots, x_n) and (2) exits (y_1, \dots, y_m) . Such structure implies that K is the number of the experiment tests, x_i is the independent variables, y_j —dependent variables. The dependency modeling of the static variables of MM means that each output of y_j is the function of inputs (x_1, \dots, x_n) . In this case, each dependency is defined with a function φ_j , and general MM is defined by the Y vector function:

$$\left. \begin{aligned} y_j &= \varphi_j(x_1, \dots, x_n), \quad j = \overline{1, m}; \\ Y &= \Phi(x_1, \dots, x_n) = (y_1, \dots, y_m)^T. \end{aligned} \right\} \quad (1)$$

In addition to the general structure of the experimental data, it is necessary to consider their internal structure. When carrying out a passive experiment, this structure can be order-less, which means that the entrance data lists are formed in a random way, and are not connected with each other, thus through defined dependencies. When carrying out the experiment, usually, the input data are built on the regular basis. Then, n - ki (the vector or the sequence having n elements) of input variables is connected by the internal dependency, where their values and change of variables acquire a quite regular character. Most often, the so-called coordinate-wise principle for the variables variation in an experiment is used. The example of such an experiment creation is given in Table 1.

In this case, the force F_x of the side offset of the airship is the output variable, which is interesting to the researcher performing the experiment. The experimental results indicate that there is an influence on this force, which is coming from certain airship flight parameters, which are: height h , angle of heel α , and airship takeoff

Table 1 The dependences of the strength of the lateral airship displacement resulting from the flight parameters

Speed of rise	Altitude of fly	Angle of heel, α , angle degree					
		0	15	30	45	60	75
$v, m/s$	h, km	$F(h), kN$					
2.5	0	0.086	11.90	19.26	21.89	9.491	3.625
	5	0.050	6.996	19.12	13.03	5.422	2.871
	10	0.027	4.193	10.39	7.234	3.081	2.513
	15	0.012	1.957	4.707	3.382	1.435	0.720
4	0	0.224	30.19	46.28	57.61	22.88	12.44
	5	0.132	20.44	47.45	33.85	14.27	9.331
	10	0.071	12.30	27.24	18.54	8.056	5.605
	15	0.032	5.010	11.37	8.684	3.530	2.061
5	0	0.366	35.65	87.22	87.99	36.68	25.84
	5	0.208	26.47	67.39	52.48	23.09	17.01
	10	0.113	22.48	42.77	28.84	12.30	8.501
	15	0.051	7.841	17.72	13.77	5.482	2.238
6	0	0.550	61.54	119.43	127.3	58.23	37.38
	5	0.300	36.71	96.68	77.62	32.76	22.34
	10	0.166	22.96	60.82	41.88	19.97	11.48
	15	0.074	11.35	25.56	19.89	8.192	4.371
7.5	0	0.894	80.35	180.3	185.4	92.46	55.31
	5	0.480	79.17	133.1	123.3	50.86	27.49
	10	0.261	42.74	84.90	66.40	28.04	24.42
	15	0.117	18.24	44.90	30.76	13.34	8.445

speed v . These parameters are acquired from the flight experiment through the limited number sequences. As a result, for 2-dimensional dependences, it is possible to use the matrix-vector data representation. However, for 3-dimensional data, as an example given in Table 1, it is necessary to define a 3-dimensional matrix, to represent its structure. In general, these data can be displayed only by several matrixes, having chosen the fixed 3rd parameter for each matrix. Such data are presented in Table 1: 5 matrixes of dimension 4×6 —with varying h and α , and with 5 values of speed. It can be noted that the smooth structure of the approximated dependences doesn't create difficulties when applying the mathematical methods.

However, this approach can be significantly more difficult when the data is not smooth, and has a fragmentary structure. The “fragmentary structure” has a piecewise nature, where the mutual change of the specific arrangement is represented with the pointwise data, making it possible to allocate certain sites (the differing sites of the approximation surface) with the obvious dependency, where the fragments can have significantly various inclinations through their contact lines. The example of the “fragmentary structure” of dependences is quite well illustrated

by the data shown in Table 1. The tabulated or matrix representation does not always allow estimating this characteristic, while the graphic form, as presented in Fig. 1, made this property more visible.

In these cases, the applied various methods are capable to fulfill the required accuracy, which guarantee the sufficient condition to have a solvable task, thus to receive the mathematical description for such nonlinearities. The piecewise approximation [1–3], in which dependence fragments are accepted as “pieces”, is quite the simplest and the most efficient manner to cope with a problem of the data fragmentation. This method is applicable for any required approximation accuracy, but unfortunately, it has an important shortcoming. The discontinuities of the derivatives, arising on the lines, which are joining the fragments, are not defined as the analytical transformations of the related approximations. In that case, the spline approximation is more effective and closest to the piecewise approximation, for the mathematical description of the essential nonlinearities [4–6]. However, this approach considerably complicates the MM analytical transformation.

The regression analysis [7–10], the numerous methods applying special polynomial decompositions [11–13], radial basis functions [14–16], etc. are related to them. However, these methods are not adapted to approximate the piecewise dependences, as they do not provide sufficient accuracy [7–13], or they are focused on the description and representation of the graphical images [14–16].

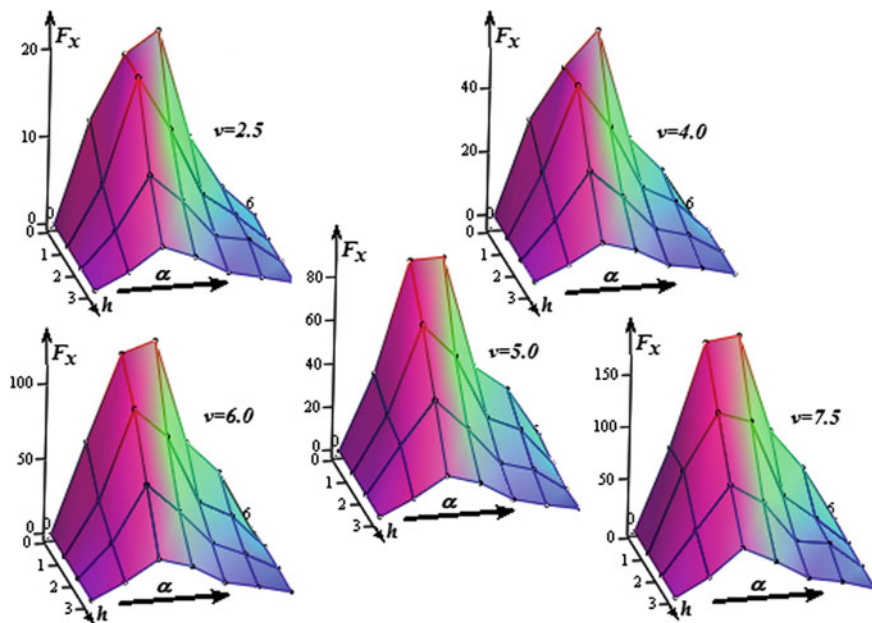


Fig. 1 2-dimensional fragments for arguments $-\alpha$, defined for $4h$ values defining 3-dimensional piecewise experimental dependences

2 Basic Provisions and Boundaries for Application of “Cut-Glue” Approximation

For elimination of the specified shortcomings the cut-glue approximation method has been developed [17–19]. The method allows presenting the piecewise dependences with one analytical function, which has an additive structure consisting of multiplicative members. These members perform the multiplication of 2 functions: (1) the function approximating some fragment (FAF) of dependence, and (2) the function, which multiplicatively is cutting out this fragment (MCF).

The multiplication of FAF and IMF provides two results: (1) the FAF values within the fragment borders remain almost invariable, (2) all values of the multiplicative member behind the “cut-out” fragment borders become almost zero. The obtained result is the interval, which is isolating the analytical function (IIF) [17, 18]. The analytical property of IIF enables the algebraic addition of the multiplicative members, having the smooth piecewise dependency approximation with the improved accuracy, peculiar to IIF. At the same time, the coefficient of the parametrical identification ε , which is one of the MCF arguments, allows in addition, to adjust the general accuracy of the approximation. This function represents the united approximating function (UAF), which mathematically describes all the experimental data. At the same time, the coefficients of the parametrical identification ε , as arguments of MCF, in addition, allow to adjust the accuracy of the approximated data with the use of UAF.

In articles [17, 18], the bases of the cut-glue approximation for the solution of 1-dimensional tasks are developed. In article [19] this method is generalized for the 2-dimensional case. Often, there is a need to approximate the multidimensional dependences [1, 4, 9, 10, 19–24]. For example, the strength properties of the composite materials depend both, on the concentration of components, and on technological parameters of their production [26–28]. The positioning of the robot multilink working body is also described by multidimensional nonlinear dependences. For some positions, the relative bodies positioning has a discontinuity in their mathematical description [23, 29, 30]. In order to finalize the solution in a case of the nonlinear object control, only the mathematical model description is not sufficient, as it needs to contain the analytical functions to describe its dependencies, which synthesize the control law this object [30, 31, 32].

For example, in work [22], a similar dependence is represented as in Fig. 1 for the 2-dimensional MM, which is received from the cut-glue approximation. The model describes the communication of the airship moment from the side heel, with the climbing speed (v , m/s) and with angle of the heel (α , angular degrees). However, the dependence is 3-dimensional, as illustrated in Table 1, and shown with the 3D images in Fig. 1, where this dependence has the 3rd state variable—flight altitude (h , km), which is added up to the 2 already specified state variables. The 2-dimensional cuts of the modelled dependence are constructed in Fig. 1, and have obvious breaks along the dividing lines. The nature of dependence change is not resulting from the experiment error. It is caused by the breakaway of the air

stream, which flows around the airship at certain combinations of v , α and density of air, largely depending on h . In operation [22] it was succeeded to describe such dependence function of 2 variables, with fulfilling the acceptable accuracy, only by the cut-glug approximation. To define a similar dependence, by involving 3 variables, is becoming a much more complex problem. Therefore, to solve the 3-dimensional problem, it is necessary to adapt the “cut-glug” approach to find a solution for the bigger dimension problem.

3 Problem Formulation

In this article, the possibility to define the mathematical description and the related experimental dependences for any n -dimension, by applying the “cut-glug” approximation method, as developed in [17–20] is analyzed. In other words, it is necessary to assert the general approach for the creation of the uniform analytical differentiable function, which can describe any nonlinear dependence, including the discontinuous derivatives. According to the “cut-glug” approximation, the method has to be realized with use of the multiplicative “cutting out” of n -dimensional fragments, modeled with the n -dimensional surface. The fragments need to have the general mutual borders, providing the full range coverage of the approximated dependences. The general uniform MM with the approximated dependences has to associate the created fragments by applying the algebraic summation.

4 Experimental Fragmentation of Multidimensional Strongly Nonlinear Dependencies

The process of the fragmentation is connected with the sufficient allocation of smooth sites dependence to each coordinate. This process is very difficult, as in many cases the dependence curvature can significantly change, due to the variation influenced with other coordinates. Such property of the multidimensional dependences is well visible in the 3D images, as shown in Fig. 1.

Usually, such dependences are dividing intervals, based on the respective variable. To make it more visual appealing in the multidimensional case, even for 3-dimensional dependence, it is quite difficult to achieve it. For example, the above described 3-dimensional dependence $F_x(v, h, \alpha)$, is illustrated in Table 1 by numerical values, and shown in Fig. 1. It is demonstrated by the 3D—projections, which are constructed in the plane of arguments $h - \alpha$. The smooth curvature of the F_x dependency on the h argument, and the existence of breaks with the extremum are well visible for the same dependency on an argument α . However, it is difficult to estimate the nature of its curvature depending on the v argument.

It is possible to reconstruct the table and 3D-projections in the plane with the $v - \alpha$ arguments, in order to achieve the visual assessment. Then, the 3D-projections of $F_x(v, h, \alpha)$ are done on this plane and for the matrixes, and by fixing h it is possible to estimate the nonlinearity influence of h on F_x . Besides that, during the regular creation of the coordinates grid, the experiment entrance data can be submitted as a multidimensional matrix. Thus, the data of Table 1 can be submitted by a 3-dimensional matrix, which sides are 2-dimensional matrixes, as shown in Fig. 2. However, both procedures are quite cumbersome. With the increase of the model dependencies dimension the complexity of the assessment of its properties in the factorial space, and respectively, the complexity of the fragmentation is increasing rapidly. Due to the revealed features of the fragmentation procedure for the experimental data with the multivariate dependences (for $n \geq 3$) it is worth to notice that the relevance of automation of the fragmentation procedure is an important software part. Without such software support, the cut-glue dependency approximation for 3 and more variables would not be achievable.

Despite the specified difficulties, for the presented multidimensional application of the “cut-glue” approximation for the 3-dimensional mathematical model with the $F_x(v, h, \alpha)$ dependency, resulting from the experimental data given in Table 1, has been defined and solved.

The 3-dimensional matrix in Fig. 2, where the red rectangles show the projections of the selected 3-dimensional fragments to « $v - \alpha$ », « $h - \alpha$ » and « $v - h$ » planes (front, top and side of the 3-dimensional data matrix). The analysis of such

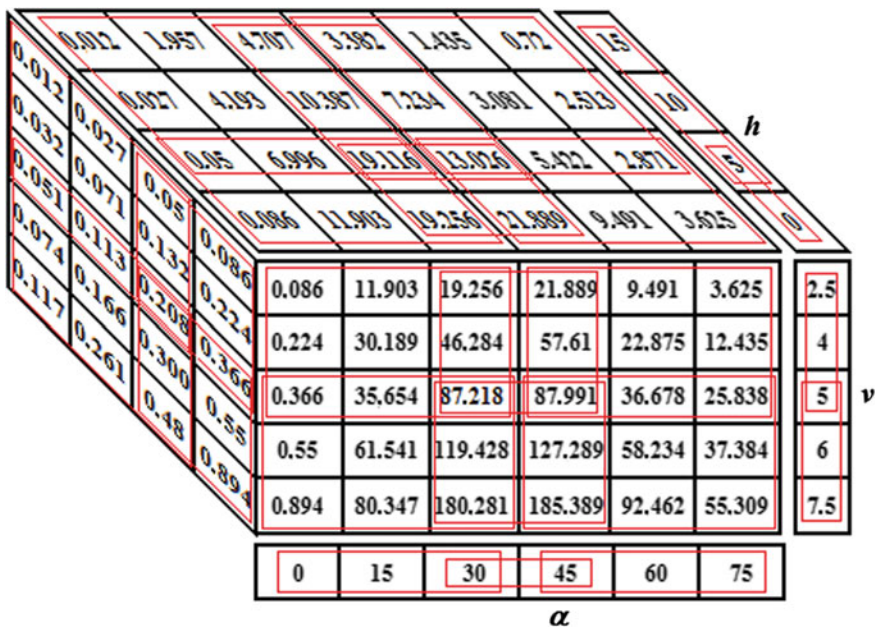


Fig. 2 3-dimensional fragmentation of the 3-dimensional piecewise experimental dependency

configurations for the allocated sub-matrixes shows that the presence of the coinciding peripheral areas, at the adjacent fragments, is in general having very low fragmentation. The dimension of a bordering subspace is always one dimension less than the dimension of the adjoining subspaces encompassing such multidimensional space of the basic data. The 2-dimensional surfaces (parallelograms) for the next 3-dimensional fragments (parallelepipeds) are coinciding. The 1-dimensional edges (intervals) of these parallelograms and 0-dimensional boundary points of these intervals are coinciding too.

The fragmentation of the data matrix is a consequence of the fragmentation of the vectors, which are constructed from the arguments values, which varied in an experiment to certain levels. In this case, the input variables vectors of an experiment $\vec{x}_i, i = \overline{1, n}$ are represented by a set of subvectors.

$$\vec{x}_i, i = \overline{1, n}, j = \overline{1, n_i}, \quad \text{where } \vec{x} = \begin{pmatrix} x_1 \\ \dots \\ x_n \end{pmatrix}; \quad \vec{x}_i = \begin{pmatrix} x_{i_1} \\ \dots \\ x_{i_{n_i}} \end{pmatrix}. \quad (2)$$

In the fragmentation option presented in Fig. 2, these sub-vectors are defined as follows:

$$\vec{x}_1 = \vec{h} = \begin{pmatrix} \vec{h}_1 \\ \vec{h}_2 \end{pmatrix}; \quad \vec{x}_2 = \vec{v} = \begin{pmatrix} \vec{v}_1 \\ \vec{v}_2 \end{pmatrix}; \quad \vec{x}_3 = \vec{\alpha} = \begin{pmatrix} \vec{\alpha}_1 \\ \vec{\alpha}_2 \\ \vec{\alpha}_3 \end{pmatrix}; \quad (3)$$

$$\vec{h}_1 = \begin{pmatrix} 0 \\ 5 \end{pmatrix}; \quad \vec{h}_2 = \begin{pmatrix} 5 \\ 10 \\ 15 \end{pmatrix}; \quad \vec{v}_1 = \begin{pmatrix} 2.5 \\ 4.0 \\ 5.0 \end{pmatrix}; \quad \vec{v}_2 = \begin{pmatrix} 5.0 \\ 6.0 \\ 7.5 \end{pmatrix}; \quad \vec{\alpha}_1 = \begin{pmatrix} 0 \\ 15 \\ 30 \end{pmatrix};$$

$$\vec{\alpha}_2 = \begin{pmatrix} 30 \\ 45 \end{pmatrix}; \quad \vec{\alpha}_3 = \begin{pmatrix} 45 \\ 60 \\ 75 \end{pmatrix}. \quad (4)$$

Thus, the 3-dimensional dependency data, provided in Table 1, are divided into 12 3-dimensional fragments of the experimental data (FED) represented, generally as parallelepipeds.

The further implementation stage, of the cut-glue approximation method, consists in approximating each FED by an analytic function of N - (in this case 3-) variables. The data approximation shall provide the required accuracy, which is set for such solvable data domain task, and within the respective fragment. This function is called above FAF, and behind a fragment borders the FAF values can be any, but excepting to support the exponential growth to infinity. As the method applies the polynomial equations of the regression, such property for FAF is not applicable.

5 Multidimensional Approximation of Fragments for Experimental Dependences

According to the paradigm of the cut-glue approximation method [17–19, 22], the approximation in each fragment is selected for all the experimental data of n -dimensions in the second stage of the method. The approximation of the fragments is defined with the analytical FAF of n -arguments $\vec{x} = (x_1, \dots, x_n)'$. The defined n -FAF functions $y_{(i_1, \dots, i_n)}$ receive the approximated fragments. They are identified with n -tuplets indices, which indicate the fragment contribution in the R^n —space— (i_1, \dots, i_n) :

$$y_{(i_1, \dots, i_n)} = \varphi_{(i_1, \dots, i_n)}(\vec{x}). \tag{5}$$

where i_j is the number of the fragment interval on x_j axis.

The fragments partition of variables \vec{x}_i is defined by formulas (2)–(4). For example, the fragment (2,1,3), and function— $y_{(2,1,3)}$ mean that the fragment receives the input from the intervals: [5,15] for h , [2.5,5.0] for v and [45,75] for α . The receiving FAF uses the classical regression analysis to approximate experimental data with the specified polynomial degree. Therefore, in the presented example, the 12 polynomial equations have to be resulting from this second stage. The order and structure of each equation is defined by the number of data entering to ‘FED’, and by the accuracy imposed by the studied subject domain. Since, for the creation of the regression equations, the standard software algorithms, sometimes called standard software packages, are used. Thus this aspect in this article is not considered. After receiving all the FAF-s (as described in the example: $y_{(1,1,1)}$ — $y_{(2,2,3)}$) it is possible to progress with the realization of the 3rd stage of the cut-glue approximation method. This stage is the creation of the interval-isolated functions (IIF). For this purpose, and according to the CGA paradigm, the specially designed functions—MCF—are defined. They have a number of unique mathematical properties. Therefore, first of all, the structure and properties of MCF, which depend on the application domain—structure and properties of the received FAF are considered.

6 Multiplicative Cutting-Out Function, Its Types and Properties

The kernel of the multiplicative method, when isolating a 1-dimensional fragment (a jog) of FAF on the x_j axis, consists in the multiplication of the FAF with the special 1-dimensional MCF (1-MCF) [17, 18], which has the following form:

$$\lambda_{j_i}(x_j, x_{j_{i-1}}, x_{j_i}, \varepsilon) = 0.25 \cdot \sigma_l(x_j, x_{j_{i-1}}, \varepsilon) \cdot \sigma_r(x_j, x_{j_i}, \varepsilon) / \delta(x_j, x_{j_{i-1}}, x_{j_i}, \varepsilon), \quad (6)$$

where

$$\begin{aligned} \sigma_l(x_j, x_{j_{i-1}}, \varepsilon) &= x_j - x_{j_{i-1}} + \sqrt{(x_j - x_{j_{i-1}})^2 + \varepsilon^2}; \\ \sigma_r(x_j, x_{j_i}, \varepsilon) &= x_{j_i} - x_j + \sqrt{(x_{j_i} - x_j)^2 + \varepsilon^2}; \\ \delta(x_j, x_{j_{i-1}}, x_{j_i}, \varepsilon) &= \sqrt{\left[(x_j - x_{j_{i-1}})^2 + \varepsilon^2 \right] \cdot \left[(x_{j_i} - x_j)^2 + \varepsilon^2 \right]}. \end{aligned}$$

The multiplicative function has the following form

$$\lambda_{(i_1, \dots, i_n)}(\vec{x}, \vec{x}_{(i_1-1, \dots, i_n-1)}, \vec{x}_{(i_1, \dots, i_n)}, \varepsilon) = \prod_{j=1}^n \lambda_{j_i}(x_j, x_{j_{i-1}}, x_{j_i}, \varepsilon) \quad (7)$$

and represents the pulse in space of R^{n+1} . The pulse amplitude approaches to 1 inside a fragment, and behind the fragment boundaries, the value of n-MCF is almost equal to 0.

Thus, expression (7) represents the n-dimensional MCF, or n-MCF. According to the cut-glu approximation method [19, 22], and by using n-FAF (8) and n-MCF (7), and with applying the multiplicatively construct for the n-dimension IIF, called n-IIF, as follows:

$$f_{(i_1, \dots, i_n)}(\vec{x}) = \varphi_{(i_1, \dots, i_n)}(\vec{x}) \cdot \lambda_{(i_1, \dots, i_n)}(\vec{x}, \vec{x}_{(i_1-1, \dots, i_n-1)}, \vec{x}_{(i_1, \dots, i_n)}, \varepsilon). \quad (8)$$

The functions 1-MCF and 2-MCF are developed and investigated in articles [18, 19], and have a number of important properties. The functions n-MCF has these properties too. A number of quantitative characteristics of these properties depend on the IMF dimension. Besides, depending on the space dimension, the new properties are added. Therefore, the full set of the inherited and new n-MCF properties is given below.

6.1 Properties of n-MCF

(1) Function (7) is symmetric in the middle of the approximated fragment range

$$\vec{x}_{i0} = \left(\frac{x_{i_{i-1}} + x_{i_1}}{2}, \dots, \frac{x_{i_{j-1}} + x_{j_i}}{2}, \dots, \frac{x_{i_{n-1}} + x_{i_n}}{2} \right). \quad (9)$$

(2) Function (7) has only the maximum in a point \vec{x}_{i0} depending on a set of its adjusting parameters $\{x_{j_{i-1}}, x_{j_i}, \varepsilon_j | j \in [1, n]\}$ and 0 infimum in such set, as follows:

Table 2 The boundary values on the MCF borders for various functions dimensions

n	1	2		3		
Border	Curve segment	Polygon side	Polygon vertex	Polyhedron face	Polyhedron edge	Polyhedron vertex
Value	0.5	0.5	0.25	0.5	0.25	0.125

$$\vec{X}_0 = \left\{ \vec{x} \mid \sqrt{x_1^2 + \dots + x_n^2} \rightarrow \infty \right\}. \tag{10}$$

(3) With reduction of the adjusting parameter ε , the functions (8) can accept the value, as much as close to 1 in any range $[\vec{x}_{i-1}, \vec{x}_i]$ set as follows:

$$\forall \vec{x}, \vec{x}_{i-1}, \vec{x}_i : \vec{x} \in]\vec{x}_{i-1}, \vec{x}_i[\rightarrow \lim_{\varepsilon \rightarrow 0} \lambda_{(i_1, \dots, i_n)}(\vec{x}, \vec{x}_{(i_1-1, \dots, i_n-1)}, \vec{x}_{(i_1, \dots, i_n)}, \varepsilon) = 1. \tag{11}$$

(4) Function (7) in the ranges $[-\infty, (\vec{x}_{i-1})]$ and $[(\vec{x} - \vec{1}), \infty]$ can accept value extremely close to 0 as follows:

$$\forall \vec{x}, \vec{x}_{i-1}, \vec{x}_i, \varepsilon : \vec{x} \notin [\vec{x}_{i-1}, \vec{x}_i] \rightarrow \lim_{|\vec{x}| \rightarrow \infty} \lambda_{(i_1, \dots, i_n)}(\vec{x}, \vec{x}_{(i_1-1, \dots, i_n-1)}, \vec{x}_{(i_1, \dots, i_n)}, \varepsilon) = 0 \tag{12}$$

- (5) Function (7) allocates the n -dimensional parallelepiped in the R^n space. Values of the IMF (7) at the border sides, edges, which are parts, tops and so forth of this n -dimensional parallelepiped, aspire at $\varepsilon \rightarrow 0$ to the sizes depending only on n . For $n = 1, 2, 3$ the limits for the border values are given in Table 2.
- (6) Use of IMF (7) in formula (8) provides the approach to $f_{(i_1, \dots, i_n)}(\vec{x})$ to $\varphi_{(i_1, \dots, i_n)}(\vec{x})$ with any accuracy depending on ε (except regional sides, edges and tops).
- (7) The function (10) is infinite number of times continuously differentiated, as well as any function with the fractional exponent of degree.

7 Illustrative Example Creating IIF with FAF and MCF

For the descriptive reasons the graphic representation of the 2-dimensional approximation is considered. FAF of the fragment with the experimentally modeled dependency is described by the polynomial function of the 3rd order, and received by the KRA method having 2 arguments:

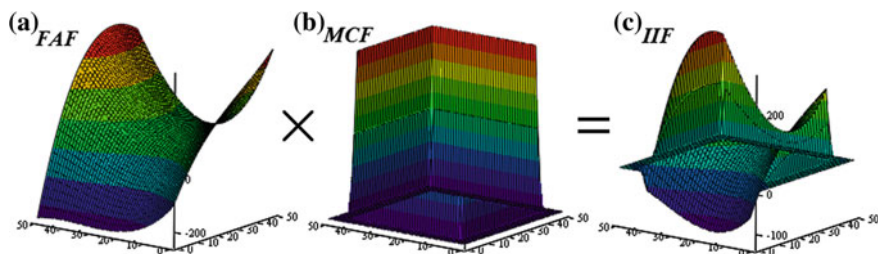


Fig. 3 Illustrate “cuttings” IIF from FAF by means of IMF; **a** FAF—analytical function approximation of fragment; **b** MCF—multiplicative cutting out function of fragment; **c** IIF—“isolated” function, describing only the fragment

$$z(x, y) = -108.91 - 66.87 \cdot x + 87.59 \cdot y + 10.5 \cdot x^2 - 3.25 \cdot x \cdot y - 7.741 \cdot y^2 - 0.52 \cdot x^3 + 0.98 \cdot x^2 \cdot y - 0.89 \cdot x \cdot y^2 + 0.37 \cdot y^3. \quad (13)$$

Its 3D image is shown in Fig. 3a. The borders of the fragment are determined by the intervals [5,45] with scales indicated on the horizontal axes. According to the drawing, it is visible that behind the fragment borders, the value of the approximating function, at the left and on the right is sharply increasing, and in the left frontal plane—sharply decreasing. However, it does not violate the conditions defining the FAF properties since function (13) is the polynomial. For “cutting out” the isolated IIF from FAF, the MCF is constructed by the use of formulas (6) and (7). This function has a parallelepiped representation, with top almost equal to 1 at the fragment borders, and almost 0 values outside these borders, see Fig. 3b. The horizontal axes in the 3D image are perpendicular to the paper page, i.e. the figure is shown as seen from the front and from below. The vertical axis is hidden behind IMF.

In Fig. 3, the multiplication of FAF and IMF allows to receive IIF—a basic element of “cut-glue” of approximation—are shown.

8 Additive Join of the Interval Isolating Functions into the Approximation United Function

The last stage of the cut-glue approximation method of n -dimensional data is to join the fragments constructed as IIF into one EAF function. Its role consists to approximate experimental data in the form of the analytical function—as united whole. The big advantage of this method is that such assembly is carried out by simple algebraic addition. The only condition to enable such combining is the explicit form of the output variable for all the IIF functions, which require the explicit form of their multiplicative components: FAF and IMF. The structure of

IMF is defined by formula (6), which is explicit form of the relatively $\lambda_{j_i}(\ast)$ function. The choice for FAF, to have the polynomial structure, provides its explicit character. Therefore, the EAF function completing the cut-gluе approximation method can be defined as follows:

$$f(\vec{x}) = \sum_{i_1} \dots \sum_{i_n} f_{(i_1, \dots, i_n)}(\vec{x}). \tag{14}$$

In other words the IIF “f” functions $f_{(i_1, \dots, i_n)}(\vec{x})$ are added together coordinate-wise, and according to the coordinate-wise numbering of the fragments. The additive formation of EAF naturally inherits all the IIF properties, and, first of its analytical form, is the most important property of the “cut-gluе” approximation method.

9 Illustrative Example of 3-Dimensional “Cut-Glue” Approximation Solution

The “cut-gluе” approximation solution for the 3-dimensional data is given in Table 1 below. The full volume of the dependency data for the F_x force—the airship side shift—depends on the three flight parameters given in Table 1 angle of heel α , heights h and speed of its climbing velocity v is too complex for the demonstration of the approximation procedure to be put in this article. Therefore, the most important part of the studied characteristic containing its “hump”, which is well visible in all the 5 3D-images shown in Fig. 1. Therefore, the most important part of the studied characteristic containing its “hump” requires fragmentation of the all the dependences, which require, at least 12 fragments. In this article, 4 fragments are described, as found to be the most important for covering the operational properties of the airship flight: $\alpha \in [0,60]$, $h \in [5,15]$, $v \in [2.5,7.5]$.

The data in Table 1 of the appointed range are highlighted in gray. The dependency form as shown in the 3D-images of Fig. 1, indicates that the fragmentation is done for coordinate α covering two adjacent subranges: $[0,30]$ both $[30,60]$, and v coordinate covering two adjacent subranges: $[2.5,5.0]$ and $[5.0,7.5]$. The regrouping of data for the 4 selected fragments has allowed constructing Table 3.

The data for each fragment in Table 3 are processed by the CRA mathematical method, which receives polynomials of the second and third order. The approximation of the fragments with the polynomials of the second order leads to too high approximation error of the experimental points, respectively for the described fragments: 1–8%, 2–8.1%, 3–5.7%, 4–12.3%. The approximation of the same data polynomials of the third order provides approximately twice higher precision: 1–4.1%, 2–5.7%, 3–2.6%, 4–5.1%. Further increase in the accuracy applying the polynomial approximation is only possible by applying special methods, since the

number of data for each fragment is equal to 27. The size of the full polynomial of the third order makes 20 members, and the size of the full polynomial of the fourth order makes 35 members. Therefore, further increase in accuracy of the approximation by increasing the polynomial order is impossible, and in this example, the order of the approximation is limited to the third order with the worst accuracy of 5.7%, as determined by the third fragment. Thus, FAF for all the fragments has an identical structure:

$$F_x^p(x) = \beta_0^p + \sum_{i=1}^3 \beta_i^p \cdot x_i + \sum_{i=1, j=1}^3 \beta_{ij}^p \cdot x_i \cdot x_j + \sum_{i=1, j=1, k=1}^3 \beta_{ijk}^p \cdot x_i \cdot x_j \cdot x_k; k = \overline{1,4}. \quad (15)$$

The 3-dimensional 3-MVF is constructed, as shown above, on the base of 1-MCF with the intervals, which are predefined. According to the structure of n-IMF, and according to formula (7) all four 3-MCF for the isolated fragments are defined by the common expression, having the following form:

$$\lambda_{(i_1, i_2, i_3)}(\vec{x}, \vec{x}_{(i_1-1, i_2-1, i_3-1)}, \vec{x}_{(i_1, i_2, i_3)}, \varepsilon) = \prod_{p=1}^3 \lambda_{p_i}(x_p, x_{p_{i-1}}, x_{p_i}, \varepsilon), \quad (16)$$

here $i_1 = \overline{1,2}; i_2 = 1; i_3 = \overline{1,2}; \vec{x} = (x_1, x_2, x_3)'; x_{1_{10}} = 0^\circ; x_{1_{11}} = x_{1_{20}} = 30^\circ; x_{1_{21}} = 60^\circ; x_{2_{10}} = 5.0 \text{ km}; x_{2_{11}} = 15.0 \text{ km}; x_{3_{10}} = 2.5 \text{ m/s}; x_{3_{11}} = x_{3_{20}} = 5.0 \text{ m/s}; x_{3_{21}} = \text{m/s}.$

The applied IIF of the fragments are defined according to Eq. (8), as follows:

$$f_{(1,1,1)}(\vec{x}) = \varphi_{(1,1,1)}(\vec{x}) \cdot \lambda_{(1,1,1)}(\vec{x}, \vec{x}_{(0,0,0)}, \vec{x}_{(1,1,1)}, \varepsilon), \quad (17.1)$$

$$f_{(1,1,2)}(\vec{x}) = \varphi_{(1,1,2)}(\vec{x}) \cdot \lambda_{(1,1,2)}(\vec{x}, \vec{x}_{(0,0,1)}, \vec{x}_{(1,1,2)}, \varepsilon), \quad (17.2)$$

$$f_{(2,1,1)}(\vec{x}) = \varphi_{(2,1,1)}(\vec{x}) \cdot \lambda_{(2,1,1)}(\vec{x}, \vec{x}_{(1,0,0)}, \vec{x}_{(2,1,1)}, \varepsilon), \quad (17.3)$$

$$f_{(2,1,2)}(\vec{x}) = \varphi_{(2,1,2)}(\vec{x}) \cdot \lambda_{(2,1,2)}(\vec{x}, \vec{x}_{(1,0,1)}, \vec{x}_{(2,1,2)}, \varepsilon), \quad (17.4)$$

where values of indices in the brackets are specifying the coordinate number of the fragment: the first and third index specify the numbers of α angle of heel fragments and v speeds, respectively, and the coordinate number for 'h' as the second index, which does not change, since the fragments belong to all the range of this variable.

The total EAF is formed according to Eq. (14), where the additive expression has the following form:

$$f(\vec{x}) = f_{(1,1,1)}(\vec{x}) + f_{(1,1,2)}(\vec{x}) + f_{(2,1,1)}(\vec{x}) + f_{(2,1,2)}(\vec{x}), \quad (18)$$

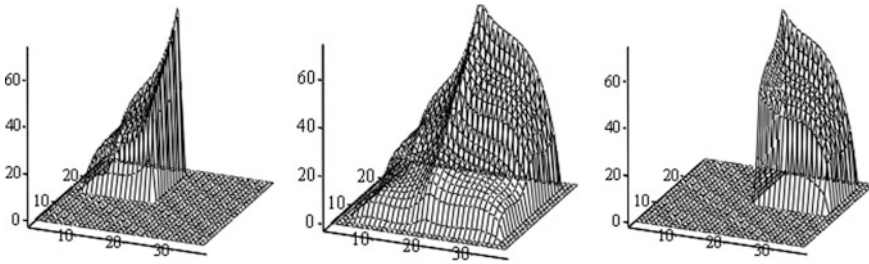


Fig. 4 The 2 of 4 IIF, and the total EAF (sections for $h = x_2 = 10$ km)

The analysis of EAF (17.1–17.4) has shown that the module of the greatest approximation error of this united function (5.64%) does not exceed the greatest fragments error (5.7%). The check is made for the wide range of values $\varepsilon \in [0.01–0.10]$. It confirms operability of the cut-gluе approximation method for the 3-dimensional data.

In Fig. 4, the 3D-images illustrating the isolation stages of IIF from the corresponding FAF are shown. In addition the result of the association of the four IIF in EAF is shown too. Due to the impossibility of an evident illustration of the received 3-dimensional dependencies coming from 4-dimensional space, in Fig. 4, the projections of the constructed 4-dimensional figures are representing 3-dimensional subspace formed by independent variables $x_1 - \alpha$ and $x_3 - \nu$, and also the F_x output variable, called “sections”.

10 Conclusion

1. The research on the mathematical models and algorithms defining the main stages of the cut-gluе approximation method of the multidimensional experimental data has been shown, indicating the possible applications of this method, as the viable solution in approximating n-dimensional problems.
2. For the first time, this conclusion is illustrated, by showing the solution of a problem requiring the approximation of 3-dimensional dependences, based on the experimental data from the performed research in designing a real airship.
3. This research has accomplished all the stages of the cut-gluе approximation method with the multidimensional experimental data, and showed high performance with the mixed computer and manual methods resources for the data processing, when approximating higher than 2-dimensions.
4. The final conclusion shows the urgent need to formalize the algorithms for all stages of the studied method, and their full automation, in order to ensure a broad and universal application of the CGA method for tackling the multidimensional approximation problems.

References

1. Loran P (1975) Approximation and optimization. Trans with English, World, Moscow, 496p
2. Insung I, Naylor B (1990) Piecewise linear approximations of digitized space curves with applications. Computer Science Technical Reports. Report Number: 90-1036. Paper 37. <http://docs.lib.purdue.edu/cstech/37>. Accessed 12 Jul 2016
3. António M, Pinheiro G, Ghanbari M (2010) Piecewise approximation of contours through scale-space selection of dominant points. *IEEE Trans Image Process* 19(6). doi:10.1109/TIP.2010.2043008
4. Ahlberg J, Nilson E, Walsh J (1967) The theory of splines and their applications. Academic Press, New York
5. De Boor C (1978) A practical guide to splines. Springer, New York
6. Micula G, Micula S (1999) Handbook of splines. Kluwer Academic Publishers, Dordrecht
7. Rawlings J, Pantula S, Dickey D (1998) Applied regression analysis: a research tool, 2nd edn. Springer, New York, 671p. ISBN 0-387-98454-2, SPIN 10660129
8. Bates D, Watts D (1988) Nonlinear regression analysis and its applications. Wiley, New York, p 365
9. Drapper N, Smith J (1981) Applied regression analysis, vol 1. Wiley, New York, p 366
10. Drapper N, Smith J (1981) Applied regression analysis, vol 2. Wiley, New York, p 351
11. Vilmos T (2005) Orthogonal polynomials. In: Surveys in approximation theory. pp. 70–125, vol 1, ISSN 1555-578X
12. Khrushchev S (2008) Orthogonal polynomials and continued fractions from Euler's point of view. Atilim University, Turkey: Cambridge University Press, www.cambridge.org/9780521854191. Accessed 12 Jul 2016
13. Powell M (1992) The theory of radial basis function approximation. In: Light W (ed) Advanced numerical analysis, vol II. OUP, Oxford University Press, Oxford, pp 105–210
14. Sarra S, Kansa E (2009) Multiquadric radial basis function approximation methods for the numerical solution of partial differential equations. Marshall University and University of California, Davis, June 30, 220p. www.ScottSarra.org/math/math.html. Accessed 13 Jul 2016
15. Buhmann M (2003) Radial basis functions: theory and implementations. Cambridge University Press, Cambridge. <http://www.math.ucdavis.edu/~saito/data/jim/buhmann-actanumerica.pdf>. Accessed 13 Jul 2016
16. Neydorf R (2014) Approximating creation of mathematical models on dot experimental data by cut-glue method. *DSTU Bull* 14(75)45–58
17. Neydorf R (2014) “Cut-Glue” approximation in problems on static and dynamic mathematical model development. *Proc ASME Intl Mechan Eng Congr Expos (IMECE)*, 1. doi:10.1115/IMECE2014-37236
18. Neydorf R (2015) Bivariate “Cut-Glue” approximation of strongly nonlinear mathematical models based on experimental data. *SAE Int J Aerosp* 8(1):2015. doi:10.4271/2015-01-2394. <http://papers.sae.org/2015-01-2394>. Accessed 13 Jul 2016
19. Neydorf R, Sigida Y (2014) Identification of traction and power characteristics of air-screw propulsors in mathematical description of airship. *SAE Technical Paper* 2014-01-2134. doi:10.4271/2014-01-2134
20. Neydorf R, Sigida Y, Voloshin V, Chen Y (2013) Stability analysis of the MAAT feeder airship during ascent and descent with wind disturbances. *SAE Technical Paper* 2013-01-2111, 2013. doi:10.4271/2013-01-2111
21. Neydorf R, Neydorf A (2016) Technology of cut-glue approximation method for modeling strongly nonlinear multivariable objects. *Theoretical Bases and Prospects of Practical Application*, *SAE Technical Paper* 2016-01-2035, 2016. doi:10.4271/2016-01-2035
22. Pshikhovop V, Medvedev M, Gaiduk A, Neydorf R et al (2013) Mathematical model of robot on base of airship. In: 52nd conference on decision and control, Florence, Italy, 10–13 Dec 2013. Proceedings of the IEEE conference on decision and control, p 959

23. Pshikhopov V, Medvedev M, Neydorf R, Krukhmalev V, Kostjukov V, Gaiduk A, Voloshin V (2012) Impact of the feeder aerodynamics characteristics on the power of control actions in steady and transient regimes. SAE Technical Paper 2012-01-2112. doi:[10.4271/2012-01-2112](https://doi.org/10.4271/2012-01-2112)
24. Voloshin V, Yong Ch, Neydorf R, Boldyreva A (2013) Aerodynamic characteristics study and possible improvements of MAAT feeder airships. SAE Technical Paper 2013-01-2112. doi:[10.4271/2013-01-2112](https://doi.org/10.4271/2013-01-2112)
25. Osiaev OG (2010) Resource-saving forecasting method of long durability of polymeric materials in case of multiple-factor loading. In: Osiaev OG, Neydorf RA (eds) Reviews of SFU. Technical science. Thematic release “Methods and means of adaptive management in power”. TTI SFU Publishing House, Taganrog, vol 1, no 102. [http://izv-tn.tti.sfedu.ru/wp-content/uploads/PDF/2010_1\(102\).pdf](http://izv-tn.tti.sfedu.ru/wp-content/uploads/PDF/2010_1(102).pdf). Accessed 14 July 2016
26. Osiaev OG (2010) The formalized analysis of settlement cases of loading and resource of operation of aircraft. In: Osiaev OG, Neydorf RA (eds) Control systems and information technologies, vol 2, no 40. Scientific Book Publishing House, Moscow, Voronezh. <http://www.sbook.ru/suit/contents/100200.pdf>. Accessed 14 Jul 2016
27. Osiaev OG (2010) Numerical forecasting method of the difficult stress-strain state of designs of flight vehicles. Reviews of SFU. Technical science. Thematic release: “Perspective systems and tasks of control”. TTI SFU Publishing House, Taganrog, vol 3, no 104. <http://izv-tn.tti.sfedu.ru/wp-content/uploads/2010/3/35.pdf>. Accessed 15 Jul 2016
28. Pshikhopov V, Medvedev M, Gaiduk A, Neydorf R et al (2013) System of position and trajectory management of a robotic aeronautic platform: mathematical model. Mechatron Autom Control 6:14–21. http://novtex.ru/mech/mech2013/Mh613_web.pdf. Accessed 15 July 2016
29. Pshikhopov V, Medvedev M, Gaiduk A, Neydorf R et al. (2013) System of position and trajectory management of a robotic aeronautic platform: control algorithms. Mechatron Autom Control 7:13–20. <http://novtex.ru/mech/mech2013/Mh713.pdf>
30. Neydorf R, Novikov S, Fedorenko R (2013) Continuous-positional automatic ballonet control system for airship. 2013 SAE Intl J Aerosp 6(2). ISSN: 1946-3855
31. Neydorf R, Novikov S, Kudinov N (2014) Airship positioning fuzzy multi-ballonet control study. SAE Technical Paper 2014-01-2146, 2014. doi:[10.4271/2014-01-2146](https://doi.org/10.4271/2014-01-2146)

Robot Path Planning Based on Ant Colony Optimization Algorithm for Environments with Obstacles

Rudolf Neydorf, Orhan Yarakhmedov, Victor Polyakh,
Ivan Chernogorov and Dean Vucinic

Abstract In modern industrial processes, robotic equipment is widely used, and one of the most pressing problems is to have to have navigation available for mobile robots. In this paper, the ant algorithm for laying and optimizing the robots paths in 2-dimensional environments with obstacles, is described and shown on construction site examples. The most important requirement is to be able to plan the shortest or permissible robot navigation route in such a complex environment with obstacles. It is well known that one of the most effective solutions to resolve such optimization problems of route seals is provided by the ant colony optimization (ACO) algorithm. The exploratory nature of the ant colony behaviour requires a classical partition of the search space, which is incomparably smaller, when compared to the obstacles fragments, as considered within this paper. The ant's agents use the traditional logic of selecting the transition from fragment to fragment: the memory of the most popular routes based on pheromone are investigated, and formulated within the task elements, adopting appropriate tactics and situational awareness, and based on the random decisions. In addition, the new elements of the decision-making tactics are formulated for each task. For example, "feeling" of targeted routes by laying points is added to the algorithm. The natural analogue of this mechanism is similar to sensing the odors by the mustaches of real ants.

R. Neydorf (✉) · O. Yarakhmedov · V. Polyakh · I. Chernogorov
Don State Technical University, Rostov-on-Don, Russia
e-mail: ran_pro@mail.ru

O. Yarakhmedov
e-mail: orhashka@gmail.com

V. Polyakh
e-mail: silverpolyah@gmail.com

I. Chernogorov
e-mail: hintaivr@gmail.com

D. Vucinic
Vrije Universiteit Brussel, Brussels, Belgium
e-mail: dean.vucinic@vub.ac.be

The special software tool “Path Planning Optimization with Obstacle Avoidances by Ant Algorithm” is designed as the research test bed. A comprehensive study of the proposed algorithm, which shows superior performance, is done by utilizing the developed software. The examples, of the construction site with different complexity, are provided to explain the finding of the suboptimal routes for the specially designed test tracks, with defined obstacles in the simulated construction site landscape. The analysis of the results confirms the relevance and effectiveness of the developed software, which is based on the ant algorithm for the robot path planning, and validated for the environments containing complex obstacles.

Keywords Optimization · Route · Obstacle · Mathematical model · Group behavior · Ant colony algorithm · Pheromone

1 Introduction

Robots are widely used for the production of all kinds of goods, in military, construction and other working environments. Their widespread and continuous applications require new tasks that should be solved. One such problem is the “navigation and route optimization task”. For example, the navigation of different groups of robots in one construction site requires to perform a variety of parallel works, like the on-site navigation of the construction machinery. To solve such problems, it is adequate to use various heuristic algorithms, as they provide acceptable results within an adequate timeframe.

One of the superior heuristic group of algorithms is the ant colony (ACO) group of algorithms [1, 2]. These algorithms are simulating the real ants behavior. For the first time, these algorithms have been applied in the combinatorial graph task, for the well-known traveling salesman problem [3]. They focus on the solution of various graph problems, which makes it reasonable to apply ACO to solve the optimization problems of the trajectory, in order to move robots in the environment with static obstacles. Some known applications of ACO [4, 5] have shown competitive results.

2 Formulation of the Problem

The purpose of this article is to study the capabilities and features of applying the modified ACO to solve the problem of planning and optimization of the trajectory within the static environment containing obstacles.

The analysis of the ACO application results is necessary to be performed on the specially generated environment test scenes.

3 ACO Description

In this paper we consider the modified classical ACO [4–9], which is adapted to find a solution to the problem of laying out the route within the flat environment containing obstacles. The algorithm is based on the mechanism simulating the real ants behavior, when they are looking for food. As in the classical ACO [6, 7], this modification can be divided into conditional steps, such as: placement and initialization, movement of agents, pheromone update and breakpoint condition checking.

All the space considered is divided into equal fragments, in which the agents travel to contribute to the process of the route optimization. To each fragment, a small amount of the positive pheromone is allocated. In order to solve such a problem, it is necessary to construct a route between 2 points (start and finish). We need to allocate the “Start” fragment and place all the agents in it (the analog of the colony). Respectively, the other allocated fragment is the “Finish” point (analogue to the food place).

At the heart of the ant movement mechanism is the classical probability model [5], which is updated with some appropriate modifications.

When the ant moves, it has 8 different options for further travel, as shown in Fig. 1.

The ant transition probability k -th, for the t iteration in each adjacent fragment $i \in [1; 8]$ is calculated according to the modified formula [5], as

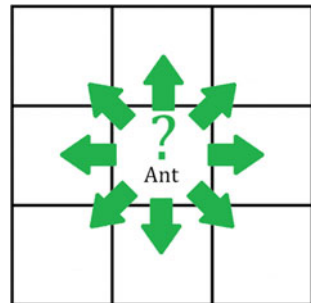
$$P_{ij,k} = \begin{cases} \frac{(1 + \tau_{ij})^\alpha \times \eta_{ij}^\beta}{\sum_{l=1}^8 (1 + \tau_{ij})^\alpha \times \eta_{ij}^\beta}, & \text{if } ij \text{ available}^*, \\ 0, & \text{if } ij \text{ not available}^*, \end{cases} \tag{1}$$

where conditions are preferably transition assessment, and related to the goal direction described by the following model, as proposed by the authors:

$$\eta_{ij} = (\cos(\gamma) + 2) + (\cos(\gamma) + 1)^\lambda \tag{2}$$

where: ij is the fragment; k is the ant number; τ is the pheromone level; η is the “visibility”; α, β, λ are variable coefficients; γ is the angle between goal position,

Fig. 1 Direction options for the agent to travel



current position and next element position; * means available if fragment is both, adjacent and do not have an obstacle.

At the core of Eqs. (1) and (2), the proposed model is a classic ant algorithm, as used for the optimization of routes in a graph [1–3, 6, 7, 10]. However, there are number of incorrect situations that may arise from the calculation related to the probabilities of moving the ants within the specific areas. This fact forced the developers to introduce a number of modifications to this model.

First, the estimated concentration of the pheromone τ may be less than an unity found under a certain conditions. Therefore, when calculating the probabilities of the introduced displacement, at each iteration τ , the summation operation is with this unity. This is done in order to maintain a direct dependence between the pheromone value and the degree coefficient.

There was also a component, which the authors reworked in the heuristic algorithm part [see Eq. (2)], and which is responsible for the attraction to the goal. The classical implementation of the attractiveness, to a particular graph vertex, depends on its distance. This relationship is not direct, and depends on the angle between the point considered to be moving, and the current position of the ant and the finish point.

Also, it should be noted that this addition has added to the algorithm another configuration parameter λ , which made this modification even more flexible, to meet the challenges of varying difficulty. Figure 2 shows dependences graphs of the “attraction” values η for different λ values.

Once all the agents reach the finish point, and on all the investigated area, the pheromone is updated applying the following model:

$$\tau_{ij}(t+1) = (1 - \rho) * \tau_{ij}(t) + \frac{Q}{L_k}, \quad (3)$$

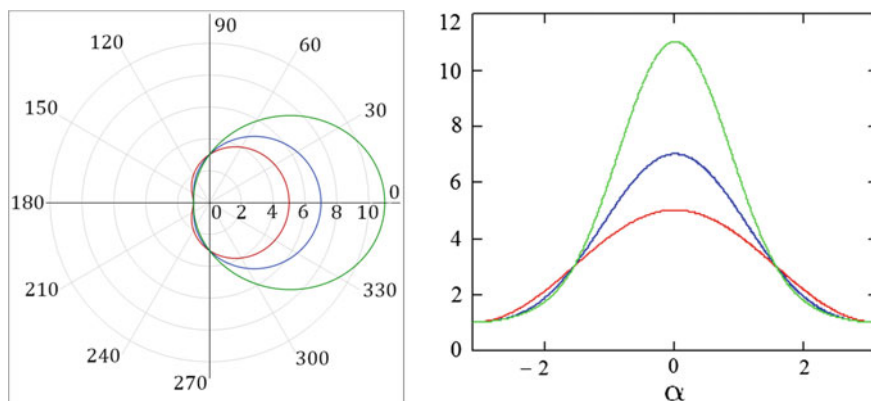


Fig. 2 Graphics of dependence of the “attraction” for different λ values in polar and Cartesian coordinate systems

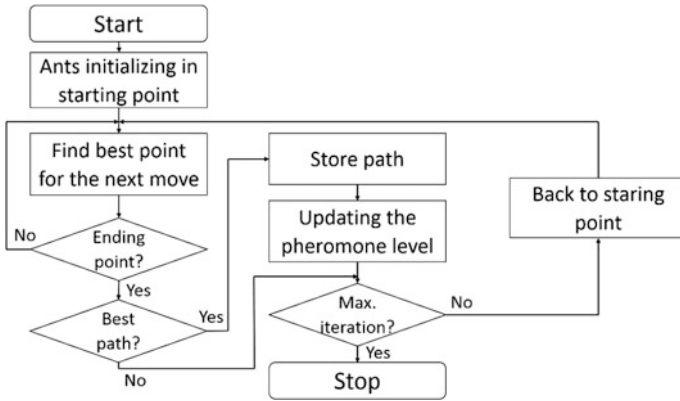


Fig. 3 Flowchart of ACO

where: ij is the fragment; k is the ant number; ρ is the evaporation coefficient; τ is the pheromone level; t is the iteration number; Q is the constant; L is the route length.

Thus, in the whole space, there is an uniform evaporation of the pheromone, and also on fragments, while the agents built the routes the pheromone is incremented. Moreover, the increment value depends on the length of the route.

The last step is to verify the breakpoint conditions. In this case the breakpoint condition is limited by the number of iterations.

When applying the algorithm, we are observing the iterative improvement of the route, which is building up to avoid obstacles.

Figure 3 shows the flowchart of the algorithm.

4 Examples of the Algorithm

Based on the above mentioned ant movement and the update of the pheromone models Eqs. (1–3), a software tool “PPO_OA_AA” (Path Planning Optimization with Obstacle Avoidances by Ant Algorithm), is designed and implemented to support the experiments.

To check the efficiency of the algorithm 3 test polygons, with obstacles of varying difficulty, were created. Figure 4 shows the defined polygons. The difficulty in this case is linked to the number of obstacles encountered within the zone of movement.

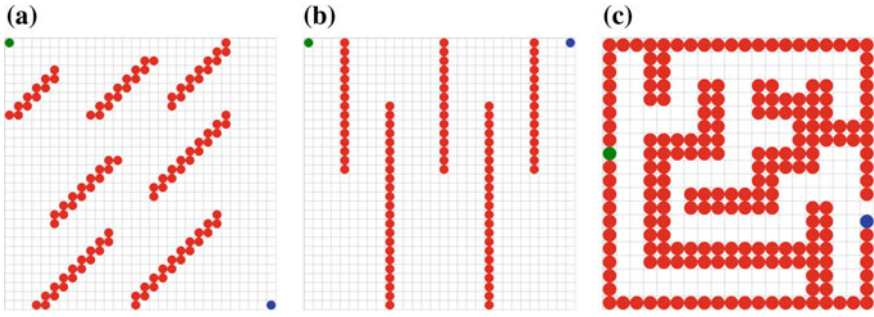


Fig. 4 Test polygons (a 1st, b 2nd, c 3rd)

5 Parametric Optimization

Since the algorithm depends on Eqs. (1–3) having variable parameters, it is advisable to optimize it parametrically. The developed software provides the opportunity to adjust the tuning parameters.

On the basis of previous works [6, 7, 11, 12], 4 key factors (parameters) have been identified to have the greatest influence on the result.

A small number of factors allowed the use of the full factorial experiment (FFE). The applied varying factors values, on 2 levels reduce time and number of required experiments. At the same time, the total factors variation allows to investigate, not only their linear effects, but also the interaction effects [13]. The first test site was selected for the parametric optimization. It was planned for the 2-tier paradigm, the FFE consists of 16 unique combination of factors. For each combinations of factors, 5 tests have been done having 10 parallel experiments in each of them. This was done with the purpose to diversify the random data generated with pseudorandom number generator provided in the computer systems. The initial parameters for these experiments are offered in Table 1. These values were selected based on earlier works [6, 7, 11, 12] performed.

The plan of this experiment is partially presented in Table 2. The applied optimization criterion is the percentage of the best optimal route length in the sample experiments. For this test site the best route length is 41 step.

Table 1 Intervals of considered values

Factor	Plan center	The range of variation	Lower limit	Upper limit
Designation in the alg./in FFE	The value in the alg./in FFE	The value in the alg./in FFE	The value in the alg./in FFE	The value in the alg./in FFE
α/x_1	2.3/0	0.3/1	2/-1	2.3/+1
β/x_2	0.2/0	0.1/1	0.1/-1	0.3/+1
λ/x_3	1/0	0.5/1	0.5/-1	1.5/+1
ρ/x_4	0.7/0	0.2/1	0.5/-1	0.9/+1

Table 2 Plan of the experiment

Plan													
	α	β	λ	ρ	Combinations						Y avge. %	Dispersion	SD
No	$\times 0$	$\times 1$	$\times 2$	$\times 3$	$\times 4$	12	...	123	...	1234	–	–	–
0	0	0	0	0	0	0	...	0	...	0	8	70	8.3666
1	1	-1	-1	-1	-1	1	...	-1	...	1	10	150	12.2474
2	1	-1	-1	-1	1	1	...	-1	...	-1	56	130	11.4018
3	1	-1	-1	1	-1	1	...	1	...	-1	12	20	4.4721
4	1	-1	-1	1	1	1	...	1	...	1	58	120	10.9545
5	1	-1	1	-1	-1	-1	...	1	...	-1	6	80	8.9443
...													
16	1	1	1	1	1	1	1	1	1	1	4	30	5.4772

Since the values of the regression coefficients and parameters of combinations do not exceed the standard deviation value, it is not necessary to use the gradient method. The parameters α and β are fixed on the lower level, and the parameter λ is fixed for the center of the plan, as it gives the same results, as the one for the upper and the lower level of variation.

Thus, in the view of the specific nonlinear dependence, the ρ value has been found to have the greatest influence. At one of its extremes, the algorithm shows the highest efficiency, thus it was decided to explore the value of 0.9. The results are given in Fig. 5.

It is obvious that the value of $\rho = 0.9$ provide the maximum efficiency of the algorithm. 10 tests with 10 experiments for each of them were carried out to validate the results, taking into account the following values of the parameters: $\alpha = 2$, $\beta = 0.1$, $\lambda = 1$, $\rho = 0.9$. Figure 6 shows a probability chart for the computed results.

Figure 6 indicates that the probability of getting the best result is equal to 42.73%. To increase this probability, ACO should be applied to this problem with n-th number of times, which can be calculated from the formula:

$$k = \log(1 - p_{no}^k) / \log p_{no}^1, \tag{4}$$

where p_{no}^1 is the probability of nonappearance optimal results in one solution to the problem; p_o^k is the single occurrence probability of optimal result in k-sample set of solutions.

Thus, with a probability of $p_o^k = 0.8$ to get at least one global optimum results by using parametrically suboptimized ACO, it is necessary to apply this algorithm to the problem

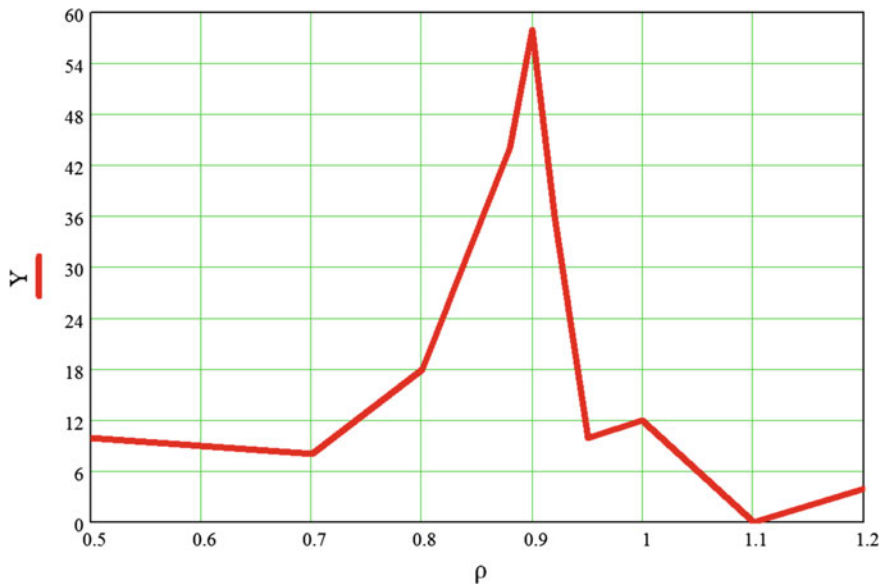
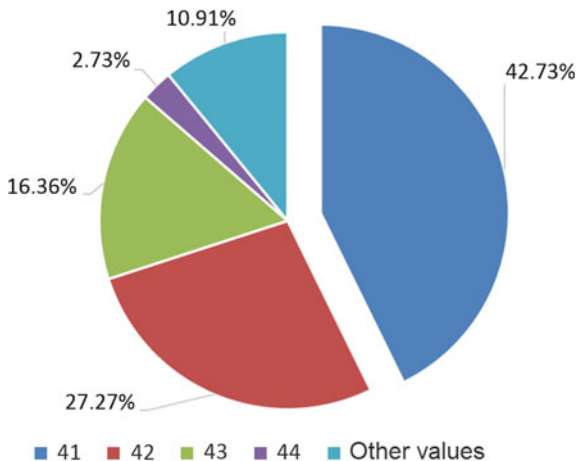


Fig. 5 Dependence of the optimization criterion based on the rho value

Fig. 6 Probability of the obtained values



$$k = \log(1 - 0.8) / \log(1 - 0.4273) = -0.6989 / -0.242 = 2.888 \approx 3 \text{ times.}$$

Table 3 shows the results of calculating Eq. (4) to define the number of tests in order to obtain the optimal results, and in addition the suboptimal results for the different specified trust probabilities.

Table 3 Number of experiments to get the specified result

The desired probability (%)	80	90	95	99	99.9
The number of tests to get the optimum result (41)	3	5	6	9	13
The number of tests to get the suboptimum result (42)	2	2	3	4	6

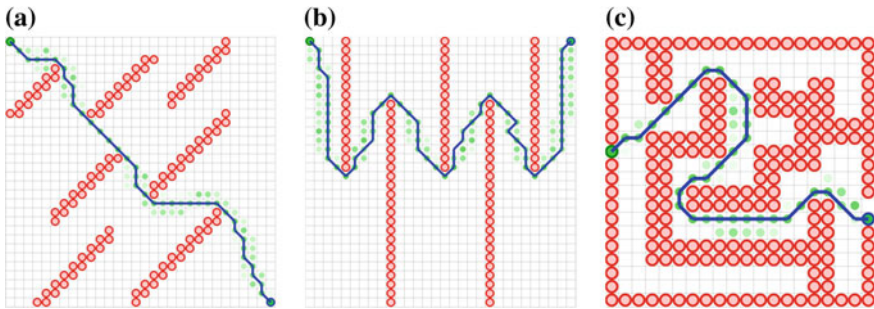


Fig. 7 Best routes results

6 Application Parametrically Optimized ACO

This section presents the results of the tests, which have been obtained by using the parametric suboptimized ACO. Figure 7 shows the shortest routes, which were found for all the 3 earlier described test polygons.

In all 3 cases, the global optimal results were achieved in 100 iterations.

7 Conclusion

The results of these studies indicate that the proposed modification effectively manifested them as the solution to the problem in finding the laying route with obstacles.

The parametric suboptimization significantly has improved the quality of the result. It should be noted that for each particular task, it is required to perform its parametric optimization, as it is strongly influenced by the variety of the test conditions.

Also worth noting is that with almost 100% certainty we can get close to the optimum or even optimal results, when repeating its application to the problem. This indicates that the sub-optimization of the algorithm should be carried out, by focusing not only on the accuracy of the solution, but more important, on the time given to solve the optimization problem.

References

1. Dorigo M, Gambardella LM (1997) Ant colony system: a cooperative learning approach to the traveling salesman problem. *IEEE Trans Evol Comput.* doi:[10.1109/4235.585892](https://doi.org/10.1109/4235.585892)
2. Dorigo M, Di Caro G, Gambardella LM (1999) Ant algorithms for discrete optimization. *Artificial Life.* doi:[10.1162/106454699568728](https://doi.org/10.1162/106454699568728)
3. Kazharov AA, Kurejchik VM (2010) Muravinye algoritmy dlja reshenija transportnyh zadach (Ant algorithms to solve transport problems). *Teoriya i sistemy upravlenija (Theory and control systems)*, No 1, pp 30–43. ISSN: 0002-3388
4. Toksari MD (2006) Ant colony optimization for finding the global minimum. *Appl Math Comput.* doi:[10.1016/j.amc.2005.09.043](https://doi.org/10.1016/j.amc.2005.09.043)
5. Liu X, Fu H (2010) An effective clustering algorithm with ant colony. *J Comput.* doi:[10.4304/jcp.5.4.598-605](https://doi.org/10.4304/jcp.5.4.598-605)
6. Neydorf RA, Yarahmedov OT (2015) Razrabotka, optimizacija i analiz parametrov klassicheskogo muravinogo algoritma pri reshenii zadachi kommivojazhera v polno-svjaznom grafe (Design, optimization and analysis of the parameters of classical ant algorithm for solving the traveling salesman problem in a fully-connected graph). *Mezhdunarodnyj nauchnyj zhurnal «Nauka. Tehnologii. Proizvodstvo» (International scientific journal “Science. Technologies. Production”)*. 3/2:18–22
7. Neydorf RA, Yarahmedov OT (2015) Issledovanie vozmozhnostej optimalnogo reshenija zadachi kommivojazhera parametricheski optimizirovannym muravinym algoritmom (Analysis of abilities of optimal solution of the travelling salesman problem by parametrically optimized ant algorithm). *Trudy XXVIII Mezhdunarodnoj nauchnoj konferencii «Matematicheskie metody v tehnike i tehnologijah» (Proceedings of the XXVIII International Scientific Conference “Mathematical Methods in Engineering and Technology”)*. MMTT-28, vol 6, p 108
8. Fatemeh KP, Fardad F, Reza SN (2013) Comparing the performance of genetic algorithm and ant colony optimization algorithm for mobile robot path planning in the dynamic environments with different complexities. *J Acad Appl Stud* 3(2):29–44
9. Pang CY, Li X (2009) Apply ant colony algorithm to search all extreme points of function. *5th IEEE Conf Ind Electron Appl.* doi:[10.1109/ICIEA.2010.5514672](https://doi.org/10.1109/ICIEA.2010.5514672)
10. Dorigo M (1992) *Optimization, learning and natural algorithms*. Politecnico di Milano, Italy
11. Neydorf RA, Chernogorov IV, Polyakh VV, Iarakhmedov OT (2015) Solving possibilities of multiextremal optimization tasks by heuristic methods. *Her Don State Tech Univ.* doi:[10.12737/issn.1992-5980](https://doi.org/10.12737/issn.1992-5980)
12. Neydorf RA, Chernogorov IV, Polyakh VV, Iarakhmedov OT (2016) Detection and estimation of extremal characteristics of the search space by heuristic algorithms, *H&ES Research.* 2/8:16–25
13. Adler JP, Markova EV, Grankovsky YV (1976) *Planirovanie jeksperimenta pri poiske optimal'nyh uslovij (Experiment planning in the search for optimal conditions)*. M.:Nauka

“Cut-Glue” Approximation Based on Particle Swarm Sub-optimization for Strongly Nonlinear Parametric Dependencies of Mathematical Models

Rudolf Neydorf, Ivan Chernogorov, Orkhan Yarakhmedov,
Victor Polyakh and Dean Vucinic

Abstract The difficulties in the experimental and computer modeling of the static and dynamic transport media are associated with a significant non-linearity of the present model dependencies. This is due to the mechanical friction effects, backlash, aerodynamic effects and other physical phenomena. The construction of the mathematical models (MM) for such objects is most often associated with the mathematical treatment of the experimental data. The point-like dependencies of the output variables linked to the input are essentially non-linear, piecewise and sometimes discontinuous. These dependencies, when approximated with polynomial or spline functions, are difficult to control, and thus associated with large errors. The radically new solution to this problem is proposed in paper [1]. This method is called the «cut-glue» approximation (CGA) method. It is based on partitioning the simulated dependence within specified areas; approximating each fragment with the polynomial dependencies; multiplicative “cutting” for each dependence is the fragments along border area; the additive “gluing” of these fragments is grouped into a single function, as the approximated dependence model. The analytical characteristics of this approximating “gluing” function is the main feature and advantage, properties of functions allow to analyze analytically the model and its application for simulating the dynamic models of the transport media. For a broad CGA method introduction in the experimental modeling research

R. Neydorf (✉) · I. Chernogorov · O. Yarakhmedov · V. Polyakh
Don State Technical University, Rostov-on-Don, Russia
e-mail: ran_pro@mail.ru

I. Chernogorov
e-mail: hintaivr@gmail.com

O. Yarakhmedov
e-mail: orhashka@gmail.com

V. Polyakh
e-mail: silvervpolyah@gmail.com

D. Vucinic
Vrije Universiteit Brussel, Brussel, Belgium
e-mail: dean.vucinic@vub.ac.be

practice, it is necessary to develop, justify and explore the local methodologies implementation of these stages. One of the CGA stage is the “glue” process, when the additive fragments are “glued” into a single function. The auxiliary multiplicative allocation function (MAF) is used for that. The MAF structure includes the edge steepness parameter— ε . In this paper, the algorithm is developed based on the modification of the particle swarm optimization (PSO) method, which is used in this research, together with the sub-optimization ε parameter. The hybrid PSO method smoothly includes the basic prototype of the fundamental equations defining the mechanic laws, gravitation and the stochastic “blurring” movement parameters. The developed special software tool, as a research test bed, for conducting the numerical experiments is illustrated in this paper.

Keywords Optimization · Approximation · Mathematical model · Experimental data · Heuristic · Particle swarm optimization

1 Introduction

The simulation of complex dynamic objects (aircraft, vehicles, processes and systems) leads to a differential equations system, which is based on the physical laws. Thus, this system of differential equations defines the object individual elements and their relationship, and in addition, it links the object reaction to the set of external influences. Often, this is due to the significantly different description of such nonlinear phenomena: the mechanical effects of dry friction and aerodynamic “stall” backlash effects [2–4], the complex electromagnetic and thermodynamic processes and to many other factors. Usually, these objects are not define with appropriate theoretical methods, due to the incomplete laws knowledge of these processes. In this paper, the physical tests of real objects or their scale models have been performed. The examples are, the wind tunnel simulations of the airplane or motorcar models. The experiments based on the computer modeling for the universal systems [2–8] are widely used. The models parameters are specified on the basis of these experiments. However, there are difficulties associated with a significant non-linearity present in these models [5–8].

For the technical devices, processes and systems, which are largely based on the heuristic designers ideas, when developed for the first time, the analytical modeling is generally unavailable or results in a very unsatisfactory accuracy, because it is determined by numerous hard accounted factors. In this case, it is advisable to pursue the models construction taking directly their experimental characteristics. Often, these characteristics are essentially nonlinear. In many cases, when approximating the static characteristics, it is sufficient to define a piecewise approximation. However, in dynamic models, such decision creates considerable difficulty in defining the models solution and their mathematical transformations.

The background of the approximation problem for the effective solution is published in several references [1–3, 5, 6]. The proposed CGA method is based on the multiplicative “cutting” of the modeled dependences, which are well-approximated sections, and the additive “gluing” combines them into a single analytic function. At the same time, for the used “cut” analytic function makes the final expression characterized with the analytic properties. The latter, is the main feature and advantage of the method, because it is not only numerical, but in addition, analyzes the resulting conversion model.

Today, the effectiveness of the proposed approximation solution is theoretically proved and practically confirmed only for 1- and 2-dimensional dependencies [1, 9]. In [10], the possibility and prospects of the proposed approach application for approximating the arbitrary dimension dependencies are demonstrated. This significantly broadens the method scope and its importance in the field of science and practice.

“Cut” is a process in CGA that “cut” a fragment, which approximates some experimental dependence, which is plotted on the selected fragment boundaries [1]. Mathematically, this corresponds to the experimental data single matrix cut into several fragments, while preserving the common borders. The boundaries are defined by the description accuracy condition of the section, which is approximated by the analytic function. The MAF structure includes the edge steepness parameter— ε . In a previous work [1], the author cited a condition for the most effective option, when using this parameter. This effectiveness is due to programming expertise, and, as the research shows, it is only effective for a sufficiently accurate reproduction of the approximation function for the fragment boundaries.

“Glue” is the process in CGA that provides a single analytic function, describing the researching region of the object characteristics [1]. The combined fragments, i.e., gluing them together after the “cut” operation, are obtained by performing the algebraic summation. After the series of pilot experiments, the authors have found that the variation in the ε values for the various coordinates in a multidimensional space can improve the approximation result for the “glue” procedure. It is decided to investigate the possibility of optimizing the ε parameter for each selected fragment of the specific 2-dimensional CGA problem.

2 Problem Formulation

The objective is to research MAF, its approximation characteristics and its general mathematical special properties, by providing the reception of the interval isolated fragments (IIF) from the approximated fragment function (AFF), which is locally approximating the fragments of the experimental dependences. The develop methodology for the MAF settings ensures the highest approximation accuracy.

3 Research Techniques

According to the CGA theoretical foundations the ε parameter is a real number, and to optimize it is desirable to use the algorithm from the continuity optimization methods group. In addition, the analytical complexity of the n-dimensional MAF and the resulting CGA function make use of the search optimization algorithm. One of the proven methods, to meet the challenges of finding the optimal research objects parameter, are heuristics algorithms, which are based on the groups behavior of animals, insects, etc. The obvious representative of this trend is PSO. The algorithm is similar to the behavioral characteristics of the insects swarm [11–15].

Previously, the authors carried out a number of works [16–19] on PSO research and its performance, as well as the modifications to improve the accuracy, resource finding optima efficiency, in order to expand its application functionality. In particular, its adaptation to the multiextremal tasks solution. However, the pilot investigations revealed that the 2-dimensional case, with ε_x and ε_y , has only one value, which varies depending on the selected criterion, when considering a range of values in the matrix of the absolute errors. In this paper, we seek to research the ε parameter in 2-dimensional search space covering x and y of each selection. We need to compare the obtained and pilot research results. This implies further research, with the structural modifications and parametric optimization of the PSO mechanical model parameters.

4 PSO MM Modification

The swarming is physically connected with the movement of the real inertial particle, with the equations defining the fundamental mechanical laws:

$$X_{it} = X_{(t-\Delta t)i} + \vec{V}_{(t-\Delta t)i} \Delta t, \quad (1)$$

$$\vec{V}_{it} = \vec{V}_{(t-\Delta t)i} + \vec{A}_{(t-\Delta t)i} \Delta t, \quad (2)$$

$$\vec{A}_i = \vec{A}_{pi} + \vec{A}_{tri}, \quad (3)$$

$$\vec{A}_{pi} = \vec{A}_{pi}^G + \vec{A}_{pi}^L, \quad \vec{A}_{pi}^Q = \vec{G}_Q m_i m_r / (r^2 + \varepsilon) \quad Q \in \{G, L\}, \quad (4)$$

$$\vec{A}_{tri} = -\mu \vec{V}_{(t-\Delta t)i}, \quad (5)$$

where: $X_{(t-\Delta t)i}$ and X_{it} —is the previous and current position of the i th particle; Δt —is the integration interval by time; $\vec{V}_{(t-\Delta t)i}$ and \vec{V}_{it} —is the speed of the i th particle in

the previous and current times; $\vec{A}_{(t-\Delta t)_i}$ —is the particle acceleration at previous moment; $\vec{A}_{p_i}^G, \vec{A}_{p_i}^L$ —is the “biological attraction” acceleration of the particles to a global extremum and to the best position for the particle at all time; \vec{A}_{fr} —is the slowing by friction; \vec{G}_Q —is the “biological gravity” analogue; $m_i = m_r$ —is the attracted particles masses biosimilars; r —is the distance between the current particle position and the current extremum; ε —is the small correction constant ($\varepsilon = 1e-15$, eliminating the problems at $r = 0$), μ —is the friction coefficient.

To simulate some features, which are inherent to the living beings, an incomplete behavior predictability model is used that form the stochastic “blur” [16] of its basic parameters (geometric, kinematic and dynamic), as defined in the Eqs. 1 and 2. For this purpose, in the model is introduced the random function, with the symmetrical distribution in respect to the nominal value and adjustable range, specifying the “blurring” part of each parameter:

$$\lambda^\pi(\xi) = \lambda \cdot (1 + 2\xi \cdot (rnd(1) - 0.5)), \lambda^\pi(\xi) \in \{\mu, \vec{G}_Q, C_Q, An, D\}, \quad (6)$$

where: ξ —is the relative departure of the distorted parameter from the nominal value; $rnd(1)$ —is a random real number in the [0, 1] range; C_Q —is the apparent particles gravity center; An —is the angle of particles reflection from the consideration boundary; D —is the dissipation factor (loss of energy in an inelastic particle collision of the border).

The composition of the total acceleration is caused by the attractive forces (biological analogues) of the particles including the conditional “global” and “local” attraction.

5 MAF Parameters Influence on the Approximation Quality in IIF “Gluing”

The final step in the general CGA procedure is the cut of IIF from AAF, and their subsequent “gluing” into a single MM. According to [10], the transformation is using the following formulas:

$$f_{(i_1, \dots, i_n)}(\vec{x}) = \varphi_{(i_1, \dots, i_n)}(\vec{x}) \cdot \lambda_{(i_1, \dots, i_n)}(\vec{x}, \vec{x}_{(i_1-1, \dots, i_n-1)}, \vec{x}_{(i_1, \dots, i_n)}, \varepsilon_j), \quad (7)$$

$$\lambda_{(i_1, \dots, i_n)}(\vec{x}, \vec{x}_{(i_1-1, \dots, i_n-1)}, \vec{x}_{(i_1, \dots, i_n)}, \varepsilon_j) = \prod_{j=1}^n \lambda_{j_i}(x_j, x_{j_{i-1}}, x_{j_i}, \varepsilon_j), \quad (8)$$

$$\lambda_{j_i}(x_j, x_{j_{i-1}}, x_{j_i}, \varepsilon_j) = 0.25 \cdot \sigma_l(x_j, x_{j_{i-1}}, \varepsilon_j) \cdot \sigma_r(x_j, x_{j_i}, \varepsilon_j) / \delta(x_j, x_{j_{i-1}}, x_{j_i}, \varepsilon_j), \quad (9)$$

where:

$$\sigma_l(x_j, x_{j-1}, \varepsilon_j) = x_j - x_{j-1} + \sqrt{(x_j - x_{j-1})^2 + \varepsilon_j^2};$$

$$\sigma_r(x_j, x_j, \varepsilon_j) = x_j - x_j + \sqrt{(x_j - x_j)^2 + \varepsilon_j^2}.$$

$$\delta(x_j, x_{j-1}, x_j, \varepsilon_j) = \sqrt{[(x_j - x_{j-1})^2 + \varepsilon_j^2] \cdot [(x_j - x_j)^2 + \varepsilon_j^2]}, \quad (10)$$

$$f(\vec{x}) = \sum_{j=1}^n \sum_{i_j=1}^{n_j} f_{(i_1, \dots, i_j, \dots, i_n)}(\vec{x}). \quad (11)$$

The initial data for the preliminary problem solution have been generated by the authors. As a result, for the selected conditional experiment parameters: the equation in the form of a 3rd degree polynomial function with 2 variables and corresponding coefficients b is defined as follows:

$$F(x, y) = b_0 + b_1x + b_2y + b_{11}x^2 + b_{12}xy + b_{22}y^2 + b_{111}x^3 + b_{112}x^2y + b_{122}xy^2 + b_{222}y^3, \quad (12)$$

where: $b_0 = 200$, $b_1 = 8$, $b_2 = -12$, $b_{11} = 1.95$, $b_{12} = -0.18$, $b_{22} = 1.72$, $b_{111} = 0.08$, $b_{112} = 0.023$, $b_{122} = -0.08$, $b_{222} = 0.1$; 10-dimension vector x , 8-dimension vector y , defining the simulated experiment grid.

The resulting matrix is divided into 4 contiguous areas with common borders. Figure 1 displays the original experimental data. The rows in the figure correspond to the x values, the columns correspond to the y values. Figure 2 displays the data graphics.

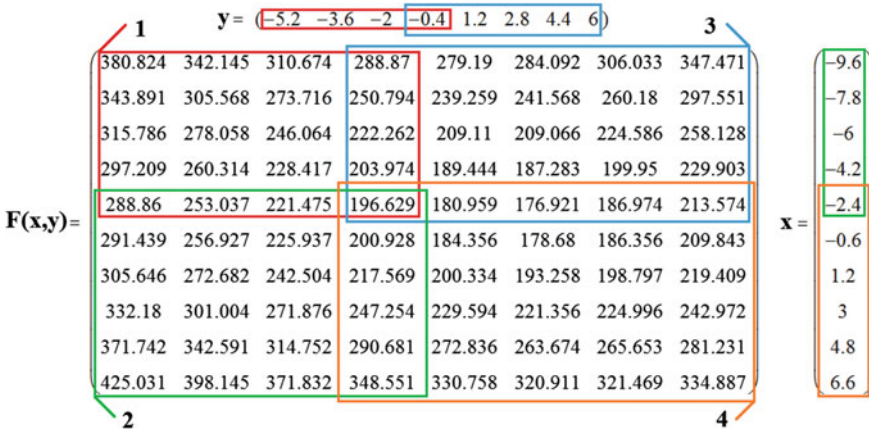


Fig. 1 Experimental data matrix

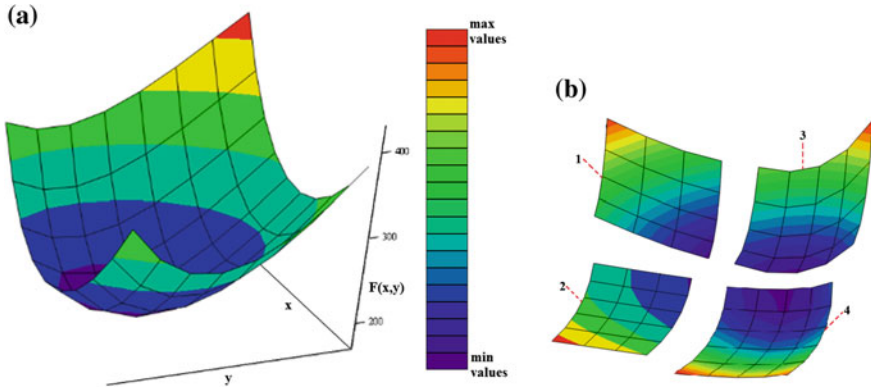


Fig. 2 Experimental data graphs: **a** entire, **b** by fragment

Table 1 Obtained b coefficients from 4-regression equation

	b^1	b^2	b^3	b^4
b_0	-8e-3	-0.904	0.3646	-0.5314
b_1	1.36	3.040	0.712	2.392
b_2	-11.82	-16.84,856	-14.65,208	-12.42,488
b_{11}	196.6	199.966,688	198.317,312	198.47,456
b_{12}	5.6587	7.05,072	8.70,432	8.00,976
b_{22}	1.5256	1.6544	2.0116	2.1404

For each fragment, the 2nd regression equation with the corresponding coefficients b (see Table 1) is defined as:

$$\varphi^i(x, y) = b_0^i + b_1^i x + b_2^i y + b_{11}^i x^2 + b_{12}^i xy + b_{22}^i y^2, \quad i \in \{1, 2, 3, 4\}, \quad (13)$$

In accordance with the problem statement, for the experiments the following data are selected: $(\varepsilon_{xi}, \varepsilon_{yi}) \in (0, 1], i \in \{1, 2, 3, 4\}$, the iterations number—300, the particles number—100. In addition, other PSO mechanical model parameters were set for the problem under consideration. The assessment criterion and the minimization of the error for the entire dependence approximation and fragments in the pilot research are the mean-square deviation (MSD) and the max error in the absolute errors matrix. In addition, the experience has shown that it is appropriate to identify the matrix key areas, which also apply to the selected assessment criterion. Therefore, the objects approximation accuracy ranking can be result in several mathematical constructs derived from CGA. First, these include the entire matrix of the experimental data. Second, the following can be considered: the matrix without border values (according to (9), corner and edge function value, except the conjugating values, little dependence on ε , and, to a greater extent, depending on the order approximated). Third, the “gluing” fragments common border, not including the border values of the entire matrix (these elements are mostly depending on ε).

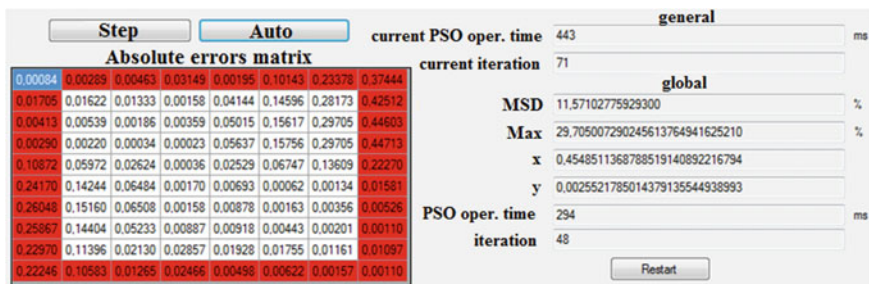


Fig. 3 Outputs in “Glue_MSP” software

Fourth and fifth, viewed separately the “gluing” fragments common edges (vertical and horizontal). All these CGA accuracy ranking objects are used in the current work.

In this research, the PSO agents search is done in the 8-dimensional space and their movement is displayed without releasing the projections in the subspace (3 degree maximum). For clarity, Figs. 3 and 4 illustrate the data, displayed in the window parts of the developed software, resulting from the search for an extremum in 2-dimensional space. Figure 3 shows the output data. Figure 4 shows the visualization of the swarm movement at the extremum localization time. The two experiments results are performed with the selected criteria and considering the areas defined in the absolute errors matrix, as shown in Table 2.

Fig. 4 Visualization the swarm movement in “Glue_MSP” software

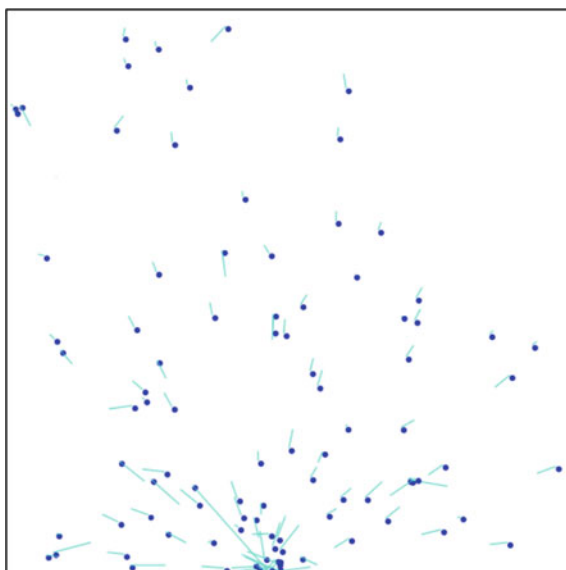


Table 2 Experimental result

Considered values in absolute errors matrix	Criteria	MSD %	Max %	ϵ_{x1}	ϵ_{y1}	ϵ_{x2}	ϵ_{y2}	ϵ_{x3}	ϵ_{y3}	ϵ_{x4}	ϵ_{y4}
Entire matrix	MSD	9.14	26.93	1e-6	0.99	0.99	1e-6	1e-6	1e-6	0.99	0.99
	Max	9.39	26.75	1e-6	0.99	0.99	0.99	1e-6	1e-6	0.99	1e-6
Matrix without boundaries	MSD	5.62	26.87	1e-6	0.99	0.7	0.44	1e-6	8e-6	0.99	0.74
	Max	5.77	26.75	1e-6	0.99	0.99	0.99	1e-6	1e-6	0.99	1e-6
«Glue» submatrix	MSD	2.98	28.51	1e-6	0.81	0.99	0.99	1e-6	1e-6	0.47	1e-6
	Max	3.1	26.75	1e-6	0.99	0.99	0.99	1e-6	1e-6	0.99	1e-6
Horizontal of «glue» submatrix	MSD	3.65	29.16	0.99	0.99	0.99	0.99	1e-6	1e-6	1e-6	1e-6
	Max	3.71	26.77	1e-6	0.99	1e-6	0.99	1e-6	1e-6	0.99	1e-6
Vertical of «glue» submatrix	MSD	0.39	35.49	1e-6	0.99	1e-6	1e-6	0.25	0.99	1e-6	1e-6
	Max	1.06	26.75	1e-6	0.99	0.99	0.99	1e-6	1e-6	0.99	1e-6

Table 3 Test results comparison

			Research			
			Pilot	Current	Pilot	Current
		Criteria	Max %		MSD %	
		Considered values in absolute errors matrix	Entire matrix	MSD	11.08	9.14
Max	11.57			9.39	29.7	26.75
Matrix without boundaries	MSD		7.65	5.62	31.42	26.87
	Max		7.88	5.77	29.71	26.75
«Glue» submatrix	MSD		3.74	2.98	30.07	28.51
	Max		3.81	3.1	29.7	26.75
Horizontal of «glue» submatrix	MSD		4.32	3.65	30.07	29.16
	Max		4.36	3.71	29.7	26.77
Vertical of «glue» submatrix	MSD		0.54	0.39	33.49	35.49
	Max		0.9	1.06	29.7	26.75

The total operation time spent to carry out all the experiments with 300 iterations is ~ 1.1 s. The PSO operation time spent on finding the extrema, is described in Table 2, with ~ 160 iteration— ~ 0.7 s. As can be seen from Table 2, the obtained values of MSD, Max, ε_x and ε_y are highly dependent on the selected criteria range values.

Table 3 contains the results obtained from the ε parameter optimization, performed for each fragment and the ε parameter optimization for all fragments within the pilot research.

The data comparison have shown the following: the total operation time spent on carrying out all experiments with 300 iterations, has reduced by $\sim 50\%$, MSD and max errors have decreased by ~ 17 and $\sim 8.3\%$, respectively.

6 Conclusion

The following conclusions can be drawn from the current work results:

- ε parameter has not, in general, a universal value for all the fragments;
- in ε parameter optimization for each fragment, the values of these parameters depend only on the problem properties, and the visible relationships were found between them;
- ε parameter in 2 dimensions for each fragment has only one value, which varies according to the chosen criterion, and within the considered range of values in the absolute errors matrix;

- when optimizing ε parameter for each fragment, MSD and max absolute error decreased by ~ 17 and $\sim 8.3\%$ respectively, which is relative to the common ε parameter optimization results for all the fragments, obtained in the pilot research;
- the authors developed the PSO modification, which has proved to be an effective tool for the ε parameter sub-optimization problems solution in 2-dimensional CGA MAF.

References

1. Neydorf R (2015) Bivariate “Cut-Glue” approximation of strongly nonlinear mathematical models based on experimental data. SAE Int J of Aerosp. doi:[10.4271/2015-01-2394](https://doi.org/10.4271/2015-01-2394)
2. Neydorf R, Sigida Y (2014) Identification of traction and power characteristics of air-screw propulsors in mathematical description of airship. SAE Tech Pap. doi:[10.4271/2014-01-2134](https://doi.org/10.4271/2014-01-2134)
3. Neydorf R, Sigida Y, Voloshin V et al (2013) Stability analysis of the MAAT feeder airship during ascent and descent with wind disturbances. SAE Tech Pap. doi:[10.4271/2013-01-2111](https://doi.org/10.4271/2013-01-2111)
4. Voloshin V, Chen Y, Neydorf R et al (2013) Aerodynamic characteristics study and possible improvements of MAAT feeder airships. SAE Tech Pap. doi:[10.4271/2013-01-2112](https://doi.org/10.4271/2013-01-2112)
5. Pshikhopov V, Medvedev M, Neydorf R et al (2012) Impact of the feeder aerodynamics characteristics on the power of control actions in steady and transient regimes. SAE Tech Pap. doi:[10.4271/2012-01-2112](https://doi.org/10.4271/2012-01-2112)
6. Pshikhopov V, Medvedev M, Gaiduk A et al (2013) Mathematical model of robot on base of airship. Proc 52nd IEEE Conf Decis Control. doi:[10.1109/CDC.2013.6760006](https://doi.org/10.1109/CDC.2013.6760006)
7. Neydorf R, Krukhmalev V, Kudinov N et al (2013) Methods of statistical processing of meteorological data for the tasks of trajectory planning of MAAT feeders. SAE Tech Pap. doi:[10.4271/2013-01-2266](https://doi.org/10.4271/2013-01-2266)
8. Neydorf R, Sigida Y, Kudinov N et al (2014) Aerostatic aircraft flight environment modelling and investigation. SAE Tech Pap. doi:[10.4271/2014-01-2147](https://doi.org/10.4271/2014-01-2147)
9. Neydorf R (2014) “Cut-Glue” Approximation in problems on static and dynamic mathematical model development. Proc ASME2014 Int Mech Eng Congr Expo. doi:[10.1115/IMECE2014-37236](https://doi.org/10.1115/IMECE2014-37236)
10. Neydorf R (2016) Technology of Cut-Glue approximation method for modeling strongly nonlinear multivariable objects. Theoretical bases and prospects of practical application. SAE Tech Pap. doi:[10.4271/2016-01-2035](https://doi.org/10.4271/2016-01-2035)
11. Eberhart RC, Kennedy JA (1995) A new optimizer, using particle swarm theory. Proc 6th Int Symp Micromac Hum Sci. doi:[10.1109/MHS.1995.494215](https://doi.org/10.1109/MHS.1995.494215)
12. Kennedy J, Eberhart R (1995) Particle swarm optimization. Proc IEEE Int Conf Neural Netw. doi:[10.1109/ICNN.1995.488968](https://doi.org/10.1109/ICNN.1995.488968)
13. Shi Y, Eberhart R (1998) A modified particle swarm optimizer. Proc IEEE Congr Evol Comput. doi:[10.1109/ICEC.1998.699146](https://doi.org/10.1109/ICEC.1998.699146)
14. Clerc M, Kennedy J (2002) The particle swarm-explosion, stability, and convergence in a multi-dimensional complex space. Proc IEEE Trans Evol Comput. doi:[10.1109/4235.985692](https://doi.org/10.1109/4235.985692)
15. Mendes R, Kennedy J, Neves J (2004) The fully informed particle swarm: simpler, maybe better. Proc IEEE Trans Evol Comput. doi:[10.1109/TEVC.2004.826074](https://doi.org/10.1109/TEVC.2004.826074)
16. Chernogorov IV, Neydorf RA (2015) Parametrical research of the swarming particles algorithm in the problem of finding the global extremum. Proc 28th Int Sci Conf “Math Methods in Eng and Technol”. 3(73)/3:75–80

17. Neydorf RA, Chernogorov IV, Iarakhmedov OT et al (2015) Experimental study on solution possibilities of multiextremal optimization problems through heuristic methods. Her Don State Tech Univ. doi:[10.1109/12737/16074](https://doi.org/10.1109/12737/16074)
18. Neydorf RA, Chernogorov IV, Iarakhmedov OT et al (2016) Possibilities solving of multiextremal optimization tasks by heuristic methods. *Hi-tech Earth Space Res* 2(8):16–25
19. Neydorf RA, Polyakh VV, Chernogorov IV et al (2016) Study of heuristic algorithms in planning and optimization of routes problem in the environment with obstacles. *Proc S Fed Univ Tech Sci* 3(176):127–143

Computational Evaluation of Transverse Thermal Conductivity of Natural Fiber Composites

Zia Javanbakht, Wayne Hall and Andreas Öchsner

Abstract The finite element analysis is used to investigate the sensitivity of the effective transverse thermal conductivity of polymeric composites reinforced with Manila hemp fibers in terms of their degree of saturation. It is predicted that the hierarchical structure of the fiber bundle will highly magnify the rate of water absorption and in consequence, the effective transverse thermal conductivity of the composite is altered. This influence is quantized in terms of the volume fraction of the fiber bundle and the lumen to produce a homogenized representative continuum. It was found that increasing the fiber volume fraction in a dry medium results in a decrease in the thermal conductivity whereas an increase of conductivity will be evident in a wet condition. Furthermore, the increase in the volume fraction of the lumen enhances the thermal conductivity by retaining more water during saturation which supports the developed hypothesis.

Keywords Thermal conductivity · Finite element method · User subroutine · Water content · Moisture

1 Introduction

Natural fibers are widely used in various polymeric media for their typical low density, moderate cost, good specific strength, abundance and renewability of resources, and biodegradability among other favored qualities. Nevertheless, the natural variability of properties, deficient fiber-to-matrix bonding, and more importantly their hydrophilic character introduce some challenges to their appli-

Z. Javanbakht (✉) · W. Hall · A. Öchsner
Griffith School of Engineering, Griffith University, Gold Coast, QLD 4214, Australia
e-mail: zia.javanbakht@gmail.com

W. Hall
e-mail: w.hall@griffith.edu.au

A. Öchsner
e-mail: a.oechsner@griffith.edu.au

cation. For instance, outdoor usage of natural composites is limited because of the susceptibility of their fiber reinforcements to some environmental factors [1, 20].

The porous structure of natural fibers makes them better thermal insulators compared to synthetic fibers such as glass or carbon [16]. On the other hand, their relatively low thermal conductivity may cause heat dissipation difficulties in some cases [13]. This trade-off attracted researchers in the past decades to investigate the naturally anisotropic thermal behavior of these composites in terms of their volumetric composition [24], volume fraction of fibers [14], fiber orientation [3], and thermal diffusivity [13, 17] among other effective parameters.

The mechanical properties of cellulose fibers are sensitive to the moisture content, particularly when incorporated into polymeric resins [7]. Namely, the hygroscopic behavior of natural fibers results in dimensional instabilities, i.e., swelling and shrinkage, which may induce residual stresses and microcracks into the composite as well as the debonding of the fibers [4, 21]. From a macroscopic point of view, moisture initiates the degradation process of the natural fibers which in consequence, affects the properties of the composite. For instance, reduction of the elastic modulus and tensile strength [5, 6], fluctuation of the impact strength [2], and even the initiation of a fungal decay process [23] is foreseeable. Moreover, considering the porosity of the fibrous structure, the thermal conductivity of natural fibers is predicted to be affected by the presence of water.

Various theoretical and experimental methods were used to predict the thermal behavior of natural fibers but the scarcity of the research on the effect of saturation motivated the current work which is basically a computational effort to envision the big picture of the saturation process. In the current study, the effect of water content on the insulation role of a composite—reinforced with Manila hemp fibers in a high density polyethylene (HDPE) matrix—is investigated using the finite element method. A list of the used symbols in the current work is also provided (see Table 1).

Table 1 List of symbols

γ	Mesh density
ϕ	Volume fraction
ϕ_{fb}	Volume fraction of the fiber bundle
ϕ_ℓ	Volume fraction of the lumen
ΔT	Prescribed temperature gradient
a	Element edge length
k_{eff}	Effective thermal conductivity of the composite
w	Width of the representative volume element (RVE), i.e., the distance between the boundary faces
A_0	Cross-sectional area perpendicular to direction of the flux
\dot{Q}	Total heat flux
S_w	Degree of saturation
V_w	Volume of the water
V_{void}	Total volume of the voids

2 Methodology

In the current study, the finite element method [18, 19] was used to estimate the effective thermal conductivity of unidirectional Manila hemp fiber bundles in the transverse (i.e., perpendicular to the principal fiber axis) direction. A four-phase continuum was created using the MSC Marc (version 2014.2) commercial finite element package. This software was selected due to its capability of incorporating user-written pieces of code into its core algorithm. Namely, the customized procedures can be carried out using the subroutines written in the Fortran programming language [10]. This facility—along with the provided Python scripting tool—makes it possible to fully automatize the parametric study [11, 12].

The composite is assumed to be made up of unidirectional hemp fiber bundles (see Fig. 1). Each fiber bundle consists of a set of lumens which are basically slender tubular structures that provide the air cavities [26]. Since the porosity of a natural fiber defines its capacity to hold water [21], the storage of moisture is done by filling the tubes with water and creating a wet lumen.

A recent research shows that the bulk property of the fibrous structure can be properly modeled, within an acceptable margin of error, irrespective of the exact micro-level structure [15]. Therefore, a unit cell of the composite is selected as the RVE of the whole composite. In order to capture the hierarchy of the structure, the accumulated effect of the individual sub-structures are considered in four distinct layers:

1. a polymeric matrix of HDPE,
2. the solid part of the Manila hemp fiber bundle,

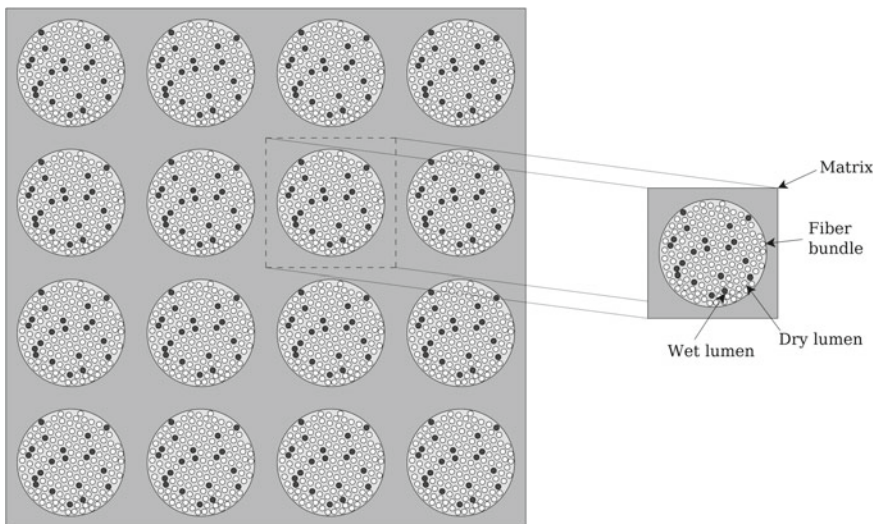


Fig. 1 Selected RVE from the unidirectional composite

3. the water contained in the lumens, and
4. the air which fills the remaining volume.

These four phases take part in the occurring conduction process within the composite (see Fig. 2). The thermal conductivities of these individual components are listed in Table 2. This implies the fact that since the encapsulated water is stationary, no convection is taking place and the only means of heat transfer is the conduction mechanism [21].

A 2D finite element model, with a thickness of the unit length, was created using a uniform mesh of elements of type 39, i.e., the 4-node bilinear isoparametric planar heat transfer elements. The uniform mesh density (γ) is defined using the following equation:

$$\gamma = \frac{1}{a}, \quad (1)$$

where a is the characteristic dimension of the element, i.e., the edge length of each square element. Following several sensitivity analyses, it was observed that the mesh sensitivity was diminished for mesh densities over 300, and thus a mesh density of 400 is used in the simulations.

It is worth emphasizing that only one type of element was used with four different material properties which represented the four distinct phases of the problem. Based on the volume fraction values of fiber bundle and lumen plus the degree of saturation of the fiber, the occupied volume of each phase was calculated at the beginning of each analysis. In the next step, different properties were assigned to the elements by means of the ANKOND user subroutine. This subroutine is responsible for the anisotropic thermal behavior of the material and it was called upon the material assignment stage of the finite element analyses.

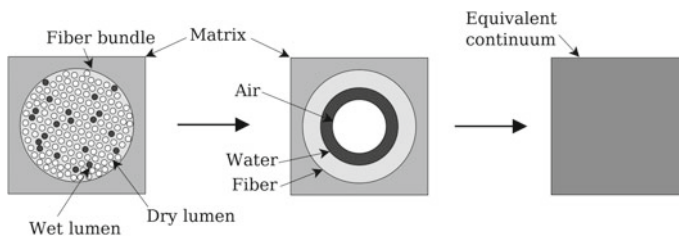
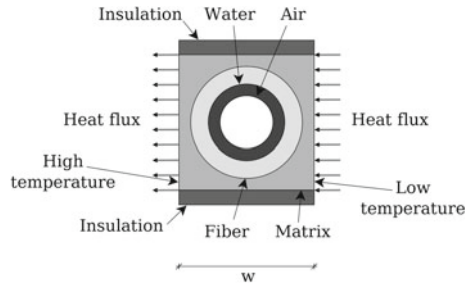


Fig. 2 Homogenization process of the RVE

Table 2 Thermal conductivity of the composite components

Component	Material	Conductivity ($\frac{W}{m \cdot K}$)
Matrix	HDPE	0.4025 [22]
Solid fiber	Hemp	0.1847 [15]
Lumen	Air	0.0026 [15]
Moisture	Water	0.606 [25]

Fig. 3 Finite element model of the composite RVE



Inasmuch as the prescribed temperature boundary conditions provide the most precise results in thermal conductivity analyses [9], two set of prescribed temperatures were assigned to the left- and right-hand nodes of the RVE. Namely, a high temperature of 20°C and a lower temperature of 0°C was assigned as the boundary conditions. This established a temperature gradient which was followed by a heat flux in the transverse direction (see Fig. 3). The reaction heat flux of the lower temperature region was summed up and used to calculate the effective transverse thermal conductivity of the composite by means of the Fourier’s law [8]:

$$k_{\text{eff}} = \frac{\dot{Q}}{A_0} \cdot \frac{w}{\Delta T}, \tag{2}$$

where k_{eff} is the effective thermal conductivity of the composite, \dot{Q} is the total reaction flux in the top boundary conditions, A_0 is the cross-sectional area perpendicular to direction of the flux, w is the width of the RVE (distance between the boundary faces), and ΔT is the prescribed temperature difference.

To represent the water content of the specimens, the degree of saturation (S_w) was used, which can be defined as follows:

$$S_w = \frac{V_w}{V_{\text{void}}}, \tag{3}$$

where V_w is the volume of the water, and V_{void} is the total volume of the voids.

Finally, in the current study, the assumptions can be summarized into the following points:

- the porosity of the matrix is neglected,
- the effect of the thermal barrier resistance is neglected,
- it is assumed that the thermal conductivity of the solid portion of hemp fiber bundles is independent of the lumen size,
- the thermal conductivity of all the components is assumed to remain constant by increasing the temperature, and
- the solid portion of the hemp fiber bundle is assumed to have no porosity and all the porosity is provided by the lumens.

3 Results and Discussion

In a typical hemp fiber, the average diameter of the fiber bundle and lumens are 213 and 16.5 microns, respectively. Also an average number of 137 lumens exists in every fiber bundle which results in an average lumen volume fraction of 30.87% [15]. The saturation of this typical hemp fiber is simulated and the effective transverse thermal conductivity is calculated using the accumulated reaction heat fluxes (see Fig. 4). It can be noted that by increasing the degree of saturation, the effective thermal conductivity experiences an increase which happens in a higher rate for the higher fiber bundle volume fractions. For instance, for a fiber bundle volume fraction of 60%, the saturation causes an increase of the thermal conductivity by 25.79% whereas the same value was only improved by 3.79% for a volume fraction of 10%. In other words, although the lumen fraction is kept constant, the amount of absorbed water increases due to the overall increase in the cross-sectional area of the fiber bundle.

The effect of lumen volume fraction is investigated for two extreme fiber bundle volume fractions, i.e., a high volume fraction of 60% and low volume fraction of 10% (see Figs. 5 and 6). Increasing the lumen volume fraction in either case results in an increase in the effective thermal conductivity due to saturation. This effect is augmented in higher fiber bundle volume fractions. For example, the complete saturation of a low fiber content composite with a small lumen volume fraction increases the transverse thermal conductivity by only 1.24% whereas a high content fiber with a high lumen volume fraction undergoes a 44.61% improvement.

In the dry composite samples, increasing the fiber bundle volume fraction reduces the effective thermal conductivity for a specific lumen volume fraction.

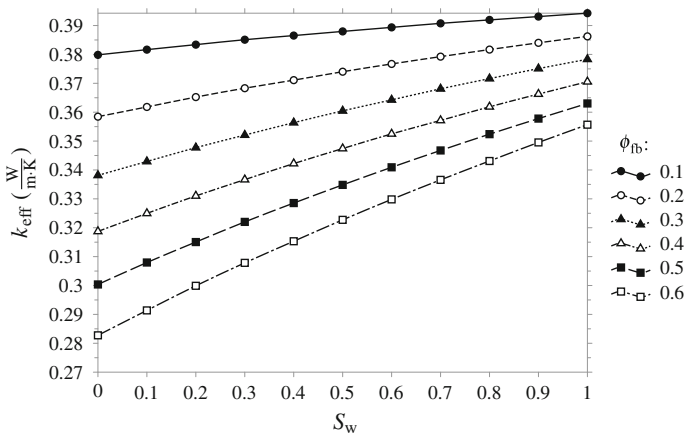


Fig. 4 Effective transverse thermal conductivity of a typical lumen fraction ($\phi_l = 30.87\%$)

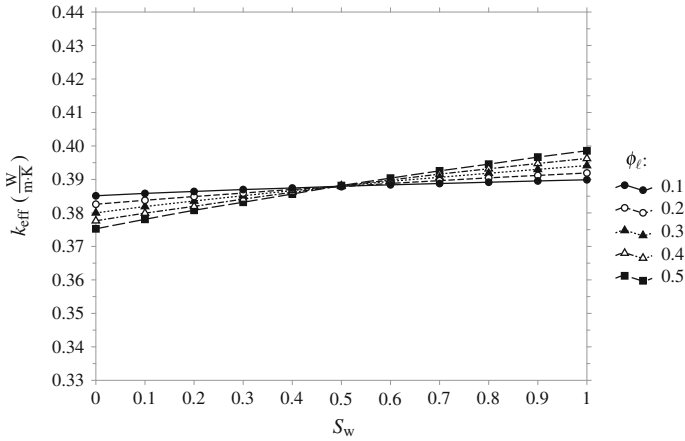


Fig. 5 Effective transverse thermal conductivity of low fiber volume fraction composite ($\phi_{fb} = 10\%$)

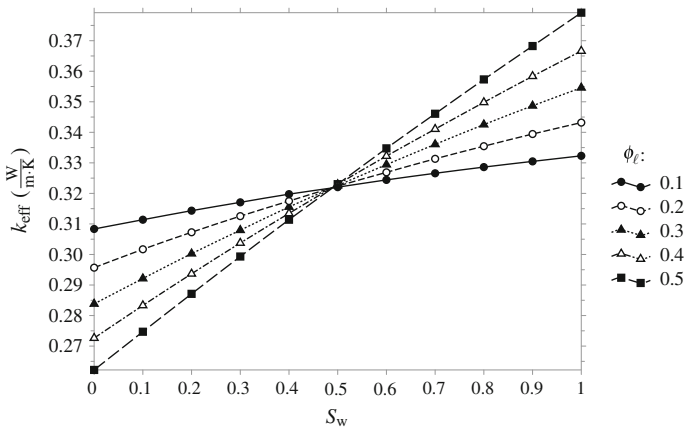


Fig. 6 Effective transverse thermal conductivity of high fiber volume fraction composite ($\phi_{fb} = 60\%$)

Similarly, increasing the lumen volume fraction for a specific fiber bundle volume fraction, decreases the thermal conductivity of the specimen (see Fig. 7). On the other hand, in a fully saturated composite sample, the effect is opposite to that of the dry sample due to the higher thermal conductivity of the absorbed water compared to air (see Fig. 8).

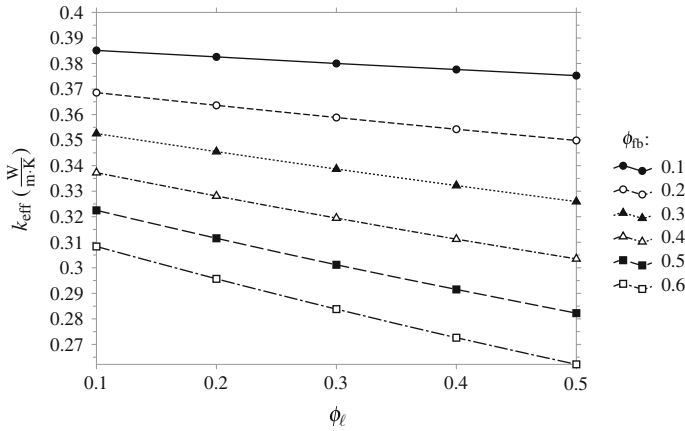


Fig. 7 Effective transverse thermal conductivity of dry composite specimens

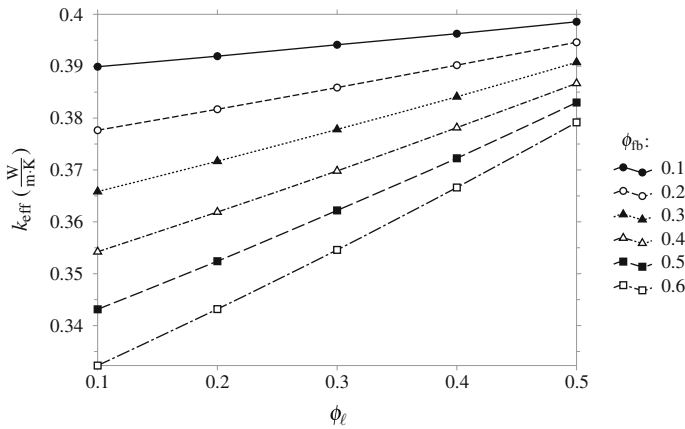


Fig. 8 Effective transverse thermal conductivity of fully saturated composite specimens

4 Conclusion

In summary, the porosity of the Manila hemp fiber bundles affected the effective transverse thermal conductivity of the natural composite. Namely, a decrease was observed in the dry samples whereas an improvement in the effective thermal conductivity of the composite happened for the fully saturated samples. This effect was highly augmented in high fiber bundle volume fractions or high lumen volume fractions. In either case, the amount of water absorption was increased due to increased volume of the voids within the fiber bundle and in consequence, increased the effective transverse thermal conductivity of the composite.

References

1. Assarar M, Scida D, El Mahi A, Poilâne C, Ayad R (2011) Influence of water ageing on mechanical properties and damage events of two reinforced composite materials: flax–fibres and glass–fibres. *Mater Des* 32(2):788–795
2. Athijayamani A, Thiruchitrambalam M, Natarajan U, Pazhanivel B (2009) Effect of moisture absorption on the mechanical properties of randomly oriented natural fibers/polyester hybrid composite. *Mater Sci Eng, A* 517(1–2):344–353
3. Behzad T, Sain M (2007) Measurement and prediction of thermal conductivity for hemp fiber reinforced composites. *Polym Eng Sci* 47(7):977–983
4. Céline A, Freour S, Jacquemin F, Casari P (2014) The hygroscopic behavior of plant fibers: a review. *Front Chem* 1:1–12
5. Chow CPL, Xing XS, Li RKY (2007) Moisture absorption studies of sisal fibre reinforced polypropylene composites. *Compos Sci Technol* 67(2):306–313
6. Dhakal H, Zhang Z, Richardson M (2007) Effect of water absorption on the mechanical properties of hemp fibre reinforced unsaturated polyester composites. *Compos Sci Technol* 67(7–8):1674–1683
7. Faruk O, Bledzki AK, Fink HP, Sain M (2012) Biocomposites reinforced with natural fibers: 2000–2010. *Prog Polym Sci* 37(11):1552–1596
8. Fiedler T, Hosseini S, Belova IV, Murch GE, Öchsner A (2009) A refined finite element analysis on the thermal conductivity of perforated hollow sphere structures. *Comput Mater Sci* 47(2):314–319
9. Islam MR, Pramila A (1999) Thermal conductivity of fiber reinforced composites by the fem. *J Compos Mater* 33(18):1699–1715
10. Javanbakht Z, Öchsner A (2017) Advanced finite element simulation with MSC Marc: application of user subroutines. Springer, Cham
11. Javanbakht Z, Hall W, Öchsner A (2016a) Automated estimation of the effective thermal conductivity of carbon fiber reinforced composite materials. *Defect Diffus Forum* 370:177–183
12. Javanbakht Z, Hall W, Öchsner A (2016b) Finite element evaluation of effective thermal conductivity of short carbon nano tubes: a comparative study. *Defect Diffus Forum* 372:208–214
13. Kalaprasad G, Pradeep P, Mathew G, Pavithran C, Thomas S (2000) Thermal conductivity and thermal diffusivity analyses of low-density polyethylene composites reinforced with sisal, glass and intimately mixed sisal/glass fibres. *Compos Sci Technol* 60(16):2967–2977
14. Li X, Tabil LG, Oguocha IN, Panigrahi S (2008) Thermal diffusivity, thermal conductivity, and specific heat of flax fiber–hdpe biocomposites at processing temperatures. *Compos Sci Technol* 68(7–8):1753–1758
15. Liu K, Takagi H, Yang Z (2011) Evaluation of transverse thermal conductivity of manila hemp fiber in solid region using theoretical method and finite element method. *Mater Des* 32(8–9):4586–4589
16. Liu K, Takagi H, Osugi R, Yang Z (2012) Effect of lumen size on the effective transverse thermal conductivity of unidirectional natural fiber composites. *Compos Sci Technol* 72(5):633–639
17. Mangal R, Saxena NS, Sreekala MS, Thomas S, Singh K (2003) Thermal properties of pineapple leaf fiber reinforced composites. *Mater Sci Eng, A* 339(1–2):281–285
18. Öchsner A (2016) Computational statics and dynamics: an introduction based on the finite element method. Springer, Singapore
19. Öchsner A, Merkel M (2013) One-dimensional finite elements: an introduction to the FE method. Springer, Berlin and Heidelberg
20. Placet V (2009) Characterization of the thermo-mechanical behaviour of hemp fibres intended for the manufacturing of high performance composites. *Compos A Appl Sci Manuf* 40(8):1111–1118

21. Rakovsky SK (2014) Analytical tools and industrial applications for chemical processes and polymeric materials. Apple Academic Press, Point Pleasant
22. Rauwendaal C (2014) Polymer extrusion, 5th edn. Hanser Publications and Hanser Publication, Munich and Cincinnati
23. Schirp A, Wolcott MP (2007) Influence of fungal decay and moisture absorption on mechanical properties of extruded wood-plastic composites. *Wood Fiber Sci* 37(4):643–652
24. Shah DU, Bock MCD, Mulligan H, Ramage MH (2016) Thermal conductivity of engineered bamboo composites. *J Mater Sci* 51(6):2991–3002
25. Singh RP, Heldman DR (2014) Introduction to food engineering, 5th edn. Food science and technology international series. Elsevier Academic Press, Amsterdam
26. Wang H, Xiao Y, Qin QH (2016) 2D hierarchical heat transfer computational model of natural fiber bundle reinforced composite. *Scientia Iranica Trans B, Mech Eng* 23(1):268

Morphology and Elemental Composition of Metal Based Granules in Wings of Bumblebees

Kateřina Dědková, Petr Jandačka, Rostislav Váňa, Jana Kukutschová and Nikola Vítkovská

Abstract The paper addresses detection and elemental analysis of solid metal-based particles/clusters present in wings of laboratory bread bumblebees. The goal of the article is detection and characterization of morphology and chemical composition of those particles. A combination of Gallium Focused Ion Beam (FIB)—Scanning electron microscopy (SEM) and energy dispersive X-ray spectroscopy (EDS) mapping were used for evaluation of particles/clusters localization in the samples. FIB allowed etching of subsurface structures and deeper understanding of particles/clusters structure. EDS mapping revealed distribution of single elements in detected particles/clusters. It was found that all evaluated particles/clusters were based on iron or iron oxides and were associated with calcium structures. Several other elements such as Al, Mg, Ti, Zn or Si were also detected. Several hypotheses for role of the detected particles were introduced, however the real purpose was not revealed.

Keywords Biomineralisation · Bumblebee · Iron granules · Magnetoreception

K. Dědková (✉) · J. Kukutschová
Nanotechnology Centre, VŠB—Technical University of Ostrava, 17. listopadu 15,
70833 Ostrava-Poruba, Czech Republic
e-mail: katerina.dedkova@vsb.cz

K. Dědková · J. Kukutschová
Regional Materials Science and Technology Centre, VŠB—Technical University of Ostrava,
17. listopadu 15, 70833 Ostrava-Poruba, Czech Republic

P. Jandačka · N. Vítkovská
Institute of Physics, Faculty of Mining and Geology, VŠB—Technical University of Ostrava,
17. listopadu 15, 70833 Ostrava-Poruba, Czech Republic

R. Váňa
TESCAN Brno, s.r.o., Libušina třída 1, 62300 Brno, Czech Republic

1 Introduction

Appearance of metal based particles in several organisms was proved. Solid particles based on metal and metal oxides were found in pigeons [10], ants [1], larvae of flies [5], mammals [3] or humans [4], however in several cases their function or purpose was not clarified yet. Several discussions are kept in order to uncover this issue.

For purpose to clarify insect magnetoreception [21] and detect requisite magnetosensor we recently discovered iron-based magnetic structures in the head and in the wings of bumblebees [13], in roots of surface hairs. The energy dispersive X-ray spectroscopy in SEM, X-ray powder diffraction and Mössbauer measurements revealed that these structures should be present in form of iron oxides but exact mineralogical composition is still unclear. In this paper advanced analysis of the mentioned structures is presented.

Several histological discoveries on animals that seemed to be promising in sense of magnetoreception, for example a magnetite in pigeon upper beak [8–10] or magnetic cells in trout olfactory epithelium [7], were subsequently designated as a metabolic waste or contamination of tissue [6, 11, 19]. To avoid similar potentially incorrect hypotheses we had to deal with several possibilities how to interpret the presence these magnetic corpuscles.

In our previous work [13] we stated three potential hypotheses about a role of these structures in body of bumblebees. The first role is as a metabolic waste, the second as ferritin based clusters that serve as an iron-storage for hairs and the third possibility is for magnetosensation of geomagnetic field for space orientation in the environment. Using the analogy between surface hairs and ear hairs, the iron storage hypothesis can be supported by works where a deficit of Fe in nutriment for rats induced a damage of their inner ear receptor hairs [16, 17]. Alternatively as fourth possibility an external mechanical contamination (caused e.g., by wear of stainless cutting tools) was rejected since the cuticular surface is obviously not damaged around the iron-based structures.

According the work [13] where the iron based granules were detected in the basis of hairs on head and wings of bumblebees arose the question and need to characterize those particles more deeply. Need to propose their function led the work to focus on the better detection and characterization of morphology and chemical composition those particles. This study is focused only on particles detected on wings of bumblebees.

2 Materials and Methods

2.1 Biological Samples

Bumblebee species *Bombus terrestris* was used in the study. Bumblebees were obtained from a special breed from the Research Institute for Fodder Crops

(VUP) in Brno—Troubsko, Czech Republic. There bumblebees were bred at 25 °C and 50–60% humidity. They were fed with sugar solution and pollen, which is collected from honeybees. Two groups of bumblebees were obtained—juveniles (at least 24 h old) and adults. Their death was caused by freezing. Their wings were carefully cut of in flow-box, put into Eppendorf tubes and used in further analysis.

2.2 *Microscopic Analysis*

We used ultra-high resolution SEM with Schottky field emission cathode in combination with gallium Focused Ion Beam (FIB) column—Cobra type (TESCAN GAIA3 GMU Microscope) enabled serial etching of detected metal based granules. The microscope was equipped with SE (Everhart-Thornley) detector, In-Beam SE detector, Motorized Retractable Low-Voltage BSE detector and In-Beam BSE detector. EDS analysis was performed with X-Max^N 150 (Oxford instruments) and the EDS data were processed in AZtec software. Analyzed wings were attached on the carbon tape and sputter coated with thin film of platinum due to the conductivity.

3 Results and Discussion

Five pairs of wings of each group (adult and juvenile individuals) were examined using SEM-FIB system. Combination of SE and BSE detectors enabled to see shape and also material contrast, which proved to be very useful in searching and determining metal and metal oxide based granules. The gallium FIB has been proved to be very useful for better understanding of the structure of detected particles and especially their internal structure. All particles/clusters that were found occurred only in one area of a wing analyzed (see Fig. 1). Those particles were detected in both juvenile wings as well as adult wings.

All detected particles were solid and deposited shallow under the cuticle. Almost all detected particles/clusters were somehow connected with the presence of calcium and they were covered or gripped in it. Iron was found in all detected particles/clusters. Some of them were consisted mainly of iron. Nevertheless most of the detected particles/clusters were created also by other metals such as aluminum, titanium and chromium. Oxygen, silicon and other elements were present in minority (see Figs. 2, 3, 4 and 5).

Therefore a question was how these particles/clusters arose in the tissue. According to the process of sample preparation and storage it can be assumed that metal based particles does not come from a contamination. Bumblebees were not bred in sterile conditions however they were not exposed to metal pollution. It is

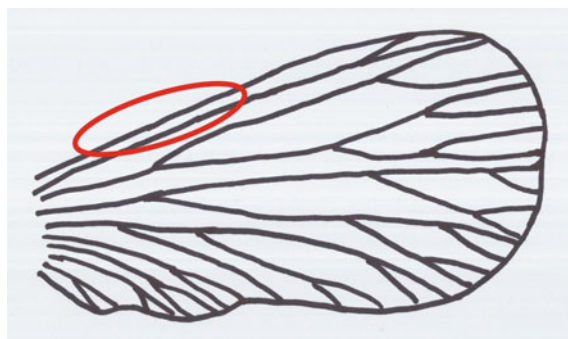


Fig. 1 Schematic figure of bumblebee's wing with localization of detected particles/clusters

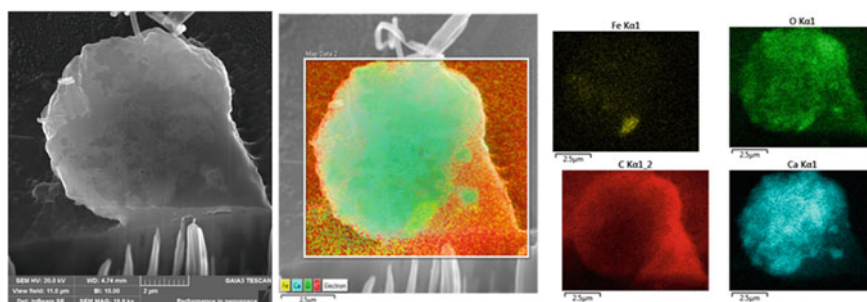


Fig. 2 Image of the detected particle/cluster No. 1 in SE mode, over layered image of elemental distribution and distribution of each detected element

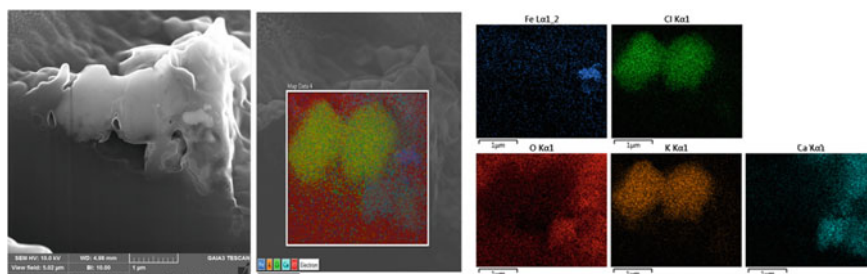


Fig. 3 Image of the detected particle/cluster No. 2 in SE mode, over layered image of elemental distribution and distribution of each detected element

visible from comparison of SE and BSE images (Figs. 6, 7, 8 and 9) that those particles are present under the cuticle.

This observation also supports this assumption. Edelman with his colleagues [6] studied extracellular structures composed of iron, titanium, silicon and chromium in

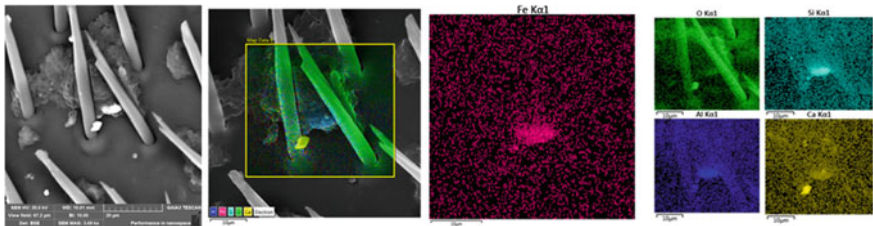


Fig. 4 Image of the detected particle/cluster No. 3 before etching in SE mode, over layered image of elemental distribution and distribution of each detected element of the detected particle/cluster No. 3 after etching in SE mode

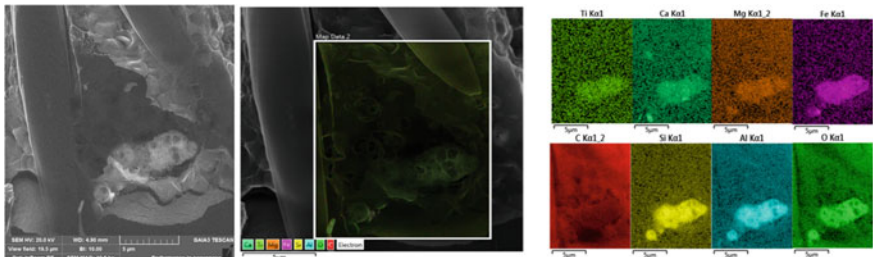


Fig. 5 Image over layered image of elemental distribution and distribution of each detected element

the respect to their magnetic properties in cells of pigeon’s brain. They assumed that those structures based on titanium and chromium cannot be of biogenic origin and presume their presence to be a contamination form laboratory environment and from tools used during their work. However, they also discovered iron-rich organelle in the hair cells in the pigeon and declared the need of development of advanced microscopic techniques like focus ion beam for better description of those structures. Amor [2] discovered chemical signature of magnetotactic bacteria where trace elements such as zinc, cobalt or manganese were found incorporated in magnetite. These trace elements are cofactors of metalloenzymes and are essential for bacterial metabolism.

The magnetometric study of ferritin in cells of inner ear cells of birds was conducted by Jandačka [12]. This study tried to find an answer to the question if cuticulosomes serve as magnetosomes. Fleissner with colleagues [9] studied iron-crusted vesicles in the upper beak of homing pigeons. From the obtained results they draw that these vesicles allow birds to detect their geographic position by the magnetic vector and serve as magnetoreceptors. Improvement of analytical methods allowed Treiber [20] found out that these clusters of iron-rich cells are not magnetosensitive neurons but macrophages. Analysis of ultrastructure showed their subcellular architecture containing ferritine-like granules, siderosomes,

Fig. 6 Image of the detected particle/cluster No. 4 before after etching in SE and BSE mode, overlaid image of elemental distribution and distribution of each detected element

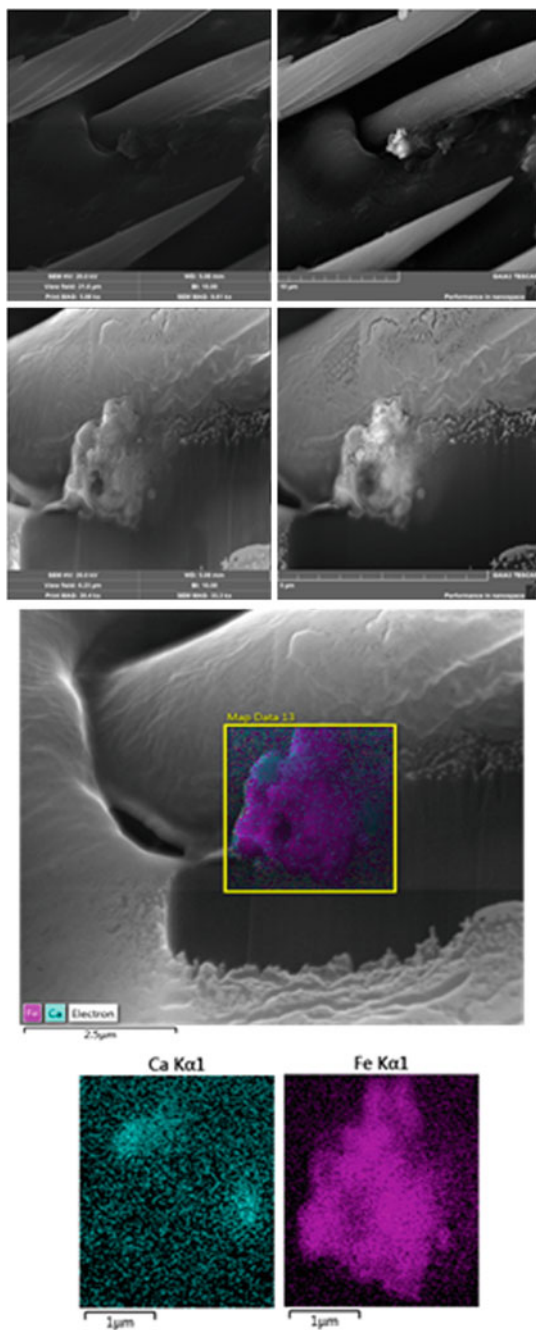


Fig. 7 Image of the detected particle/cluster No. 5 before after etching in SE and BSE mode, over layered image of elemental distribution and distribution of each detected element

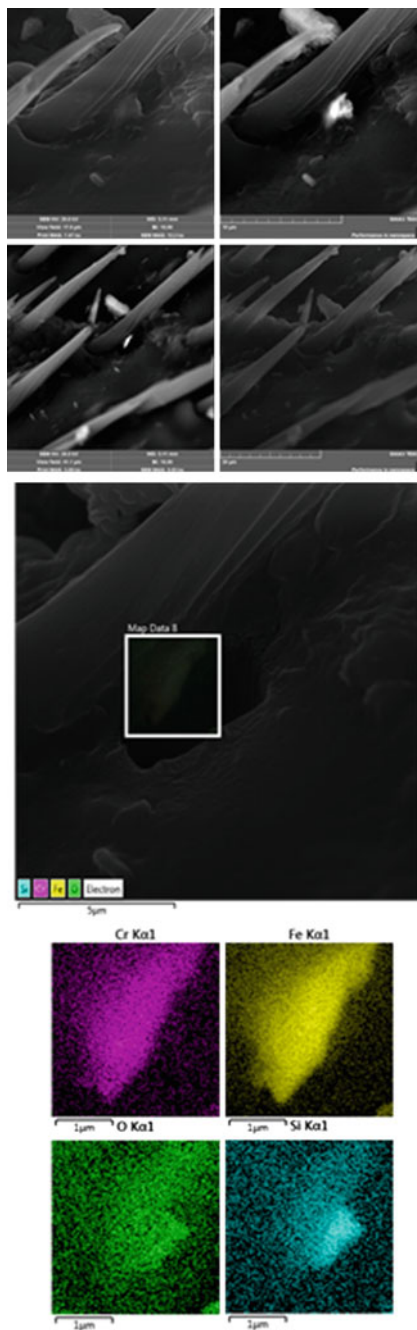
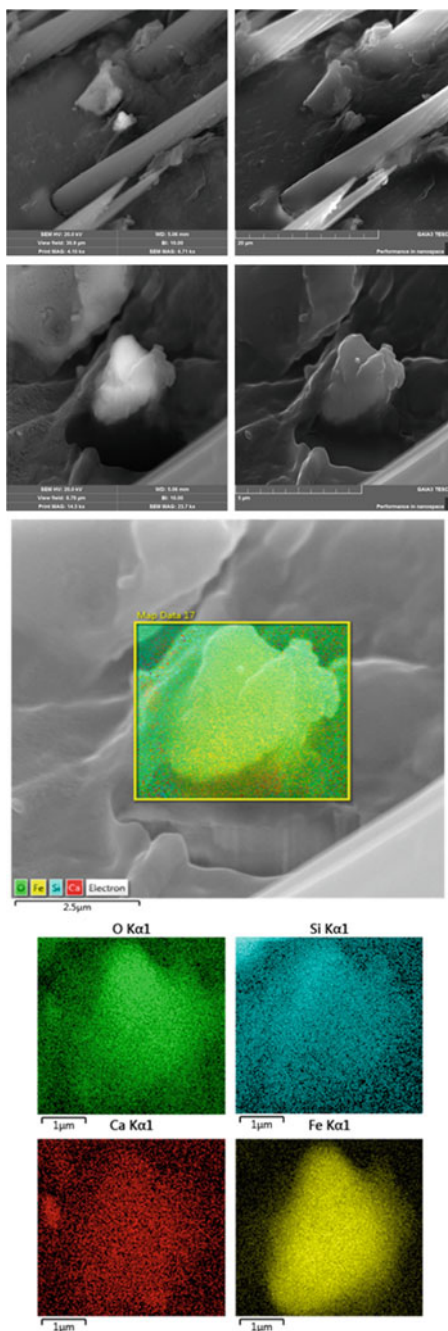


Fig. 9 Image of the detected particle/cluster No. 7 before after etching in SE and BSE mode, over layered image of elemental distribution and distribution of each detected element



hemosiderine and filopodia. The results are also supported by immunohistological studies.

Therefore it offers the possibility that metal-based particles/clusters detected in analyzed bumblebee's wings might have metabolic origin. With this premise another questions arise. What is the source of these metals and how long does it take to metabolize them and create such deposits? Juveniles were at least 24 h old and particles/clusters were found in their wings. If the origin of these particles is metabolic incorporations to decrease their possible toxicity it means quite fast metabolic response to the metals. It was described that nanoparticles induce inflammatory response of human body which leads to calcification of those particles [14, 18]. However this process takes up several years.

Other reason of the presence of those particles is that they serve as some sensors. Bio-sensors generally can be originated via biomineralization. During biomineralization transformation of amorphous carbonate into calcite occurs. Magnetosomes of certain strains of marine bacteria are originated due to the transformation of iron salts into magnetite [15]. This process is akin to biomineralization. The presence of calcium around metal-based particles might be associated with biomineralization process and with creation of some sensor.

In this moment we cannot say which explanation is the right one. Further studies will be focused on phase characterization of metal-based particles. If the iron present in particles is ferritin, it can indicate that these particles serve as reservoirs of iron for hairs on wings.

4 Conclusions

In this paper application of dual beam system Gallium Focused Ion Beam (FIB)—Scanning electron microscopy was introduced in the study of metal based clusters in bumblebee's wings. FIB allowed etching of detected particles/cluster and EDS mapping provided information about distribution of chemical elements. This method provided more information about the metal based particles/clusters however did not help to unclear the issue of particles/clusters origin. Further studies including FIB-SEM etching, nanomanipulation and phase analysis should help to find an answer on the questions.

Acknowledgements This paper was created on the Faculty of Metallurgy and Materials Engineering in the Project No. LO1203 “Regional Materials Science and Technology Centre—Feasibility Program” funded by Ministry of Education, Youth and Sports of the Czech Republic. The works were partially financed by project of students grant competition reg. no. SP2016/94 organized by Technical University of Ostrava, Faculty of Mining and Geology.

References

1. Abracado LG, Esquivel DMS, Wajnberg E (2008) Oriented magnetic material in head and antennae of *Solenopsis interrupta* ant. *J Magn Magn Mater* 320:E204–E206
2. Amor M, Busigny V, Durand-Dubief M, Tharaud M, Ona-Nguema G, Gélabert A, Alphandéry E, Menguy N, Benedetti MF, Chebbi I et al (2015) Chemical signature of magnetotactic bacteria. *Proc Natl Acad Sci* 112:1699–1703
3. Begall S, Malkemper EP, Cerveny J, Nemeč P, Burda H (2013) Magnetic alignment in mammals and other animals. *Mamm Biol* 78:10–20
4. Cabalova L, Cabanova K, Bielnikova H, Kukutschova J, Dvorackova J, Dedkova K, Zelenik K, Kominek P (2015) Micro—and nanosized particles in Nasal Mucosa: a pilot study. *Biomed Res Int*
5. Dommer DH, Gazzolo PJ, Painter MS, Phillips JB (2008) Magnetic compass orientation by larval *Drosophila melanogaster*. *J Insect Physiol* 54:719–726
6. Edelman NB, Fritz T, Nimpf S, Pichler P, Lauwers M, Hickman RW, Papadaki-Anastasopoulou A, Ushakova L, Heuser T, Resch GP et al (2015) No evidence for intracellular magnetite in putative vertebrate magnetoreceptors identified by magnetic screening. *Proc Natl Acad Sci* 112:262–267
7. Eder SHK, Cadiou H, Muhamad A, McNaughton PA, Kirschvink JL, Winklhofer M (2012) Magnetic characterization of isolated candidate vertebrate magnetoreceptor cells. *Proc Natl Acad Sci* 109:12022–12027
8. Fleissner G, Holtkamp-Rotzler E, Hanzlik M, Winklhofer M, Fleissner G, Petersen N, Wiltshcko W (2003) Ultrastructural analysis of a putative magnetoreceptor in the beak of homing pigeons. *J Comp Neurol* 458:350–360
9. Fleissner G, Stahl B, Thalau P, Falkenberg G, Fleissner G (2007) A novel concept of Fe-mineral-based magnetoreception: histological and physicochemical data from the upper beak of homing pigeons. *Naturwissenschaften* 94:631–642
10. Hanzlik M, Heunemann C, Holtkamp-Rotzler E, Winklhofer M, Petersen N, Fleissner G (2000) Superparamagnetic magnetite in the upper beak tissue of homing pigeons. *Biometals* 13:325–331
11. Jandacka P, Alexa P, Pistora J, Trojkova J (2013). Hypothetical superparamagnetic magnetometer in a pigeon's upper beak probably does not work. *Eur Phys J E* 36
12. Jandacka P, Burda H, Pistora J (2015). Magnetically induced behaviour of ferritin corpuscles in avian ears: can cuticulosomes function as magnetosomes? *J R Soc Interface* 12
13. Jandacka P, Kasparova B, Jiraskova Y, Dedkova K, Mamulova-Kutlakova K, Kukutschova J (2015) Iron-based granules in body of bumblebees. *Biometals* 28:89–99
14. Revuelta NC, Gonzalez-Fajardo JA, Bratos MA, Alvarez-Gago T, Aguirre B, Vaquero C (2014) Role of calcifying nanoparticle in the development of hyperplasia and vascular calcification in an animal model. *Eur J Vasc Endovasc* 47:640–646
15. Shastri VP (2015) Biomineralization: a confluence of materials science, biophysics, proteomics, and evolutionary biology. *MRS Bull* 40:473–477
16. Sun AH, Wang ZM, Xia SZ, Li ZJ, Lin DY, Liang ZF, Hu ZY, Wang GY, Ye XT (1991) Noise-induced hearing-loss in iron-deficient rats. *Acta Otolaryngol* 111:684–690
17. Sun AH, Xiao SZ, Zheng Z, Li BS, Li ZJ, Wang TY (1987) A Scanning electron-microscopic study of cochlear changes in iron-deficient rats. *Acta Otolaryngol* 104:211–216
18. Taverna D, Boraldi F, De Santis G, Caprioli RM, Quaglino D (2015) Histology-directed and imaging mass spectrometry: an emerging technology in ectopic calcification. *Bone* 74:83–94
19. Treiber CD, Salzer M, Breuss M, Ushakova L, Lauwers M, Edelman N, Keays DA (2013) High resolution anatomical mapping confirms the absence of a magnetic sense system in the rostral upper beak of pigeons. *Commun Integr Biol* 6:e24859

20. Treiber CD, Salzer MC, Riegler J, Edelman N, Sugar C, Breuss M, Pichler P, Cadiou H, Sunders M, Lythgoe M et al (2012) Clusters of iron-rich cells in the upper beak of pigeons are macrophages not magnetosensitive neurons. *Nature* 484:367–370
21. Valkova T, Vacha M (2012) How do honeybees use their magnetic compass? can they see the North? *Bull Entomol Res* 102:461–467

Modifications of Viscoelastic Properties of Natural Rubber/Styrene-Butadiene Rubber Blend by Electron Beam Irradiation

Ivan Kopal, Pavel Košťal, Zora Jančíková, Jan Valíček,
Marta Harničárová, Peter Hybler and Milena Kušnerová

Abstract The influence of high-energy electron beam irradiation on the viscoelastic properties of natural rubber/styrene-butadiene rubber blend has been investigated in the study presented in this paper. Changes in viscoelastic properties were studied as a function of radiation dose and temperature using the dynamic mechanical analysis in the temperature range from 10 to 240 °C at frequency of 0.5 Hz. The samples of material under the investigation were irradiated in the presence of air, at room temperature, using the 5 meV electron beam in the dose range from 50 to 300 kGy, with the maximum beam power of 50 W. The experimental results have shown that an increase in the radiation dose leads to an increase in the storage modulus and a corresponding decrease in the damping factor. With

I. Kopal (✉) · P. Košťal · J. Valíček · M. Harničárová · M. Kušnerová
Faculty of Mining and Geology, Institute of Physics, VŠB—Technical University of Ostrava,
Ostrava, Czech Republic
e-mail: ivan.kopal@vsb.cz

I. Kopal
Faculty of Industrial Technologies in Puchov, Alexander Dubcek University of Trencin,
Puchov, Slovakia

P. Košťal
Department of Material Engineering, VŠB—Technical University of Ostrava,
Ostrava, Czech Republic

Z. Jančíková
Department of Automation and Computing in Metallurgy, VŠB—Technical University
of Ostrava, Ostrava, Czech Republic

J. Valíček
Institute of Clean Technologies for Mining and Utilization of Raw Materials for Energy Use,
VŠB—Technical University of Ostrava, Ostrava, Czech Republic

J. Valíček · M. Kušnerová
RMTVC, Faculty of Metallurgy and Materials Engineering, VŠB—Technical University
of Ostrava, Ostrava, Czech Republic

P. Hybler
Slovak Medical University in Bratislava, University Centre of Electron Accelerators
in Trencin, Trencin, Slovakia

increasing radiation dose, the curing process of tested rubber blend begins and ends at lower temperatures, with a higher initial and final storage modulus and a lower initial damping factor, whereas the radiation dose has almost no impact on the final value of damping factor. The unified regression model describing analytically the dependence of all monitored properties of tested rubber blend on radiation dose with a high level of reliability was found as well using the multi-parametric fitting technique by a trust region algorithm of a nonlinear least-squares method.

Keywords Thermoplastic polyurethane · Relaxation transitions · Activation energy · Dynamic mechanical analysis

1 Introduction

The radiation technology is widely used to modify properties of various materials [1–3], particularly polymers, for specific practical applications. The most frequent way today is the exposure of polymeric materials to high-energy ionizing radiation that seems to be a very promising fashion of the polymers modification [4]. During irradiation of polymers by ionizing radiation several extremely reactive products are formed: excited atoms, molecules, ions and radicals. Secondary chemical reactions such as crosslinking, chain scission, modification of surface structure and number of others, which cause changes in chemical structure and properties of polymeric materials, are induced [5]. In general, the modifications of polymers as a result of irradiation depend on type and energy of incident particles, radiation dose used, internal structure of the polymer, temperature, pressure and other conditions of irradiation process [6]. Currently, the most frequently used way of modification of polymers is irradiation by γ -rays and by high-energy electron beams. The advantages of γ -radiation are simplicity of technology equipments, good diffusion of γ -rays through irradiated material as well as significantly lower demands on energy consumption compared to electron accelerating devices [7, 8]. However, the last allow high radiation doses and therefore very short processing time, significantly lower radiation hazard, very good control of performance, shape, energy and also electron beam intensity, therefore, they are more efficient for the polymer industry. The main limitation is the low electrons penetration into the polymeric material. On the other hand, the electron beam irradiation is really variable, quick, less energy-intensive, highly ecological and relatively very inexpensive method. It also provides new opportunities for industrial production, e.g. production of high-quality recycled rubbers for various practical applications, for instance in the sphere of automotive and tire industry [9, 10]. There are three basic reactions of polymers for electron beam irradiation: crosslinking, chain scission and neutral reaction which has small or almost no impact on the properties of the irradiated material. Using the electron beam irradiation, several changes in properties of polymeric materials can be achieved, e.g.: changes in mechanical strength, hardness, stress, Young's modulus, impact strength and flexural strength, melting index, swelling, as well as

solubility properties, surface topography, surface wetting properties and surface reactivity, adhesion of coatings by crosslinking of the organic layer and the substrate, etc. [11]. In recent times, the reports on effects of electron beam irradiation on rubber/styrene-butadiene rubber (NR/SBR) blends, that are used in a variety of industrial and household applications, are scarce. Particularly, the influence of electron beam irradiation on dynamic mechanical properties of these compounds is not yet sufficiently investigated due to their great diversity. Therefore, the aim of this study is to investigate the effect of electron beam irradiation on the dynamic mechanical properties of NR/SBR blend, namely the effect of high-energy electron beam irradiation on its viscoelastic behaviour quantified by the value of both, the dynamic storage modulus as well as the damping factor. This type of elastomeric compounds is frequently used in the rubber industry to obtain desirable physical properties, process ability and lower cost. Recently, the high-energy electron beam irradiation seems to be an ecological and relatively cheap alternative to conventional chemical methods of their thermal crosslinking [12, 13].

2 Experiment

2.1 Materials

The NR/SBR blend consisted of 23.5% styrene and 76.5% butadiene (Buna VSL 5025-0, LANXESS, Germany) which were mixed with Malaysian natural rubber (SVR 3L, Thuan Loi, Vietnam) in the ratio of 1:1. The mixture also contained the following additives: carbon black (N-550, Shizhong Industry, China), ZnO, stearic acid (Stearin III), antioxidants, antidegradants, plasticizer, accelerators, paraffin wax and sulphur. Any radiation vulcanization accelerators were not added to the mixture. The composition of the NR/SBR blend under investigation is presented in Table 1.

The studied compound was prepared by four-stage stirring. In the first stage of stirring, carbon black, ZnO, Stearin III and antidegradant (Dusantox IPPD, Duslo a. s., Slovakia) were mixed in the 30 ml chamber (Plastograf, Brabender, Germany) at 130 °C. The mixing time was 6 min. In the second stage, stirring was carried out at

Table 1 Compound of NR/SBR blend

Materials	Sign	Parts by weight (g)
Natural rubber	SVR 3L	745.97
Styrene-butadiene rubber	Buna VSL 5025-0	745.97
Carbon black	N-550	298.39
ZnO	ZnO	44.76
A mixture of stearic acid and palmitic acid	Stearin III	14.92
N-isopropyl -N'-phenyl-p-phenylenediamine	Dusantox IPPD	14.92
N-cyclohexyl-2-benzothiazolesulfenamide	Sulfenax CBS	14.92
S	Sulphur	14.92

60 °C and vulcanization accelerators (Sulfenax CBS, Duslo a.s., Slovakia) as well as sulphur were added. In the third and fourth stages of stirring, the above mentioned ingredients were added in small quantities to create a specific optimum composition of the mixture. The melt blending of mixture in the Haake Rheomix apparatus (Hake PolyLab, USA) was performed at 130 °C and the rotor speed of 50 rpm per 10 min. Then the blend was compression moulded into 2 mm thick sheets under the pressure of 150 kg cm⁻² in the electrically heated hydraulic press at 60 °C. After three minutes, these sheets were immediately cooled down to the temperature of 25 °C between two plates. From the prepared sheets, rectangular shape samples with dimensions of 50 mm (length) × 10 mm (width) × 2 mm (thickness) were cut off for the next dynamic mechanical analysis.

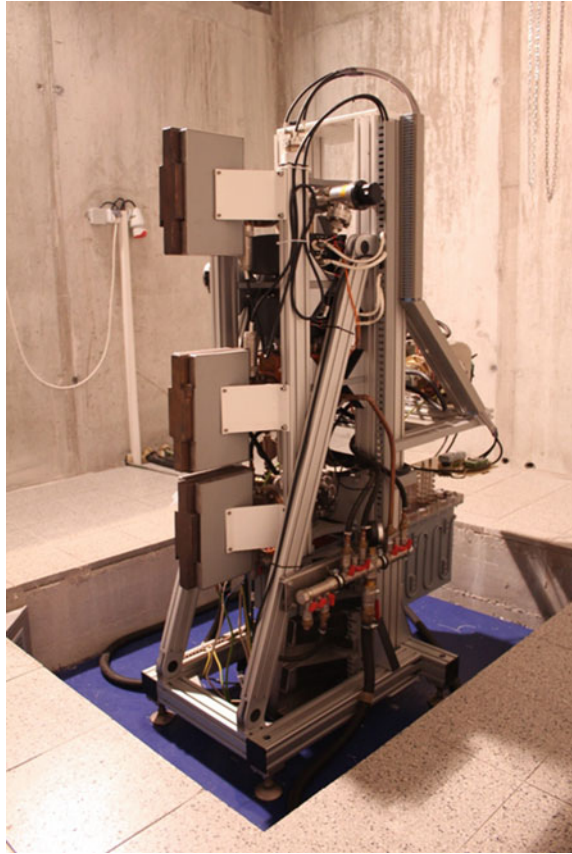
2.2 Radiation Treatment

Irradiation was carried out in the University Centre of Electron Accelerators of Slovak Medical University in Bratislava, Slovak Republic. The linear electron accelerator UELR-5-1S (RadiaBeam, Russia) was used for irradiation of tested NR/SBR samples. Parameters of the UELR-5-1S accelerator during experiment were as follows: energy of the electron beam was 50 meV, the maximum beam power was 50 W, the maximum output current in the beam window was 200 μA, electron gun was equipped with indirectly heated BaNi cathode, electrons were accelerated by high-frequency electromagnetic field produced by the magnetron operating in the pulse mode at frequency of 2998 MHz, pulse length was 3.5 μs and pulse frequency was 240 Hz. The samples were placed on a conveyor belt. To avoid an excess increase in sample temperature at higher radiation doses, the irradiation dose per exposure was 50 kGy and total irradiation given to each sample was controlled by the total number of passes. The time elapsed between two phases of exposure was about 20 min. Only one side of each test specimen was exposed to irradiation as the thickness of the tested specimen, equal to approximately 2 mm, was enough for penetration of the electron beam. The applied radiation doses were 50, 100, 150, 200, 250 and 300 kGy. Dosimetry was performed using cellulose tri-acetate. Irradiation was performed after every sample air cooling to room temperature and at the conveyor belt speed of 1 mm s⁻¹. The total radiation dose deviation was ±5%. The detail of the linear electron accelerator used can be seen in Fig. 1.

2.3 Dynamic Mechanical Analysis

The dynamic mechanical analysis (DMA) is a commonly used technique enabling the investigation of mechanical response of polymers. Recently, it has represented the most sensitive method used to study the viscoelastic behaviour of polymers. In the DMA test, a sinusoidal stress is applied at various frequencies, and the strain in

Fig. 1 The linear electron accelerator UELR 5-1C



the specimen of known geometry is recorded as temperature increases. It allows to determine the storage modulus E' , loss modulus E'' , damping factor $\tan \delta$, the relaxation transition temperatures and other material characteristics as a function of time, frequency, stress, temperature, atmosphere, eventually as a combination of several of these parameters [14]. The storage modulus (stiffness) provides a measure of elastic energy stored in the material, while the loss modulus (energy absorption) refers to the amount of energy dissipated in each cycle of deformation. The ratio of the loss modulus E'' to the storage modulus E' gives the damping factor $\tan \delta$. Due to the viscoelastic nature of the material, the sinusoidal strain lags behind the applied stress by a phase angle δ which is a measure of viscoelastic damping or internal friction [15]. By investigations of dynamic mechanical properties of polymeric materials, results are typically provided as a graphical representation of E' , E'' and $\tan \delta$ versus temperature or time at various frequencies.

In this study, DMA measurements were performed for rectangular NR/SBR blend test specimens of $50 \text{ mm} \times 10 \text{ mm} \times 2 \text{ mm}$ using the Perkin Elmer Pyris Diamond 8000 DMA Analyzer (PerkinElmer, Germany), in tension clamp mode

with the temperature scan time, at frequency of 0.5 Hz with amplitude of 10 μm , over the temperature range from 10 to 240 $^{\circ}\text{C}$, at constant heating rate of 3 $^{\circ}\text{C min}^{-1}$, amplitude of applied dynamic stress of 0.1 MPa and strain rate of 0.1 s^{-1} . Strain measurements were performed by the linear variable differential transformer of DMA equipment in the span of 2 mm with the mean resolution of 2 nm. Measurements were done with 10 non-irradiated samples as well as 10 irradiated samples by using high-energy electron beams at doses of 50, 100, 150, 200, 250 and 300 kGy. The storage modulus and damping factor were established as functions of temperature for all the samples under the same experimental conditions. The average values of E' and $\tan \delta$ for each temperature and radiation dose were calculated. The measurement deviation was $\pm 2\%$.

3 Results and Discussion

The experimental dependence of storage modulus E' and damping factor $\tan \delta$ on temperature in the temperature interval from 10 to 240 $^{\circ}\text{C}$ at a frequency of 0.5 Hz for the non-irradiated NR/SBR blend is presented in Fig. 2.

The same temperature dependence for the NR/SBR blend irradiated by radiation doses of 50, 100, 150, 200, 250 and 300 kGy as for the non-irradiated NR/SBR blend is shown in Figs. 3 and 4.

At temperatures over 75 $^{\circ}\text{C}$, the storage modulus apparently grows with increasing dose of irradiation. The elasticity of the tested material, by reason of creating new links after its electron beam irradiation, was increased, resulting in a corresponding fall in the value of the damping factor. In the temperature range between 20 and 120 $^{\circ}\text{C}$, the studied material exhibits two secondary relaxation

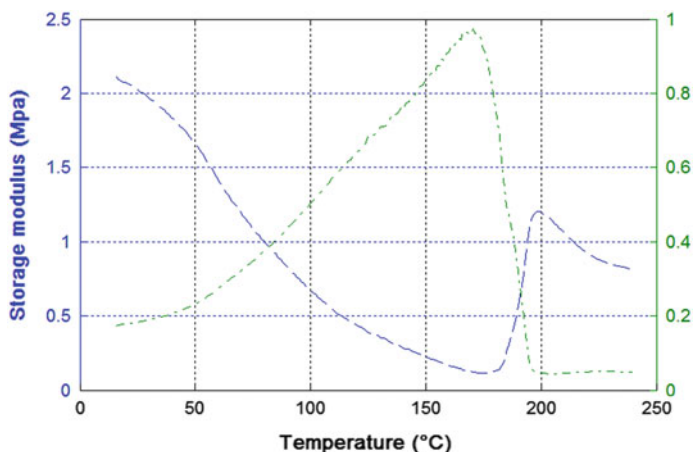


Fig. 2 Temperature dependence of storage modulus E' and damping factor $\tan \delta$ for non-irradiated NR/SBR blend at frequency of 0.5 Hz

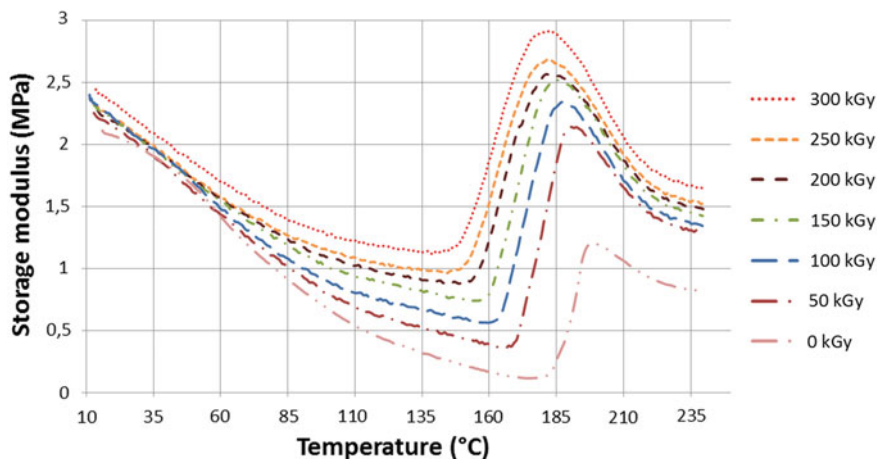


Fig. 3 Temperature dependence of storage modulus for various radiation doses beside the non-irradiated NR/SBR blend at frequency of 0.5 Hz

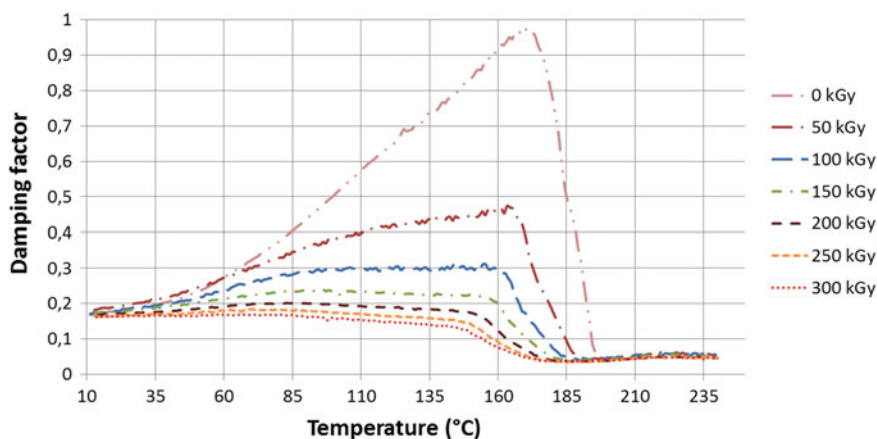


Fig. 4 Temperature dependence of damping factor for various radiation doses beside the non-irradiated NR/SBR blend at frequency of 0.5 Hz

transitions due to the large scale mobility of main chains and chain slippage (as can be seen mainly in the shape of $E'(T)$ curves) [16, 17]. The effect of electron beam irradiation on its course requires a separate study, so we do not pay attention to this issue in this work. With increasing temperature, the storage modulus E' decreases until it reaches the minimum value at the temperature from which it starts to grow. This temperature corresponds to the temperature of an onset of rapid decrease in $\tan \delta$ and is taken as the initial curing temperature at which the crosslinking has progressed to the continual forming of a polymer network in the whole volume of

the sample. The increase in E' continues until it reaches its maximum value at the maximum curing temperature. Above this temperature, which corresponds to the temperature of reaching the minimum value of $\tan \delta$, the rate of curing reaction reduces significantly as crosslinking requires further diffusion of molecules through the polymer network. The curing rate drops significantly because the material is so viscous that the bulk reaction stops. The further increase in the temperature leads to a decrease in E' while $\tan \delta$ does not in fact depend on the temperature, which is a consequence of partial crosslinking of the tested elastomeric material. The minimum value E'_{min} and the maximum value E'_{max} of the storage modulus E' increase with increasing radiation dose x (Fig. 5), the maximum value of the damping factor $(\tan \delta)_{max}$ decreases (Fig. 6), whereas the radiation dose has almost no impact on its minimum value (Fig. 4).

From the dependence of E'_{min} , E'_{max} and $(\tan \delta)_{max}$ on radiation dose x , presented in Figs. 5 and 6, it is clear that with increasing radiation dose the curing process of the NR/SBR blend under investigation starts and ends with higher values of the storage modulus and starts with lower values of the damping factor, so the irradiated material after its crosslinking is more elastic compared to non-irradiated one. The minimum of $\tan \delta$ unlike the minimum of E'_{min} does not depend on the radiation dose markedly. The initial curing temperature T_i and the maximum curing temperature T_m (Fig. 7) as well as the temperature T_{min} of reaching the minimum of and T_{max} of reaching the maximum of $\tan \delta$ (Fig. 8) shift towards lower values.

The diagrams of dependence of T_i , T_m , T_{min} and T_{max} on radiation dose applied, presented in Figs. 7 and 8, indicate that with increasing dose of irradiation, the curing process of the tested NR/SBR blend begins and ends significantly earlier, i.e. at significantly lower temperatures. The changes in all seven parameters E'_{min} , E'_{max} , $(\tan \delta)_{max}$, T_i , T_m , T_{min} and T_{max} as the functions of the radiation dose applied can be described analytically by the regression model, obtained by a multi-parametric fitting of experimental data using a trust region algorithm of a nonlinear least-squares method [18], in the form of

$$P(x) = A \exp(Bx) + C \exp(Dx) \quad (1)$$

Fig. 5 Dependence of storage modulus minimum value E'_{min} and storage modulus maximum value E'_{max} on radiation dose

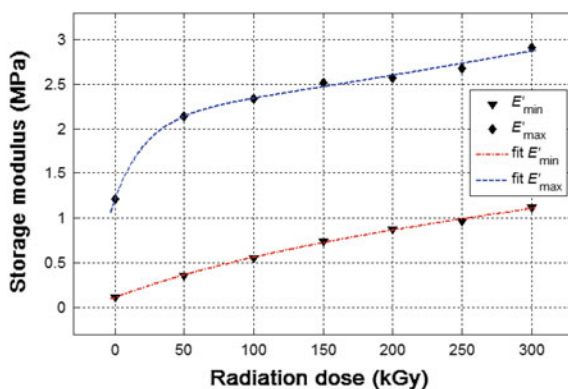


Fig. 6 Dependence of damping factor maximum value $(\tan \delta)_{\max}$ on radiation dose

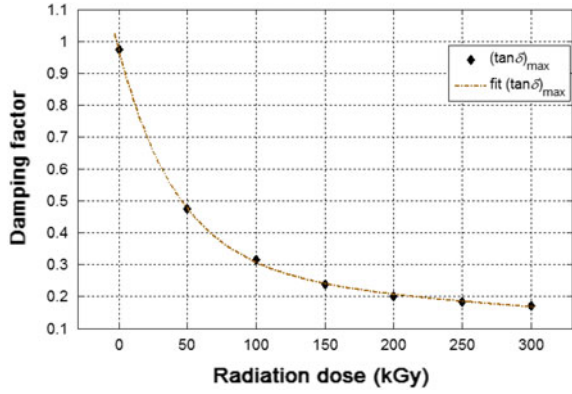


Fig. 7 Dependence of T_i and T_m on radiation dose

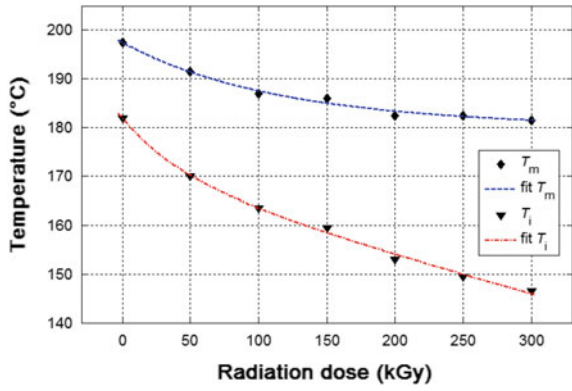


Fig. 8 Dependence of T_{\min} and T_{\max} on radiation dose

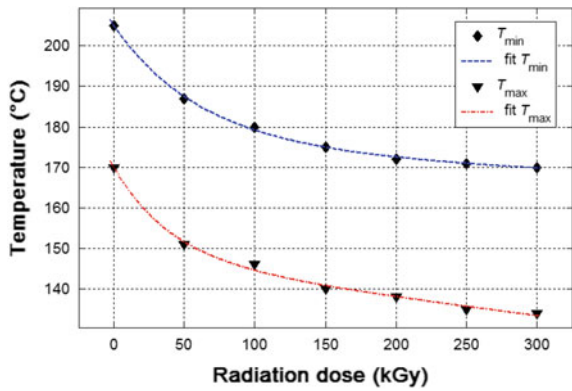


Table 2 Parameters of regression model and goodness of fit coefficient

P(x)	A	B	C	D	R-square
E'_{\min}	0.7874	0.0013911	-0.6745	-0.006787	0.9983
E'_{\max}	2.1291	0.0009967	-0.9248	-0.045111	0.9961
$(\tan \delta)_{\max}$	0.6838	-0.02327	0.289	-0.001834	0.9998
T_i	10.59	-0.02311	171.4	-0.0005359	0.9971
T_m	16.09	-0.009193	181.4	-0.0000171	0.9898
T_{\min}	29.89	-0.01598	175	-0.0001056	0.9986
T_{\max}	22.46	-0.02445	147.5	-0.000335	0.9917

with a goodness of fit *R-square* coefficient. Values of parameters *A*, *B*, *C*, *D* as well as values of *R-square goodness* of fit coefficient for particular radiation dose dependent material properties *P(x)* are presented in Table 2.

Composition of the mixture, see Table 1, shows that the tested rubber blend does not contain any radiation crosslinking accelerators.

Therefore, it is highly probable that if such accelerators are applied, the curing process will begin at substantially lower temperatures, will run faster, and the final value of the storage modulus will be significantly higher.

4 Conclusions

The dynamic mechanical analysis of the virgin natural rubber/styrene-butadiene rubber blend and the blend irradiated with different doses of high-energy electron beam by using a linear electron accelerator was carried out in this study. Experimental results have shown that high-energy electron beam irradiation, under the studied conditions, induces significant changes in the viscoelastic behaviour of the material under investigation. With increasing dose of radiation, the storage modulus increases and the damping factor decreases, the curing process of rubber blend begins at lower temperatures, is faster and ends at lower temperatures with the higher storage modulus compared to the non-irradiated material, which corresponds to the lower damping factor value. The unified regression model describing analytically the dependence of all monitored properties of the tested rubber blend on radiation dose with a high level of reliability was found as well.

Acknowledgements This research work has been supported by the Slovak grant agency KEGA, project No. 005TnUAD-4/2016 and SGS SP2016/94.

References

1. Goddard JM, Hotchkiss JH (2007) Polymer surface modification for the attachment of bioactive compounds. *Prog Polym Sci* 32:698–725
2. Burkert S et al (2009) Tuning of surface properties of thin polymer films by electron beam treatment. *Appl Surf Sci* 255:6256–6261
3. Murray KA et al (2013) Characterisation of the surface and structural properties of gamma ray and electron beam irradiated low density polyethylene. *Int J Mater Sci* 3:1–8
4. Woods RJ, Pikaev AK (1994) *Applied radiation chemistry: radiation processing*. Wiley, New York
5. Chmielewski AG et al (2005) Progress in radiation processing of polymers. *Nucl Instrum Meth B* 236:44–54
6. Drobny JG (2010) *Radiation technology for polymers*. CRC Press, Boca Raton
7. Drobny JG (2010) *Ionizing radiation and polymers: principles, technology and applications*. Elsevier, Oxford
8. Satti AJ et al (2015) The role of unsaturations in the gamma irradiation of crosslinkable polymers. *Radiat Phys Chem* 115:119–126
9. Meszaros L et al (2012) EB-promoted recycling of waste tire rubber with polyolefins. *Radiat Phys Chem* 81:1357–1360
10. Krmela J, Krmelova V (2016) Replacement of belt structure for FEA of tire. *Procedia Eng* 136:132–163
11. Makuuchi K, Cheng S (2012) *Radiation processing of polymer materials and its industrial applications*. Wiley, New Jersey
12. Noriman NZ, Ismail H (2011) The effects of electron beam irradiation on the thermal properties, fatigue life and natural weathering of styrene butadiene rubber/recycled acrylonitrile–butadiene rubber blends. *Mater Des* 32:3336–3346
13. Frounchi M et al (2006) Comparison between electron beam and chemical crosslinking on silicone rubber. *Nucl Instr Meth Phys Res B* 243:354–358
14. Brinson HF, Brinson LC (2014) *Polymer engineering science and viscoelasticity*. Springer, Berlin
15. Ward IM, Sweeney J (2012) *Mechanical properties of solid polymers*. Wiley, New York
16. Ramachandran VS et al (2002) *Handbook of thermal analysis of construction materials*. William Andrew Publishing, Norwich
17. Menard KP (2008) *Dynamic mechanical analysis: a practical introduction*. CRC Press, Boca Raton
18. Snieder R (2012) *A guided tour of mathematical methods*. Cambridge University Press, Cambridge

Chosen Electrical Properties of Montmorillonite/Polyaniline Composites

Pavel Košťal, Ondrej Bošák, Ivan Kopal, Zora Košťalová Jančíková,
Jan Valíček and Marta Harničárová

Abstract The paper deals with the electrical properties of Montmorillonite (MMT)/Polyaniline (PANI) composites. These materials show specific electrical properties as relatively high anisotropic electrical conductivity, pressure dependent electrical resistance with relatively high hysteresis. Metallographic analyse as well as the Vickers micro-hardness of sample surfaces is presented. All these properties predetermine this material as an interesting piezoresistor.

Keywords PANI/MMT structure · dc. electric conductivity · Piezoresistive effect

P. Košťal (✉) · I. Kopal · Z. Košťalová Jančíková · J. Valíček · M. Harničárová
VŠB—Technical University of Ostrava, 17. listopadu 15/2172,
Ostrava 70833, Czech Republic
e-mail: pavel.kostial@vsb.cz

I. Kopal
e-mail: ivan.kopal@vsb.cz

Z. Košťalová Jančíková
e-mail: zora.jancikova@vsb.cz

J. Valíček
e-mail: jan.valicek@vsb.cz

M. Harničárová
e-mail: marta.harnicarova@vsb.cz

O. Bošák
Faculty of Material Science and Technology in Trnava, Slovak University of Technology
in Bratislava, Paulínska 16, 91724 Trnava, Slovak Republic
e-mail: ondrej.bosak@stuba.sk

I. Kopal
Faculty of Industrial Technologies in Puchov, Alexander Dubcek University of Trencin,
Puchov, Slovakia

1 Introduction

Clay minerals are widely represented not only in the older sedimentary rocks, but also form the basis of recent sediments and soils. Major component of clay minerals and sheet silicates form the minor component is a mineral of allophane, also hydroxides, oxy-hydroxides, or oxides of aluminium and iron [1].

Phyllosilicates are minerals whose structure is characterized by a layered structure. The individual layers with one another are stronger bond than the bond between the atoms in a layer [2]. All phyllosilicates are generally made up of SiO_4 pyramids, of which three oxygen atoms shared with the neighbouring tetrahedral with which creates an infinite two-dimensional grid.

The work [3] is focused on the effect of MMT content on the thickness, morphology and electrical conductivity of PANI/MMT nanocomposite films. An increase in MMT content led to an increase in film thickness and surface roughness and to a decrease in conductivity from a maximum value of 356 S/m to a minimum value of 76 S/m.

Authors in [4] present pressed tablets from polyaniline/phyllosilicate nanocomposites which have been prepared under various conditions in order to optimize anisotropic conductivity of composite by ordering of flat phyllosilicate particles intercalated with polyaniline (PANI). The in-plane conductivity for PANI/MMT was 0.084 S/cm, i.e. 1000x higher than in the direction perpendicular to the tablet plane. Increase of pressure up to 128 MPa led to dramatic decrease of conductivity.

In the work [5] has been proved that nanostructure of PANI affects the conductivity. In the works [6–8] authors studied distinguished structures of polyaniline and their chemical and physical properties.

Clay minerals with the layered structure (phyllosilicates) have been often used as matrices for such type of organo-inorganic composites [9, 10].

2 Results and Discussion

The samples were prepared by “one step method” described in [3]. Surfaces of prepared samples were investigated by metallographic microscope ZEIS Axio Observer 3.

Result for the sample surface perpendicular to applied pressure (in-plane further IP). Figure 1 clearly demonstrates PANI chains visible as line structure on the surface of the sample. Surface picture in perpendicular direction to IP (abbreviated as PD) is in Fig. 2.

Table 1 shows measurements of Vickers hardness for IP and PD surfaces. It is seen higher hardness for IP than PD surface; nevertheless both values are relatively low. PD surface on the other hand is highly porous.

Fig. 1 Structure of MMT/PANI for IP surface

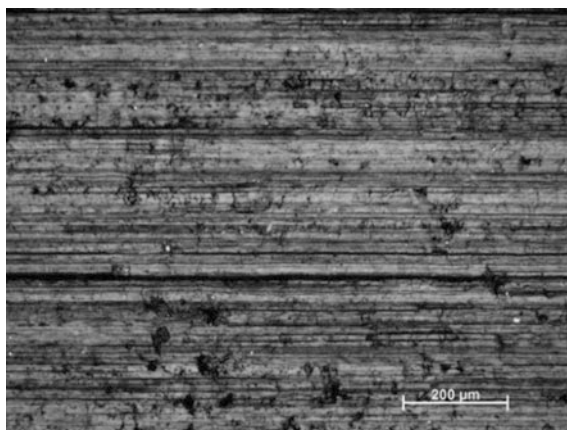


Fig. 2 Structure of MMT/PANI for PD surface

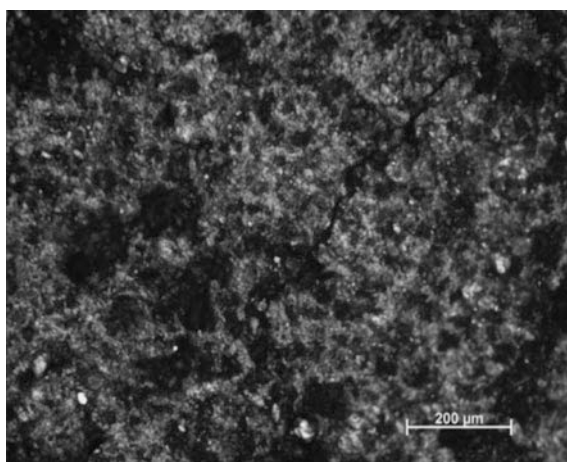


Table 1 Micro hardness HV for samples IP and PD

Sample	Micro-hardness HV	
	IP	PD
PANI/MMT	12.2 HV	3.6 HV

Basic issue of this paper create electrical properties of samples under investigation. We focused our attention on dc. electric conductivity. PANI chain is described in Fig. 3. Volt-Ampere characteristics (V-A) for Figs. 4 and 5 present results for IP and PD surfaces. V-A characteristics are in both cases linear. Main differences are in values of specific conductivity. From these results we can see that $\sigma = 0.85$ [S/m] for IP surface and $\sigma = 0.38$ [S/m] for PD one.

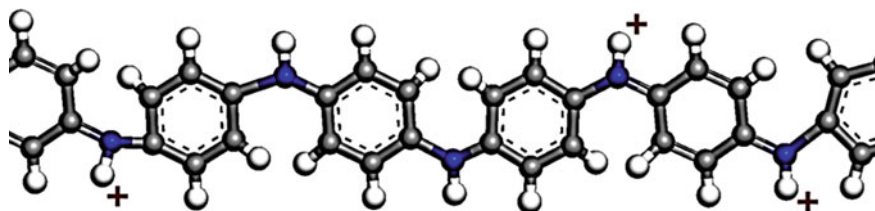


Fig. 3 Structure of conductive PANI

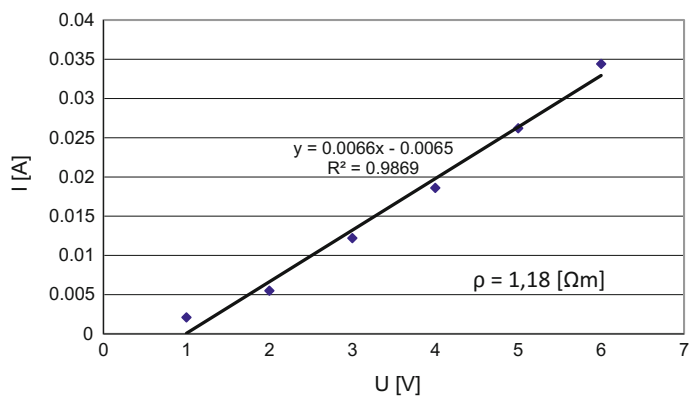


Fig. 4 V-A characteristic for IP surface

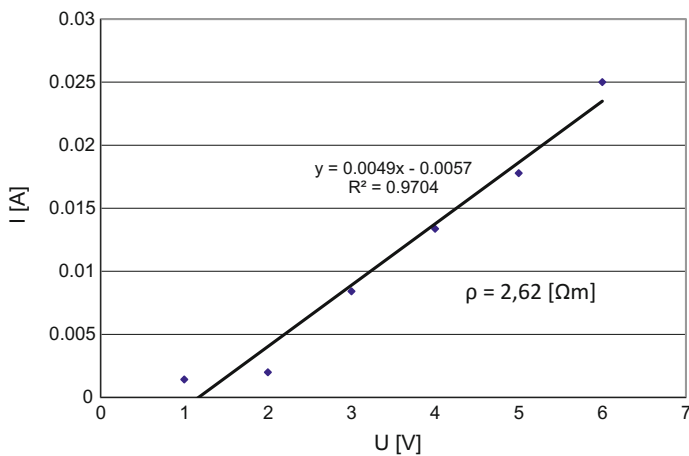


Fig. 5 V-A characteristic for PD surface

Polyaniline exists in various forms depending on a degree of oxidation or reduction. Figure 3 is a conductive form of polyaniline called emeraldine salt. Polyaniline chain is composed of a system of conjugated double bonds (in the structure are regularly alternating single and double bonds). For electrical conductivity, in addition to conjugation, it is important presence of the charge carriers which mediate their transfer along the chain. This is achieved by doping or protonation of the nitrogen in polyaniline chain.

Furthermore, we have found during the measurement of the electric resistance of samples of PANI/MMT that it is relatively highly dependent on an applied pressure. In Fig. 6 is shown that after sample loading there was a relatively sharp decrease in the resistance of samples and its gentle drift. At the same measurement we have seen hysteresis after lightening of the sample. The weight of every load was 124 g.

To conclude this problem, we have made another experiment consisted in the fact that the sample was loaded by pressure pulse with trigger weights 124 g from a height of several centimetres. In Fig. 7 we can see the sample response from which is seen generated electrical impulse, which was caused by changing the voltage on the resistance of the sample and registered on the reference resistance. Based on this measurement, we can clearly say that there is a phenomenon called piezoresistive effect. As it is well known piezoresistive effect consists in a change of electrical resistance in dependence on the applied pressure.

Measured parameters of the pulse are shown in Fig. 7 where we see that the increase of the voltage on the reference resistance from zero to a maximum after about 470 μs , which is relatively rapid. Real view on the experiment is in Fig. 8.

Fig. 6 Dependence of the electric resistance versus sample for IP surface

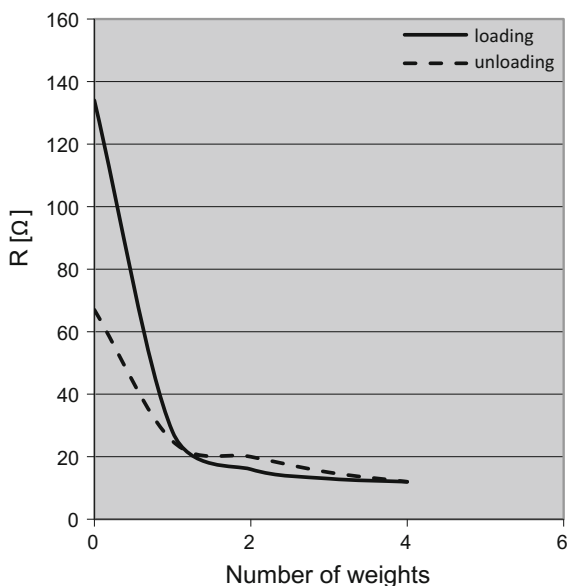


Fig. 7 Parameters of electrical impulse created by impact of 124 g load on IP surface

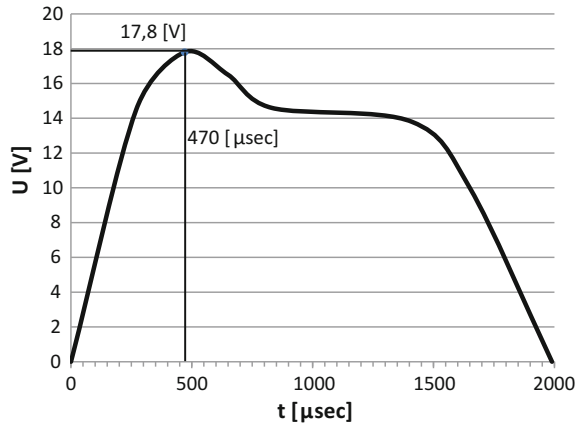
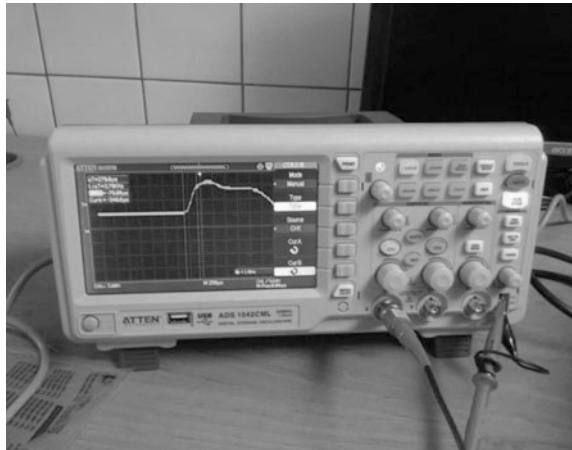


Fig. 8 Real view on the impulse shape on oscilloscope screen



3 Conclusions

PANI/MMT samples have relatively strong anisotropy visible also on metallographic images of IP and PD surfaces. Samples are relatively soft and brittle. Samples under investigation show also anisotropy of dc. electric conductivity. V-A characteristics are linear. Studied samples have piezoresistive effect.

Acknowledgements This paper was created on the in the framework of project of students grant competition No. SP2017/38 and SP2017/63 organized by Technical University of Ostrava, Faculty of Metallurgy and Materials Engineering.

References

1. Weiss Z, Kunžvart M (2005) *Jílové minerály: jejich nanostruktura a využití*. Karolinum, Praha
2. Nelson SA (2003) *Silicate structures*. Tulane University USA. http://www.tulane.edu/~sanelson/eens211/silicate_structures.htm. Accessed 6 Nov 2014
3. Kulhánková L, Tokarský J, Matějka V, Peikertová P, Vallová S, Kutlákova KM, Stýskala V, Čapková P (2014) Electrically conductive and optically transparent polyaniline/montmorillonite nanocomposite thin films. *Thin Solid Films* 562:319–325
4. Tokarský J, Kulhánková L, Stýskala V, Kutlákova KM, Neuwirthová L, Matějka V, Čapková P (2013) High electrical anisotropy in hydrochloric acid doped polyaniline/phyllsilicate nanocomposites: effect of phyllosilicate matrix, synthesis pathway and pressure. *Appl Clay Sci* 80–81:126–132
5. Gregory RV, Kimbrell WC, Kuhn HH (1989) Conductive textiles. *Synthetic Mater* 28: 823–835
6. Sapurina I, Stejskal J (2008) The mechanisms of the oxidative polymerization of aniline and formation of supramolekular structure. *Polym Int* 57:1295–1325
7. Sapurina I, Riede A, Stejskal J (2001) In-situ polymerized polyaniline films 3. Film formation. *Synthetic Metals* 123:503–507
8. Lu J, Zhao XP (2002) Electrorheological properties of a polyaniline/montmorillonite clay nanocomposite suspension. *J Mater Chem* 12:2603–2605
9. Lerf A, Čapková P (2004) *Encyclopedia of nanoscience and nanotechnology*. American Scientific Publishers, CA
10. Lagaly G, Ogawa M, Dékány IF, Bergaya BKG, Theng G (2006) *Handbook of clay science. Developments in Clay Science*. Elsevier, Amsterdam

Improvement of Optical Properties of White LED Lamps Using Green-Emitting Ce_{0.67}Tb_{0.33}MgAl₁₁O₁₉:Ce,Tb Phosphor

Nguyen Doan Quoc Anh and Nguyen Ngoc Long

Abstract This study presents the improvement of performance of multi-chip white LED lamps (MCW-LEDs) having average CCTs of 7000 and 8500 K by using green-emitting Ce_{0.67}Tb_{0.33}MgAl₁₁O₁₉:Ce,Tb (CeTb) phosphor. The performance includes luminous efficacy and color uniformity which is analyzed based on Mie theory. Effects of CeTb concentration on optical properties of MCW-LEDs are also investigated. Optical simulations are employed by Light Tools software based on Monte Carlo method. Moreover, the scattering enhancement in CeTb case is demonstrated by Mie theory and Matlab soft-ware. The results show that both the luminous efficacy and color uniformity grow with CeTb concentration.

1 Introduction

Multi-chip white LED lamps bring various advantages for LED lighting applications [1]. Therefore, many methods for improving the quality of MCW-LEDs are seriously considered with the improvement of yellow YAG:Ce phosphor layer [2, 3]. In general, the yellow YAG:Ce phosphor material is mixed with silicone glue to form a phosphor compounding which absorbs the blue light of the blue chips and emits the yellow light. Light rays light passing through phosphor particles are scattered in the phosphor admixing. Throughout the scattering during the propagation, the blue light is combined with the yellow light.

The yellow YAG phosphor particle absorbs blue light and emits yellow light. It means that if the scattering increase the blue light is impaired gradually whereas the reformed yellow light is enhanced. Correspondingly, the variation of light intensity distributions can cause a yellow ring phenomenon [2].

N.D.Q. Anh (✉)

Power System Optimization Research Group, Faculty of Electrical and Electronics Engineering, Ton Duc Thang University, Ho Chi Minh City, Vietnam
e-mail: nguyendoanquocanh@tdt.edu.vn

N.N. Long

Faculty of Applied Science, Ton Duc Thang University, Ho Chi Minh City, Vietnam

© Springer International Publishing AG 2018

A. Öchsner and H. Altenbach (eds.), *Improved Performance of Materials*,
Advanced Structured Materials 72, DOI 10.1007/978-3-319-59590-0_20

239

There are several way to improve light performance such as applying the multiple phosphors or the optimizing optical structures of white LED lamps. Won et al. [4] have proved the substantial impact of phosphor geometry on the lumen output of LED lamps by adding green $(\text{Ba,Sr})_2\text{SiO}_4:\text{Eu}^{2+}$ and red $\text{CaAlSiN}_3:\text{Eu}^{2+}$ phosphors in various phosphor structures. Oh et al. [5] have introduced G-A-R multi-package LED produces higher lumen output and high CRI. Zheng et al. [6] improved the CRI of the LED lamp by using multi-chromatic phosphor. Generally, the purposes of these research concentrate on increase CRI and lumen output without working on ACU improvement. Furthermore, the studies only focus on single-chip white LED, they have not solved these problems on multi-chip white LED lamps yet.

In this work, we introduced a new approach to improve color uniformity and lumen output of MCW-LEDs by adding green CeTb phosphor particles into the phosphor layer. We illustrated that the presence of the CeTb particles leads to the enhancement of the scattering of light during propagate through the phosphor layer. As a result, the spatial color distribution of the LED become more uniform. Our research process includes three main steps: (1) Modeling LEDs; (2) Adding CeTb into the phosphor layer of the MCW-LEDs; (3) Reviewing the influences of CeTb percentages on MCW-LEDs performance, containing the increase of emission spectra and scattering event. The simulation results show that angular color uniformity (ACU) and lumen output can be enhanced remarkably after combining green CeTb with yellow YAG:Ce phosphors.

2 Enhancement of Emission Spectra

MCW-LEDs models simulated with LightTools program are coated by flat silicone. The main modeling work includes (1) Building the optical structures and properties of MCW-LED lamps; (2) considering the optical variations of phosphor compounding with various CeTb percentages. The conformal structure of MCW-LEDs are shown in Fig. 1. The measurements of the reflector of these structures are 8 mm of bottom length, 2.07 mm of height and 9.85 mm of top surface length. 0.08 mm thick conformal phosphor layer covers the nine blue chips, which have a dimension of 1.14 mm \times 1.14 mm and a height of 0.15 mm. Each blue chip has a radiant flux of is 1.16 W and an emission wavelength of 453 nm. The chips is coated by the mixed phosphor layer conformally. The scattering of phosphor particles will be analyzed in agreement with Mie-theory [7]. In this research, the average radii of phosphor particles are set at 7.25 μm . The mixed phosphor layer is a combination of the CeTb and YAG:Ce and the silicone glue.

The refractive indexes of CeTb and YAG:Ce phosphors and its silicone glue are 1.85, 1.83 and 1.52, respectively. Besides, we also determine the color spectra of the mixed phosphor composite.

The color spectra of the conformal phosphor layer are verified by enhancing CeTb concentration from 0 to 28%, as presented in Fig. 2. The results indicate that

Fig. 1 Simulation of the conformal phosphor packaging (CPP)

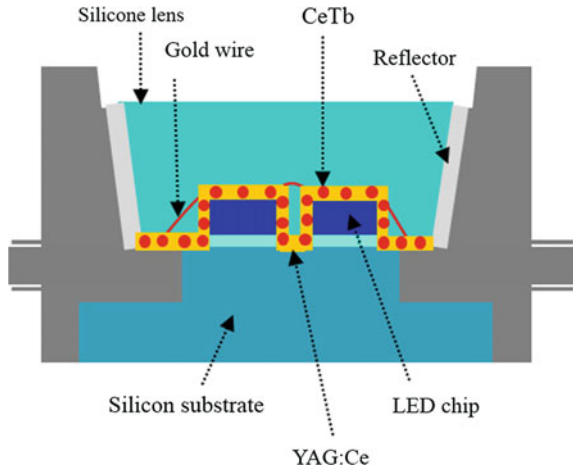
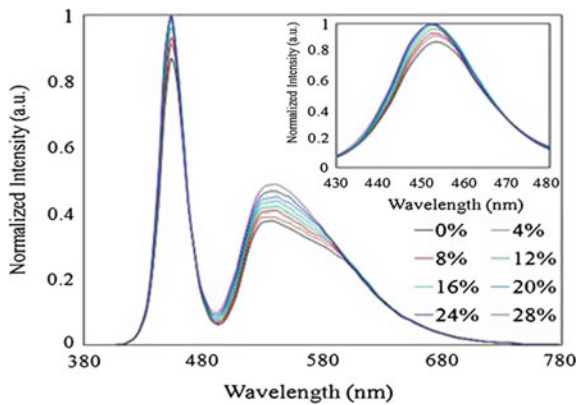


Fig. 2 Emission spectra of CPP



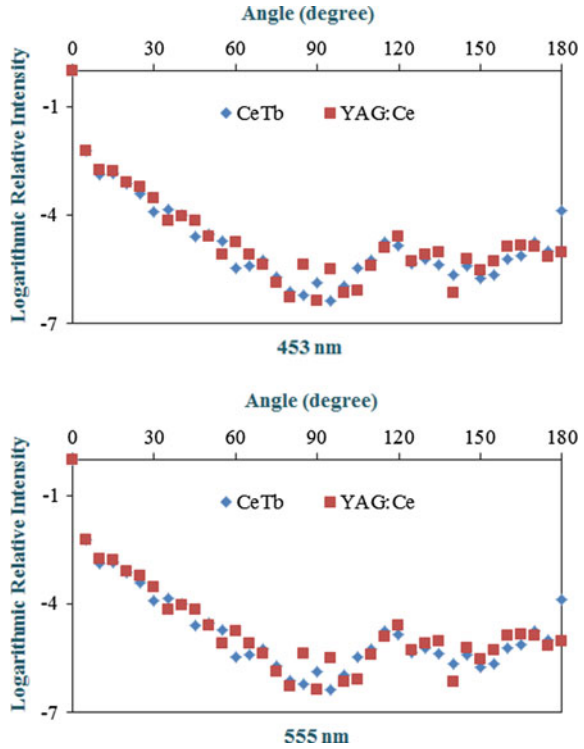
the lumen output of MCW-LEDs should be enhanced by injecting CeTb particles into phosphor layer.

3 Scattering of Phosphor Particles

In this part, in consonance with Mie theory, the scattering of phosphor particles is calculated in an angle range from 00 to 3600. The angular light scattering intensities can be expressed as following:

$$i_1 = \sum_{n=1}^{\infty} \frac{2n+1}{n(n+1)} [a_n(x, m)\pi_n(\cos \theta) + b_n(x, m)\tau_n(\cos \theta)] \quad (1)$$

Fig. 3 The light scattering distribution of CeTb and YAG:Ce particles in the phosphor layer of MCW-LEDs: (top) 453 nm; (bottom) 555 nm



$$i_2 = \sum_{n=1}^{\infty} \frac{2n+1}{n(n+1)} [a_n(x, m)\tau_n(\cos \theta) + b_n(x, m)\pi_n(\cos \theta)] \quad (2)$$

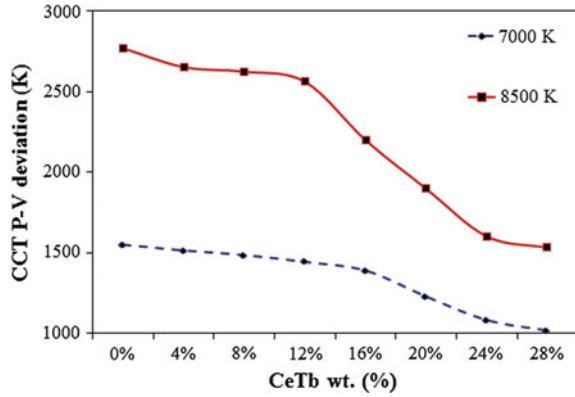
In Eqs. (1) and (2), m is a refractive index, x is a size parameter, and are the angular dependent functions, and are the expansion coefficients. The scattering intensities are calculated for 555 and 453 nm wavelengths, which are the emission wavelength of the yellow YAG:Ce phosphor and the blue chips, respectively.

The intensity distributions of scattered light ray of CeTb and YAG:Ce particles is shown in Fig. 3. After injecting CeTb phosphor into phosphor layer of scattering even increases, significantly. Correspondingly, the angular color distribution of MCW-LEDs can be improved.

4 Simulation Results and Discussions

In this research, to achieve the product specification of LED, the MCW-LED is necessarily kept to work at mean CCTs of 7000 and 8500 K. If the green CeTb phosphor increases its concentration, it is necessary to reduce the yellow YAG:Ce

Fig. 4 The angular CCT peak-valley (P-V) deviation with various CeTb concentration



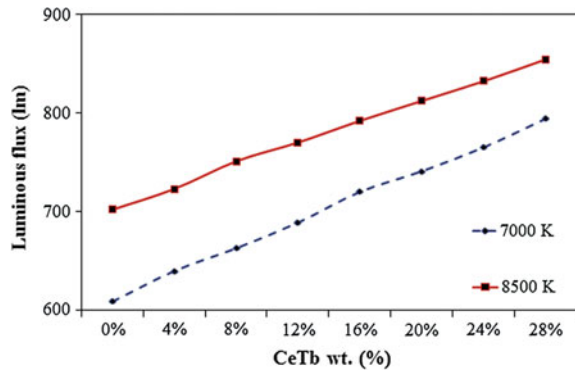
phosphor in order to obtain the mean CCTs of 7000 and 8500 K. The weight percentage of the LED phosphor layer can be calculated by:

$$\sum W_{pl} = W_{\text{yellow phosphor}} + W_{\text{silicone}} + W_{\text{green phosphor}} = 100\% \quad (3)$$

In Eq. 3, the W_{silicone} , $W_{\text{yellow phosphor}}$ and $W_{\text{green phosphor}}$ are the weight percentage of the silicone glue, the yellow YAG: Ce phosphor and the green CeTb phosphor respectively.

The weight of CeTb in the conformal phosphor packaging grows continually from 0 to 28%. The angular color deviation of MCW-LED with CeTb and without it in the phosphor compounding was simulated and its results are shown in Fig. 4. It can be seen that the CeTb existence causes a significant decrease in the CCT peak-valley deviation. In other words, the spatial color distribution of MCW-LEDs with CeTb is much flatter than that of the one without CeTb. According to the achieved simulation results in Fig. 5, it can be realized that the lumen output increases in proportion with the concentration of the CeTb. Generally, it is possible to design the MCW-LED packages which having advance correlated color temperature (CCT) uniformity.

Fig. 5 The lumen output at average CCTs 7000 and 8500 K with different CeTb concentration



5 Conclusions

In this paper, the green CeTb phosphor is applied to intensify the spatial color uniformity and the lumen output of MCW-LED lamps. By inserting CeTb particles into phosphor compounding, the angular distribution of the lamp light can be regulated by increasing the scattering event, resulting in the growth of the ACU. Besides, the emission spectra of multiple phosphors increase with the CeTb concentration, which results the significant growth in lumen output of MCW-LEDs concentration, so that the lumen output of MCW-LEDs increases significantly.

Acknowledgements This research is funded by Vietnam National Foundation for Science and Technology Development (NAFOSTED) under grant number 103.03-2015.62.

References

1. Anh QND, Lai MF, Ma HY (2014) Enhancing of correlated color temperature uniformity for multi-chip white-light LEDs by adding SiO₂ to phosphor layer. *J Chin Inst Eng* 38:1–7
2. Liu Z, Liu SL, Wang K (2008) Analysis of factors affecting color distribution of white LEDs. International conference on electronic packaging technology & high density packaging (ICEPT-HDP), Shanghai, 28–31 July 2008, New York, IEEE, pp 1–8
3. Lai MF, Anh NDQ, Ma HY (2014) Scattering effect of SiO₂ particles on correlated color temperature uniformity of multi-chip white light LEDs. *J Chin Inst Eng* 39:468–472
4. Won YH, Jang HS, Cho KW (2009) Effect of phosphor geometry on the luminous efficiency of high-power white light-emitting diodes with excellent color rendering property. *Opt Lett* 34:1–3
5. Oh JH, Eo YJ, Yang SJ (2015) High-color-quality multipackage phosphor-converted LEDs for yellow photolithography room lamp. *IEEE Photonics J* 7:1300308
6. Zheng M, Ding W, Yun F (2014) Study of high CRI white light-emitting diode devices with multi-chromatic phosphor. In: International conference on electronic component technology, Orlando, 27–30 May 2014, IEEE, New York, pp 2236–2240
7. Liu S, Luo X (2011) Design manufacturing and testing. Wiley, Beijing

“Cut-Glue” Approximation Based on Pseudo-genetic Algorithm for Strongly Nonlinear Parametric Dependencies of Mathematical Models

Rudolf Neydorf, Victor Polyakh, Ivan Chernogorov,
Orhan Yarakhmedov and Dean Vucinic

Abstract In the present work we consider one of the basic methods of Cut-Glue approximation—the approximation method for fragments with essentially nonlinear dependencies. As an instrument of approximation, a hybrid application of the classical regression analysis is used and specially developed for the evolutionarily modified genetic algorithm. The proposed approach allows finding the optimal dependence of the specified fragment.

Keywords Optimization · Approximation · Regression analysis · Mathematical model · Experimental data · Heuristic methods · Evolutionary-genetic algorithm

1 Introduction

The experimental and computer modeling of the static and dynamic objects is a difficult task. This is due to the fact that the processes of such test objects are essentially governed by nonlinear laws [1, 2]. The nonlinearity arise from the presence of various factors, such as: complicated electromagnetic effects, mechanical effects of friction and backlash dry, thermodynamic phenomena, aerodynamic

R. Neydorf (✉) · V. Polyakh · I. Chernogorov · O. Yarakhmedov
Don State Technical University, Rostov-on-Don, Russia
e-mail: ran_pro@mail.ru

V. Polyakh
e-mail: silvervpolyah@gmail.com

I. Chernogorov
e-mail: hintavr@gmail.com

O. Yarakhmedov
e-mail: orhashka@gmail.com

D. Vucinic
Vrije Universiteit Brussel, Brussels, Belgium
e-mail: dean.vucinic@vub.ac.be

effects, patterns of chemical transformations [3], etc. The required experimental models of these objects are created with mathematical data processing. The processed dependences, connecting the output to the input data, are essentially non-linear. Often there are cases, when the generated curves from these data, have the character, which is close to be discontinuous. The task to approximate such curves, even with the use of spline functions, is time-consuming and in addition associated with the introduction of the significant errors. However, in recent years, there have been quite effective solutions for approximation problems with strongly nonlinear dependencies [4, 5]. The proposed method [6] is based on a multiplicative “cutting” of the well-approximated fragments with the application of the analytical functions, followed by the additive “gluing”, which combines them into a single analytic function. The described method of data processing technology is called the «Cut-Glue» approximation method.

The main steps of the «Cut-Glue» method are:

- splitting the array of the experimental data into fragments, which are well approximated by analytical functions;
- optimized approximation of the selected fragments by analytical functions;
- formation of the special non-linear functions, that can perform the multiplicative “cut” of the approximated fragments;
- implementation of the multiplicative operation «cut» by multiplying the approximate and cut functions;
- implementation of the additive operation «glue», by providing the union of the cut pieces with a single analytic function, which is the mathematical model of the investigated dependences.

This paper deals with one of the key parts in the “Cut-Glue” method, which is the construction of the analytical functions, as the approximation of the selected data fragments source [6].

2 Approximation Algorithm of Data Fragments

Based on the papers [7–9], the implementation phase for the construction of the analytic functions, approximating the fragments dependency is advisable to entrust to the well-proven machine of regression analysis (RA) [10–12]. The possibility of having a convenient structure (membership of a polynomial) and parametric (optimal regression coefficients) to vary the polynomial functions of the classical RA, allows to find the optimal description (in the framework of the polynomial) to study dependences. Some experience in the field of search engine optimization, specially focusing on the use of the heuristic algorithms, has shown that the optimization of the approximating function based on the evolutionary genetic algorithm (EGA) [13–18] may be effective.

The structure of the arbitrary polynomial of the n th dimension and the m th degree is defined as follows:

$$\begin{aligned}
 q(x) = & b_0 + b_1 \cdot x_1 + \dots + b_n \cdot x_n + b_{11}x_1^2 + b_{12}x_1x_2 + b_{13}x_1x_3 + \dots + b_{22}x_2^2 + b_{23}x_2x_3 \\
 & + \dots + b_{nn}x_n^2 + b_{111}x_1^3 + b_{112}x_1^2x_2 + b_{113}x_1^2x_3 + \dots + b_{222}x_2^3 + b_{223}x_2^2x_3 + \dots + b_{nnn}x_n^3 + \dots \\
 & + b_{1111}x_1^4 + b_{1112}x_1^3x_2 + \dots + b_{111n}x_1^3x_n + b_{1122}x_1^2x_2^2 + b_{1123}x_1^2x_2x_3 + b_{1124}x_1^2x_2x_4 \dots
 \end{aligned}
 \tag{1}$$

where b are the coefficients of the n th dimension polynomial of the m th degree, x_n are the parameters of the studied dependencies, which can be formulated by the pseudo linear polynomial, with expanding dimension:

$$q(\tilde{x}) = \sum_{i=0}^{\tilde{n}} \tilde{b}_i \cdot \tilde{x}_i
 \tag{2}$$

where \tilde{b}_i are the coefficients of the polynomial of the n th dimension and the m th degree, \tilde{x}_i are the parameters of the studied dependencies, where $\tilde{x}_0 = 1$.

It is well known that any variant polynomial coefficient, which is defining the simulated dependence, is computed from the known matrix equation:

$$\tilde{b} = (X^T X)^{-1} X^T y,
 \tag{3}$$

where y is the vector of values of the dependent variable, X is the investigated input matrix, consisting of \tilde{x}_i rows, where line numbers correspond to the experience number, the column numbers correspond to the polynomials terms. It should be noted that the values \tilde{x}_0 of the first column of the matrix X is equal to 1.

In a special way, the EGA tool regression polynomial can be considered to be simulating the chromosome structures. At the same time, the basis of the genetic chromosomal structure of the arbitrary polynomial of n -th dimension and the m -th degree can be coded with the binary pattern that is formulated as a complete polynomial, and similar to the n -th dimension and the m -th degree. The location of these polynomial elements is responsible to enable the combinatorial rules of the coefficients ascending indices, which corresponds to the growing number of the structural and parametric indices of the polynomial coefficients:

$$\begin{aligned}
 & 0, 1, \dots, n, 11, 12, \dots, 1n, 22, 23, \dots, 2n, \dots, 33, 34, \dots, 3n, \dots, nn, \dots, 111, 112, \dots, \\
 & 11n, \dots, 122, 123, \dots, 12n, \dots
 \end{aligned}
 \tag{4}$$

The example is based on Eqs. (1) and (2), showing the complete polynomial, where the member's number of this polynomial is equal to 15. The increasing number of the structural and parametric indices of the respective polynomial coefficients has the following form:

$$0, 1, 2, 11, 12, 22, 111, 112, 122, 222, 1111, 1112, 1122, 1222, 2222.
 \tag{5}$$

The requirement to find the structural and parametric optimal variant of such polynomial approximation is determined by the fact that, often, the full polynomial does not guarantee the best accuracy. This is due to the fact that some properties of the nonlinear terms are not consistent with the nature of the approximated dependence. Therefore, it is necessary to vary the polynomial partial structure, from its small to complete version. In addition, for each case of such polynomial structure, the approximated data accuracy needs to be evaluated. As the result coming from varying the polynomial structure (structural-parametric optimization), its optimal variant can be found, as being the best approximation of the investigated dependence. The parametric optimization component is provided with the RA methods.

Therefore, this rise the question about the polynomial variation structure of the n -order, which has showed the accuracy deterioration of the data approximation from its full version, to to its $(n-1)$ order form. It should be noted that the combinatorial search through all the possible structures of the polynomial is the NP-complete algorithm. In this regard, the authors have initially focused on the use of heuristic algorithms, which are considered to be the only effective means of solving such high dimensionality problems, i.e. difficulties. In particular, in this case, the attempt was to construct the polynomial similar in the structure to support a genetic (pseudo genetic) algorithm (PGA), which is designed as the exploratory tool to analyze the varying members composing the polynomial.

3 Pseudo-Chromosomal Genetic Mode

The essence of the algorithm is to use a pseudo-chromosomal genetic model in which the PGA chromosome structure is defined by the full members set of the m th degree polynomial. An example is the chromosome that describes a polynomial of the 4th degree. It was noted that the genetic chromosomal structure of the polynomial has the binary model. It means that the description of the polynomial structure (gene sequences in the chromosome PGA) can be coded as a record, where “1” indicates that the polynomial term is used in its final structure [corresponding to the regression coefficient, as calculated by the formula (1)], and “0” indicates that the member is excluded from the final polynomial structure (chromosome PGA), i.e. the regression coefficient is considered to be zero and thus, not calculated. To conclude, each position has a chromosome that consists of 2 alleles: 0 and 1.

The model of the complete polynomial of 4th degree has the binary form, as follows:

1111111111111111

However, due to the chromosome mutation, the polynomial structure can change in accordance to its current genetic chromosomal description, where the chromosome variants change as:

11011111110101

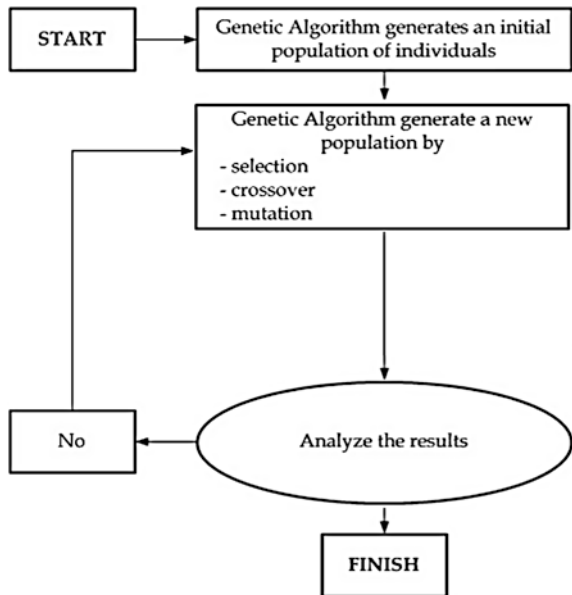
from its total structure of being the 4th degree polynomial, resulting by eliminating its 3rd ($a_{22}x_2^2$), 12th ($a_{1222}x_1x_2^3$) and 14th ($a_{1122}x_1^2x_2^2$) member.

The proposed PGA, as the classic genetic algorithm includes the use of the crossover, mutation and selection operators. The chromosome of PGA includes the binary record, which has the polynomial structure, where gens—are members of the full polynomial (regression coefficients), and may be included or excluded, and by doing so define the final polynomial structure.

4 Pseudo Genetic Algorithm

The used PGA includes the major operators from the classical EGA: crossover operator, mutation operator and selection operator. The structure of the PGA input parameters includes the populations number, the size of the population within one generation, the probability of the crossover and mutation probability. In the first stage, PGA forms the initial population resulting from the mutation operator and one-point crossover operator, as shown in Fig. 1. In the next step, the selection operator is used for each received individual, which makes the decision about its inclusion or non-inclusion in the next generation of PGA.

Fig. 1 Block diagram of the pseudo-genetic algorithm



5 Crossover Operator

The PGA crossover operator is developed, as shown in Fig. 2, which randomly selects a few individuals from the given generation, followed the random selection of the crossover point (break) for the chromosomes involved in the cross pair process. After selecting the crossover point, follows the creation of descendants, which happens through the exchange of the special parts between the parental chromosomes, before and after the break point.

The findings resulting from the application of the crossover operator, where individuals may be exposed to a mutation (depending on a given probability of such mutation), after which all the selected PGA individuals are entering into the next generation of PGA. The example of the crossover operator is shown in Fig. 2, in the paper’s upper part the offspring chromosomes are presented, and the chromosomes obtained by crossing of 2 parent individuals are presented at the bottom of Fig. 2, the red line indicates the point of crossing-over (burst).

6 Mutation Operator

The mutation operator can be considered as the key operator of the proposed PGA, since it is zeroing the members of the considered polynomial. It should be noted that this operator is changing the reporting structure of the polynomial. As the consequence, it is changing the values of the analytical data that allow calculating the individual fitness assessment. During the first stage the mutation operator randomly selects the set of individuals that are mutated, then it sets the number of chromosomes for each gene to which the mutation operator is applied, and their position is then randomly selected. In the last stage the mutation operator inverts the selected gene values in the binary-type chromosomal gene structure, where the gene values = “1” are replaced with the value = ‘0’ value, and the gene values = “0” are replaced with the value = “1”. The example of the mutation operator application to the individual chromosome, described with the 3rd degree polynomial, is shown in Fig. 3.

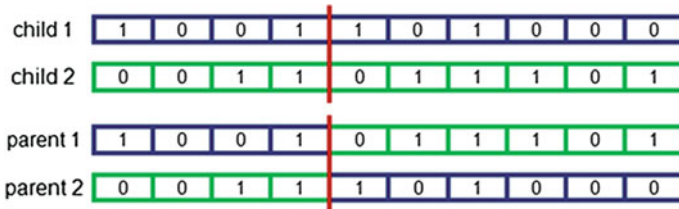


Fig. 2 Example of a crossover operation

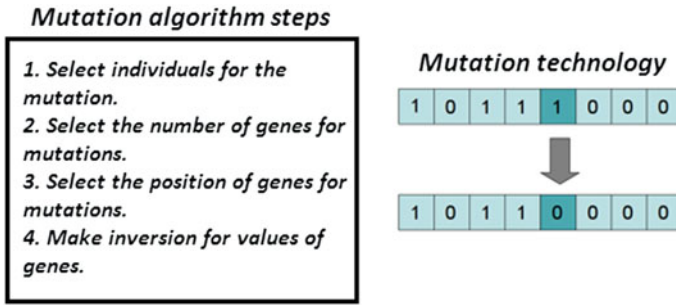


Fig. 3 An exemplary of mutation operator

7 Selection Operator

The selection operator is derived from the mutation and crossover operators, where the binary chromosomes representation carry the information about their structures, and forms the special PGA options polynomials. Then, a specially developed program implements the algorithm to calculate the coefficients resulting from the applied linear regression. The regression result calculated from such equation represents the simulated dependence value, which are corresponding to the experimental points. Furthermore, the comparison of the analytically obtained values with the experimental values is done. The comparison is based on finding the absolute error, and the subsequent calculation is performed for the overall assessment of the deviation between analytically obtained dependence and the experimental data. As a rule, a general assessment means standard deviation (SD), but for the authors, the overall assessment is using the average value of the absolute error, as obtained from the analytical data.

As an example, the experimental data matrix $M^{exp}(v, a)$ from paper [4], conditionally designate 2 of its arguments, identified as x_1 and $x_2(M^{exp}(x_1, x_2))$.

The elements of matrix m_{ij}^{exp} are approximated by the dependence $\varphi^m(x_1, x_2)$, which can be obtained from the classical regression analysis. For calculating the estimated torque values with the function $F(x_1, x_2)$, the argument values x_1 and x_2 are corresponding to the same experimental data, and the matrix of with the calculated values $M^{calc}(x_1, x_2)$ is equal to $M^{exp}(x_1, x_2)$ dimension. The comparison of the respective matrix members is carried out by subtracting them, resulting in the matrix of errors:

$$\Delta M^{err}(x_1, x_2) = M^{calc}(x_1, x_2) - M^{exp}(x_1, x_2)$$

The members of the $M^{err}(x_1, x_2)$ matrix:

$$\Delta m_{ij}^{err} = m_{ij}^{calc} - m_{ij}^{exp}$$

represent the absolute error of the experimental dependence approximation $M(x_1, x_2)$ (floating and x_2 roll). This error can be both positive and negative. It is depending on the $M^{exp}(x_1, x_2)$ structure and the type obtained by the regression describing the data of the functions $\varphi^m(x_1, x_2)$. To unify the approximation assessment different techniques of the error sign exclusion from are considered. The present study used the module error, i.e.:

$$m_{ij}^{err} = \left| \Delta m_{ij}^{err} \right|$$

Thus, the estimation the approximation accuracy can be carried out according to 2 criteria

1. the average error for the entire set

$$m^{mid} = \frac{1}{n \cdot m} \cdot \sum_{i=1}^n \sum_{j=1}^m m_{ij}^{err}$$

2. the maximum error for the entire set

$$m^{max} = \max_{i,j} m_{ij}^{err}$$

The optimum was found by using the EGA zooid, provided that it gives the lowest value of the total deviation of the analytically obtained dependence from the experimental data. It is important to note that after performing the EGA simulations, the best found combination of the polynomial terms did not meet the specified accuracy. This fact indicates that the fragment under study needs to be, either broken down into the smaller fragments, or to be completely modified [6].

8 Example of Pseudo Genetic Algorithm for Fragment Approximation Sub-optimization

The proposed approach has been studied on the example of the matrix m , taken from a set of experimental data, which describes the dependence of the aerodynamic torque arising from the airship, on its speed v and the angle of its tilt α , taken from [4], and as shown in Fig. 4.

	500	1000	1500	2000	2500	3000
0	440	1148	2438	4470	6632	8989
10	330	944,9	2238	4299	6550	8916
20	-100	472,9	1732	3693	6060	8456
30	-700	-216,9	922,8	2911	5222	7884
40	-1550	-1037	70,5	1860	4179	6899
50	-2700	-1859	-1090	592,8	2877	5637
60	-4200	-2709	-2313	-864,5	1339	4081
70	-6300	-3515	-3562	-2445	-379	2288

Fig. 4 Initial matrix of experimental values

From the detailed examination of the matrix m , it has been found that its data have the significant non-linearity characteristics, which greatly complicates the data approximation process of this matrix m . Due to the approximation complexity of the entire matrix, to be treated at once, the authors applied the Cut-Glue method, which is described in detail in [4, 5]. The first step breaks the matrix m into fragments [6], in order to approximate each fragment separately. In Fig. 4, it is shown that the matrix m is divided into 4 fragments ($m11$, $m21$, $m12$, $m22$). The approximation algorithm for each fragment is identical.

The investigated dependence (fragment) is described using the full polynomial of the 2nd order. With the classical regression analysis, the polynomial coefficients are calculated, and then by using the obtained coefficients, the analytical values of the test matrix fragment are calculated too. Based on the analytically obtained values the maximum absolute error is calculated with the respect to the values, which are experimentally obtained. Further on, and in order to improve the accuracy of the studied approximation dependence (fragment) the full 3rd order polynomial is applied to calculate the coefficients of this polynomial, and with the obtained coefficients are used to calculate the analytical values of the test track. The analytical values represent the base to calculate the maximum absolute error. After this, the biggest absolute error is obtained applying the polynomial of the 3rd order, and it is compared with the largest absolute error obtained by the 2nd order polynomial. In the case, when the maximum absolute error is decreasing, it should be noted that the improvement was obtained at the transition and in accordance to the description of the higher order polynomial.

In general, it is assumed that the transition to the description of the fragment by the higher order of polynomial, improves the accuracy of the investigated dependency. In fact, this is not always respected. If the transition to the description by the higher degree polynomial, is significantly deteriorating the approximation quality, it

can be concluded that the description of the investigated dependency is incomplete and the n -th order polynomial can provide improvements for the approximation function accuracy, which is relative to the function obtained by the complete polynomial of the $(n - 1)$ degree.

The pseudo genetic algorithm is presented as the tool of the part-polynomial study. Within the framework of this specific research the initial part of the chromosome is taken, in order to meet the full chromosome polynomial of the $(n - 1)$ order, and during the pseudo genetic algorithm only the tail part of the chromosome vary, which is in charge of the n -th order. Thus, by using the proposed algorithm, the problem of structural and parametric optimization can be solved, more specifically, the problem to find the most appropriate polynomial structure of the approximation. If the structure variation of the polynomial tail part with n -improving degree description is not giving the investigated dependency, it should be noted that the most suited structure for the description of the studied dependency is the polynomial of the $(n - 1)$ degree.

With the procedures described above, and applied to each fragment, the following results were obtained, as shown in Table 1.

Based on the data presented in Table 1, it can be noted that at the transition for the fragment $m12$, from the polynomial of 2nd order to the polynomial of 3rd order the biggest relative error was reduced to ~ 3.20 (improvement was 56%), for the fragment $m21$ decreased by ~ 15.8 (improvement was 51%), for the fragment $m22$ at ~ 83.9 (improvement was 79%).

In Table 2, the missing values of the largest absolute error for the $m11$ and $m21$ fragments are completely described by the 4th order polynomial. This is due to the fact that in this particular case, the corresponding number of experimental data fragments is smaller than the full number of terms of the 4th order polynomial and the regression analysis of this type of description was omitted.

The data presented in Table 2 show that the fragment $m11$ is the most accurately described by the 2nd order polynomial. The $m11$ fragment description by 3rd order polynomial deteriorate the values of the biggest absolute error. However, there is the likelihood that the description of this fragment by using the partial 3rd order polynomial (number of members less than 12) may provide the best results. This is possible for $m12$ and $m22$ fragments, where the transition from the description of the relevant fragments of the complete polynomial of 3rd order to the complete

Table 1 Values of the biggest absolute error

Matrix fragment $m1$	The value of the biggest absolute error Degree of complete polynomial		
	2	3	4
$m11$	18.5	194	–
$m12$	46.7	26.4	18830
$m21$	32.4	16.6	–
$m22$	93.7	29.8	5535

Table 2 Top structure describing the fragments of studied dependences

Fragment of matrix <i>m</i>	Polynomial structure (chromosome)	Polynomial order	The biggest absolute error	The average absolute error
<i>m11</i>	11101	2	18.1	7.7
	111111110	3	10.1	3.1
<i>m12</i>	11111	2	46.7	22.2
	111111111	3	26.4	10.4
	111111111110110	4	23459	21519
<i>m21</i>	11111	2	32.4	13.9
	111111110	3	11.0	3.4
	111111111111000	4	1550.7	1390
<i>m22</i>	10111	2	90.7	54.6
	111110101	3	26.5	17.5
	111111111111110	4	20.5	8.6

polynomial of the 4th order gives a significant deterioration in the biggest absolute error. However, there is the likelihood that the description of this fragment by using the partial 4th order polynomial (number of members less than 15) may provide the best results. Also, in such cases (polynomial order is equal to 4 or higher) it is necessary to check the biggest absolute error values by describing the studied fragments by incomplete polynomials of smaller dimensions. In this way, it is worth noting that for the *m12* and *m22* fragments also makes sense that their incomplete description by polynomial of the 3rd order, as there is likelihood that any of the structures approximates its corresponding fragments better than all possible variations of the partial 4th order polynomial. For the fragment *m21* we can note the following: despite the fact that the description of the fragment is using the polynomial of the 3rd order, it gives a good result, to improve the accuracy of approximation is the meaning of its description with the help of an incomplete 3rd order polynomial.

It should be noted that in the case where the number of members of the full polynomial is small, the search of all possible variations of its incomplete form is easy to be done, but when the number of the complete polynomial members is large, the task of finding the best describing polynomial structure by trying all possible variations of its incomplete kind, turns into the NP-complete type problem. The authors propose to solve this problem by the PGA method described in this paper.

The structure of the input parameters of the used pseudo genetic algorithm includes: the size of the starting population = 100, the number of generations = 1000.

The best obtained values for each fragment under consideration are highlighted with the blue background. For the fragment *m11* the best finding value was

obtained by examining the partial 3rd order polynomial in the 15th generation, it has an absolute error ~ 10.1 and the average absolute error ~ 3.1 . For the fragment $m12$, the best value of the biggest absolute error has not improved, and corresponds to the complete 3rd order polynomial (absolute error ~ 26.4 , average error ~ 10.4). For the fragment $m21$, the best value was obtained from the incomplete 3rd order in the 17th generation, it has an absolute error ~ 11.0 and the average absolute error ~ 3.4 . For the fragment $m22$, the best value was obtained, when investigating the 4th order polynomial in the 7th generation, it has an absolute error ~ 20.5 and the average absolute error ~ 8.6 .

For example, it is worth noting that the transition to the description for the incomplete fragments of the higher degree polynomials does not always lead to the improved accuracy (the results obtained for the $m12$ and $m21$ fragments). In certain cases, even the best values of the absolute errors are obtained by the 4th degree polynomial is worse than the best values of the absolute errors obtained by using the 3rd order polynomial.

From the analysis of the data shown in Table 1, it can be stated that the description of the fragments with the complete polynomials, on average have the best absolute error, which was ~ 22.8 . However, after the application of the proposed pseudo genetic algorithm for the study of the partial polynomials, there was a significant improvement in the result (maximum absolute error was ~ 17) relative to that obtained with the help of the description of the test pieces according to complete polynomials, where the improvement was about 25.5%.

9 Conclusion

1. This study has shown that the use of hybrid CRA and proposed pseudo genetic algorithm was effective.
2. It is shown that the approximation is advisable to start by using CRA, by consistently exploring the experimental dependence, which starts with with the polynomials of the minimum order.
3. In the case of the accuracy deterioration found in the output result, when the transition to the polynomial of the next higher is made to resort to the use of pseudo-genetic algorithm (at low dimension of the problem, and a smaller polynomial order, direct combinatorial enumeration can be used).
4. The developed approach is a variant of the algorithm for the structural parameter optimization, which allows to find the suboptimal structure, thus the polynomials describing the studied fragments of the approximated based, and can be used as the instrument at the relevant stage of the “Cut-Glue” approximation method.

References

1. Vidyasagar M (1993) *Nonlinear systems analysis*, 2nd edn. Prentice Hall, Englewood Cliffs, New Jersey
2. Isidori A (1995) *Nonlinear control systems*, 3rd edn. Springer Verlag, London
3. Khalil HK (2002) *Nonlinear systems*, 3rd edn. Prentice Hall, Upper Saddle River, New Jersey
4. Neydorf RA (2015) Bivariate “Cut-Glue” approximation of strongly nonlinear mathematical models based on experimental data, *SAE Int J Aerosp* 8(1):47–54. doi:[10.4271/2015-01-2394](https://doi.org/10.4271/2015-01-2394)
5. Neydorf RA (2016) Technology of Cut-Glue approximation method for modeling strongly nonlinear multivariable objects, Theoretical bases and prospects of practical application, SAE Technical Paper
6. Neydorf RA, Chernogorov IV, Polyakh VV, Iarakhmedov OT (2016) Formal Characterization and Optimization of Algorithm for the Modelling of Strongly Nonlinear Dependencies Using the Method “Cut-Glue” Approximation of Experimental Data, SAE Technical Paper, doi:[10.4271/2016-01-2033](https://doi.org/10.4271/2016-01-2033)
7. Fisher RA (1954) *Statistical methods for research workers*. Oliver and Boyd, Edinburgh. ISBN 0-05-002170-2
8. Mogull RG (2004) *Second-semester applied statistics*, Kendall/Hunt Publishing Company, p 59. ISBN 0-7575-1181-3
9. Meade N, Islam T (1995) Prediction intervals for growth curve forecasts. *J Forecast* 14: 413–430
10. Dennis RC (1982) Sanford weisberg criticism and influence analysis in regression. *Sociol Methodol* 13:313–361
11. Lindley DV (1987) *Regression and correlation analysis*. New Palgrave: A Dictionary of Economics 4:120–123
12. Sen A, Srivastava M (2011) *Regression analysis—theory, methods, and applications*. Springer-Verlag, Berlin
13. Neydorf RA, Polyakh VV (2015) Metod mnogoextremalnogo poiska s ispol’zovaniem evolucionno-geneticheskogo algoritma I vyborochnogo kriteriya Studenta (Method of multi search using evolutionary genetic algorithm and sample t-test) *Innovacionnaya nauka*, 3, pp 135–140, Ufa. http://aeterna-ufa.ru/sbornik/IN_3.2015.pdf
14. Neydorf RA, Polyakh VV (2015) Issledovanie mnogoextremalnyh zavisimostey s ispol’zovaniem geneticheskogo metoda i odnovyborochnogo kriteriya Studenta, (Study of multi dependencies using an evolutionary genetic method and one sample Student’s t test), *MMTT-28*, Saint Petersburg, 6, pp 108–112
15. Neydorf RA, Polyakh VV (2015) Lokalizaciya oblastey poiska evolucionno-geneticheskogo algoritma pri reshenii zadach mnogoextremalnogo haraktera (Localization search scopes evolutionary genetic algorithm for solving problems of multi nature), *Nauka Proizvodstvo Tehnologija* 2(6):18–22
16. Neydorf RA, Chernogorov IV, Polyakh VV, Iarakhmedov OT (2015) Experimental study on solution possibilities of multiextremal optimization problems through heuristic methods. *Herald of DSTU, Rostov-on-Don*, №4 vol 15(83), pp 82–93
17. Neydorf RA, Chernogorov IV, Polyakh VV, Iarakhmedov OT (2016) Possibilities solving of multiextremal optimization tasks by heuristic methods, *H&ES Res* 8(2):16–25
18. Neydorf RA, Chernogorov IV, Polyakh VV, Iarakhmedov OT (2016) Study of heuristic algorithms in planning and optimization of routes problem in the environment with obstacles, *Proceedings of SFU, Technical science* №3(176), pp 127–143

Design and Manufacturing of a Dry Electrode for EMG Signals Recording with Microneedles

Araceli Guadalupe Santana Rayo, Luis Héctor Hernández Gómez,
Alejandro Tonatiu Velázquez Sánchez,
Juan Alfonso Beltrán Fernández, Juan Alejandro Flores Campos,
Guillermo Urriolagoitia Calderón, Víctor Manuel Santana Rayo
and Arturo Enrique Flores Peñaloza

Abstract Electromyography (EMG) is usually done with wet electrodes. They are commonly made with Ag/AgCl (silver chloride). In this case, an interface with the skin is created with a gel. The problem with such electrodes is that the signal is affected by the way the electrodes are fixed over the skin and the use of gel. Besides, they irritate the skin and they are sensible to artifacts of movement and other interferences. In order to avoid these problems, dry electrodes with micro-needles, which records the EMG signals, were manufactured. The microneedles

A.G.S. Rayo · L.H.H. Gómez (✉) · A.T.V. Sánchez · J.A.B. Fernández · J.A.F. Campos · G.U. Calderón

Instituto Politécnico Nacional Sección de Estudios de Posgrado e Investigación,
ESIME Unidad Zacatenco, Edificio 5. 3er Piso. Unidad Adolfo López Mateos.
Colonia Lindavista, 07738 Ciudad de México, México
e-mail: luishector56@hotmail.com

A.G.S. Rayo
e-mail: ara_0588@hotmail.com

A.T.V. Sánchez
e-mail: alexrobsis@hotmail.com

J.A.B. Fernández
e-mail: jbeltranf@hotmail.com

J.A.F. Campos
e-mail: alejandro.jhane@gmail.com

G.U. Calderón
e-mail: urri0332@hotmail.com

V.M.S. Rayo · A.E.F. Peñaloza
Universidad Tecnológica de la Región Norte de Guerrero. Dirección de Ingeniería
Metal-Mecánica, Edificio H, Planta Baja. Colonia Ciudad Industrial, 40030 Iguala,
Guerrero, Mexico
e-mail: rayo_1017@hotmail.com

A.E.F. Peñaloza
e-mail: ingarturo@gmail.com

pierced the stratum corneum of the skin. They improved the contact with the skin and avoided the interference caused by the dead cells. Besides, the application of a conductor gel and the preparation of the skin was not required. The microneedles were manufactured on a copper substratum with a laser beam. They were coated with gold, which is a biocompatible material. Although the size of the microneedles was very small, a good shape was obtained. The manufacturing process was carried out with a high precision and its repeatability was guaranteed. This manufacturing process is quick and cheap. The determination of the operation parameters of the dry electrodes was based on the contact impedance between the skin and the electrode. The performance of the proposed electrodes was compared with the performance of the commercial wet electrodes. The average impedance obtained were 6.5 and 9 k Ω for the wet and dry electrodes, respectively.

1 Introduction

The Mexican Health Service reported that there were 5 million individuals with a disability in our country in 2012. Besides, the National Academy of Surgery established that 75 individuals are amputated daily for different reasons [1]. As a result, there are 900,000 individuals, who are amputees and require a physiotherapeutic treatment. Regarding their monitoring and rehabilitation, electromyography (EMG) is required.

EMG is related with the recording and the analysis of the physiological signals from the muscles of the human body. Such signals give information about the state of activation of muscles and their intermuscular coordination [2]. Also, these signals are used in the development of a prosthesis. They give information about specific movements. The EMG signals are usually recorded with wet electrodes, which are made with Ag/AgCl (silver chloride). In this case, the electrodes provide an interface with the skin by using a conductive gel in conjunction with a skin preparation. This preparation consists in shaving and sanding the detection zone.

Despite its widespread use, the wet electrodes have limitations: (1) They cause irritations and skin allergies; (2) Time is required for the diffusion of the gel into the diverse skin layers; (3) If the gel spreads, a short circuit can take place; (4) Long term measurements can not be taken because the gel evaporates; and (5) The stiffness of the electrode does not allow to adapt properly to the skin, among other reasons.

An alternative is the employment of dry electrodes. They do not use any gel and a previous preparation of the skin is avoided [3, 4]. They have microstructures or microneedles over their surface. Some of them are capacitive or isolated. These dry electrodes are also employed in the recording of other biopotentials like electrocardiography (ECG) and during electroencephalography (EEG) [5–8].

Some design features of the dry electrodes, which are used in EMG applications, overcome the disadvantages of the wet electrodes [9–12]. However, they have a high impedance of contact. They are sensible to movement and other interferences. They do not have a proper contact with the skin and their manufacturing process is complicated. This generates a high cost of production.

The use of microneedles over the surface of the electrode allows a good contact with the skin. In this case, the electrode has a direct contact with the cells, as it penetrates the stratum corneum. One has to keep in mind that there are dead cells in this layer which increase the impedance and prevent the flux of an ion current to the electrode. The size of the needles is commonly small. As a results, the contact with the nerve terminals is avoided or the development some adverse effect on the cells. They do not cause pain and are not invasive.

In this paper, the design and manufacturing of a dry electrode with microneedles is presented. They record EMG signals. Besides, the microneedles improve the contact with the skin and the stability with the electrode. The small size of the electrode allows the detection of signals more precisely. The proposed dry electrode has a low manufacturing cost.

2 Materials and Methods

2.1 *Manufacturing of the Dry Electrode*

A micromachining process with laser was used in the manufacturing of the dry electrode. This manufacturing process is inexpensive and allows the production of diverse shapes in small scales. For this purpose a SMARK machine, model 500, was used. It is commonly used in jewelry manufacturing and engraving. In the case of this work, this machine was used in conjunction with Inkscape, version 0.91, code. This is an editor software.

The laser parameters, which were established initially, were the power, frequency and engraving speed, among others. Preliminary specimens were obtained. In this step, diverse manufacturing parameters were evaluated in order to obtain the best shape of the microneedles. Aluminum and copper were used to produce the required substrates. 22 specimens were produced. They are shown in Fig. 1. The first twelve have microneedles of 1 mm diameter. They were arranged in a 1.5 mm × 1.4 mm area. The other ten specimens have microneedles, whose diameter is 70 μm. They were arranged in an 8 mm × 4 mm area.

The final electrodes were manufactured with copper (see Fig. 2). They were 12 mm × 12 mm. They have 10 × 10 microneedles, which were separated by 1 mm. Their average height was 320 μm. The angle of the tip of each microneedle with respect to the base was 42.28°. In the final step, the electrodes were coated with a thin gold layer by electrodeposition. This is a biocompatible material.

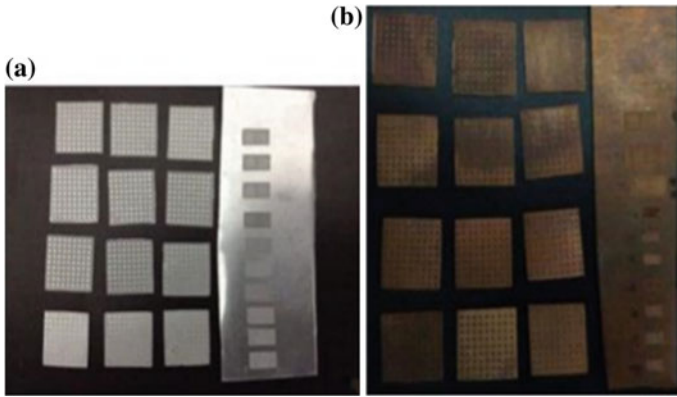


Fig. 1 Preliminary specimens. **a** Aluminum y **b** Copper

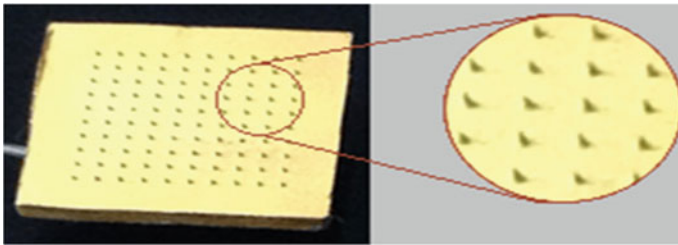


Fig. 2 A dry electrode

2.2 *Measurement of the Contact Impedance*

The contact impedance between the dry electrode and the skin was analyzed with the method of the three electrodes [13]. They were located on the forearm with adhesive tapes (Figs. 3 and 4). Before each measurement, the skin was cleaned with alcohol. The measurement circuit was developed with an instrumentation amplifier AD620, a generator of functions and a known impedance was established. Its proposed value was around $10^3 \Omega$. In this case, the skin was undamaged.

The circuit has two nets. The first was built with a function generator, an auxiliary electrode, the skin, the electrode which was evaluated, and the proposed impedance. The voltage drop across the electrodes and the skin was considered equal to zero, because the impedance of the skin is much lower. Thus, the current flowing in the net was the proposed impedance current.

The elements of the second net were the electrode which was evaluated, the skin, an auxiliary electrode and the input resistance of the amplifier. In this case, the impedance of the amplifier was high. Therefore, the current which flowed between the auxiliary electrode and the skin is minimum. As a result, the input voltage of the

Fig. 3 Schematic arrangement for the evaluation of impedance

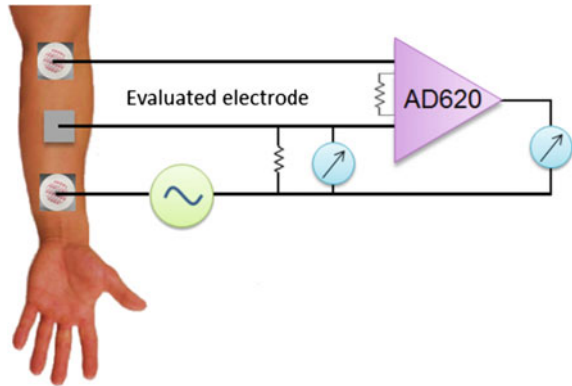
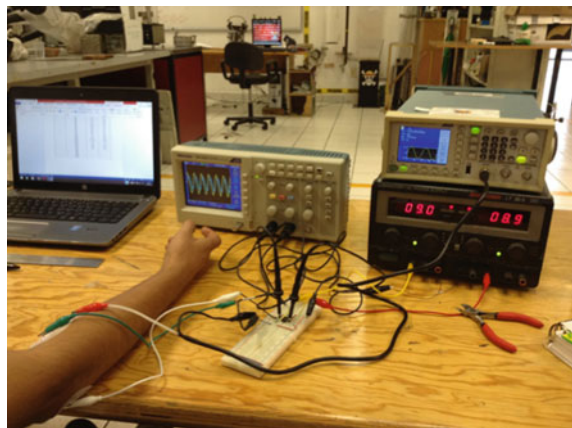


Fig. 4 Experimental setup for the evaluation of the contact impedance



amplifier in a differential mode was the voltage in the electrode which was evaluated. With this information, the voltage and the current at the electrode were known. The impedance was calculated with the following equation.

$$ZE = \frac{Vo_z}{GV_z}$$

where ZE is the impedance of the electrode which was evaluated, Vo and G are the output voltage and the amplifier gain, respectively, Z is the proposed impedance and V_z is the associated voltage.

Two series of data were collected in a wide range of frequencies. These evaluations were made with ten healthy individuals. The first set of data was recorded with a wet electrode which was fixed with gel. The second set of data was obtained with a dry electrode which was designed in this work. This task was done 24 h later with the same individuals. All the data was taken every 10 Hz in a range between 10 and 100 Hz. Later, these measurements were taken every 100 Hz in a range

between 100 and 1000 Hz. Finally, this process was repeated every 1000 Hz in a range between 1000 and 10,000 Hz. All the calculation were done with the equation mentioned above.

3 Discussion of the Results

3.1 Manufacturing of the Electrodes

Micromachining with laser beams is a simple manufacturing process. Different geometries can be obtained at diverse scales. In jewelry, manufacturing with laser beams is commonly used in the cut and engraving of very small pieces with a high precision. For this reason, this sort of machining was used in the fabrication of electrodes. In this case, microneedles with an excellent definition were obtained.

Preliminary specimens were made with aluminum and copper. They were analyzed with a metallographic microscope with inverted light (see Fig. 5). The results showed that all the specimens had microstructures with deformations.

The manufacturing parameters varied. This experience showed that the manufacturing process was complicated when the laser power was low and the microneedles were not obtained. On the other hand, if the power of the laser beam was increased, a good definition of the area of micro needles was observed. However, there is an upper limit of the power level. Furthermore, the engraving speed has to be around 200 mm/s. If this speed was increased, the material wore easily and a lower definition of microneedles was obtained. A 10 kHz frequency was selected. The incidence of the laser beam over the material was also evaluated.

With these ideas in mind, it was possible to obtain a good shape of the microneedles of the dry electrodes. Figure 6 shows the details of the microneedles. They have a conical shape, which easily allows a deeper penetration of the stratum corneum. The effective area of contact of the electrode with skin was established by the pressure at the instant in which the electrode was applied.

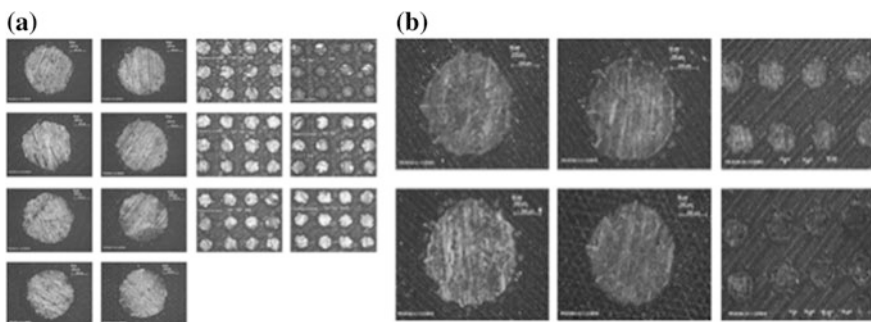


Fig. 5 Preliminary specimen made with **a** aluminum and **b** copper

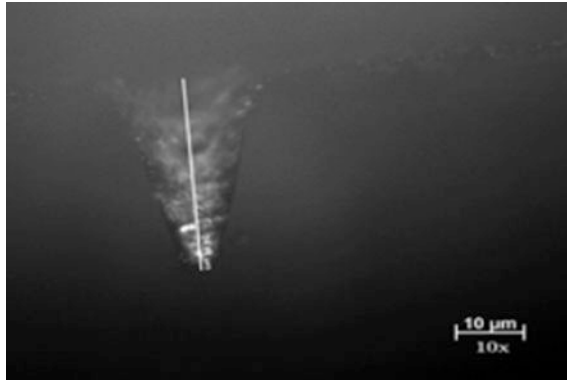


Fig. 6 Detail of microneedle

3.2 Measurement of the Contact Impedance

The interface which was developed between the electrode and the skin, was an important factor. It determines the quality of the recorded signal [14]. The EMG signal has a small range of amplitude (100 μV–90 mV). Thus, the signal is easily detected, when there is a good contact. In other words, the interferences developed by the skin deformation and movement artifacts has a lower impact. If the dry electrodes has such microneedles, the impedance generated by the dead cell is avoided.

Figure 7 shows the results of the impedance measurement at different frequencies. They were made with wet and dry electrodes with microneedles. It can be observed that the impedance was reduced as the frequency increased. The range of evaluation of an EMG signal was between 20 and 500 Hz. In this range, the signal has a greater power and the average impedance was 6.5 and 9 kΩ for the wet electrodes and dry electrodes, respectively. The impedance of the manufactured electrodes was greater. However, this value was considered as acceptable. The

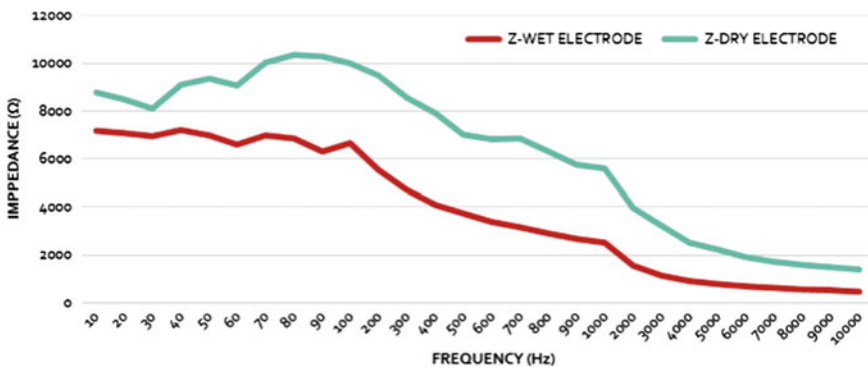


Fig. 7 Evaluation of the contact impedance with dry and wet electrodes

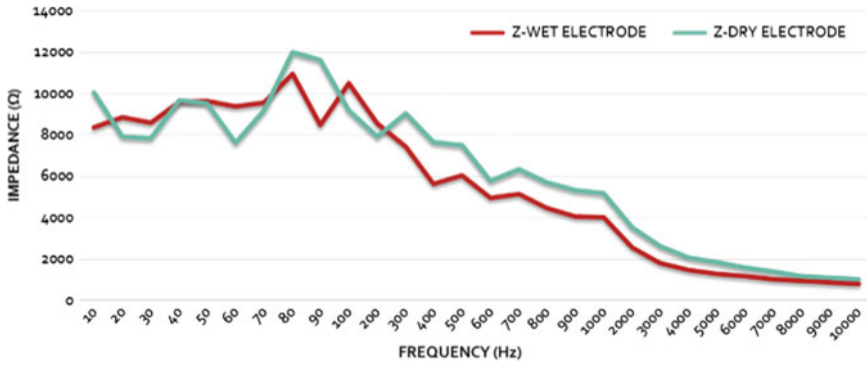


Fig. 8 Evaluation of the contact impedance with one individual

impedance variation was due to the location of the electrodes. While the wet electrodes have their own adhesive tape, the dry electrodes were placed on the skin with a band aid. In both cases, the glue irritated the skin. It is necessary to improve the way in which the electrodes were fixed to the skin.

Figure 8 illustrates the best evaluation obtained. The impedance of both electrodes had a similar behavior. The impedance in the range of interest was around 9 k Ω for each electrode. The average impedance was approximately 5.5 and 6 k Ω for the wet and dry electrodes, respectively. These results support the fact that the variation of the impedance, observed in Fig. 7, was due to an improper fixation of the dry electrode over the skin. However, as it was mentioned above, the impedance of contact of our dry electrode was low, even if they were placed with a band aid. These results are encouraging because the contact quality of the microneedles with the skin was improved.

4 Conclusions

A dry electrode with microneedles, for the evaluation of EMG signals, was manufactured. It was done with a micromachining process using a laser beam. Diverse sizes and a good geometry of the microneedles were obtained when small length of wave of the laser beam was used.

When the microneedles pierced the stratum corneum, the interface with the skin was improved and the contact impedance was reduced. The impedance behavior of the dry electrode, which is proposed in this work, was similar to the impedance of a wet electrode.

The small variations of the measurements with the dry electrodes originated due to their fixation over the skin. It is important to mention that the microneedles were unbroken during the evaluation of the contact impedance. Besides, the dry electrodes did not develop pain or irritation on the skin of the individuals.

Although these results are encouraging, it is necessary to evaluate the EMG signals. In this way, the criterion that supports this application can be obtained. Furthermore, more tests are required in order to evaluate the performance of the dry electrodes in a long term.

In accordance with a previous experience of the authors [15], it is possible to apply these results in the design of a robotic hand.

Acknowledgements The grants for the development of this project awarded by Consejo Nacional de Ciencia y Tecnología (CONACYT) and the Instituto Politécnico Nacional are kindly acknowledged. Besides, the support given by the Universidad Tecnológica de la region Norte de Guerrero is also kindly acknowledge.

References

1. Vázquez E (2015) Los amputados, un reto para el estado. Academia Nacional de Medicina, México, D. F. Acta de la sesión del 4 de marzo del 2015
2. Soderberg GL, Cook TM (1984) Electromyography in biomechanics. *Phys Ther J* 64:1813–1820
3. Searle A, Kirkup L (2000) A direct comparison of wet, dry and insulating bioelectric recording electrodes. *Physiol Meas* 21:271–283
4. Chi YM, Jung TP, Cauwenberghs G (2010) Dry-contact and noncontact biopotential electrodes: methodological review. *IEEE Rev Biomed Eng* 3:106–119
5. Griss P, Enoksson P, Tolvanen-Laakso HK et al (2001) Micromachined electrodes for biopotential measurements. *J Microelectromech Syst* 10:10–16
6. Ng WC, Seet HL, Lee KS et al (2009) Micro-spike EEG electrode and the vacuum-casting technology for mass production. *J Mater Process Technol* 209:4434–4438
7. Fonseca C, Silva JP, Martins RE et al (2007) A novel dry active electrode for EEG recording. *IEEE Trans Biomed Eng* 54:162–165
8. Chen Y, Pei W, Chen S et al (2013) Poly(3,4-ethylenedioxythiophene) (PEDOT) as interface material for improving electrochemical performance of microneedles array-based dry electrode. *Sens and Actuators B Chem* 188:747–756
9. Dias NS, Carmo JP, Ferreira da Silva A et al (2010) New dry electrodes based on iridium oxide (IrO) for non-invasive biopotential recordings and stimulation. *Sens and Actuators A* 164:28–34
10. Rajaraman S, Bragg JA, Ross JD et al (2011) Micromachined three-dimensional electrode arrays for transcutaneous nerve tracking. *J Micromech Microeng* 21:13
11. Forvi E, Bedoni M, Carabalona R et al (2012) Preliminary technological assessment of microneedles-based dry electrodes for biopotential monitoring in clinical examinations. *Sens and Actuators A* 180:177–186
12. Kaitainen S, Kutvonen A, Suvanto M et al (2014) Liquid silicone rubber (LSR)-based dry bioelectrodes: The effect of surface micropillar structuring and silver coating on contact impedance. *Sens and Actuators A* 206:22–29
13. Spach MS, Barr RC, Havstad JW et al (1996) Skin-electrode impedance and its effect on recording cardiac potentials. *Circ J Am Heart Assoc* 34:649–656
14. Webster JG (2009) *Medical instrumentation: application and design*. John Wiley & Sons, New York
15. Hernández-Gómez LH, Velázquez AT, Lugo E et al (2012) Research advances and perspective of multi-articulated and robotic hands. In: Öchsner, A, da Silva et al (eds) *Characterization and development of biosystems and biomaterials of the series advanced structured materials* 29, pp 109–128

Biped Robot Prototype Based on the Human Anthropometric Measurements

David Alvarado, Leonel Corona, Saúl Muñoz, Alfonso Campos and Alejandro Escamilla

Abstract This work presents the development of an anthropometric biped robot based on a system with inertial sensors. The objective is to obtain, quantify and analyse information to detect and correct the abnormal posture of the human body either at rest or in motion. The work is divided into 3 sections: 1. Obtaining variables describing the kinematics and dynamics of the bone elements to determine the position in the human body. 2. Imitation of the human body, 3. Quantification of body posture abnormalities at rest and in motion. Two products arise: the first sensorial system capable of obtaining the angles of movement of a person, and second, a biped robot prototype responsible for the imitation of movements.

Keywords Biped robot · Anthropometric measurements · Structural and electrical design

1 Introduction

The first section of this work starts with the creation of a biped robot prototype which emulates the articulatory movements of the human body, such as flexion, extension, adduction, abduction, supination and pronation, movements that can be found in the knees, hips, shoulders, elbows, and ankles.

D. Alvarado (✉) · L. Corona · S. Muñoz · A. Campos · A. Escamilla
IPN, CDMX, Mexico
e-mail: a.r.david92@gmail.com

L. Corona
e-mail: lcoronaramirez@hotmail.com

S. Muñoz
e-mail: antares_ars@hotmail.com

A. Campos
e-mail: ing_campos@hotmail.com

A. Escamilla
e-mail: aescamin@hotmail.com

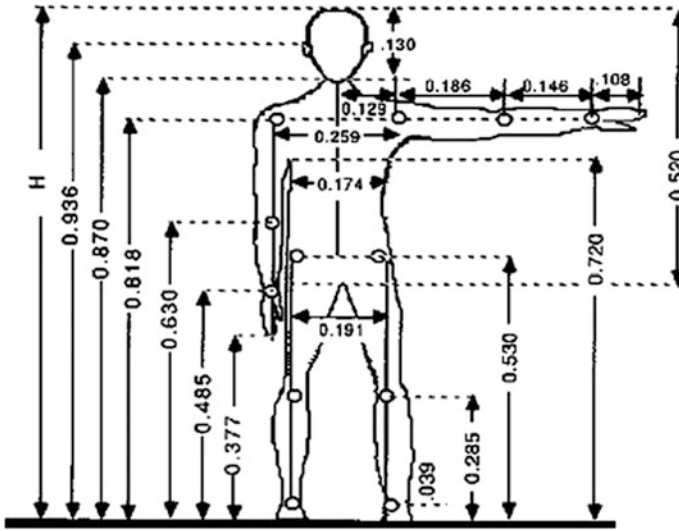


Fig. 1 Anthropometry of the human body [1]

It is planned to use an electric actuator type servomotor for the robot for each degree of freedom, making the final system with 18 DOF, all joints are rotational, a DOF joint to the knee, elbow, back and head, two DOF for ankles, hip and shoulder. The actuators have an operating range of 0–180 degrees.

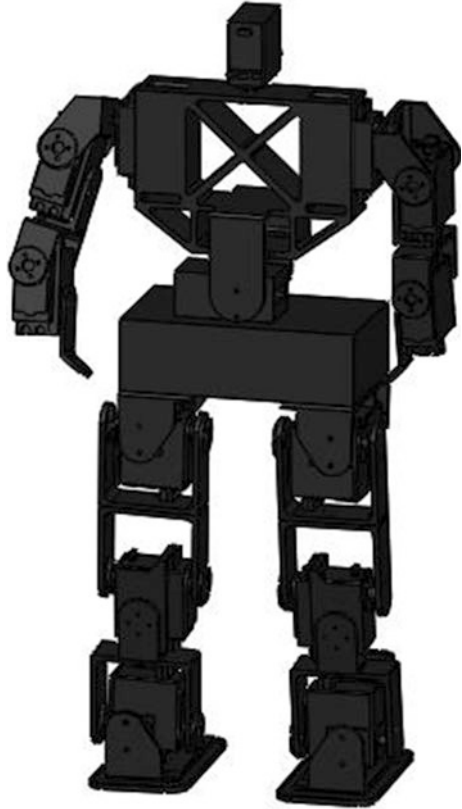
The anthropometry of the human body (see Fig. 1) shows how the proportions of upper and lower limbs affect locomotion while walking or to perform various activities. That is why it is vital for the development of this work to determine the longitudinal measures of extremities of the biped, to ensure a structural relationship to the Human Body.

Per the anthropometry of the human body shown in Fig. 1, a height of 43 cm for the biped robot was determined, using this relationship, the length for each joint of the robot is calculated. It can be stated that the biped robot respects the longitudinal values from the anthropometric human.

2 Mechanical Design and Construction of Robot

2.1 Design of Structural Parts

The design considerations for the structure of the biped robot are based on the anatomy of the lower and upper limbs of the human body. A model was made in CAD (Computer Aided Design) using the software SolidWorks 2014™. The morphology of structural elements was designed to accommodate the characteristics

Fig. 2 Biped robot assembly

of the actuators (TowerPro[®] MG995 [2]), such that the servomotors operate correctly.

The structural elements of the robot consist of 49 pieces, designed to support the 18 actuators, which in turn induce movements towards the biped.

Robot design has special features regarding the imitation of the human body movements such as flexion, extension in hip, knee, elbow and shoulder, adduction and abduction in hip and shoulder, pronation and supination in ankles, the tilt back and rotation of the head. Figure 2 shows the final assembly of the biped robot.

2.2 *Simulation of Stress Analysis*

Once the CAD model is generated, a simulation of stress analysis is performed thus verifying the parameters' set design, measuring the plastic deformation and the breaking point of each structural element. Such analysis is generated with the

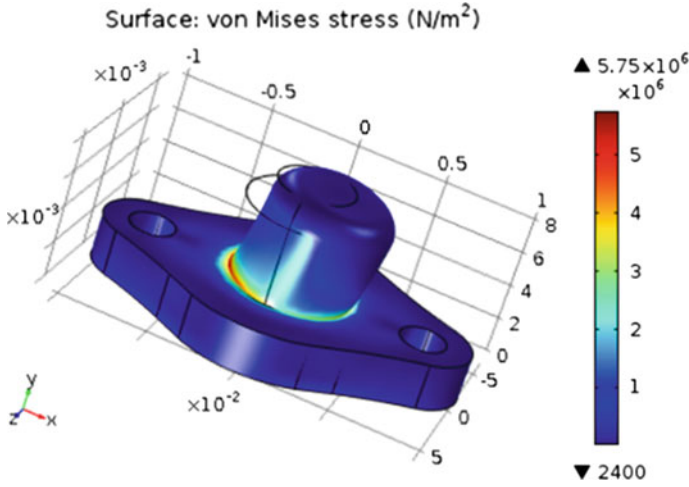


Fig. 3 Stress simulation in element “shaft”

assistance of the COMSOL 5.1™ software, where each structural part of the robot is under a load of 30 N, the theoretical weight of the biped. The material used in simulation is Acrylonitrile Butadiene Styrene, suitable for manufacturing the mechanical links. The material properties are presented in Table 2.

An example of the von Mises stress can be seen in Fig. 3. This information and the maximum strain experienced by elements are considered in the simulation parameters which indicate if the links and the material provide the required performance for the robot dynamics. The results are shown in Table 1. This data is related to Eqs. 1 and 2 respectively, where: σ_1, σ_2 and σ_3 are the greatest stresses acting on the element by applying a force, these are obtained from the stress tensor [3]. N (or safety factor) is the ratio of the efforts given by von Mises (σ_{VM}) and the maximum value of the tensile strength of the material (σ_m).

$$\sigma_{VM} = \sqrt{\frac{(\sigma_1 - \sigma_2)^2 + (\sigma_2 - \sigma_3)^2 + (\sigma_3 - \sigma_1)^2}{2}} \tag{1}$$

$$N = \frac{\sigma_m}{\sigma_{VM}} \geq 1 \tag{2}$$

In Table 1, it can be identified that the safety factor of each element is always greater than one, therefore, mathematically it ensures that the weight of the robot does not compromise the mechanical structure.

Table 1 Results of stress analysis

Piece.	Von Mises stress (Pa)	Displacement (m)	Safety factor
Foot base	1.14E+04	3.43E-09	3.73E+03
Foot	1.20E+06	1.81E-05	3.54E+01
Leg/Thigh	2.04E+06	1.32E-05	2.08E+01
Knee/Elbow	1.41E+07	3.88E-04	3.01E+00
Shell 1	1.35E+07	4.43E-04	3.15E+00
Shell 2	1.71E+07	3.98E-04	2.49E+00
Shell 3	1.13E+07	3.21E-04	3.76E+00
Shell 4	1.10E+07	3.15E-04	3.86E+00
Hip	6.89E+06	2.90E-04	6.17E+00
Back	1.00E+07	4.83E-05	4.25E+00
Arm	6.42E+06	4.73E-05	6.62E+00
Forearm	1.93E+06	8.86E-06	2.20E+01
Hand	2.23E+07	4.32E-04	1.91E+00
Shaft	5.75E+06	8.48E-06	7.39E+00

Table 2 Mechanical properties of ABS

Elongation at break	45%
Coefficient of friction	0.5
Resistance to traction	4.1–4.5 MPa
Density	1.05 g/cm ³
Young module	2.1–2.4 Gpa

2.3 Material Selection

3D printers work mostly with two materials, namely ABS and PLA. The mechanical properties of these two materials are very similar, but there are two points where a difference is clear; one is the elongation when the material breaks, and the other is the impact resistance. In general, these values have a greater magnitude in the ABS [4], and therefore this material was chosen. In Table 2 some features of this material are shown.

3 Electrical Design

3.1 Actuators

The TowerPro[®] MG995 [2] actuator controlling the movement of the links of the robot were chosen based on the torque exerted on the shaft of each servomotor. Using Eq. 3, where τ is the moment of force, F is the force applied to an element in

Table 3 Maximum torque between links

Links	Maximum torque ($N \cdot m$)
Hip and knee	0.3789
Hip and ankle	0.89123
Hip and foot	1.04
Hip and back	1.407
Shoulder and hand	0.336
Forearm and hand	0.249

this case is the weight, and d is the length of lever arm, ranging from the motor shaft to the end of the link, the maximum torques between the links was obtained, presented in Table 3.

$$\tau = F \cdot d \tag{3}$$

With the information shown in Table 3 and considering the maximum torque of the actuators of $1471 \text{ N} \cdot \text{m}$ it was concluded that the servomotors are suitable for use in the biped robot. The location of the servomotors and degrees of freedom of each member is shown in Fig. 4 and are located to respect the degrees of freedom.

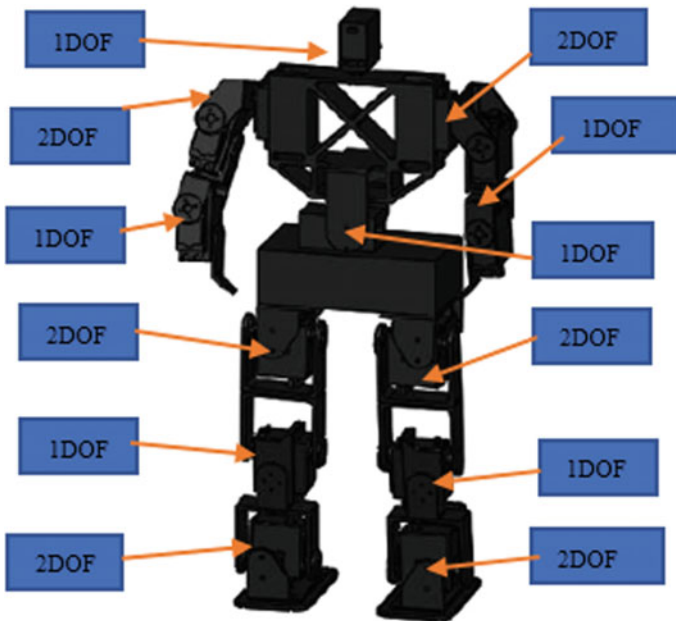


Fig. 4 Location of degrees of freedom robot

Fig. 5 Servomotor calibration system



3.2 Controller of Servomotors

The servo control system consists of ten microcontrollers implementing a communication protocol of type I^2C , a Bluetooth[®] 2.0 receiver (HC-05) [5], and 4 voltage regulators.

The master microcontroller (ATmega48 [6]), is responsible for receiving and processing instructions generated by the Bluetooth[®] receiver and synchronize the slave microcontrollers (ATmega8 [7]), which have as main function the transmission of PWM (Pulse-Width Module) signals to each of the eighteen motors.

Since the actuators are not able to generate a normal position with respect to the PWM signal, a system was developed to calibrate the servo motors, as shown in Fig. 5.

The system calibration gives two particularities for each servomotor; first, the characteristic response curve of the PWM, with respect to control angle, and second, the transfer function present at the frequency of oscillation. In Fig. 6 the answer obtained in a typical response of the servomotor is observed.

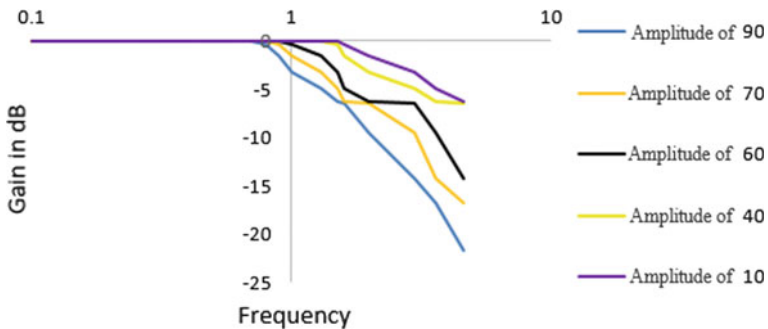


Fig. 6 Frequency response graph of the servomotor

From Fig. 6, it can be noted that the gain of the servomotor depends on two factors; the oscillation frequency and the range of the ranging amplitude.

To characterize the response of the servomotor, the most critical case observed in the graph is considered. This event occurs when the motor acts in the entire amplitude range.

When acquiring the actuator response, the maximum operating speed is obtained and its transfer function performed. The maximum speed reached is 360°/s. With this information, we ensure that the system works correctly if the speed is not exceeded.

The transfer function of the servomotor is adapted to the needs of the dynamics of the robot, and is valid in the operating range of the servomotor from 0° to 180°. With the information obtained in the test, it can be stated that for any amplitude a frequency response is required. Equation 4 shows the transfer function of the engines.

$$H(s) = \frac{88.83}{s^2 + 18.85s + 88.83} \quad (4)$$

The supply of electric power to the servomotors was determined by three main features, which are the type of battery, the current, and the voltage required by each engine to work properly. It was decided to use 4 controllers, XL4015 DC to DC Buck-based chip controllers capable of performing efficiency up to 96% to 5 A, ensuring lower power dissipation and allowing heat durability of the power supply.

Practically, one Buck controller was enough to feed 5 servomotors. This was achieved by measuring the current to the uncharged servomotor and taking the maximum current value. Such measurements were made with the current sensor ACS712. The experiment was performed by connecting the sensor to power the servomotor, then transmit a sine wave PWM, with an amplitude from 0° to 180°, a frequency of 1 Hz and a power of 6 V.

Current measurements were performed each 0.008 s obtaining the data shown in Table 4. To obtain current data it is remarkable that the maximum current is 1 A, appearing when the servomotor rotation changes. To ensure that the regulator provides adequate current, the maximum value of consumption and the amount of maximum current the regulator gives are considered.

The power supply is an indispensable component for the robot to work as planned, with characteristics, such as greater than or equal to 6 V (recommended

Table 4 Current consumption of servomotor MG995

Consumption	Current (A)
Maximum	1
Typical	0.1324
Typical 18 servos	2.3830

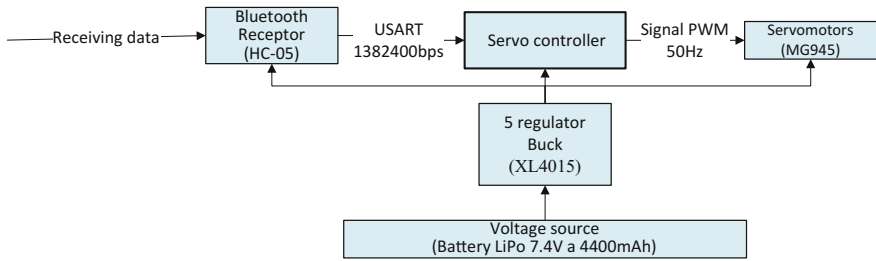


Fig. 7 Block diagram of the electronic system

voltage for the MG995) of voltage, size, portability and amperage. Because the robot is designed to work wirelessly via a LiPo battery with 7.4 V and 4.4mAh with 20 °C maximum discharge units was chosen.

Another factor of consideration for the choice of battery is the battery discharge (represented by the letter C), since with this information we know the maximum amount of current that the source provides. In this project to calculate the minimum C, the worst case current consumption was considered and it was found that the battery must have at least 3C. This value confirms that the battery will not exhibit defects to the supply power of the biped.

The block diagram of the control system and powered is presented in Fig. 7.

4 Format of Communication with the Controller of Servomotors

To send an instruction to the servo controller, is necessary to have a Bluetooth® 2.0 transmitter and establish a communication UART (Universal Asynchronous Receiver-Transmitter) [8] with the following characteristics:

- Transmission speed: 1382400 baud.
- Stop bits: 2 bit.
- Data bits: 8 bits.
- Parity: Pair.

Furthermore, the vector or word transmission must contain nineteen elements or bits, where the last bit is the character of instruction given to the decimal value 255. In Table 5 the function of each vector presented bite.

Highlighting that the values within each byte is 8 bits, therefore, they can only enter values between 0 and 255, where the value of 90 is the central value of the servomotor, if is available increasing the value of servomotor counterclockwise, otherwise decrease the value if it will progress clockwise.

Table 5 Vector transmission characteristics

Byte	Angle to modify	Byte	Angle to modify
1	Back frontal	11	Left femur frontal
2	Right humerus sagittal	12	Right tibia sagittal
3	Right humerus frontal	13	Left tibia sagittal
4	Left humerus sagittal	14	Right foot sagittal
5	Left humerus frontal	15	Right foot frontal
6	Right forearm frontal	16	Left foot sagittal
7	Left forearm frontal	17	Left foot frontal
8	Right femur sagittal	18	Head
9	Right femur frontal	19	End instructions.
10	Left femur sagittal		

5 Mathematical Model of the Robot

The powertrain provides information on the position in space of each of the elements that comprise the robot. For modeling the Denavit-Hartenberg algorithm was taken as reference as shown in Fig. 8, which represents the robot joints and their separation.

Using the Denavit-Hartenberg algorithm [9], the parameters of the kinematics of the right leg, left leg, right arm and left arm were obtained. These parameters are presented in Tables 6 and 7. From this data, rotation and translation matrices of the links and their homogeneous transformation matrices were generated.

6 Performance Testing of Robot

To verify the performance of the servomotors, a test signal was sent to a motor specifically for the case of the actuator representing the left shoulder. The signal sent is shown in Eq. (5).

$$f(x) = 80\sin(2\pi * 0.05t) \quad (5)$$

To check the engine behavior facing a sinusoidal signal, image processing is performed, on a video with a duration of 60 s. By using white markers and circular shapes, the angle is calculated from a reference point and a moving point. To obtaining said angle, we resorted to the method of the Hough transform [10] to find the radio and the position in the plane of the markers and then find the angle using the arctangent, as shown in Fig. 9, where markers are enclosed within a red circle.

As is observed in Fig. 9, the reference point is positioned at the right end of the image while the moving point is located on the left side. Using the MATLAB® software, where video processing is performed, for every ten frames an image is

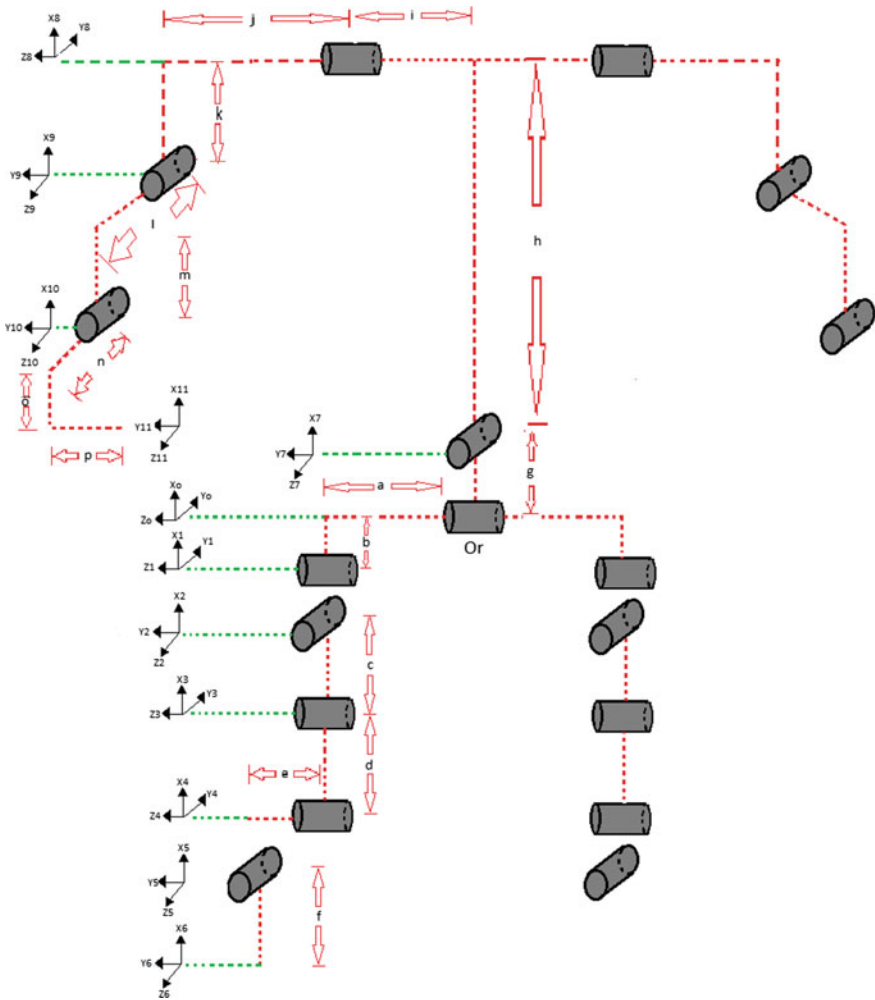


Fig. 8 Denavit-Hartenberg model of the robot

Table 6 Denavit-hartenberg parameters of the biped legs

Link	Right leg				Left leg			
	θ	d	l	α	θ	d	l	α
1	0	b	-a	0	0	-b	-a	0
2	θ_1	0	0	90	θ_1	0	0	-90
3	θ_2	0	-c	-90	θ_2	0	-c	90
4	θ_3	0	-d	0	θ_3	0	-d	0
5	θ_4	e	0	90	θ_4	-e	0	-90
6	θ_5	0	-f	0	θ_5	0	-f	0

Table 7 Denavit-hartenberg parameters of the biped arms

Link	Right arm				Left arm			
	θ	d	L	α	θ	d	l	α
1	0	0	-g	90	0	0	-g	90
2	θ_6	0	h	-90	θ_6	0	h	-90
3	θ_7	i + j	-k	90	θ_7	-i-j	-k	-90
4	θ_8	l	-m	0	θ_8	L	-m	0
5	θ_9	n	-o-p	0	θ_9	n	-o + p	0



Fig. 9 Show the markers

taken in which the angle is calculated between the two points. At the end of the path 52 samples were obtained as shown in Fig. 10.

According to the previous figure, the engine performance is very similar to the test signal. The error between the two signals was calculated, this test ensuring that the robot will respond appropriately. Other relevant data is the correlation between the two signals, which means that the relationship between the two signals is 99.76% with a phase difference of 0.069° causing a delay between signals of 0.022 s.

Using the calibration, system it was possible to get the error (Root Mean Squared Error) and behavior of all servomotors. In accordance with the results of the Table 8, we found that the error does not exceed 1.06 degrees and that the behavior of the actuator tends to be linear (see Fig. 11).

Fig. 10 Result of image processing

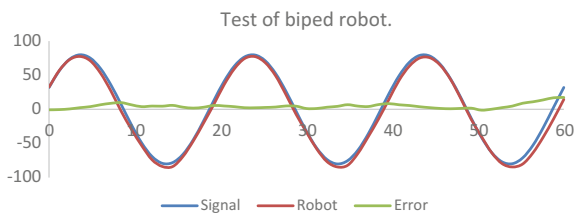


Table 8 Error of the servomotors

Error	Servomotor	Error	Servomotor
0.43°	Back frontal	0.32°	Left femur sagittal
0.38°	Right humerus sagittal	0.58°	Left femur frontal
0.47°	Right humerus frontal	0.38°	Right tibia sagittal
1.06°	Left humerus sagittal	0.68°	Left tibia sagittal
0.58°	Left humerus frontal	0.45°	Right foot sagittal
0.5°	Right forearm frontal	0.35°	Right foot frontal
0.46°	Left forearm frontal	0.27°	Left foot sagittal
0.35°	Right femur sagittal	0.37°	Left foot frontal
0.6°	Right femur frontal	0.67°	Head

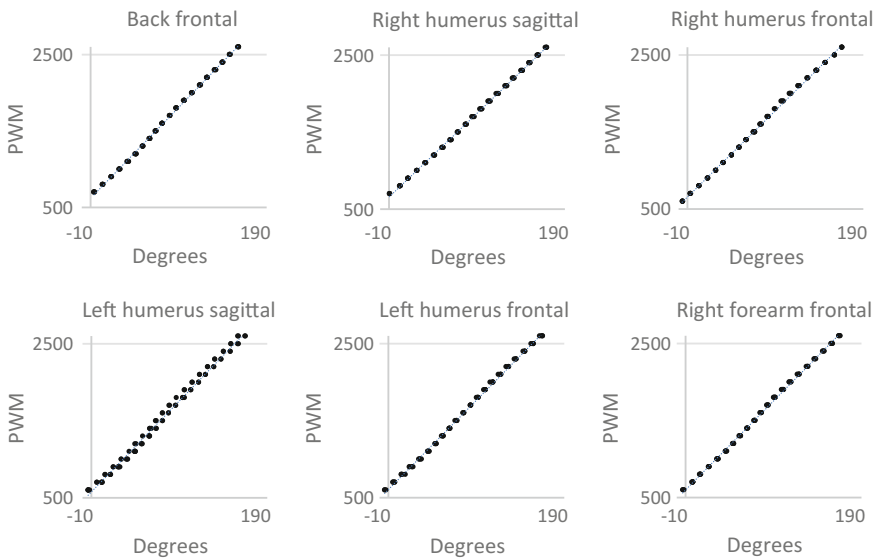


Fig. 11 Behavior of the servomotor. Angle versus PWM

7 Conclusion

In this paper the first breakthrough is presented in the development of a system of monitoring and correction of anomalies in the position of an individual, this being the first step in the development of a biped robot. Thus, the following has been achieved.

It is demonstrated that the robot constructed complies with the anthropometric measurements of the human. In addition, the chosen actuators are correct for the development of this work, since the maximum torque at each engine is subjected is

below the maximum torque according to the sheet specifications. Regarding the structural design of the robot we can affirm that the links are strong enough to support its own weight, if the robot is used for walking.

The electrical system designed to power the servomotors performed satisfactorily at controlling. Because the accuracy and torque are directly related to current, the electrical system also obtained an additional feature which helps prevent damage to the servomotor by excess current. The servomotor controller card is capable of generating communication with up to 20 actuators, the implementation of a communication protocol UART and Bluetooth[®] 2.0, allow the robot can be controlled by several electronic devices, as long as they present a communication of this type.

The actuators respond adequately to any data entry, if the received signal does not exceed a frequency of 50 Hz. The concept of imitation, it is established, to achieve a relationship between reception of data and their execution, it can be ensured, with the results obtained during the experiments, that the construction of the biped robot can help us monitor and analyze the position of an individual.

References

1. Drillis R, Contini R (1966) Body segment parameters. New York University, School of Engineering and Science, New York, N.Y
2. Geelmed SRL (2008) TowerPro MG995 Alta Velocidad & Torque, Servo Digital. http://www.geelmed.com/documents/products/producto_000000132DOC.pdf?d=1312813326. Accessed 4 May 2015
3. Mott R, Córdova Just A (1995) Diseño de elementos de máquinas. Prentice Hall Hispanoamericana. México
4. Kalpakjian S, Schmid S, Jaime Espinoza Limón (2008) Manufactura, ingeniería y tecnología. D.F. Pearson Educación, México
5. Huang A, Rudolph L (2007) Bluetooth essentials for programmers. Cambridge University Press, New York, NY
6. Atmel[®] (2015): ATMega48. Available.<http://www.atmel.com/images/doc2545.pdf>. Accessed 20 Apr 2015
7. Atmel[®] (2013) ATMega8. http://www.atmel.com/images/atmel-2486-8-bit-avr-microcontroller-atmega8_1_datasheet.pdf. Accessed 20 Apr 2015
8. Tomasi W, García Bisogmo V (1996) Sistemas de comunicaciones electrónicas. Prentice Hall, México
9. Reyes Cortes F (2012) Matlab aplicado a robótica y mecatrónica. Alfaomega Grupo Editor
10. Lira Chávez J (2010) Tratamiento digital de imágenes multispectrales. UNAM. México, D.F